AN EXPERIMENTAL STUDY OF EDDY DIFFUSIVITIES AND EDDY VISCOSITIES FOR CASES OF ANISOTROPIC AND NON-HOMOGENEOUS TURBULENCE IN SUSPENSION FLOW

Thesis by

Gary Eugene Whatley

In Partial Fulfillment of the Requirements

for the Degree of

Doctor of Philosophy

California Institute of Technology

Pasadena, California

1982

(Submitted August 27, 1981)

This thesis is dedicated to my parents,

Thelma and Luther Whatley.

ACKNOWLEDGMENTS

I would like to thank Dr. William H. Corcoran for his support and guidance in all areas of this work.

The funding provided by the Donald E. Baxter Foundation and the American Heart Association, Greater Los Angeles Affiliate, is gratefully acknowledged.

I would like to thank Hollis Reamer for his invaluable assistance in setting up and trouble shooting the experimental apparatus used in this study. The construction of the experimental apparatus would not have been possible without the assistance of George Griffith and John Yehle.

The time I spent at Cal Tech was enriched by the presence of Samir Barudi, Russ Bone, Mike Duncan, and all the members of the Chemical Engineering Department. In addition to my friends and associates at school, I greatly appreciated the friendship and support of Phil Craig, Gary Baccus, Bob and Donna Riegel, and Richard and Cyndie Riegel.

The completion of this thesis would not have been possible without the time and effort expended by Donna Riegel in the typing of this manuscript.

Finally, I would like to express my love for my parents, Thelma and Luther Whatley, whose patience, love, and understanding made my entire education possible.

ABSTRACT

An experimental study on the motion of small particles, about 120 microns in size, in turbulent pipe flow was completed. The goal of the study was to determine the effects of the anistropic, non-homogeneous turbulence generated by the pipe wall on the motion and diffusion of the particles. Measurements of the mean and rms velocities in the r, θ, and z directions were made on flows with Reynolds numbers of 8,400, 12,500, 16,700 and 20,900 for both the continuous and disperse phases. Values of eddy diffusivities for the particles and eddy viscosities for the continuous phase were determined.

Experimental data were obtained for the continuous phase (de-ionized water) in order to characterize the four flows used. All velocity measurements on the water were made at axial positions in the flow channel where the flows were fully developed. Mean velocities in the z direction were found to be well represented by the equation $u^+ = 4.0 + 2.9 \ln y^+$ over the range from $y^+ = 50$ to 550 where u^+ is a dimensionless velocity, $u^+ = \bar{V}/(\tau_o/\rho)^{\frac{1}{2}}$ and y^+ a dimensionless length, $y^+ = (y/\nu)(\tau_o/\rho)^{\frac{1}{2}}$. The buffer region in the flow was found to extend out to $y^+ = 50$. The kinematic eddy viscosity, ν_e, for each flow-rate was calculated from the velocity data. The maximum values for ν_e were 0.22, 0.33, 0.43, and 0.47 cm^2/sec for the flows at R_e = 8,400, 12,500, 16,700,

and 20,900, respectively. The maximum values of ν_e were found to occur at $r/r_o = 0.63$ for all four flows. The rms velocities of the water for the r, e, and z directions were measured across the flow channel. The measurements of the z component of the rms velocities at the center of the pipe were compared with measurements of other investigators. Figure 4.23 shows the values of $(\overline{v_z'^2})^{\frac{1}{2}}/\overline{U}_{\text{℄}}$, where $\overline{U}_{\text{℄}}$ is the mean velocity on the channel centerline, measured by invasive methods are smaller than those measured non-invasively.

Mean velocity measurements of the PVC particles showed that the velocity profiles of the particles did not develop as quickly as the velocity profiles of the fluid phase. Experimentally measured rms velocities of the particles in the r, e, and z directions were obtained at several radial positions across the channel. Other investigators have measured rms velocities of particles at the center of the channel or have calculated them from diffusion data which yields average rms velocities.

In the experiments performed in the study the values of the axial rms velocities of the particles were found to be smaller than the same values for the liquid. The r and e components for the particles did not exhibit constant relationships with the water as did the z component. The radial diffusion of the PVC particles outward from a point source was found to be inhibited after an initial diffusion

distance. The eddy-diffusion coefficients for the initial zone of diffusion were 0.31, 0.48, 0.66, and 0.72 cm^2/sec, respectively for the four different Reynolds numbers. Values of the turbulent Schmidt numbers calculated over the same region of flow were 0.45, 0.42, 0.47, and 0.74 respectively. The eddy-diffusion coefficients determined for the region of flow in which the inhibition occurred were respectively found to be 0.13, 0.17, 0.22, and 0.25 cm^2/sec. The corresponding values for the turbulent Schmidt numbers calculated with the diffusion coefficients from the region of inhibited spread were 1.39, 1.54, 1.54, and 1.56.

TABLE OF CONTENTS

LIST OF TABLES

LIST OF FIGURES

NOMENCLATURE

a_d	Non-dimensional diffusion coefficient, E_d/v^*D
a_{ds}	Non-dimensional particle diffusion coefficient; E_{ds}/v^*D
C	Concentration of diffusing species
C_a	Concentration of diffusing species at height a
C_r	Concentration of particles with settling velocity w_r
D	Pipe diameter
D_n	Nozzle diameter
d	Particle diameter
$\bar{e}_s$, $\bar{e}_i$	Unit vectors in scattering and incident directions
E_d	Eddy diffusion coefficient
E_{ds}	Eddy diffusion coefficient of a solid particle
$E_{ds,l}$	Eddy diffusion coefficient of a solid particle in lower 1/2 of pipe
$E_{ds,u}$	Eddy diffusion coefficient of a solid particle in upper 1/2 of pipe
f_s, f_i	Frequency of scattered and incident light
f_d	Doppler frequency
h	Height of water in rectangular water flow
I	Constant value of correlation coefficient
L	Length of flow channel over which pressure drop is measured
ℓ_1, ℓ_2	PVC particle dimensions
ℓ	PVC particle size; $\sqrt{\ell_1 \ell_2}$
n_i	Refractive index of medium i

P_e	Peclet number
p	Pressure
Δp	Pressure drop
R_e	Reynolds number
$R_p(t)$	Particle correlation coefficient
R(w)	Lagrangian correlation coefficient
r	Radial position in pipe flow
r_o	Pipe radius
r_o^+	Non-dimensional pipe radius; $(r_o/\nu)\sqrt{\tau_o/\rho}$
S	Relative density between particle and liquid
S_{CT}	Turbulent Schmidt number
T	Time of diffusion
T_l	Length of time over which lagrangian velocities remain correlated
T_{lat}	Integral time scale in the lateral direction
T_p	Particle relaxation time
t	Time
U_n	Velocity of fluid exiting from a nozzle
$\bar{U}_z$	Mean axial velocity in pipe flow
u+	Non-dimensional velocity parameter; $\bar{U}_z/v^*$
u	Lagrangian velocity of a fluid element
$\bar{V}_p$, $\bar{V}_f$	Particle and fluid average velocities over range $r/r_o \leq 0.8$
$\bar{V}_{str}$	Mean velocity in streamwise direction
v_r', v_θ', v_z'	Fluctuating velocity components in cylindrical coordinates

v^*	Friction velocity; $\sqrt{\tau_o/\rho}$
v_o	Initial velocity of a particle injected into a quiescent fluid
v_p	Particle settling velocity in a quiescent fluid
W	Average settling velocity
w_r	Settling velocity of a fraction of particles
x	Distance of travel of a particle
y	Distance from channel wall
y+	Non-dimensional distance; $(y/\nu)\sqrt{\tau_o/\rho}$
y_a	Distance from channel bed to reference position

Greek Symbols

μ	Molecular viscosity
ν	Kinematic viscosity
ν_e	Kinematic eddy viscosity
ξ	Dimensionless eddy diffusivity
ρ	Fluid density
ρ_p	Particle density
τ_o	Wall shear stress
ψ	Stokes number
ω	Time inverval
λ	Wave length of laser light
α_i	Angle of transmittance in medium i
σ	Standard deviation of gaussian curve

CHAPTER 1

INTRODUCTION

There are many areas in engineering design where the ability to predict the behavior of a flowing suspension is necessary for the design and construction of a unit to process the suspension. Some typical and important processes that involve suspensions are:

1) Transport of coal by slurry pipeline.
2) Oxygenation and dialysis of blood.
3) Solids removal from sewage and other waste water.

Suspensions can be composed of very small particles of micron or submicron sizes, such as in blood where the red-blood cells are on the order of 8 microns in diameter, up to particles with diameters as large as several centimeters, such as coal particles being transported by slurry pipe-line.

Flow behavior of slurries can be estimated by use of a bulk viscosity that treats the slurry as a homogeneous fluid, correlations derived from experimental data predicting the pressure drop and critical velocities in slurry pipeline flow, and the effective particle-diffusion coefficients for prediction of concentration profiles of particles across a pipe or channel. The evaluation and prediction of diffusion coefficients for suspended particles in turbulent flow are topics in need of much more work.

Diffusion coefficients of particles have been previously measured for (1) the spread of small particles (50 to 100 microns) in mesh-generated, wind-tunnel turbulence and in turbulent jets of air and (2) the diffusion in liquids of large particles (500 to 5000 microns) in the central region of turbulent pipe-flow and in turbulent flow in rectangular channels. Measurements of diffusion coefficients for small particles ($\sim$100 microns and smaller) in turbulent pipe-flow of liquids have not been made. It should be emphasized that where determinations of particle-diffusion coefficients have been made, the turbulence has approached the state of being isotropic and homogeneous such as in wind tunnels and in the core region of pipe-flow.

There are many situations in which the suspended particles are subjected to turbulence which is neither isotropic nor homogeneous. Two examples of flows of this type are the motion of red-blood cells through artificial heart valves and the motion of suspended particles in regions of pipe-flow where both shear and correlation among the fluctuating-velocity components exist.

The goal of the present work was to determine the effect of velocity gradients and Reynolds stresses in three coordinate directions on the motion and diffusion of a particle in turbulent pipe-flow. Before studying the motion of the particles, the mean and rms velocities of the sus-

pending water were measured so that the four flow-rates used could be characterized. Once the velocity data for the water had been collected, the velocity and diffusion data for the 120-micron particles of polyvinylchloride were obtained.

CHAPTER 2

BACKGROUND

2.1 General

In this chapter a review of both continuous and disperse-phase experiments has been made. The work that has been reviewed was that which was directly applicable to the experimental work discussed in this thesis. The review of continuous-phase investigation treats measurement of velocity by means of a single probe in the flow. The review of the disperse-phase studies treats the motion and diffusion of solid particles in turbulent flows.

2.2 Mean Velocity

Velocity distributions in channel flow have been investigated by many experimenters. Laufer (2-26), Schlinger and Sage (2-40), and Corcoran, et al. (2-12) have studied turbulent flow between parallel plates. Deissler (2-15), Sleicher (2-43), Nedderman (2-32), and Hettler, et al. (2-18) have studied velocity fields in turbulent pipe-flow.

A useful form for the correlation of experimentally measured turbulent velocities was proposed by von Karman (2-50). In the analysis, turbulent flow was considered to be composed of three regions. These three regions are known as:

1) viscous sublayer

2) buffer region

3) turbulent region

In dealing with these regions, the distance from the wall and the velocity were put in non-dimensional form with

$$u^+ = \bar{V}_{str} / (\tau_o/\rho)^{\frac{1}{2}}, \text{ and} \tag{2.1}$$

$$y^= = (y/\nu)\ (\tau_o/\rho)^{\frac{1}{2}}, \tag{2.2}$$

where $\bar{V}_{str}$ = the mean streamwise velocity

y = the distance from the wall,

τ_o = the wall shear stress,

ρ = the fluid density,

and ν = the kinematic viscosity.

The quantity $(\tau_o/\rho)^{\frac{1}{2}}$ has the dimensions of velocity and is referred to as the friction velocity.

Several investigators (2-38, 2-43, 2-15, 2-26) have found the velocity distribution across the viscous sublayer to be

$$u^+ = y^+. \tag{2.3}$$

The range over which Equation 2.3 is considered valid is from $y^+ = 0$ to $y^+ = 5$. Nedderman (2-32) used a photographic technique for velocity measurement that allowed instantaneous velocities to be measured down to $y^+ = 2$. In the viscous sublayer he found velocity fluctuations whose mean was close to the distribution given in Equation 2.3. These velocity fluctuations indicated that the flow was not purely

laminar. Popovich and Hummel (2-38) used a tracer injection and photographic method to measure velocities very close to the wall. They found a region, $y^+ \leq 1.6 \pm 0.4$, in which a linear velocity gradient was always present. This region was considered to be a laminar sublayer.

In the turbulent region the non-dimensional velocity, u^+, has been found to be well fit by a logarithmic velocity profile

$$u^+ = \frac{1}{K} \ln y^+ + C_n \qquad (2.4)$$

where y^+ is the non-dimensional distance from the wall and K and C_n are constants. Equation 2.4 was first developed for flow next to a flat plate, and the turbulent region under consideration was assumed to be close enough to the wall for the shear stress to be constant and equal to the wall shear stress. Howarth (2-20) points out that the agreement between experimentally observed velocities and the logarithmic velocity profile must be regarded as empirical and not a justification of the assumption of constant shear stress. The distance from the wall where Equation 2.4 begins to be valid is approximately $y^+ = 30$. The values of K and C_n that best fit the data in the turbulent region vary to some extent. Deissler (2-15) used values of $K = 0.36$ and $C_n = 3.8$ to fit his data. Laufer (2-26) used $K = 0.145$ and $C_n = 5.5$ for his. The most generally used

values of K and C_n are based on experiments of Nikuradse (2-33), where K = 0.4 and C_n = 5.5. The velocity profile given in Equation 2.4 fits the data well up to values of y^+ from 500 to 1000 before deviation from the predicted profile occurs. Diessler (2-15) developed an equation that takes into account the variation of shear stress across the tube. This equation is:

$$u^+ = \frac{1}{K}\left\{\left((1 - \frac{y^+}{r_o^+}\right)^{1/2} + \ln\left[1 - \left((1 - \frac{y^+}{r_o^+}\right)^{1/2}\right]\right\} + C_n. \quad (2.5)$$

In Equation 2.5, r_o^+ is the non dimenstional tube radius. Diessler compared Equation 2.4 and Equation 2.5, and found that the maximum value of the difference of u^+ calculated from the two equations was 2.5% out of values of $y^+ > 500$.

Schlinger and Sage (2-40) measured velocities of air flowing between parallel plates and determined that their data, for flows with Reynolds numbers greater than 35,000, were well described by Equation 2.4. For the flows with Reynolds numbers equal to 6.96×10^3, 9.11×10^3 and 17.5×10^3 the velocity parameter, u^+, did not collapse to a single-valued relation with y^+. A systematic trend for these three Reynolds numbers was seen in the plot of u^+ versus ln y^+. For any given value of y^+ greater than 15, the value of u^+ decreased as the Reynolds number increased.

The buffer zone occurs between $y^+ = 5$ and $y^+ = 30$. In this region the effects of molecular viscosity become

less important as y^+ increases. Because both viscous and turbulent effects occur in the buffer zone, neigher Equation 2.3 nor Equation 2.4 will fit the velocity profile across this region. Various fits have been applied to data in the buffer zone. Sleicher (2-43) proposed a relatively simple velocity profile,

$$u^+ = \frac{1}{0.091} \tan^{-1} (0.091\ y^+). \tag{2.6}$$

Equation 2.6 fit his data up to a value of $y^+ = 45$. Deissler (2-15) proposed a much more complex relation.

$$y^+ = \frac{1}{n} \frac{\frac{1}{(2\pi)^{\frac{1}{2}}} \int_0^{nu^+} e^{-(nu^+)^2/2}\, d(nu^+)}{\frac{1}{(2\pi)^{\frac{1}{2}}} e^{-(nu^+)^2/2}}, \tag{2.7}$$

where n is a constant chosen for the best fit of the data. For Deissler's velocity measurements the constant n was evaluated to be 0.109. Equation 2.7 fits the velocity in the region from $y^+ = 0$ to $y^+ = 25$ at which point it intersects Deissler's velocity profile for the turbulent region. Equation 2.8 is the relation proposed by von Karman (2-51) for the region $5 \leq y^+ \leq 30$,

$$u^+ = 5\ [1 + \ln\ (y^+/5)]. \tag{2.8}$$

Equations 2.6, 2.7, and 2.8 all extend to different values of y^+ indicating the distance across the buffer region is

not well defined. Measurements by several investigators also show this variation in the size of the buffer region. Nedderman (2-32) made measurements that showed the buffer region extending to $y^+ \simeq 30$, Popovich and Hummel (2-38) determined that the buffer region extended to $y^+ = 34.6$, and Hettler, et al. (2.18) measured a buffer region extending to $y^+ \simeq 70$.

By use of the velocity distributions for the viscous, buffer, and turbulent regions, good correlation of the many experimental studies in turbulent channel flow has been obtained.

2.3 Velocity Fluctuations

It is not enough to measure and characterize the mean velocities for a given turbulent flow to gain a complete understanding of that flow. Measurements on the fluctuations of the velocity field must also be made. Because the mean value of any fluctuating velocity is zero, the root-mean-square (rms) value of the fluctuating velocity is one measurement used to characterize the turbulent fluctuations. If the x, y, and z coordinate directions are considered, then the rms velocities in these directions are $(\overline{v_x'^2})^{\frac{1}{2}}$, $(\overline{v_y'^2})^{\frac{1}{2}}$, and $(\overline{v_z'^2})^{\frac{1}{2}}$. The rms velocities are a measure of the intensity of the turbulence in the respective coordinate directions. In addition to the rms velocities, the mean of the product of velocity fluctuations, such as

$\overline{v_x' v_y'}$, is generally non-zero. The reason for the non-zero value of the cross product terms like $\overline{v_x' v_y'}$ is that the velocities in the x and y directions are correlated. Measurement of the rms velocities as well as the cross product terms characterize the turbulence of the velocity field.

The measurement of fluctuating components has been made by many investigators for many different types of turbulent flows. Batchelor and Townsend (2-5) and Baines and Peterson (2-1) measured the streamwise rms-velocity fluctuations downstream from square mesh grids. Townsend (2-48) measured the mean-squared-velocity fluctuations in the three coordinate directions as well as measuring the mean product of the cross-stream and streamwise velocity fluctuations in the wake flow of a cylinder. Klebanoff (2-25) measured the three rms-velocity fluctuations in a boundary layer along a smooth wall. Laufer (2-26, 2-27) measured velocity fluctuations in fully developed flow in a pipe and between parallel plates. Because turbulent pipe flow is of interest in this work, the measurements made by Laufer will be discussed at this time.

The measurements made in flow between parallel plates (2-26) included $(\overline{v_x'^2})^{\frac{1}{2}}$, $(\overline{v_y'^2})^{\frac{1}{2}}$, $(\overline{v_z'^2})^{\frac{1}{2}}$, and $\overline{v_x' v_y'}$. The coordinate directions used in the experiment were:

x = Coordinate axis in direction of flow

y = Coordinate axis normal to the parallel walls.

z = Coordinate axis normal to x and y.

Three Reynolds numbers were used in this experiment, R_e = 12,300, 30,800, and 61,600. At all three Reynolds numbers the same trends in the data were observed. The rms velocity in the streamwise direction, $(\overline{v_x'^2})^{\frac{1}{2}}$, was larger than the other two rms velocities at all points across the channel. The rms velocities normal to the direction of flow, $(\overline{v_y'^2})^{\frac{1}{2}}$ and $(\overline{v_z'^2})^{\frac{1}{2}}$, were nearly the same through the central portion of flow with $(\overline{v_z'^2})^{\frac{1}{2}}$ becoming larger than $(\overline{v_y'^2})^{\frac{1}{2}}$ as the wall was approached. The correlation between the x and y velocity fluctuations $-\overline{v_x' v_y'}$, was a maximum near the channel wall and decreased lineraly toward zero at the channel center.

The measurements made by Laufer (2-27) in a cylindrical pipe were the same type as those he made in flow between parallel plates. The fluctuating velocity components measured were $(\overline{v_z'^2})^{\frac{1}{2}}$, $(\overline{v_r'^2})^{\frac{1}{2}}$, $(\overline{v_\theta'^2})^{\frac{1}{2}}$, and $\overline{v_z' v_r'}$. Values were obtained at Reynolds numbers of 50,000 and 400,000. For both Reynolds numbers similar relationship among the measured velocity fluctuations were observed. At the center of the pipe all three rms velocities were equal. All three rms velocities increased as the wall was approached wtih $(\overline{v_z'^2})^{\frac{1}{2}} >$

$(\overline{v_\theta'^2})^{\frac{1}{2}}$ $(\overline{v_r'^2})^{\frac{1}{2}}$. The mean product of the streamwise and radial velocity fluctuations, $\overline{v_r' v_z'}$, decreased lineraly from a maximum near the wall to zero at the center. Prediction of this behavior of $\overline{v_r' v_z'}$ was possible assuming that the instantaneous velocities of the turbulent flow satisfied the Navier-Stokes equations. The symmetry of pipe flow allows the Navier-Stokes equations to be solved for $\overline{v_r' v_z'}$, with

$$\overline{v_r' v_z'} = \frac{-r}{2} \frac{1}{\rho} \frac{\partial P}{\partial z} + \nu \frac{\partial U}{\partial r}_z. \qquad (2.9)$$

The variables in Equation 2.9 are:

$\partial P/\partial z$ = The pressure gradient along the pipe,

$\partial \bar{U}_z/\partial r$ = The velocity gradient across the pipe,

ρ = the density of the fluid,

r and z = coordinate directions,

and v_r' and v_z' = instantaneous velocities in the r and z directions.

In Laufer's pipe-flow experiment he measured $\partial \bar{P}/\partial z$ and $\partial \bar{U}_z/\partial r$ Equation 2.9 was then used to calculate $\overline{v_r' v_z'}$, as a function of position across the pipe. Agreement of his measured values of $\overline{v_r' v_z'}$ with those he calculated from Equation 2.9 was almost exact across the channel showing some deviation hear the pipe wall.

2.4 Eddy Viscosity

The concept of an eddy viscosity is analagous to that of molecular viscosity. The Reynolds stress is related to

the mean velocity gradient by this turbulent exchange coefficient,

$$\overline{v'_y v'_z} = \nu_e \frac{d\bar{U}}{dy}z, \tag{2.10}$$

where ν_e is the kinematic eddy viscosity. Equation 2.10 was first proposed by Boussinesq (2-8) who assumed ν_e was a scalar constant. Hinze (2-19) pointed out that ν_e is not constant across non-homogeneous turbulent flows so that the original scalar constant proposed by Boussinesq is not applicable in most cases of turbulent flow. Pai (2-35) showed that ν_e was different for turbulent flows in pipes if the pipes had different cross-sectional shapes.

More recently Phillips (2-34) obtained an expression for the eddy viscosity based on his proposed mechanism for the manner in which the Reynolds stress in a turbulent shear flow is supported by the turbulent components of that flow. This mechanism matched the phase of each component of the turbulent field to the local mean velocity. The eddy viscosity expression obtained by Phillips was:

$$\frac{d(-\overline{v'_y v'_z})}{dy} = \nu_e \frac{d^2\bar{U}}{dy^2}z \ . \tag{2.11}$$

Equation 2.11 equates the Reynolds-stress gradient and the mean strain-rate gradient. The eddy viscosity is the proportionality constant between these gradients. Integration of Equation 2.11 by parts leads to

$$(-\overline{v'_y\ v'_z}) = \nu_e(y)\ \frac{d\bar{U}}{dy}_z - \int_{y_o}^{y} \frac{d\ \nu_e(y)}{dy}\ \frac{d\bar{U}}{dy}_z\ dy \quad (2.12)$$

If the eddy viscosity is a constant, the integral term in Equation 2.12 is zero and the expression reduces to the classical relation given by Equation 2.10. Phillips determined the value of ν_e was related to the integral time scale for lateral velocity fluctuations, T_{lat}, and the mean-square value of the lateral velocity fluctuations, $\overline{v'^2_y}$, by

$$\nu_e = A\ T_{lat}\ \overline{v'^2_y} \quad (2.13)$$

The constant A in Equation 2.13 is less than or equal to π. The value of A is a measure of the anisotropy of the energy-containing eddies, if A = π the turbulence is isotropic.

Evaluation of the constant A in turbulent flows where the integral term in Equation 2.12 is zero has been made by Phillips (2-37) and Baldwin and Haberstroh (2-2). Phillips calculate A = 0.24 across the shear layer of a turbulent jet. Baldwin and Haberstroh calculated A at the center of a pipe for four different Reynolds numbers ranging from 2.55×10^5 to 5.73×10^5. For the pipe flow the values of A averaged 0.33 with no systematic Reynolds number trend.

The fact that ν_e is not constant and depends on the flow geometry does not invalidate the use of the eddy viscosity. Hinze (2-19) calculated ν_e across a pipe from data of Laufer and Nunner. The shapes of the eddy viscosity curves across the pipes calculated from both sets of data were

very similar. Hinze also calculated values of eddy viscosity close to a wall. The data used for this calculation were from Laufer's pipe flow experiments and Schubauer's boundary layer flow experiments. The calculated eddy viscosities were essentially equal, out to a value of $y^+ = 50$. These two calculations of Hinze demonstrate that eddy viscosities calculated for a specific turbulent flow can be used in similar turbulent flows and in certain local regions of different turbulent flows.

2.5 Particle Measurement

The study of particle motion in turbulent flow can be separated into two classes. In the first class, concentrated suspension flow, the particle concentration is high, and particle-particle interactions are important. In the second class, dilute-suspension flow, the particle concentration is low, and each particle interacts only with the fluid transporting it. The experimental work undertaken in the present study was concerned with dilute-suspension flow; however, some of the equations describing particle diffusion used in dilute-suspension studies were developed in concentrated-suspension experiments. There have also been concentrated suspension studies based on dilute-suspension work. The review of concentrated-suspension experiments that is made at this time briefly covers the experiments both in open channel and pipe flow that are related to dilute-

suspension work.

2.6 Open Channel Flow

Determination of an effective eddy-diffusion coefficient for solid particles in open channels was studied by many investigators. The basic equation used in determining the effective diffusion coefficient is written as

$$WC + E_{ds} \frac{dC}{dy} = 0 \ . \tag{2.13}$$

In Equation 2.13 the upward transport of solids due to turbulent diffusion is balanced by the settling of particles due to gravity. The concentration of particles is C, their settling velocity is W, and E_{ds} is the eddy-diffusion coefficient for the sediment. Rouse (2-39) used Equation 2.13 and the Karman-Prandtl logarithmic law.

$$\frac{du}{dy} = \frac{(\tau_o/\rho)^{\frac{1}{2}}}{ky} \ , \tag{2.14}$$

where τ_o = the wall shear stress,

ρ = the fluid density,

y = the coordinate direction normal to the wall

u = the velocity parallel to the wall,

and k = a constant,

to obtain an expression for the relative concentration of sediment at any level y in the channel

$$\frac{C}{Ca} = \left[\left(\frac{h-y}{y}\right)\left(\frac{a}{h-a}\right)\right]^{w/(k[\tau_o/\rho]^{\frac{1}{2}})} \tag{2.15}$$

In Equation 2.15 y = a is a reference level in the channel, and h is the depth of fluid in the channel. Vanoni (2-49) measured the velocity and concentration distribution in a water-sand system flowing in a rectangular channel. He calculated the eddy-diffusion coefficient and the eddy viscosity from his experimental data and found that for fine particles, those having effective diameters of around 0.10 mm, the eddy-diffusion coefficient was larger than the eddy viscosity, while for larger particles, those having diameters of around 0.16 mm, the eddy-diffusion coefficient was smaller than the eddy viscosity. Hunt (2-21) extended the analysis of Rouse to include a distribution of particle sizes and settling velocities. An effective settling velocity at a given height was found to be

$$W = \sum_r C_r W_r / \sum_r C_r \ . \qquad (2.16)$$

In Equation 2.16 C_r is the concentration fraction of particles with settling velocity W_r. Hunt pointed out that Equation 2.16 would not in general be satisfied at all depths by a constant W. He then proposed that W should be chosen to minimize the error in Equation 2.13 when a heterogeneous sample is modeled using a representative particle size and settling velocity. The best estimate of W would be obtained by sampling the particles at various bed depths and defining W as:

$$W = \int_o^h \sum_r C_r W_r \, dy / \int_o^h \sum_r C_r \, dy \qquad (2.17)$$

Jobson and Sayre (2-22) studied the diffusion of marked fluid particles (Rhodamine WT fluorescent dye), fine sediment (spherical glass beads with diameters of 0.123 mm), and course sediment (river sand which passed through a 0.390 mm sieve). In their experiment they noted the settling velocity of the coarse particles was increased 4 to 5% by the turbulence, but no decisive change was seen for the fine particles. Jobson and Sayre also explained the turbulent diffusion of solid particles as arising from two independent processes. The first process was diffusion of the particles arising from the tangential components of the turbulent velocity fluctuations. The second process was diffusion of particles due to centrifugal forces arising from the curvature of the path lines of the fluid elements for the particles. The portion of the diffusion coefficient due to the tangential components of the velocity fluctuations was found to be proportional to the eddy viscosity, with a proportionality constant less than or equal to one. This part of the diffusion coefficient was also found to increase as the particle size increased. The portion of the diffusion coefficient arising from the curvature of the path lines of the fluid was found to incrase and to reach a maximum in the regions of flow having the greatest shear.

2.7 Slurry Pipe-Flow

In addition to studies of the flow of concentrated suspensions in open channels, there has been much work on slurry transport of solids in pipes. The studies have been mainly concerned with the development of correlations relating the pressure drop in the pipe to the slurry velocity. Rather than review these correlations, a discussion will be given of some of the most recent papers which have reported on the physical behavior of slurries.

Maruyama, et al. (2-31) studied the structure of a slurry composed of spherical glass beads (diameter = 0.875 mm) using visual methods. They found that the solid particles were mixed across the entire pipe diameter by large transverse vorticies. The formation of a transverse vortex was found to be predictable by using the Kelvin-Helmholtz instability criterion for stratified flows. This analysis makes use of the fact that in the early phase of vortex formation the solid phase acts like a fluid. Maruyama, et al. also pointed out that Kazanskij and Bruhl measured velocity and pressure fluctuations in slurry and pure water flows. Their results suggested the existence of large intensive eddies in the slurry flows. These eddies were not present in the pure water flows. Weisman, et al (2-52) studied the two-phase flow of gas-li-

quid mixtures using visual methods. In this study the flow pattern established by the gas-liquid mixture was shown to be determined by the relative volumetric flow-rates of the gas and liquid.

Thomas (2-47) and Oroskor and Turian (2-34) have recently investigated the prediction of critical velocities for slurry flow in pipelines. The critical velocity is defined as the minimum velocity which separates flows in which the particles from a bed at the bottom of the pipe from those in which the solids are fully suspended.

Thomas ran experiments on slurries with silica sand as the solid. In the experiments he varied the density of the suspending fluid, the viscosity of the suspending fluid, the particle size, and the concentration of solids. His experimental results for the flow of slurries with up to 20% solids agreed well with the theory proposed by Wilson and Judge (2-53) as long as the suspending fluid was water and the particles were larger than 0.10 mm. Wilson and Judge's analysis is based on the idea that deposition occurs when the forces moving the sliding bed of particles are not large enough to overcome the friction forces between the particles. Although Thomas was not able to explain why Wilson and Judge's theory did a poor job of predicting critical velocities of slurries with suspending mediums more viscous than water, he was able to explain the experimental

results for his particles smaller than 0.10 mm. The particles he used that were smaller than 0.10 mm had mean sizes of 14 and 26 microns. These particles were smaller than the viscous sublayer next to the pipe wall, and so they settled into the viscous sublayer. Thomas was able to incorporate the effect of particles residing in the viscous sublayer into the theory of Wilson and Judge, and this extension was able to describe the data for the 14 and 26 micron particles.

Oraskar and Turian (2-34) derived an expression for the critical velocity of a slurry based on the energy required to suspend a single particle in a turbulent field. In extending the analysis from one particle to a group of particles Oraskar and Turian replaced the settling velocity for a single particle with a hindred settling velocity for the group of particles and then kept the form of the equations the same. After the final expression for the critical velocity had been obtained, the predicted critical velocity was compared with 357 data points for critical velocities and the rms deviation from the data points was calculated. The rms deviation for the data was 26%. This rms deviation between the predicted and measured critical velocities was considered to be reflective of very good agreement among the data.

2.8 Dilute Suspension

Experimental studies of dilute suspensions of particles in pipe flow and in other turbulent flows have been made in two ways. The first approach uses Equation 2.13, which was developed from concentrated suspension studies, to determine the particle-diffusion coefficient, E_{ds}. The second method uses the Lagrangian description for turbulent diffusion developed by Taylor (2-45). The experimental work that has been described by use of Equation 2.13 will be reviewed first, and then the work that uses Taylor's approach will be reviewed.

Barnard and Binnie (2-4) studied the vertical diffusivity of 0.2-inch, spherical particles ranging in density from 0.92 to 1.25 gm/cm^3. The suspending fluid used in their experiments was water. Equation 2.13 was integrated assuming that the particle diffusion coefficient was independent of position in the pipe, and E_{ds} was then determined by measuring the particle concentration across the pipe. The particle diffusion coefficient was non-dimensionalized with respect to the friction velocity and the pipe radius and was given as

$$\xi = \frac{2\ E_{ds}}{v^*(2\ r_o)} \quad . \tag{2.18}$$

From their measurements Barnard and Binnie determined an approximate value of $\xi = 0.3$ for the non-neutrally-buoyant spheres, but when the density was close to 1 gm/cm^3, the value of ξ increased to 0.7. Binnie and Phillips (2-7)

measured the mean velocity of slightly buoyant and heavy particles in turbulent pipe flow. They determined that ξ = 0.46 was the best estimate of the particle diffusivity based on the particle velocity results they obtained.

Sharp and O'Neil (2-41, 2-42) also investigated the diffusion of spherical particles in turbulent flow in a horizontal pipe. The particles used in their experiments were 0.1 inch in diameter and had specific gravities of 1.035, 1.069, and 1.126 respectively. The turbulent flow in the pipe was considered to be composed of three regions.

1) Central core; $0 \leq r/r_o \leq 0.5$
2) Annular region; $0.5 \leq r/r_o \leq 0.8$
3) Wall region; $0.8 \leq r/r_o \leq 0.95$

The wall region only extended to $r/r_o = 0.95$ because that was the position of the center of the sphere when it was touching the wall. In the first study by Sharp and O'Neill (2-42), only the central core of the turbulent flow was analyzed. Equation 2.13 was integrated, assuming E_{ds} to be constant in the core, and the relative particle concentration was found to be

$$\frac{C}{C_a} = \exp\left[-\frac{W}{E_{ds}}(y - y_a)\right], \qquad (2.19)$$

where C = the particle concentration at height y,

C_a = the particle concentration at reference height y_a,

W = the particle settling velocity,

and E_{ds} = the particle diffusion coefficient.

The diffusion coefficient was obtained by using Equation 2.19 with the concentration distribution of spheres across the pipe as obtained by experimental measurement and the settling velocity measured in an independent experiment. Sharp and O'Neill found it possible to relate the dimensionless diffusion coefficient, ξ , to the friction velocity, v*, in a straight forward manner,

$$\xi = A\ (1.0 - BW/v^*)\ S^n. \qquad (2.20)$$

In Equation 2.20 A, B and n are constants, and S is the relative density of the particle to the suspending fluid. In the central region the constants were evaluated as A = 0.38, B = 0.52, and n = 2.8. If the constants retain their values as the density of the particles approach that of the suspending fluid, a value of $\xi = 0.38$ is obtained for the neutrally buoyant case.

Sharp and O'Neill (2-41) also studied the diffusion of the spherical particles in the annular region, $0.5 \leq r/r_o \leq 0.8$. In this region, the experimental concentration distribution given in Equation 2.19 was found to fit the data if separate but constant diffusion coefficients were used for the upper half of the pipe cross-section and for the lower half of the pipe cross-section. These upper, $E_{ds,u}$, and lower, $E_{ds,l}$, diffusion coefficients were found to bound the diffusion coefficient calculated for the central region of the pipe

$$E_{ds,u} > E_{ds} > E_{ds,l} \quad . \tag{2.21}$$

Sharp and O'Neill explained the trend seen in Equation 2.21 by the existence of an additional force, acting radially outwards, in the annular region. In this hypothesis the particle diffusion coefficient is assumed constant across the entire flow channel (both core and annular region), and the difference seen in Equation 2.21 is attributed solely to the additional force existing in the annular region.

In the work done by Barnard and Binnie and Sharp and O'Neill the size of the particles used was considerably greater than the microscale of the turbulence. Karabelas (2-24) used particles with sizes comparable to the sizes of the smallest eddies in his flow system. He used two sets of particles with diameters of 210 microns and 290 microns, both of which had densities of 1.126 gm/cm^3. The diffusion experiments were run in three suspending fluids, kerosene, transformer oil, and a kerosene-transformer oil mixture. The non-dimensional particle diffusion coefficients determined from the experiments ranged from $\xi = 0.20$ to $\xi = 0.33$ with a mean value of $\xi = 0.26$. This mean value of ξ obtained by Karabelas agrees well with the values of ξ obtained by Barnard and Binnie, and Sharp and O'Neill using much larger particles.

Taylor (2-45) derived an expression for the spread of fluid elements in a field of isotropic, homogeneous turbulence. If the x direction is considered, the equation

describing the spread of fluid elements from a specified point is

$$\frac{1}{2}\frac{\overline{dx^2}}{dt} = \overline{u_{la}'^2} \int_o^t R(\omega)\,d\omega \ . \qquad (2.22)$$

Equation 2.22 can be integrated to obtain

$$\overline{x^2} = 2\overline{u_{la}'^2} \int_o^T \int_o^t R(\omega)\,d\omega dt \ , \qquad (2.23)$$

Where x is the distance traveled by the fluid element in time T; $\overline{u_{la}'^2}$ is the mean squared value of the Largrangian fluid velocity; and $R(\omega)$ is the correlation coefficient between the velocities of the fluid element at time t and time ω. $R(\omega)$ is expressed as

$$R(\omega) = \frac{\overline{u_{la}(t)\ u_{la}(\omega)}}{\overline{u_{la}'^2}} \ . \qquad (2.24)$$

The correlation coefficient is very close to unity for small differences between t and ω and goes to zero as the time difference increases. For short diffusion times $R(\omega) \simeq 1$, allowing Equation 2.23 to be related as

$$\overline{x^2} = (\overline{u_{la}'^2})\ T. \qquad (2.25)$$

As the diffusion time increased the correlation coefficient goes to zero, and there is some characteristic time, T_1, after which the value of the integral term in Equation 2.22 remains at a constant value, I. If the diffusion time is

longer than T_1, Equation 2.23 becomes

$$\overline{x^2} = (\overline{u_{la}'^2})\ (2IT) \quad . \tag{2.26}$$

Taylor's theory uses Lagrangian velocities and correlation functions, so several investigators have looked at relationships between Eulerian and Lagrangian properties. Batchelor, et al. (2-6) determined that the Eulerian mean-square velocity $\overline{u'^2}$, was equal to the Lagrangian mean-square velocity $\overline{u_{la}'^2}$, in turbulent pipe flow. Baldwin and Mickelsen (2-2) studied the relationship between Lagrangian and Eulerian correlation coefficients in the core region of turbulent pipe-flow. They formed a mixed Eulerian correlation coefficient by measuring and recording velocities at two positions and then artifically delaying the downstream velocity for a given time period. This mixed correlation coefficient was found to be approximately equal to the Lagrangian correlation coefficient. Baldwin and Mickelsen calculated the spread of a contaminant using the mixed correlation coefficient and found the calculated value to be 1.05 to 2.3 times greater than the actual spread of a helium tracer that was injected into the pipe.

Snyder and Lumley (2-44) pointed out that the equations derived for the spread of fluid elements are applicable to solid particles if the velocities used are particle velocities. They used photographic methods to measure the

Lagrangian correlation coefficient for the particle velocities. The flow system used was a vertically-positioned wind tunnel. The spheres used in this experiment were 46.5 micron hollow glass, 46.5 micron copper beads, 87 micron solid glass, and 87 micron corn pollen. The hollow glass spheres were light enough to act as fluid points, while the other spheres had enough weight for inertia to be important. Snyder and Lumley found the differences in diameters of the particles had an insignificant effect on the Lagrangian correlation coefficient. They found the correlation of particle velocities decreased faster for heavier particles than the light particles.

An eddy-diffusion coefficient has been defined in an analogous way to molecular diffusion by Brownian motion. The eddy diffusion coefficient, E_{ds}, could then be written as

$$E_d = \frac{1}{2} \left. \overline{\frac{dx^2}{dt}} \right|_{t \to \infty} = \overline{u_{1a}'^2} \, I \, . \qquad (2.27)$$

Equation 2.27 is applicable once sufficient time has passed during the diffusion process for the correlation coefficient to go to zero. In experimental studies the mean-square displacement of the diffusing species is plotted against diffusion time as shown in Figure 2.1. At small values of time, the mean-square displacement is proportional to time squared, as is shown in Equation 2.25. When the diffusion

GRAPHICAL SHAPE OF $\overline{X^2}$ vs. t CURVE

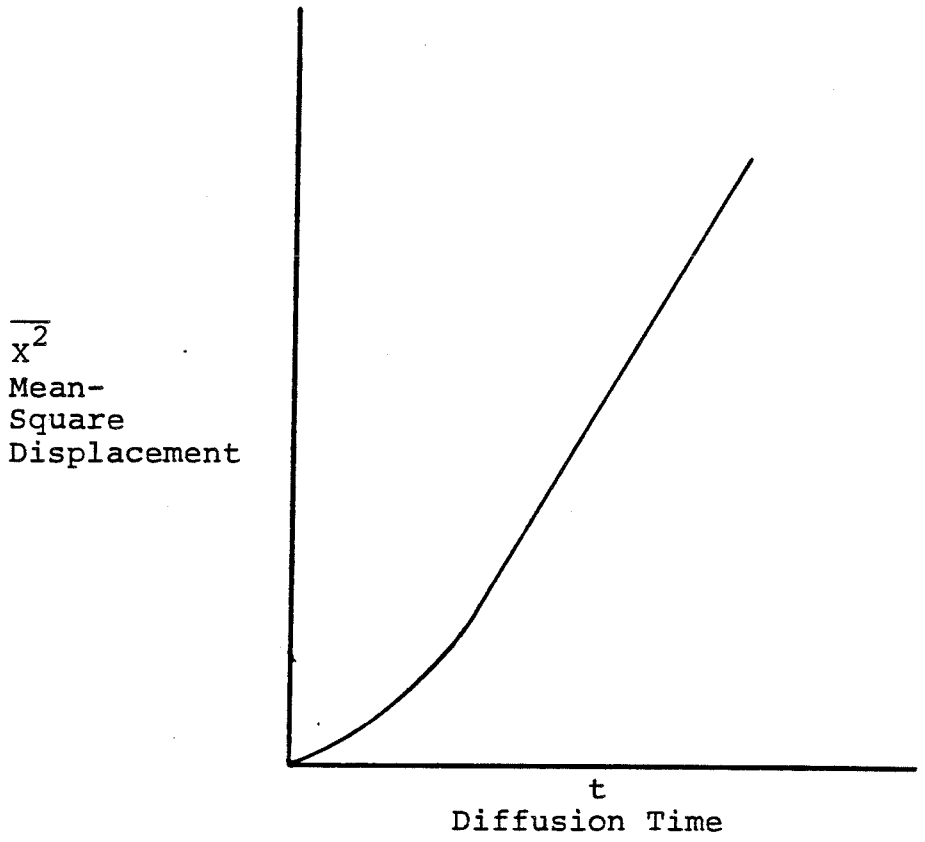

Figure 2.1

time becomes larger the mean-square displacement varies linearly with diffusion time as Equation 2.26 predicts. Evaluation of the slope of the linear section of the curve shown in Figure 2.1 allows the eddy-diffusion coefficient to be calculated using Equation 2.27.

Kalinski and Pien (2-23) measured the eddy diffusivity of both n-butyl-phthalate/benzene and carbontetrachloride/benzene mixtures in water. A rectangular flow channel was used, and the maximum eddy diffusivity occurred midway between the channel bottom and the water surface. The diffusion coefficient at the midpoint was evaluated to be 15×10^{-4} ft^2/sec.

Calabrese and Middleman (2-10) studied the turbulent diffusion of a liquid dye used as a tracer as well as liquid droplets in turbulent pipe flow. The core region of the pipe flow was the region in which the dispersion of the tracer and the droplets was observed. The droplets were composed of butyl benzoate (BB; $\rho = 1.000$ gm/cm^3), carbontetrachloride (CCL_4; $\rho = 1.595$ gm/cm^3) and n-heptane (HEP; $\rho = 0.695$ gm/cm^3). In this investigation the eddy-diffusion coefficient for the tracer was found to be $E_{d,T} = 0.42$ cm^2/sec, and the eddy-diffusion coefficient of the neutrally buoyant BB was found to be $E_{d,BB} = 0.38$ cm^2/sec. The eddy-diffusion coefficient determined for the buoyant HEP and the heavy CCL_4 were both found to be smaller than the diffusion coefficients of the BB and the tracer, $E_{d,HEP} =$

0.29 cm^2/sec and E_{d,CCL_4} = 0.22 cm^2/sec. Calabrese and Middleman note that over the size range of droplets used in the experiments (from 600 microns to 905 microns), the tracer and the BB droplets have essentially the same radial diffusion coefficients. The dense CCL_4 and buoyant BB droplets have smaller radial diffusion coefficients indicating the density difference between the droplets and the fluid causes an appreciable fall or rise in velocity for the droplets. This cross-stream velocity causes the droplets to migrate from eddy to eddy. This migration is referred to as crossing trajectories, and the reduction in radial diffusion was attributed to the crossing trajectories of the droplets.

The effect of particle size and density on the diffusion of the particles in turbulent flow has been studied by Lilly (2-30) and by Yuu et al. (2-54). The method that these investigators used to characterize the ability of particles to follow the turbulent eddies as to determine the relaxation time, T_p, of the particles. Lilly reported recruits using the ratio of the particle relaxation time to the time scale of the turbulence, T_p/T_1. Yuu et al. used the Stokes number to describe their data. The stokes number, ψ , is the ratio of the particle-stopping distance to the length scale of the flow,

$$\psi = (T_p \bar{U}/R). \qquad (2.27a)$$

These two studies will be discussed briefly starting with the work of Lilly.

Lilly (2-30) studied the diffusion of solid particles in a two-dimensional jet. Magnesium oxide particles with sizes of 0.96 microns and 9.0 microns, respectively, were used in the experiment. The diffusion of a carbon monoxide tracer gas was also studied to provide a reference for the measurements of particle diffusion. The choice of particle sizes used in the experiment was based on the relaxation times of the particles. The particle relaxation time, T_p, is defined as

$$v_p/v_o = \exp(-t/T_p). \tag{2.28}$$

Equation 2.28 represents the decay with time, t, of the particle velocity, v_p, when it is injected into a quiescent fluid with an initial velocity, v_o. If the ratio of the particle relaxation time to the time scale of the turbulence, T_p/T_l, is less than 0.22, then the particle has been shown by Fuchs (2-16) to follow all of the turbulent fluctuations. The 0.96 micron particles had ratios of T_p/T_l ranging between 0.0025 and 0.01. If the ratio T_p/T_l is between 0.22 and 10.0, the particle will be affected by a portion of the turbulent fluctuations. The 9.0 micron particles had ratios of T_p/T_l ranging from 0.23 to 0.91. Lilly reports his diffusion data in terms of turbulent Schmidt num-

bers, defined as $S_{C_T} = \nu_e/E_d$. He found the carbon monoxide tracer and the 0.96 micron magnesium oxide particles to both have a value of $S_{C_T} = 0.34$. The 9.0 micron particles of magnesium oxide had a value of $S_{C_T} = 0.17$. These results show that for their 2-D jet type of turbulent flow the eddy diffusion coefficient increased as T_p/T_l increases.

Yuu, et al. (2-54) studied particle diffusion in a round jet. In his experiments he used 15 and 20 micron particles of fly ash with a density of 2.0 gm/cm^3. In this work the Stokes number was used to classify the effect of particle inertia. The Stokes number is the ratio of particle-stopping distance to the characteristic length of the system and the relation for his experimental conditions is

$$\psi = \rho_p U_N d^2/18\mu D_N \ , \qquad (2.29)$$

where:

ψ = Stokes number,

ρ_p = Particle density,

U_n = Fluid velocity issuing from nozzle,

d = Particle diameter,

μ = Molecular viscosity of the fluid,

and D_N = Nozzle diameter.

Yuu, et al. found S_{C_T} increased linearly as the Stokes num-

ber increased. This trend shows the diffusion of the particles decreased as the size increased.

The investigations discussed to this point have been concerned with determining the eddy-diffusion coefficients of particles in a turbulent flow. Hanratty, et al. (2-17) and Patel and Tsao (2-36) have studied the diffusion of a tracer in turbulent flows with particle concentration large enough for particle-particle interaction to be important.

Hanratty, et al. (2-17) investigated the turbulent diffusion of a dye tracer in a fluidized bed. The fluidized bed particles were glass spheres 3 mm in diameter, and the channel was cylindrical with a 5.4 cm ID. Hanratty, et al. presented their data graphically by plotting the Peclet number $P_e = (d_p \bar{U}_z)/E_d$, versus the fraction of solids in the bed. They found a parabolically shaped curve with a minimum value of P_e at a solids fraction of 0.35. This result indicated that the maximum eddy diffusivity occurred at a solids fraction of 0.35.

Patel and Tsao (2-36) studied the diffusion of a salt tracer in slurry flows in pipes. The solid phase of the slurry was cornstarch particles, and the solids concentrations were 0, 0.5, 1.0, and 2.5% respectively. The eddy diffusivity of the tracer was found to increase as the solid content increased for any set flowrate. All eddy dif-

fusivities of the suspensions were greater than those determined for pure water. This study indicates the mixing of the turbulence is enhanced by increasing solids content. This result may be related to the formation of a transverse vortex as was seen by Maruyama, et al. (2-31).

2.9 Random Walk Models for Diffusion

Bugliarello and Jackson (2-9) investigated the applicability of using a discrete random walk simulation to model convective diffusion in a laminar flow field. This analysis used a two-dimensional channel with a source on the channel centerline. The computer results obtained were checked by comparision with an analysis based on the approach used by Taylor (2-46) for diffusion in laminar flow. In this approach the longitudinal diffusion of a source distributed across the channel was calculated from the diffusion equation. The longitudinal diffusion was calculated in reference to a plane moving along the flow channel at the average fluid velocity, and the transverse concentration gradient was assumed to be small. If the diffusion time of the random walk simulation was long enough to establish a distributed source across the channel, then the random walk simulation and the solution from the diffusion equation agreed very well. Bugliarello and Jackson state that the random walk simulator was able to give results for a source located off of the centerline,

for a flow with a variable diffusion coefficient, and for a three-dimensional flow field. They felt the flexibility of this approach to convective diffusion was a major point of interest in the solution of diffusion problems.

Chiu (2-11) used a random walk simulation to describe the motion of a single particle in a complex turbulent flow. The turbulent flow under consideration occurred in the corner of a rectangular flow channel where secondary flows were important. In this model both the time duration and length of each step were varied depending on the turbulent properties of the flow surrounding the particle. Chiu used both a random motion, representing the turbulent transport, and a deterministic motion, representing transport by the mean fluid flow and gravity, to describe the total motion of the particle.

Lee and Dukler (2-28, 2-29) used a stochastic differential equation to describe the turbulent diffusion. The flow used was two-dimensional with a constant gradient of the mean velocity. In both studies the random forcing functions were generated electronically and then digitized for input into a computer. In the first study (2-28), the solutions to equations developed by Corrsin (2-13) were compared to solutions to the stochastic differential equations. The random forcing functions were correlated to any degree from zero correlation to full correlation, but only the

limiting cases of correlation were compared with the solutions to Corrsin's equations. Lee and Dukler obtained good agreement between the stochastic simulations and the numerical solutions to the transport equations of Corrsin.

In an extension to the approach just discussed, Lee and Dukler (2-29) used Eulerian statistical properties of a turbulent flow to evaluate the forcing function, and a relaxation time in the stochastic differential equations. In this approach the Lagrangian correlation function is assumed to decay in the same way as the Eulerian correlation function. With atmospheric turbulence data, the stochastic differential equations predicted the diffusion of a tracer gas in the atmosphere very well.

LITERATURE CITED

(2-1) Baines, W. D., Peterson, E. G., Trans. Am. Soc. Tech. Engrs., 73, 467 (1951).

(2-2) Baldwin, L. V., Mickelsen, W. R., Trans. ASCE, 128, 1595 (1963).

(2-3) Baldwin, L. V., Haberstroh, R. D., AIChEJ, 14, 825 (1968).

(2-4) Barnard, B. J. S., Binnie, A. M., JFM, 15, 35 (1963).

(2-5) Batchelor, G. K., Townsend, A. A., Proc. Roy. Soc. London, Series A, 193, 545 (1948).

(2-6) Batchelor, G. K., Binnie, A. M., Phillips, O. M., Proc. Physics Soc., Series B, 68, 1095 (1955).

(2-7) Binnie, A. M., Phillips, O. M., JFM, 4, 87 (1957).

(2-8) Boussinesq, J., Mem. Pres. par div. Savants a Lacad. Sci. Paris, 23, 46 (1877).

(2-9) Bugliarello, G., Jackson, E. D., Jour. Eng. Mech. Div., ASCE, 90, 4003 (1964).

(2-10) Calabrese, R. V., Middleman, S., AIChEJ, 25, 1025 (1979).

(2-11) Chiu, C. L., Jour. Hyd. Div., ASCE, 203 (1967).

(2-12) Corcoran, W. H., Roudebush, B., Sage, B. H., Chem. Eng. Progress, 43, 135 (1947).

(2-13) Corrsin, S., Proc. Iowa Thermo. Symp. 5 (1953).

(2-14) Davies, J. T., "Turbulence Phenomena", New York, N.Y., Academic Press Inc., 1972.

(2-15) Deissler, R. G., NACA, Tech Note 2138 (1950).

(2-16) Fuchs, N. A., "The Mechanics of Aerosols", Oxford, Eng., Pergammon Press, 1964.

(2-17) Hanratty, T. J., Latinen, G., Wilhelm, R. H., AIChEJ, 2, 372 (1956).

(2-18) Hettler, J. P., Muntzer, P., Scrivener, O., Compt. rend., 253, 4201 (1964).

(2-19) Hinze, J. O., "Turbulence", New York, N.Y., McGraw-Hill Book Co., 1959.

(2-20) Howarth, L., Proc. Roy. Soc. London, Series A, 154, 364 (1936).

(2-21) Hunt, J. N., Proc. Roy. Soc. London, Series A, 224, 322 (1954).

(2-22) Jobson, H. E., Sayre, W. W., ASCEJ, 96, 703 (1970).

(2-23) Kalinski, A. A., Pien, C. L., Ind. and Eng. Chem., 36, 220 (1944).

(2-24) Karabelas, A. J., AIChEJ, 23, 426 (1977).

(2-25) Klebanoff, P. S., NACA, Tech. Note 3178 (1950).

(2-26) Laufer, J., NACA, Tech. 2123 (1950).

(2-27) Laufer, J., NACA Tech. Rept. 1174 (1954).

(2-28) Lee, N., Dukler, A. E., AIChEJ, 22, 449 (1976).

(2-29) Lee, N., Dukler, A. E., Chem. Eng. Sci, 33, 1169 (1978).

(2-30) Lilly, G. P., Ind. Eng. Chem. Fund., 12, 268 (1973).

(2-31) Maruyama, T., Kojima, K., Mizushma, T., Jour. of Chem. Eng. Jap., 12, 177 (1979).

(2-32) Nedderman, R. M., Chem. Eng. Sci., 16, 120 (1961).

(2-33) Nickuradse, J., V.D.I. Forschungsheft, 356, 1 (1932).

(2-34) Oroskar, A. R., Turian, R. M., AIChEJ, 26, 550 (1980).

(2-35) Pai, S. E., "Viscous Flow Theory, II-Turbulent Flow", Princeton, N. J., P. Van Nostrand Co., Inc., 1957.

(2-36) Patel, A. K., Tsao, G. T., AIChEJ, 22, 401 (1976).

(2-37) Phillips, O. M., JFM, 27, 131 (1967).

(2-38) Poppovich, A. T., Hummel, R.L., AIChEJ 13, 854 (1967).

(2-39) Rouse, H., Trans. ASCE, 102, 463 (1937).

(2-40) Schlinger, W. G., Sage, B. H., Ind. Eng. Chem., 45, 2636 (1953).

(2-41) Sharp, B. B., O'Neill, I. C., First Int. Conf. on the Hydro. Trans. of Solids in Pipes, Coventry: BHRA (1970).

(2-42) Sharp, B. B., O'Neill, I. C., JFM, 45, 575 (1971).

(2-43) Sleicher, C. A., Trans. ASME, 80, 693 (1958).

(2-44) Snyder, W. H. Lumely, J. L., JFM, 48, 41 (1971)

(2-45) Taylor, G. I., Proc. London Math. Soc., 20A, 196 (1921).

(2-46) Taylor, G. I., Proc. Roy. Soc. London, Series A, 219, 186 (1953).

(2-47) Thomas, A. D., Int. Jour. Multiphase Flow, 5, 113, (1979).

(2-48) Townsend, A. A., Australian Jour. Sci. Res., 2A, 451 (1949).

(2-49) Vanoni, V. A., Trans. ASCE, 111, 67 (1946).

(2-50) von Karman, T., Jour. Aero. Sci., 1, 1 (1920).

(2-51) von Karman, T., Trans. ASME, 61, 705 (1939).

(2-52) Weisman, J., Duncan, D., Gibson, J., Crawford, T., Int. Jour. Multiphase Flow, 5, 437 (1979).

(2-53) Wilson, K. C., Judge, D. G., Proc. 5th Int. Conf. Hyd. Trans. Solids in Pipes, Hanover, Ger. (1978).

(2-54) Yuu, S., Yasukouchi, N., Hirosawag, Y., Jotaki, T., AIChEJ, 24, 509 (1978).

CHAPTER 3

EXPERIMENTAL APPARATUS

3.1 Flow Channel

The flow channel used in the experiments is shown schematically in Figure 3.1. It consists of a straight Plexiglas tube with a length of 183 cm, an ID of 2.54 cm, and a wall thickness of 0.32 cm. At the upstream end of the measuring section there was a flow conditioner. The flow conditioner consisted of a cylindrical section 7.62 cm in diameter by 17.78 cm in length followed by a coverging section 15.24 cm long tapering to a 2.54 cm ID. A set of straightening vanes was located in the cylindrical section to eliminate any secondary flow down the flow channel. At the end of the covergent section an 80 mesh screen was installed to aid in development of the flow. The flow in the system was maintained by a centrifugal pump (Little Giant) and was controlled by a flowmeter (Fisher-Porter #10A1027). The flowmeter had a maximum capacity of 25 l/min and was calibrated from 10 to 100% in increments of 2%. All connecting tubes are 2.54 cm ID Tygon tubing.

The necessity of the straightening vanes in the flow conditioner can be understood through an examination of Figure 3.2. Prior to installation of the vanes the secondary velocity was as great as 15% of the maximum axial velocity. For the flow-rate shown in Figure 3.2 the maximum secondary

FLOW SYSTEM SCHEMATIC

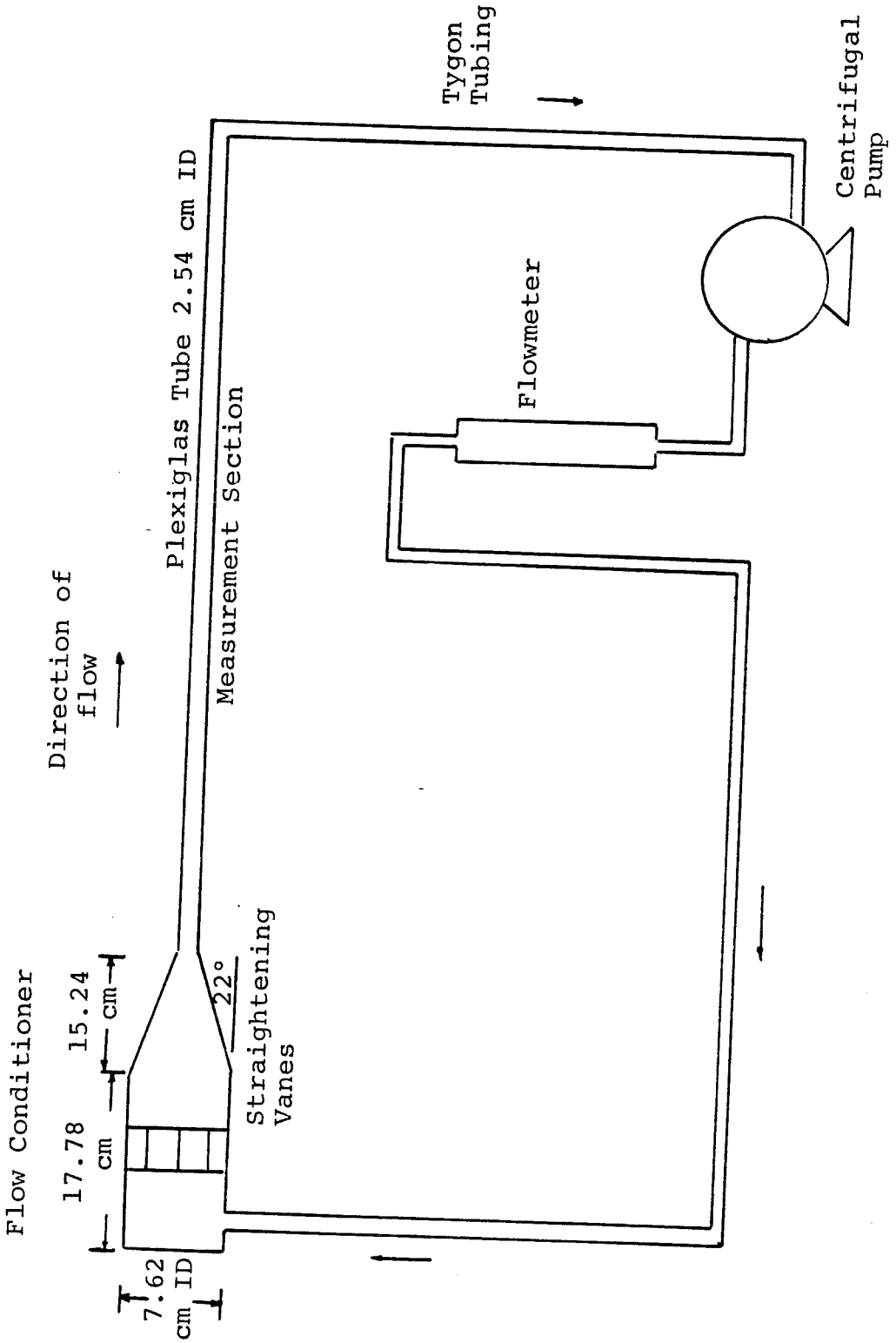

Figure 3.1

SECONDARY VELOCITY PROFILES

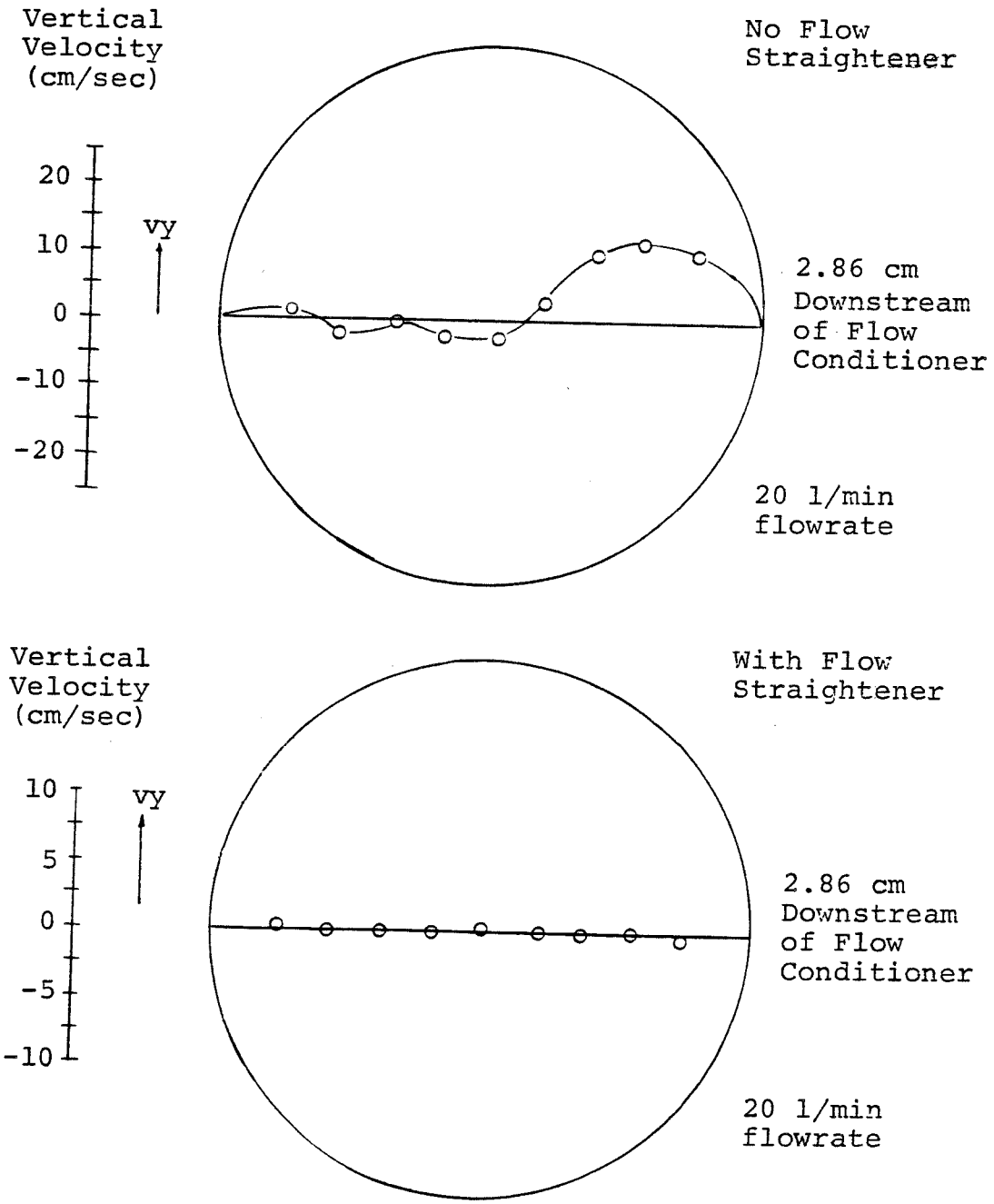

Figure 3.2

velocity was 13 cm/sec at a distance of 2.86 cm downstream of the conditioner while the maximum axial velocity was 85.1 cm/sec. At 36 diameters downstream, the position that the velocity and particle concentration measurements were taken, a maximum secondary velocity of 4 cm/sec was still present. With the straightening vanes in position the secondary velocity was 1 to 2 cm/sec at a position 2.86 cm downstream from the flow conditioner, and there was no secondary velocity 36 diameters downstream.

3.2 Particle Injection Apparatus

The additional equipment used in the particle diffusion experiments is shown schematically in Figure 3.3. The particle reservoir consisted of an 8.89 cm ID Plexiglass pipe 30 cm in length clamped between two aluminum plates. The particles used in the experiment were 120 micron polyvinylchloride particles, and will be characterized in the chapter containing the results of the particle-diffusion experiments. The particles were kept in suspension by means of a magnetic stirrer. Injection of the particles into the flow channel was achieved by pressuring the reservoir and forcing the water-particle suspension through a 305 cm length of 1 mm ID plastic tubing. The plastic tubing was connected to a 1.6 mm ID L-shaped stainless steel tube centered in the flow channel.

ADDITIONAL APPARATUS FOR PARTICLE EXPERIMENTS

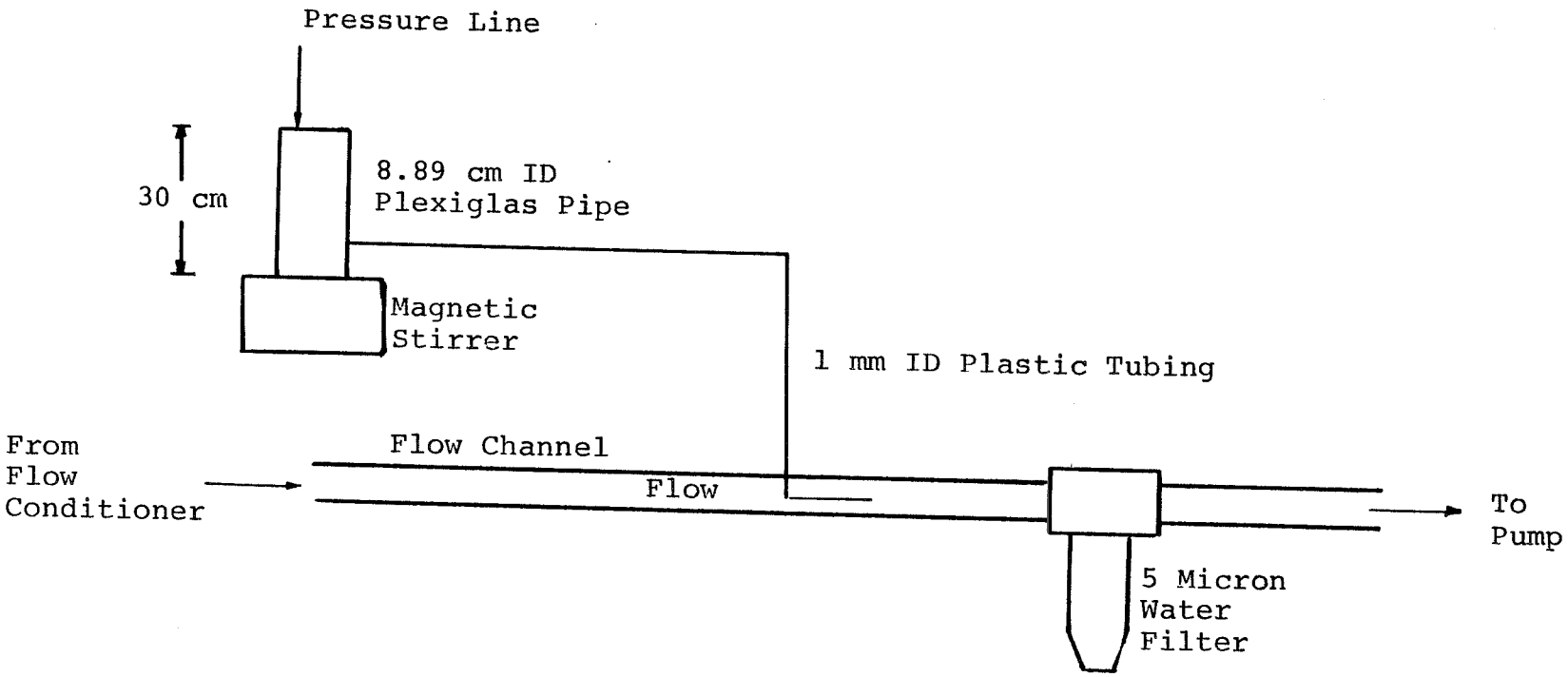

Figure 3.3

Once the particles had been injected into the system, and their relative concentration across the channel had been measured, they were removed before being counted twice. Particle removal was accomplished by passing the water through a 5-micron filter upstream from the flow conditioner.

3.3 Pressure-Drop Measurements

Pressure-drop measurements were made to establish dp/dz in the region where the velocity measurements were made. Ten pressure taps were placed along the flow channel every 5.08 cm starting 76.2 cm downstream from the flow conditioner. Pressure-drop measurements relative to the first tap were made at each successive tap downstream. A U-tube manometer using water and chlorobenzene as the two immiscible fluids was used. The manometer was sensitive enough to measure a Δp of 0.02 cm of H_2O. The probes used in the pressure taps were #18 gauge hypodermic needles with the points ground off so that the tips were completely flat.

3.4 Principles of Operation of the Laser-Doppler Anemometer

Laser-Doppler anemometry operates on the principle of comparison of the frequency of light scattered by a moving particle with the frequency of the light incident to the particle. The vector equation that relates these two frequencies is written as

$$f_s = f_i + \frac{1}{\lambda} \vec{V} \cdot (\vec{e}_s - \vec{e}_i) , \qquad (3.1)$$

where

f_s = Frequency of the scattered light,

f_i = Frequency of the incident light,

λ = Wavelength of the incident light,

$\vec{V}$ = Velocity vector of the scattering particles

$\vec{e}_s$ = Unit vector in the scattering direction

and $\vec{e}_i$ = Unit vector in the incident direction.

The difference between the scattered and incident frequencies is the Doppler frequency

$$f_d = f_s - f_i \cdot \tag{3.2}$$

A combination of Equations 3.1 and 3.2 can be written as

$$f_d = \frac{1}{\lambda} \vec{V} \cdot (\vec{e}_s - \vec{e}_i). \tag{3.3}$$

Equation 3.3 shows that the velocity of the scattering particle is directly proportional to the Doppler frequency.

The Laser-Doppler anemometer (LDA) was set up with two incident beams as shown in Figure 3.4. Scattered light from particles passing through the crossing of the beams (measuring volume) was collected by the photomultiplier tube. The output of the photomultiplier had a frequency directly related to the Doppler frequency of the scattered light. In the configuration in Figure 3.4, Equation 3.3 can be written as

$$f_d = \frac{1}{\lambda} v \ (2 \sin(\theta/2])), \tag{3.4}$$

where

f_d = Doppler frequency,

BLOCK DIAGRAM OF LDA SYSTEM

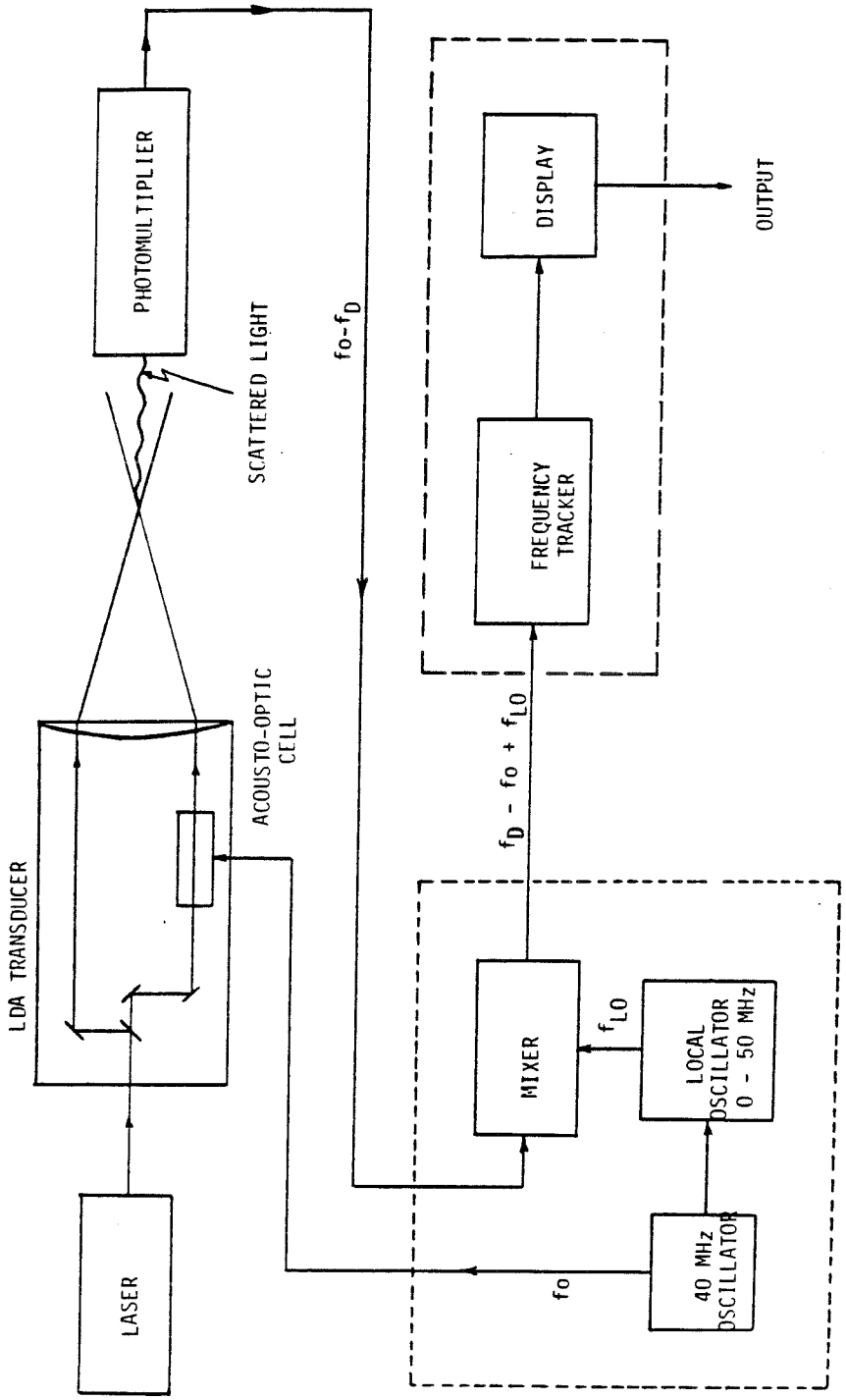

Figure 3.4

λ = Wavelength of the laser veam,

v = Component of velocity normal to the bisector of the beam intersection angle and in the plane of the beams,

and Θ = Angle between the intersecting laser beams.

Velocity is the variable of interest, so Equation 3.4 is usually written as

$$v = \frac{f_d \lambda}{2 \sin (\theta/2)} . \qquad (3.5)$$

From Equation 3.5 it can be seen that the velocity is only a function of the wavelength of the laser and the geometry of the optics.

The manner in which the Doppler frequency was generated by a scattering particle moving through the beam intersection can be visualized by considering the circular cross-section where the beams intersect. In Figure 3.5 a scattering particle is shown entering the beam crossing. The beam crossing itself can be thought of as a volume where two beams of light mix causing constructive and destructive interference fringes. A particle passing through these fringes will scatter light when illuminated and not scatter light when darkened. Figure 3.6 shows the signal from the scattering particle. The Doppler frequency is the frequency of the scattered light signal. The maximum intensity of the scattered signal occurs when the particle is at the center

BEAM CROSSING INTERFERENCE FRINGES

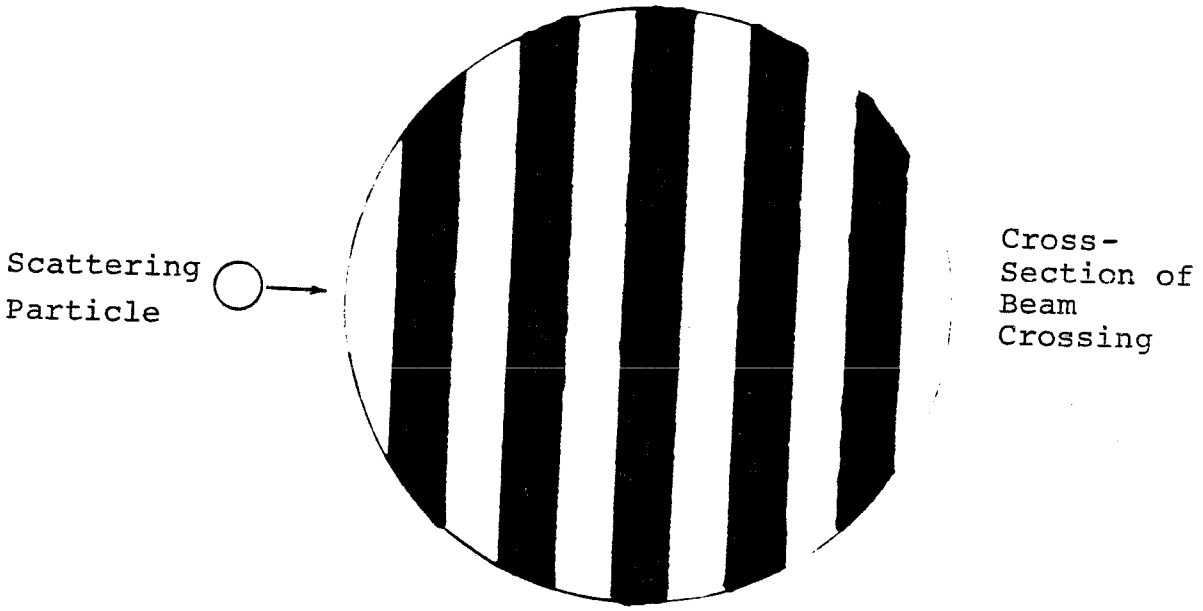

Figure 3.5

LIGHT SCATTERED FROM PARTICLE

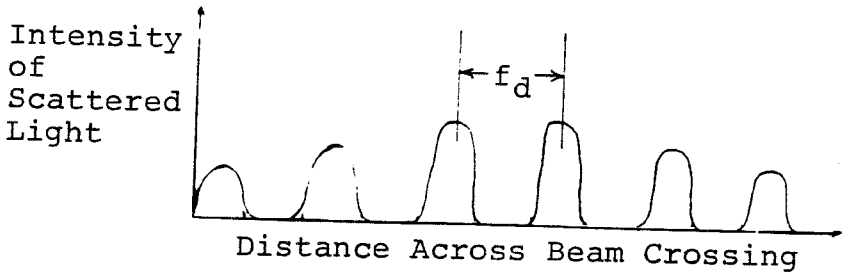

Figure 3.6

of the crossing. The intensity is not constant because the laser beams themselves do not have constant intensity across their diameters. They have a gaussian distribution of intensity with the maximum intensity occuring at the center.

The use of Equation 3.5 in calculating the velocity of the scattering particle does not allow the direction of the particle to be determined. Directional sense was obtained by passing one of the laser beams through an acousto-optic modulator known as a Bragg Cell. The Bragg Cell shifted the frequency of one laser beam by some fixed amount, 40 MHZ in our system. With one beam shifted by 40 MHZ the interference fringes swept across the measuring volume at 40 MHZ so that a stationary particle in the crossing scattered a 40 MHZ signal. The moving fringes gave directional information by scattering a signal of frequency 40 MHZ + f_d or 40 MHZ - f_d depending on whether the particle moved into or along with the fringes.

The LDA is usually used in measuring velocities in medias other than the air, in which the laser beam is initially transmitted. It was therefore important to determine what effect if any a change in the refractive index would have on the evaluation of velocity. From the laws of refraction

$$\lambda_1 \, n_1 = \lambda_2 \, n_2, \tag{3.6}$$

and

$$n_1 \sin \alpha_1 = n_2 \sin \alpha_2, \tag{3.7}$$

where

λ_1 = Wavelength of light in medium 1,

λ_2 = Wavelength of light in medium 2,

n_1 = Refractive index of light in medium 1,

n_2 = Refractive index of light in medium 2,

α_1 = Angle of transmittance in medium 1,

and α_2 = Angle of transmittance in medium 2.

For the LDA $\alpha = \theta/2$. Equation 3.7 then becomes

$$n_1 \sin(\theta_1/2) = n_2 \sin(\theta_2/2). \tag{3.8}$$

A combination of Equations 3.5, 3.6, and 3.8 gives the relation

$$v = \frac{f_d \lambda_1}{\sin(\theta_1/2)} = \frac{f_d \lambda_2}{\sin(\theta_2/2)}. \tag{3.9}$$

Equation 3.9 shows that the parameters for the laser beams crossing in air can be used to calculate the velocity of a particle in another medium.

3.5 Components of the LDA System

The laser used in the LDA system was a vertically polarized helium-neon gas laser model 124A made by Spectra-Physics. The power output was 15 mw, and the wavelength of the light was 632.8 nm. The beam diameter was 1.1 mm measured at the $1/e^2$ points on a gaussian distribution. The laser beam was steered into the transducer by means of an Oriel Corporation beam aligner. The beam aligner had 4 adjusting screws. Two were for vertical and horizontal trans-

LASER DOPPLER ANEMOMETER SYSTEM

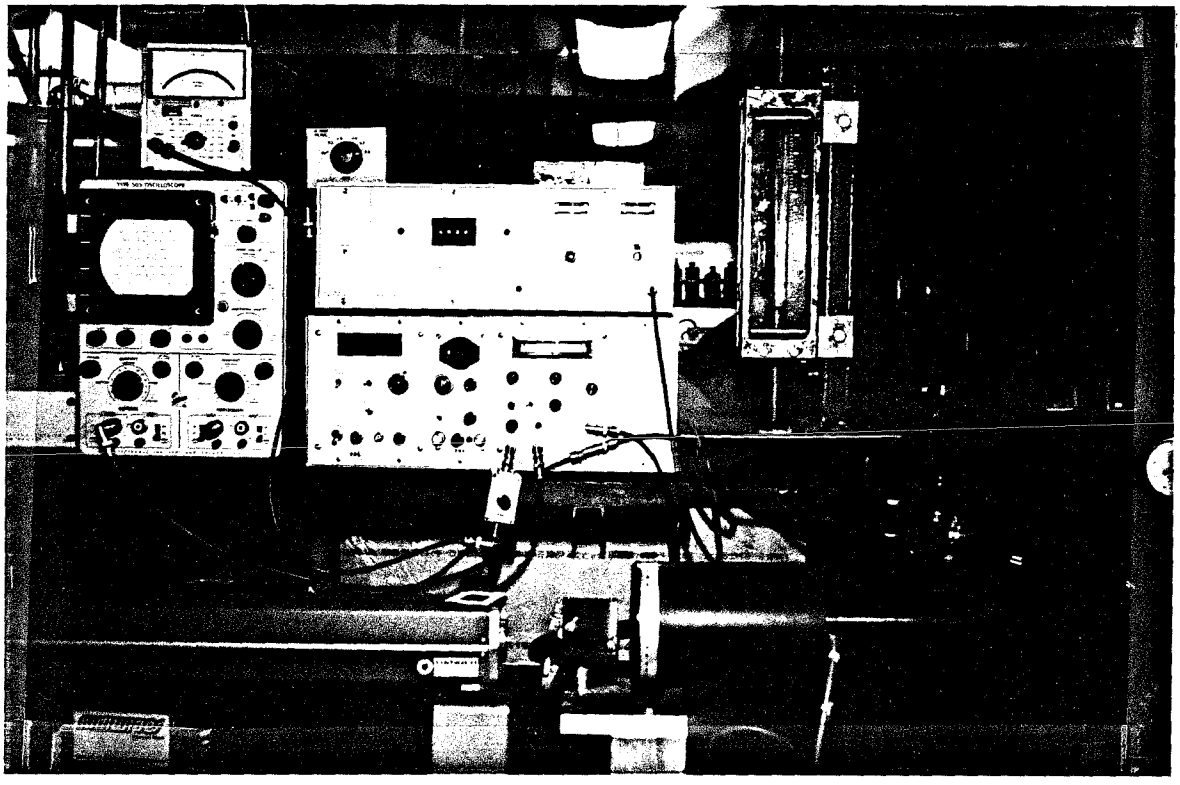

Figure 3.7

lation of the laser beam. The other two screws were for vertical and horizontal trimming of the exit laser beam angle. Once the beam had been aligned it passed into the LDA transducer section.

The LDA transducer (55L88) was built by DISA Electronics. The transducer consisted of a beam splitter and modulator section (55L83), a beam separator and lens mounting section (55L87), and a photomultiplier tube with associated optics (55L12). The beam splitter and modulator section and beam separator and lens mounting section were housed in a cylindrical casing. This casing could be rotated through 360° which allowed measurement of any velocity component in a plane normal to the transducer axis.

The laser beam entered the beam splitter and modulator section along its axis and passed through a beam-splitting prism. The prism split the beam into either a 50/50 or a 90/10-percent-intensity ratio. These two intensity ratios were obtained by two different thicknesses of metal deposits at two positions between the prisms comprising the beam splitter. Control over the selection of intensity ratios was determined by the ratio knob located on the transducer housing. This knob moved the splitting prism so that the laser beam was incident upon the correct splitting layer. In our experiments the 50/50-intensity ratio was used.

After splitting, one beam was passed through the Bragg Cell where its frequency was shifted ± 40 MHZ depending on the orientation of the Bragg Cell with respect to the incident laser beam. The Bragg Cell was composed of a block of isotropic glass with a series of piezoelectric transducers along one side and an acoustic absorber along the opposite side. The piezoelectric transducers, driven by a 40 MHZ signal, sent a series of acoustic waves across the block of glass. If the laser beam entered the Bragg Cell at the correct angle with respect to the acoustic wave fronts, the light waves and acoustic waves interacted. At this angle of incidence, known as the Bragg Angle, several beams emerge from the Bragg Cell. The emergent beams were an unshifted beam, a first-order-diffracted beam, and higher-order-diffracted beams. The first-order beam was the one that was frequency shifted by ± 40 MHZ. In our experimental set-up the frequency shift was -40 MHZ. The Bragg Angle was adjustable by means of an adjustment screw located on the beam splitter and modulator housing. The beam-stops were used to block out the unshifted beam and the shifted beams higher than first order. By optimizing the Bragg Angle and beam-stops the beam that emerged from this half of the optics was approximately 1/4 of the intensity of the original laser beam and was 40 MHZ lower in frequency.

The non-shifted beam, that was split from the original incoming laser beam, passed through a tilt-adjustment prism before leaving the splitter and modulator section. This tilt adjustment allowed the unshifted beam to be moved into the same plane as the -40 MHZ shifted beam so, upon focusing, the two beams crossed.

The unshifted and -40 MHZ shifted beams entered the beam separator and mounting section after leaving the beam splitter and modulator section. The beams could be separated by 20, 40, or 80 mm and they could be focused and crossed at 120 mm, 300 mm and 600 mm. There was one exception to the nine possible combinations of beam separation and lens focal length. The 120 mm lens could not be used with the 80 mm separator because the diameter of this lense was 49 mm. The separation of the two beams and the focal length of the lens set the angle of crossing and the size of the ellipsoid formed where the beams intersect. For the measurements that were made on both the continuous phase and the particles, the beam separation was 80 mm, and the focal length was 300 mm. For this separation and focal length the beam crossing angle was 15.18°, and the beam crossing dimensions were 2.25 mm in length and 0.3 mm in width. The volume in which the two laser beams crossed is commonly referred to as the measuring volume.

The final component in the LDA transducer was the photomultiplier tube and attached optics. The optics section had a selection of 3 lenses of 8.25, 3.25 and 1.75 diopters to be used along with the laser focusing lenses of 120, 300, and 600 mm focal length respectively. In order to insure that only light scrattered from particles passing through the measuing volume was amplified by the photomultiplier, a pinhole with a diameter of 0.1 mm was placed between the focusing optics and the photomultiplier. The focusing optics transmitted an image of the laser beams and beam crossing onto the screen containing the pinhole. The pinhole was then adjusted vertically and horizontally by two adjustment screws so that the image of the beam crossing and the pinhole coincided. With the pinhole in this position only scattered light from the measuring volume was passed through to the photomultiplier tube. This light had a frequency f_s = 40 MHZ + f_d, where f_d was the Doppler frequency. The photomultiplier then amplified this signal so that the output signal had the same frequency, f_{pm} = 40 MHZ + f_d.

The output of the photomultiplier was input to the DISA Electronics control unit (55L70). The control was made up of three subunits, the range translator (55L72), the LM exciter (55L74), and the PM exciter (55L76).

The LM exciter supplied the Bragg Cell with the 40 MHZ signal necessary to generate the acoustic waves in the glass block. The voltage of the 40 MHZ signal was adjustable by means of a level adjustment screw located on the front panel of the LM exciter. The applied voltage was adjusted until the first-order-diffracted beam reached its maximum intensity. This adjustment setting was used for all measurements made using the LDA.

The PM exciter (55L76) generated an adjustable voltage from 0 to 2 KV that was applied to the photomultiplier tube. This voltage could either be contolled automatically or manually. When automatic contol was used, the voltage was varied continuously to keep a steady output anode current from the PM tube. When the voltage was set manually, the output current varied with input signal. Particles of different sizes passing through the measuring volume scattered light of different intensities causing variation in output current if the manual setting was used. In the forward-scatter mode with sufficient scattering particles for a continuous Doppler signal, the automatic setting was preferred. If there were few particles present to scatter the light the manual setting was used so that background noise occurring between Doppler bursts was not excessively amplified. In the experiments for measuring velocity, the automatic setting was used, while in

the particle concentration experiments, the manual setting was used.

The final component in the LDA control unit was the range translator (55L72). This unit was comprised of a local oscillator, adjustable from 0 to 50 MHZ in steps of 10 KHZ, and a frequency mixer for operating on the photomultiplier signal. The local oscillator signal, f_{LO}, was mixed with the photomultiplier signal, f_{pm}, producing both the sum and difference of these two frequencies. The difference frequency, $f_m - f_{Lo} - f_{pm}$, was output from the control unit. Since f_{pm} was equal to 40 MHZ + f_d in our system, the local oscillator frequency was set below 40 MHZ. The mixer frequency could then be expressed as $f_m = (40 - f_{LO}) + f_d$.

The output from the mixer was input into a Thermo-System Inc. model 1090 tracker. The tracker converted the input signal into an analog voltage. The three basic components that made up the tracker were:

1) A phase-locked-loop
2) A frequency-to-voltage converter
3) A signal validation circuit

The phase-locked-loop (PLL) had the following five characteristics:

1) There was a center frequency, f_c, around which the PLL operated.

2) The PLL could lock onto and track an input signal whose frequency was within 15% of f_c.
3) There was an output voltage v_{PLL} that was linearly proportional to the difference between the input signal and f_c. v_{PLL} was positive for input signals less than f_c, zero for input signals equal to f_c, and negative for input signals greater than f_c.
4) When the PLL was locked onto a signal, the voltage-controlled-oscillator (VCO) had the same frequency as the input signal.
4) If the PLL was out of lock, the VCO ran at the center frequency f_c.

When a signal, f_d, was input to the tracker it was amplified and then mixed with a signal of frequency f_t so that the resulting frequency was $f_t - f_d$. The frequency f_t was adjusted so that the difference $f_t - f_d$ fell within the ± 15% range surrounding the center frequency of the PLL. There were two means of adjusting f_t. The first was manually by the Adjust-to-Null knob when the track switch was in the manual position. The second method for obtaining f_t was to place the track switch in the automatic position which allowed a feedback loop to vary f_t until v_{PLL} was zero. When v_{PLL} was zero, $f_t - f_d = f_c$. Only signals captured by the PLL were used in generating v_{PLL}.

The output voltage was obtained by summing a voltage proportional to $f_t - f_c$ ($f_{f/w}$) with the voltage from the PLL. The sum of these voltages was proportional to the Doppler frequency, f_d, as is shown below.

$$v_{out} = f_{f/w} + f_{PLL} = (f_t - f_c) + (f_d + f_c - f_t) = f_d$$

The ouptut voltage was displayed on a digital voltmeter mounted on the front panel of the tracker.

The final component of the tracker was the signal validation circuit. This circuit validated a Doppler signal only if 8 consecutive cycles of the signal had a constant phase, frequency, and amplitude. If the 8 cycle were constant, then the voltage was output to a hold circuit which held and displayed the voltage until another valid signal was ready. There was a 2-cycle delay between the end of a valid data point and the start of a new sample. This delay meant a data point had an effective length of 10 Doppler cycles.

3.6 Velocity Measurements

The velocity measurements were made with the LDA system in the dual-beam, forward-scatter mode. In this configuration the photomultiplier was situated on the opposite side of the measuring volume from the optics and focusing lens. Because both streamwise velocities, z direction, and cross stream velocities, y direction, were measured, the

photomultiplier was set up outside of both the x-z plane and the x-y plane. The offset of the photomultiplier allowed the beam crossing to be seen clearly in both z and y velocity measurements. The lens used to focus and cross the laser beams was the 300 mm lens, and the photomultiplier lens used was the 3.25 diopter lens. In this optical configuration, the beams were focused and crossed 30 cm from the transducer housing, and the photomultiplier was located 30 cm beyond the beam crossing. By using these lenses and these distances the measuring volume image was the same size as the pinhole in the photomultiplier.

With the position of the measuring volume fixed in space it was necessary to be able to move the flow channel in order to obtain velocity profiles. The channel was mounted on a milling table which allowed movement in the three coordinate directions x, y, and z. Dial micrometers mounted on the milling table allowed the distance that the channel was moved to be measured to 0.025 mm in each direction.

Velocity measurements made in the z direction used the laser beams crossing the in x-z plane, while velocity measurements made the y direction uses the laser beam crossing in the x-y plane. In order to fully characterize the flow it was necessary to be able to measure the z component and y component of velocity at any point on the

LDA TRANSDUCER AND COORDINATE DIRECTIONS

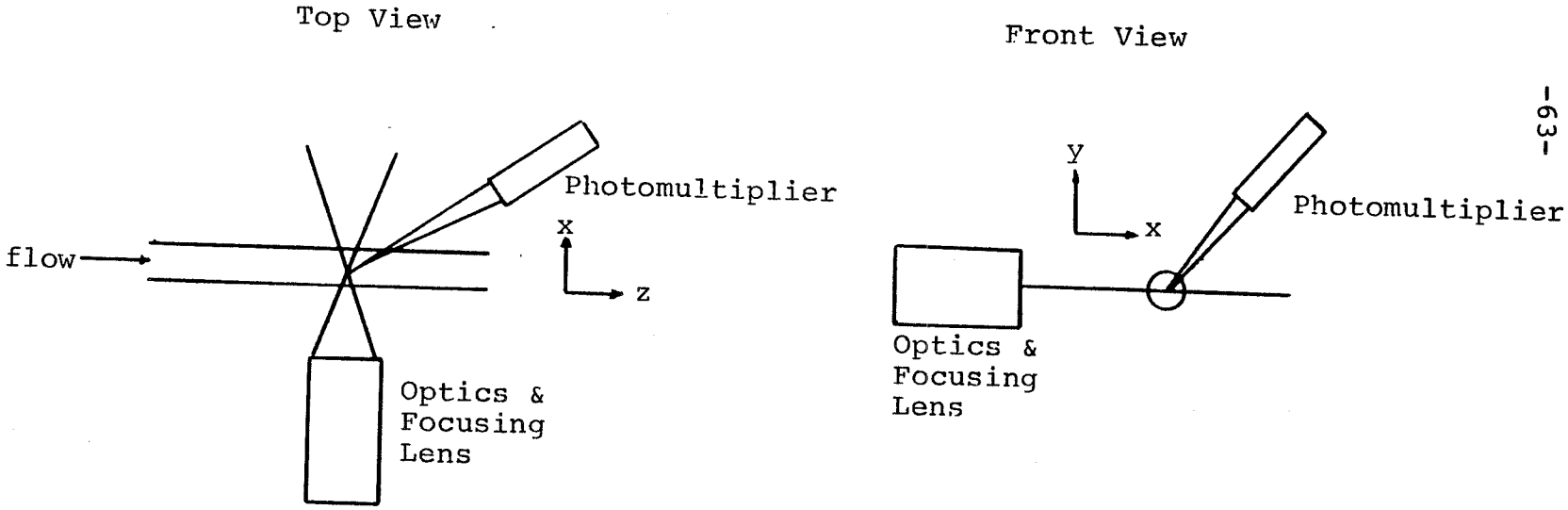

Figure 3.8

cross-section of the flow channel. For points above or below the horizontal centerline the curvature of the flow channel wall introduced problems in placing the measuring volume at the desired point in the flow. In order to minimize the curvature effect of the Plexiglass tube, a Plexiglass box was built that enclosed the flow channel. This box was 10.2 cm in length and 4.5 cm in both depth and width. The box was then filled with water surrounding the tube wall such that the refractive index inside and outside were the same. By using the index of refraction of water, n = 1.33, the index of refraction of Plexiglas, n = 1.47, and Snell's law, Equation 3.7, it was possible to calculate how far from the LDA focusing lens the flow channel had to be positioned for the beams to cross at a selected point.

It was necessary to have some means of positioning the flow channel at the beginning of each set of experiments. The method of establishing the flow channel at a known distance from the LDA was to find a stationary scattering particle on the inside wall along the horizontal centerline of the channel. The Doppler signal from this particle was optimized by adjusting the x-direction traversing gear so that the distance to the inside wall was the focal length of the focusing lense. In the experimental set up the laser beams were separated by 80 mm and the

300 mm focusing lens was used. The measuring volume was an ellipsoid with a major axis of 2.25 mm and a minor axis of 0.3 mm. Because of the length of the measuing volume, optimization of the stationary particle signal occurred over a range of approximately 1 mm. It was possible to obtain stationary particle signals on both the near and far inside walls. It was also possible to find stationary particles on the outside walls of the flow channel. By using the optimized signals from these four scattering particles and calculating the path of the beams through the Plexiglas and water, it was possible to determine the position of the flow channel with respect to the laser to within 0.5 mm.

The frequency that was detected and amplified by the photomultiplier was 40 MHZ plus the Doppler frequency. It was necessary to operate with a lower frequency in the tracking unit, so for all the experiments performed, the mixer frequency was chosen to be 39.80 MHZ. A signal of 200 KHZ plus the Doppler frequency was then output from the mixer. This signal was then routed through a high-pass filter with a cutoff frequency of 200 KHZ and then through a low-pass filter with cut-off frequencies of either 0.5, 1.0, or 2.0 MHZ. The value of cut-off frequency chosen for the low-pass filter depends on the magnitude of the Doppler frequency. The frequency-to-voltage convertor in

the tracker was set at a value of 1 volt/1 MHZ. A digital voltmeter on the tracker displayed the converter voltage. A reading of 0.2 V (200 KHZ frequency) corresponded to a stationary particle in the measuring volume. The Doppler frequency of a moving particle was obtained by subtracting 0.2 V from the digital-voltmeter reading and then using the 1 volt/1 MHZ conversion ratio. Because voltage was proportional to Doppler frequency and Doppler frequency was proportional to particle velocity, a single conversion constant could be used to calculate the scattering-particle velocity from the voltage. For the optical configuration used, the conversion factor was 238 cm/sec-V. Figure 3.9 shows a Doppler signal and the associated analog voltage for a moving scattering-particle.

The root-mean-square (rms) values of the fluctuating velocity components were also measured using the LDA. The analog voltage from the tracker was input into an rms voltmeter, and the voltage was analyzed using the same proportionality constant that was used for the mean velocity measurements. The Doppler signal entering the tracker was filtered using a 1 MHZ bandpass filter, and the voltage leaving the tracker was filtered by either a 200 EZ or a 500 HZ low-pass filter before entering the rms voltmeter. Because a 1 MHZ bandpass filter was used prior to the tracker, the mixer frequency was adjusted for each flow-rate

DOPPLER SIGNAL FROM SCATTERING PARTICLE

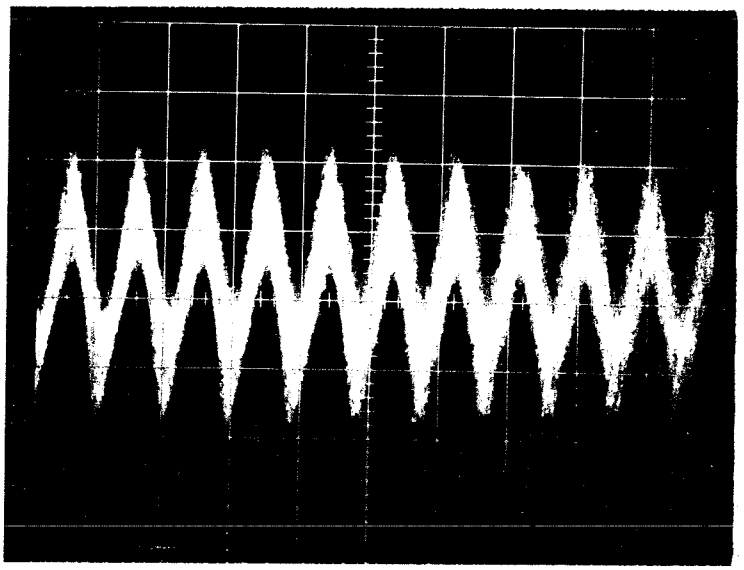

ANALOG VOLTAGE FROM TRACKER

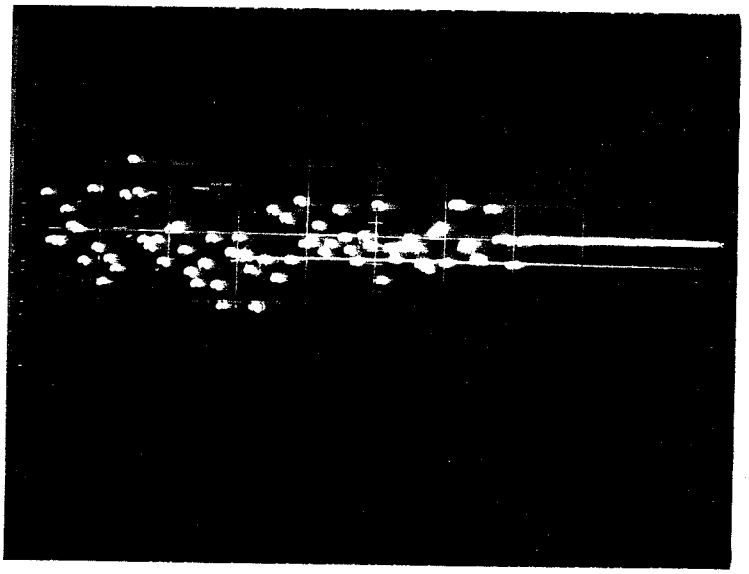

Figure 3.9

so that the Doppler signal fell into the filter band. The lowest two flow-rates, 167 cm^3/sec and 250 cm^3sec, used the 200 HZ low-pass filter. The highest two flow-rates, 333 cm^3/sec and 417 cm^3/sec used the 500 HZ low-pass filter. These filter combinations were determined by comparing rms frequencies evaluated from measurements on an oscilliscope with the rms frequencies calculated from readings off the voltmeter.

3.7 Measurement of Particle Concentration

Concentration profiles of the solid particles were measured in two ways:

1. The LDA system was used as an event counter.
2. Particles were captured in a collector grid.

The counting method using the LDA system will be discussed first.

A particle passing through the measuring volume reflected a burst of light which the photomultiplier converted to an electrical signal. This signal was converted to a lower frequency in the mixer section, Figure 3.10, and was then input into a Tektronix DC 501 frequency counter.

The DC 501 counter was capable of measuring an input frequency from 10 HZ to 110 MHZ. It was also able to count the total number of cycles of the input signal over a given time span. This count was achieved by setting the Measurement

BLOCK DIAGRAM FOR LDA USED
AS A PARTICLE COUNTER

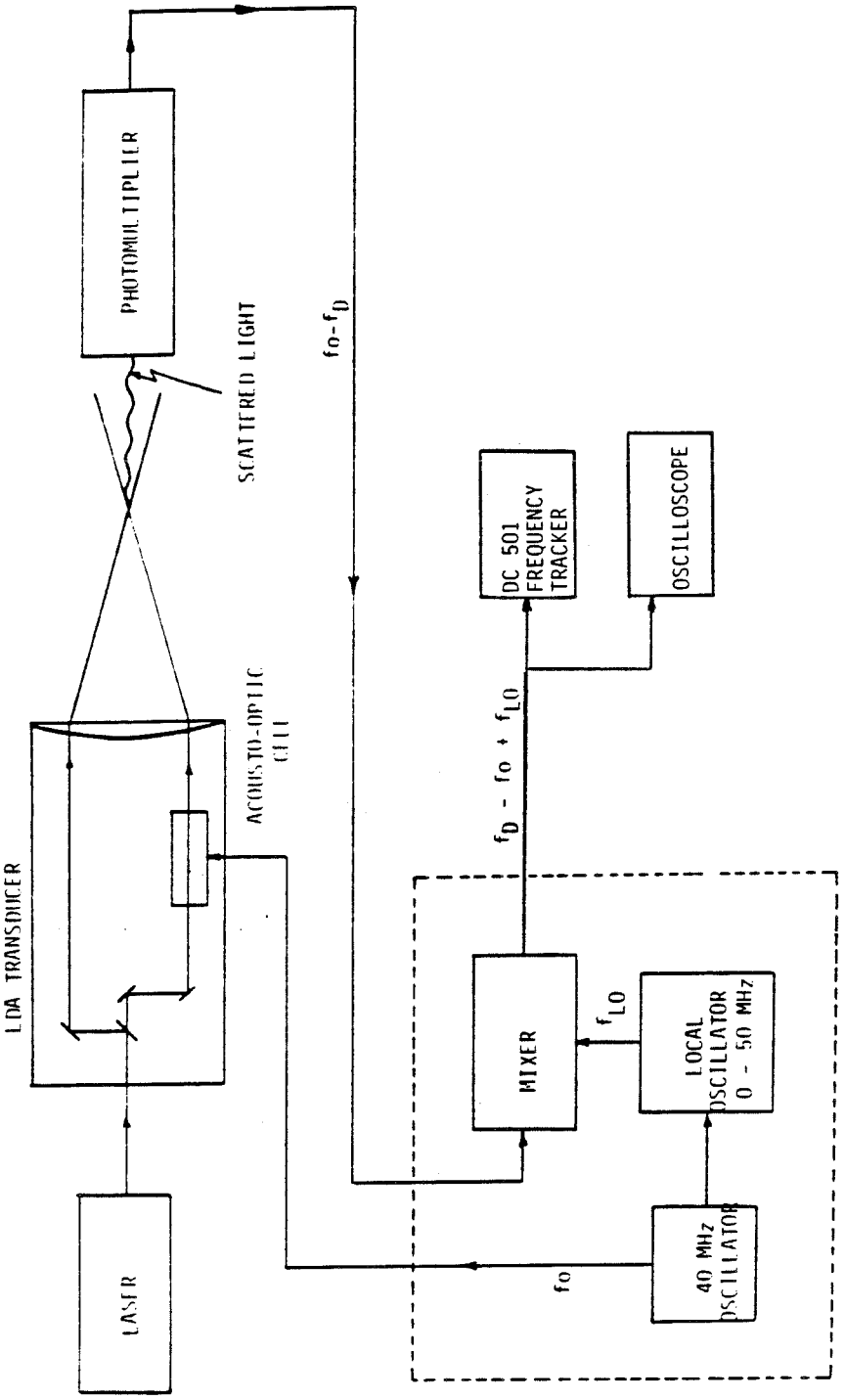

Figure 3.10

Interval switch to Manual and pushing the start/stop switch at the beginning and end of the measuring time. The Trigger Level knob allowed the DC 501 to discriminate between the desired signal and the undesired background noise. The Trigger Level could be adjusted continuously from -2 V to +2 v, and only AC signals greater in magnitude than the set Trigger Level would then be counted.

When the particles were counted, the background noise was minimized in two ways. First the 5-micron filter used for removing the injected particles also removed background particles in the water. The injected polyvinylchloride particles, with diameters of 120 microns, were much larger than any background particle, so a correspondingly greater amount of light was scattered from the PVC particles. The second means of minimizing the noise was to set the PM tube voltage to manual and dial in a preselected voltage. For the purpose of our experiments the best PM tube voltage was 1.5 KV. Under these conditions the signal was easily detected over the noise, Figure 3.11, so that the trigger level of the counter could be set to detect only the signal from the PVC particles.

The PVC particles were injected into the center of the flow channel 91.44 cm downstream from the flow conditioner. The measuring volume was then positioned at various distances downstream from the injection point. At each

PARTICLE DOPPLER BURST

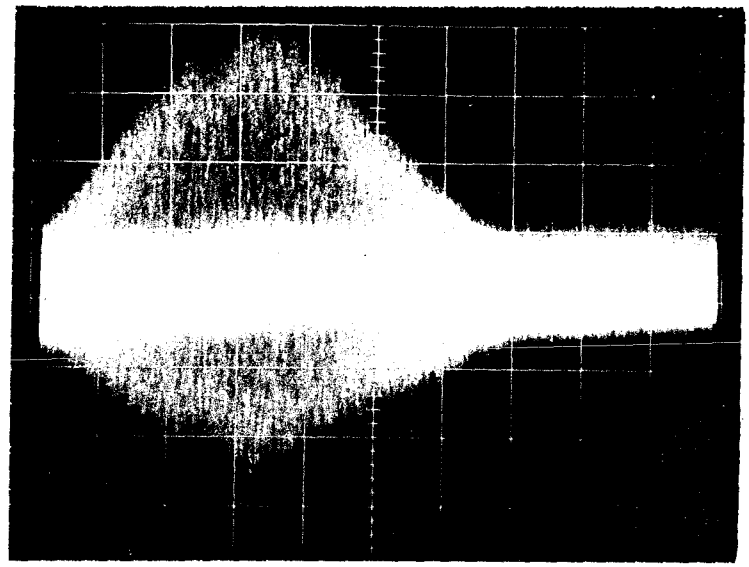

Figure 3.11

downstream position the horizontal centerline was traversed until the particle reservoir was empty and the number of counts occurring at each position on the centerline was recorded. A single particle-concentration curve was composed of data accumulated from four charges of the particle-holding reservoir.

The second method used to determine particle concentration profiles was to capture the particles in a segmented brass collector (Figure 3.12). The square holes used for separating the particles were 0.254 cm on a side. The particles were kept from mixing at the back end by a 350 mesh screen epoxied to the brass plates. The distribution of particles across the channel was determined by collecting particles for 30 minutes and then weighing the amounts caught in individual sections. The 30 minute collection period was composed of 20 individual collections each with a duration of 1½ minutes.

PARTICLE CAPTURING CELL

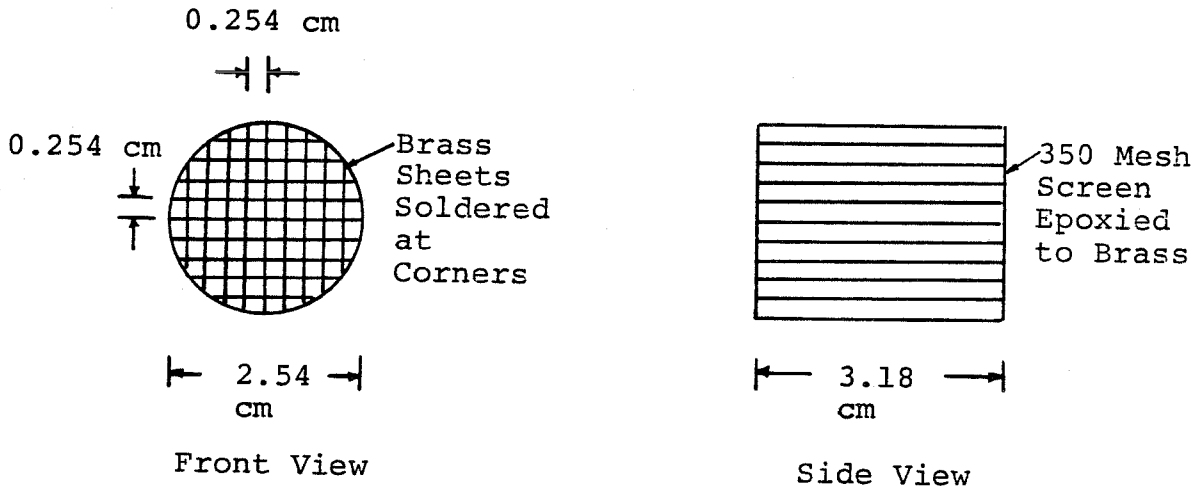

Figure 3.12

CHAPTER 4

CONTINUOUS-PHASE EXPERIMENTAL RESULTS

4.1 General

Experimental measurements of mean and fluctuating velocity components were made over the complete cross-section of the 2.54-cm-ID flow channel. These measurements were made in order to characterize the flow and to insure that the flow was both developed and symmetric. It was important that the velocity field be fully developed and symmetric so that during the second phase of experiments, when the particles were injected into the system, the diffusion of the particles would only be due to the turbulence of the flow and not in part to changes in the velocity field. Four flow-rates were used in the liquid-velocity measurements and in the particle-diffusion experiments. The flow-rates are listed in Table 4.1.

4.2 Developed Flow

The downstream distance from a pipe inlet necessary to obtain fully developed turbulent flow varies widely depending on the inlet configuration. Deissler (4-2) investigated the distance needed for development of the maximum velocity in tube flow for both a rounded entrance and a right-angle entrance. The data taken with the rounded entrance showed the maximum velocity still increasing 100

VOLUMETRIC FLOW-RATES THAT WERE USED IN BOTH THE CONTINUOUS AND DISPERSE-PHASE EXPERIMENTS

R_e $(DV_{avg}\rho)/\mu$	Volumetric Flow-rate cm^3/sec
8,400	167
12,500	250
16,700	332
20,900	417

Table 4.1

diameters downstream from the entrance. The data taken using a right-angle entrance showed the maximum velocity had developed within 45 diameters downstream from the entrance. Three flow-rates were used in Diessler's experiments. The Reynolds numbers for the three flow-rates were 48,000, 160,000 and 580,000, respectively. Rupe (4-11) obtained a fully developed flow in a smooth tube 15 diameters downstream from the tube entrance. This fast development was obtained by using an initial section of tubing 5 diameters long with a roughness factor of 0.042. The range of Reynolds numbers used in these experiments was from 30,000 to 40,000.

In the experiments discussed here, the flow was conditioned before entering the 2.54-cm-ID measurement section. The water was first subjected to a right-angle bend and then was passed through a set of straightening vanes. Following the straightening vanes, the flow was accelerated in a convergent section and finally passed through an 80-mesh screen at the entrance to the measurement section.

Mean-velocity measurements were made at 35, 65, and 105 diameters downstream from the entrance, respectively, for the flow-rates of 167 cm^3/sec and 417 cm^3/sec. These measurements were taken on the horizontal centerline of the channel to determine when the flow had developed. Figure 4.1 shows the centerline-velocity profiles for the two

VELOCITY PROFILES FOR THREE DOWNSTREAM DISTANCES FROM THE FLOW CONDITIONER

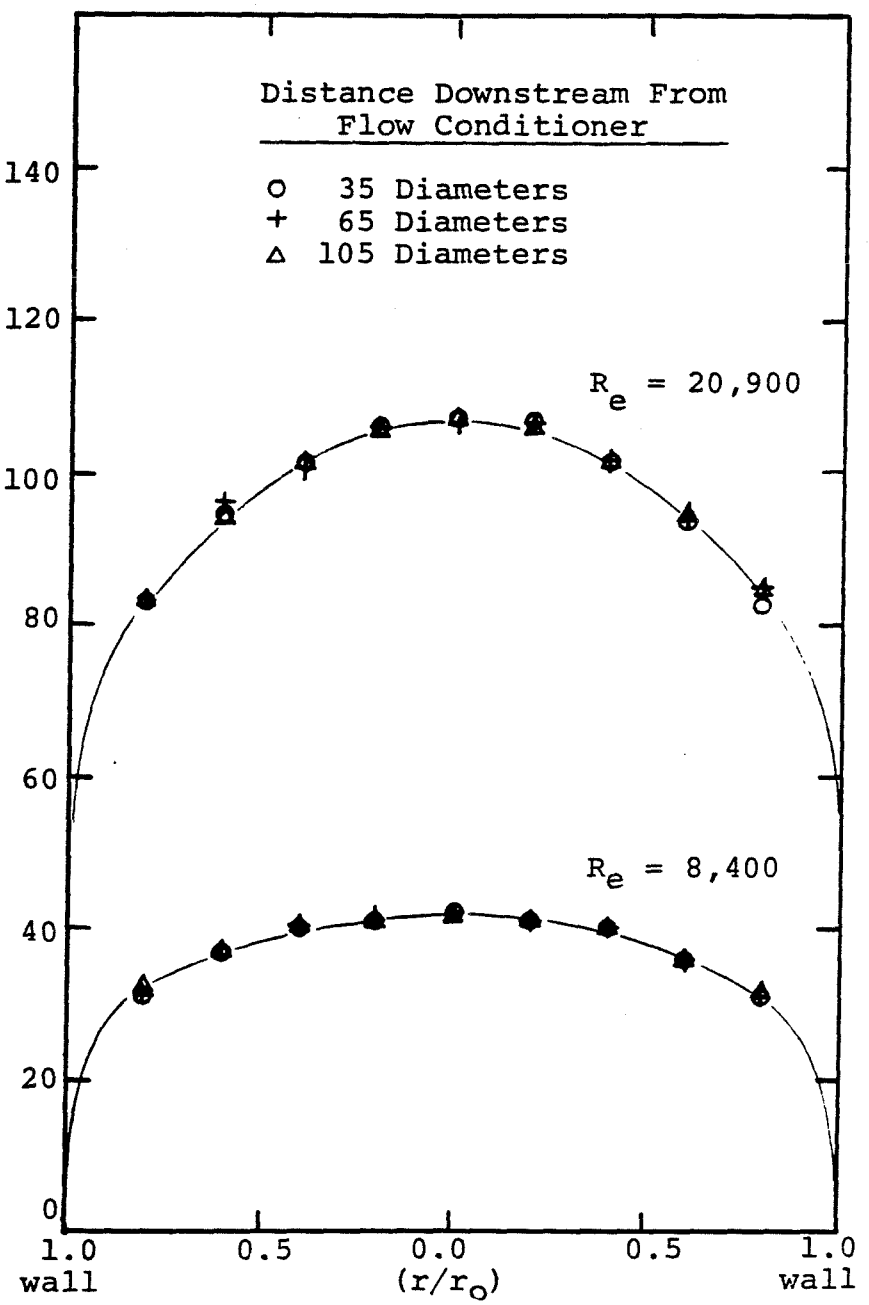

Figure 4.1

flow-rates at the three downstream distances. The velocities measured at 35, 65, and 105 diameters downstream were virtually the same for a given Reynolds number. Because both extreme flow-rates were developed by 35 diameters downstream from the flow conditioner, the intermediate flow-rates would be developed by this position also.

4.3 Mean Velocities

Axial-velocity measurements were made over the entire channel cross-section at 35 diameters downstream from the entrance. The velocities were measured at grid points located 0.25 cm from each other. This grid spacing allowed 69 measurement positions to be used over the channel cross-section. The axial-velocity measurements were made to insure that the velocity field was symmetric. A non-symmetric velocity field would introduce an inconsistent effect in the particle diffusion experiments at any given radial position. Figures 4.2 through 4.5 are contour plots of the axial velocity field 35 diameters downstream from the flow conditioner. In all four figures the velocity field was quite symmetrical showing that there was no problem with uneven velocity distributions. Typical velocities used in evaluating the controus are also shown in Figures 4.2 through 4.5. The complete axial-velocity data are listed in Tables 4.2 through 4.5. For the velocity

AXIAL VELOCITY CONTOURS

Typical points used in establishing
40 cm/sec and 35 cm/sec velocity contours

R_e = 8,400

Velocity Contours

v_z = 40 cm/sec

v_z = 35 cm/sec

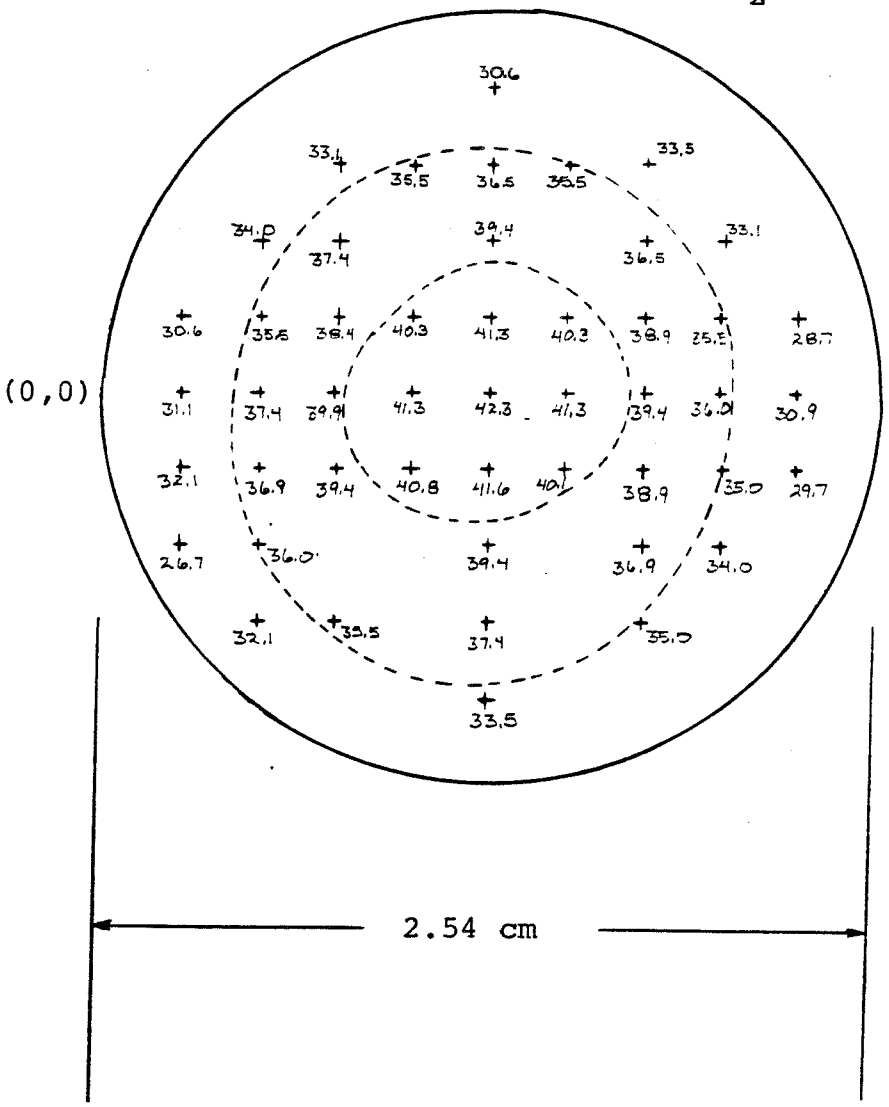

Figure 4.2

AXIAL VELOCITY CONTOURS

Typical points used in establishing
60 cm/sec and 50 cm/sec velocity contours

R_e = 12,500

Velocity Contours

v_z = 60 cm/sec

v_z = 50 cm/sec

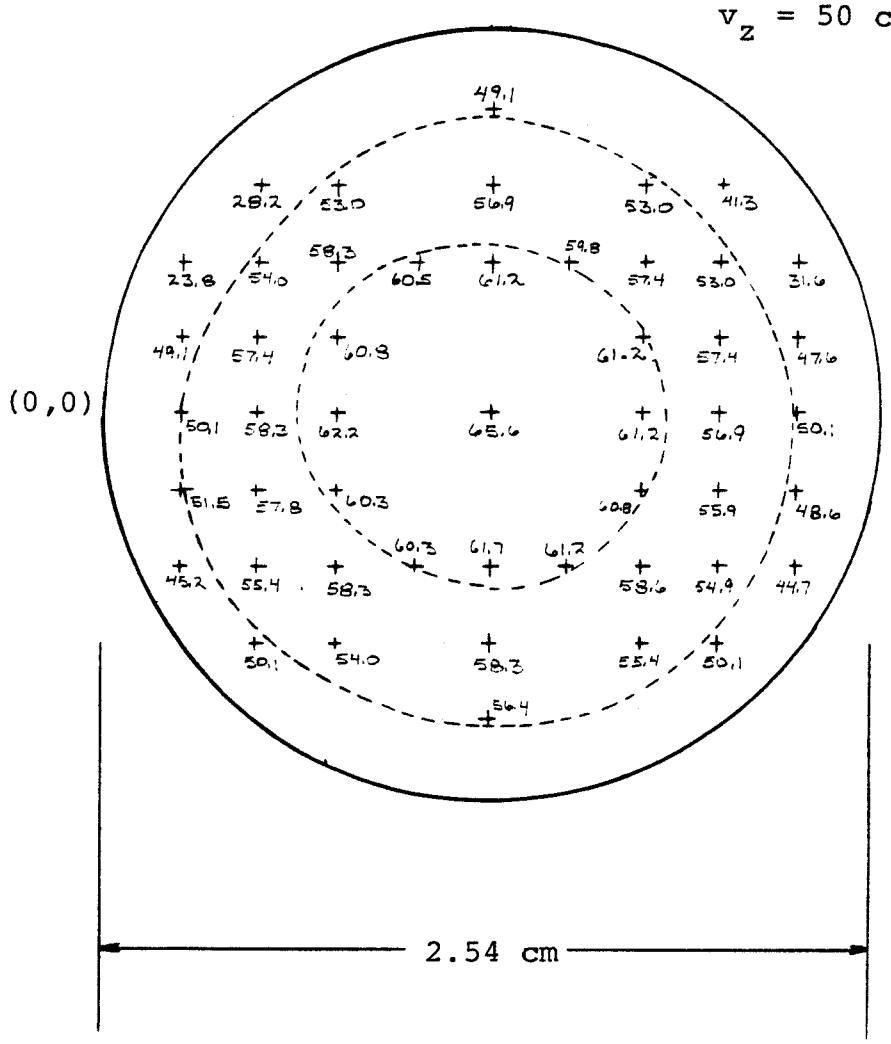

Figure 4.3

AXIAL VELOCITY CONTOURS

Typical points used in establishing
80 cm/sec and 65 cm/sec velocity contours

R_e = 16,700

Velocity Contours

v_z = 80 cm/sec

v_z = 65 cm/sec

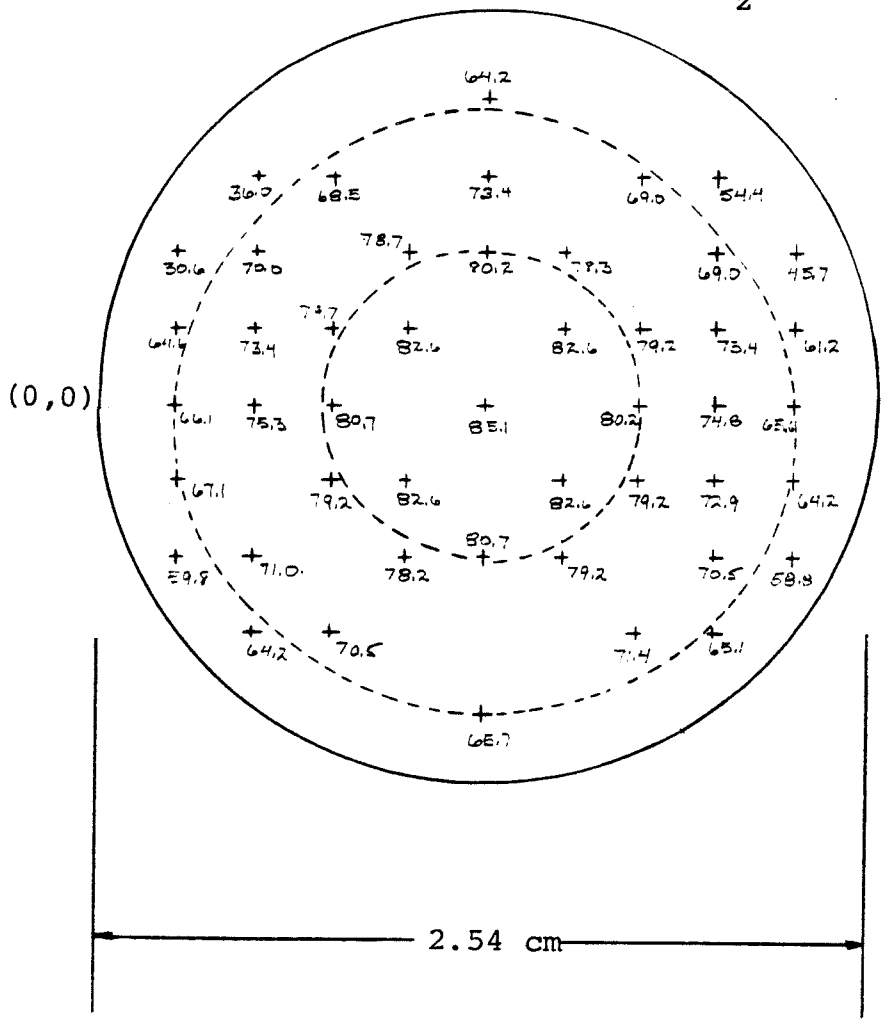

Figure 4.4

AXIAL VELOCITY CONTOURS

Typical points used in establishing
100 cm/sec and 90 cm/sec velocity contours

R_e = 20,900

Velocity Contours

v_z = 100 cm/sec

v_z = 90 cm/sec

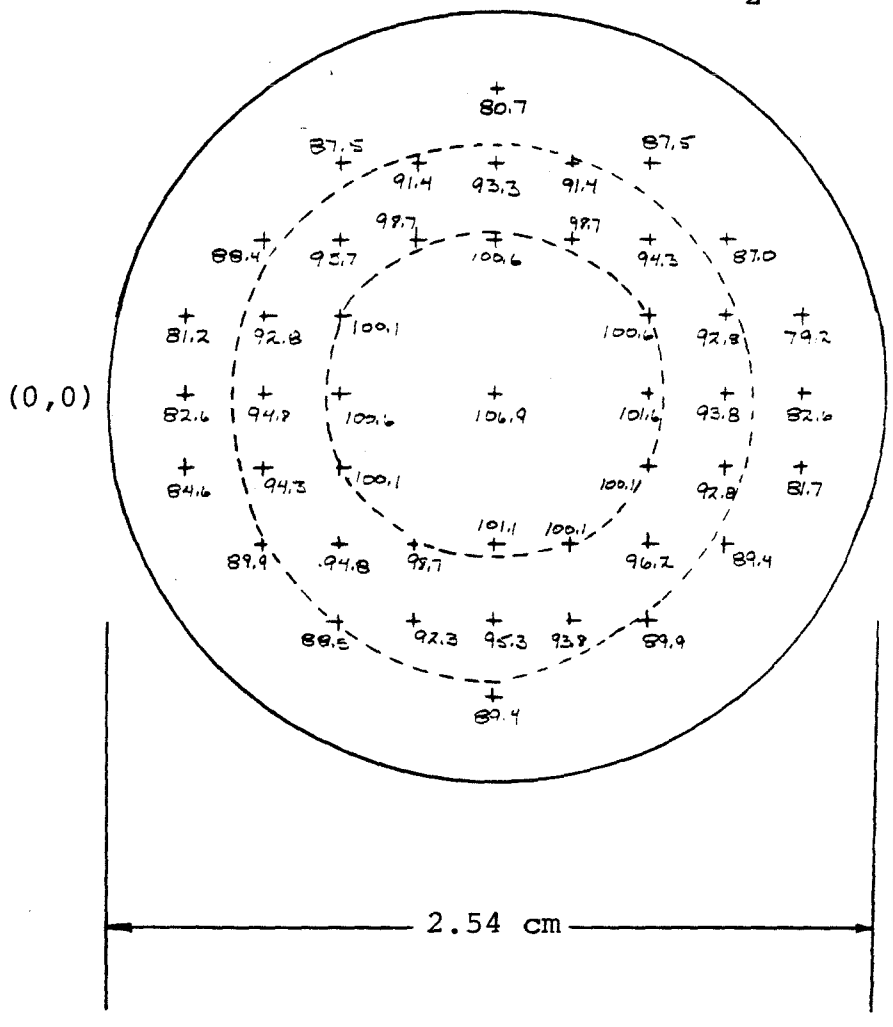

Figure 4.5

COORDINATE DIRECTIONS FOR
LASER MEASUREMENTS

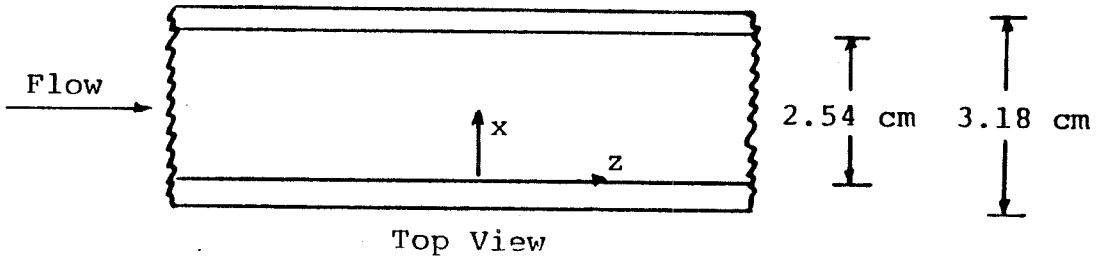

Top View

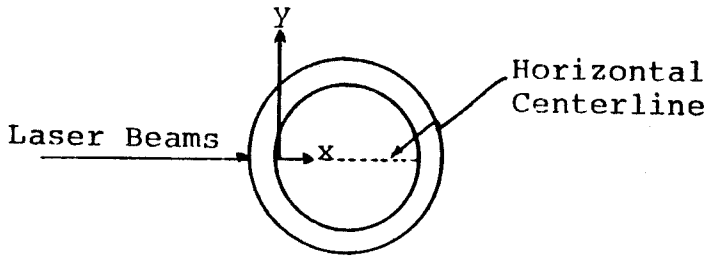

Front View

Figure 4.6

AXIAL VELOCITIES FOR THE R_e = 8,400 FLOW

Coordinates		Velocity
X(cm)	Y(cm)	V_z(cm/sec)
wall	+0.00	----
0.25	0.00	31.1
0.51	0.00	37.4
0.76	0.00	39.9
1.02	0.00	41.3
1.27	0.00	42.3
1.52	0.00	41.3
1.78	0.00	39.4
2.03	0.00	36.0
2.29	0.00	30.9
wall	0.00	4.9
wall	+0.25	6.8
0.25	0.25	30.6
0.51	0.25	35.5
0.76	0.25	38.4
1.02	0.25	40.3
1.27	0.25	41.3
1.52	0.25	40.3
1.78	0.25	38.9
2.03	0.25	35.5

Table 4.2

Table 4.2 continued

Coordinates		Velocity
X(cm)	Y(cm)	V_z(cm/sec)
2.29	0.25	28.7
wall	0.25	----
wall	+0.51	----
0.25	0.51	14.1
0.51	0.51	34.0
0.76	0.51	37.4
1.02	0.51	38.4
1.27	0.51	39.4
1.52	0.51	37.9
1.78	0.51	36.5
2.03	0.51	33.1
2.29	0.51	16.5
wall	0.51	----
wall	+0.76	----
0.51	0.76	17.5
0.76	0.76	33.1
1.02	0.76	35.5
1.27	0.76	36.5
1.52	0.76	35.5
1.78	0.76	33.5

Table 4.2 continued

Coordinates		Velocity
X(cm)	Y(cm)	V_z(cm/sec)
2.03	0.76	23.8
wall	0.76	----
wall	+1.02	----
0.76	1.02	9.2
1.02	1.02	28.7
1.27	1.02	30.6
1.52	1.02	29.6
1.78	1.02	10.2
wall	1.02	----
wall	-0.25	4.9
0.25	0.25	32.1
0.51	0.25	36.9
0.76	0.25	39.4
1.02	0.25	40.8
1.27	0.25	41.6
1.52	0.25	40.1
1.78	0.25	38.9
2.03	0.25	35.0
2.29	0.25	29.7
wall	0.25	6.3

Table 4.2 continued

Coordinates		Velocity
X(cm)	Y(cm)	V_z(cm/sec)
wall	-0.51	----
0.25	0.51	26.7
0.51	0.51	36.0
0.76	0.51	37.4
1.02	0.51	38.9
1.27	0.51	39.4
1.52	0.51	38.4
1.78	0.51	36.9
2.03	0.51	34.0
2.29	0.51	26.7
wall	0.51	----
wall	-0.76	20.4
0.51	0.76	32.1
0.76	0.76	35.5
1.02	0.76	36.9
1.27	0.76	37.4
1.52	0.76	36.5
1.78	0.76	35.0
2.03	0.76	32.1
wall	0.76	6.8

Table 4.2 continued

Coordinates		Velocity
X(cm)	Y(cm)	V_z(cm/sec)
wall	-1.02	----
0.76	1.02	28.2
1.02	1.02	33.5
1.27	1.02	34.5
1.52	1.02	34.0
1.78	1.02	30.1
wall	1.02	----

AXIAL VELOCITIES FOR THE R_e = 12,500 FLOW

Coordinates		Velocity
X(cm)	Y(cm)	V_z(cm/sec)
wall	0.00	----
0.25	0.00	50.1
0.51	0.00	58.3
0.76	0.00	62.2
1.02	0.00	64.6
1.27	0.00	65.6
1.52	0.00	64.6
1.78	0.00	61.2
2.03	0.00	56.9
2.29	0.00	50.1
wall	0.00	12.6
wall	+0.25	14.1
0.25	0.25	49.1
0.51	0.25	57.4
0.76	0.25	60.8
1.02	0.25	63.7
1.27	0.25	64.6
1.52	0.25	63.2
1.78	0.25	61.2
2.03	0.25	57.4
2.29	0.25	47.6
wall	0.25	----

Table 4.3

Table 4.3 continued

Coordinates		Velocity
X(cm)	Y(cm)	V_z(cm/sec)
wall	+0.51	----
0.25	0.51	23.8
0.51	0.51	54.0
0.76	0.51	58.3
1.02	0.51	60.5
1.27	0.51	61.2
1.52	0.51	59.8
1.78	0.51	57.4
2.03	0.51	53.0
2.29	0.51	31.6
wall	0.51	----
wall	+0.76	----
0.51	0.76	28.2
0.76	0.76	53.0
1.02	0.76	55.9
1.27	0.76	56.9
1.52	0.76	55.7
1.78	0.76	53.0
2.03	0.76	41.3
wall	0.76	----

Table 4.3 continued

Coordinates		Velocity
X(cm)	Y(cm)	V_z(cm/sec)
wall	+1.02	----
0.76	1.02	28.2
1.02	1.02	47.1
1.27	1.02	49.1
1.52	1.02	47.6
1.78	1.02	17.5
wall	1.02	----
wall	-0.25	9.7
0.25	0.25	51.5
0.51	0.25	57.8
0.76	0.25	60.3
1.02	0.25	64.2
1.27	0.25	64.6
1.52	0.25	63.7
1.78	0.25	60.8
2.03	0.25	55.9
2.29	0.25	48.6
wall	0.25	17.0
wall	-0.51	----
0.25	0.51	45.2

Table 4.3 continued

Coordinates		Velocity
X(cm)	Y(cm)	V_z(cm/sec)
0.51	-0.51	55.4
0.76	0.51	58.3
1.02	0.51	60.3
1.27	0.51	61.7
1.52	0.51	61.2
1.78	0.51	58.6
2.03	0.51	54.9
2.29	0.51	44.7
wall	0.51	----
wall	-0.76	36.9
0.51	0.76	50.1
0.76	0.76	54.0
1.02	0.76	57.4
1.27	0.76	58.3
1.52	0.76	57.8
1.78	0.76	55.4
2.03	0.76	50.1
wall	0.76	16.0
wall	-1.02	----
0.76	1.02	47.1

Table 4.3 continued

Coordinates		Velocity
X(cm)	Y(cm)	V_z(cm/sec)
1.02	-1.02	54.0
1.27	1.02	56.4
1.52	1.02	54.4
1.78	1.02	48.6
wall	1.02	----

AXIAL VELOCITIES FOR THE R_e = 16,700 FLOW

Coordinates		Velocity
X(cm)	Y(cm)	V_z(cm/sec)
wall	0.00	----
0.25	0.00	66.1
0.51	0.00	75.3
0.76	0.00	80.7
1.02	0.00	84.1
1.27	0.00	85.1
1.52	0.00	84.1
1.78	0.00	80.2
2.03	0.00	74.8
2.29	0.00	65.6
wall	0.00	19.4
wall	+0.25	20.9
0.25	0.25	64.6
0.51	0.25	73.4
0.76	0.25	79.7
1.02	0.25	82.6
1.27	0.25	83.6
1.52	0.25	82.6
1.78	0.25	79.2
2.03	0.25	73.4

Table 4.4

Table 4.4 continued

Coordinates		Velocity
X(cm)	Y(cm)	V_z(cm/sec)
2.29	+0.25	61.2
wall	0.25	----
wall	+0.51	----
0.25	0.51	30.6
0.51	0.51	70.0
0.76	0.51	76.3
1.02	0.51	78.7
1.27	0.51	80.2
1.52	0.51	78.3
1.78	0.51	74.8
2.03	0.51	69.0
2.29	0.51	45.7
wall	0.51	----
wall	+0.76	----
0.51	0.76	36.0
0.76	0.76	68.5
1.02	0.76	72.9
1.27	0.76	73.4
1.52	0.76	72.9
1.78	0.76	69.0

Table 4.4 continued

Coordinates		Velocity
X(cm)	Y(cm)	V_z(cm/sec)
2.03	+0.76	54.4
wall	0.76	----
wall	+1.02	----
0.76	1.02	34.5
1.02	1.02	61.2
1.27	1.02	64.2
1.52	1.02	62.7
1.78	1.02	40.8
wall	1.02	----
wall	-0.25	15.6
0.25	0.25	67.1
0.51	0.25	74.8
0.76	0.25	79.2
1.02	0.25	82.6
1.27	0.25	83.6
1.52	0.25	82.6
1.78	0.25	79.2
2.03	0.25	72.9
2.29	0.25	64.2
wall	0.25	25.8

Table 4.4 continued

Coordinates		Velocity
X(cm)	Y(cm)	V_z(cm/sec)
wall	-0.51	----
0.25	0.51	59.8
0.51	0.51	71.0
0.76	0.51	74.8
1.02	0.51	78.2
1.27	0.51	80.7
1.52	0.51	79.2
1.78	0.51	76.3
2.03	0.51	70.5
2.29	0.51	58.8
wall	0.51	----
wall	-0.76	47.1
0.51	0.76	64.2
0.76	0.76	70.5
1.02	0.76	73.4
1.27	0.76	75.3
1.52	0.76	74.3
1.78	0.76	71.4
2.03	0.76	65.1
wall	0.76	29.7

Table 4.4 continued

Coordinates		Velocity
X(cm)	Y(cm)	V_z(cm/sec)
wall	-1.02	----
0.76	1.02	60.8
1.02	1.02	68.0
1.27	1.02	71.4
1.52	1.02	69.5
1.78	1.02	62.7
wall	1.02	----

AXIAL VELOCITIES FOR THE R_e = 20,900 FLOW

Coordinates		Velocity
X(cm)	Y(cm)	V_z(cm/sec)
wall	0.00	----
0.25	0.00	82.6
0.51	0.00	94.8
0.76	0.00	100.6
1.02	0.00	105.5
1.27	0.00	106.9
1.52	0.00	106.4
1.78	0.00	101.6
2.03	0.00	93.8
2.29	0.00	82.6
wall	0.00	51.5
wall	+0.25	45.7
0.25	0.25	81.2
0.51	0.25	92.8
0.76	0.25	100.1
1.02	0.25	104.5
1.27	0.25	105.6
1.52	0.25	104.5
1.78	0.25	100.6
2.03	0.25	92.8

Table 4.5

Table 4.5 continued

Coordinates		Velocity
X(cm)	Y(cm)	V_z(cm/sec)
2.29	+0.25	79.2
wall	0.25	----
wall	+0.51	----
0.25	0.51	44.2
0.51	0.51	88.9
0.76	0.51	95.7
1.02	0.51	98.7
1.27	0.51	100.6
1.52	0.51	98.7
1.78	0.51	94.3
2.03	0.51	87.0
2.29	0.51	66.6
wall	0.51	----
wall	+0.76	----
0.51	0.76	46.2
0.76	0.76	87.5
1.02	0.76	91.4
1.27	0.76	93.3
1.52	0.76	91.4
1.78	0.76	87.5

Table 4.5 continued

Coordinates		Velocity
X(cm)	Y(cm)	V_z(cm/sec)
2.03	+0.76	73.4
wall	0.76	----
wall	+1.02	----
0.76	1.02	56.4
1.02	1.02	77.8
1.27	1.02	80.7
1.52	1.02	78.3
1.78	1.02	64.6
wall	1.02	----
wall	-0.25	46.7
0.25	0.25	84.6
0.51	0.25	94.3
0.76	0.25	100.1
1.02	0.25	104.0
1.27	0.25	105.5
1.52	0.25	104.5
1.78	0.25	100.1
2.03	0.25	92.8
2.29	0.25	81.7
wall	0.25	40.1

Table 4.5 continued

Coordinates		Velocity
X(cm)	Y(cm)	V_z(cm/sec)
wall	-0.51	----
0.25	0.51	77.8
0.51	0.51	89.9
0.76	0.51	94.8
1.02	0.51	98.7
1.27	0.51	101.1
1.52	0.51	100.1
1.78	0.51	96.2
2.03	0.51	89.4
2.29	0.51	75.8
wall	0.51	22.8
wall	-0.76	65.6
0.51	0.76	81.2
0.76	0.76	88.5
1.02	0.76	92.3
1.27	0.76	95.3
1.52	0.76	93.8
1.78	0.76	89.9
2.03	0.76	82.6
wall	0.76	55.9

Table 4.5 continued

Coordinates		Velocity
X(cm)	Y(cm)	V_z(cm/sec)
wall	-1.02	41.8
0.76	1.02	76.8
1.02	1.02	85.5
1.27	1.02	89.4
1.52	1.02	88.5
1.78	1.02	79.2
wall	1.02	----

Y VELOCITY COMPONENT

R_e = 8,400

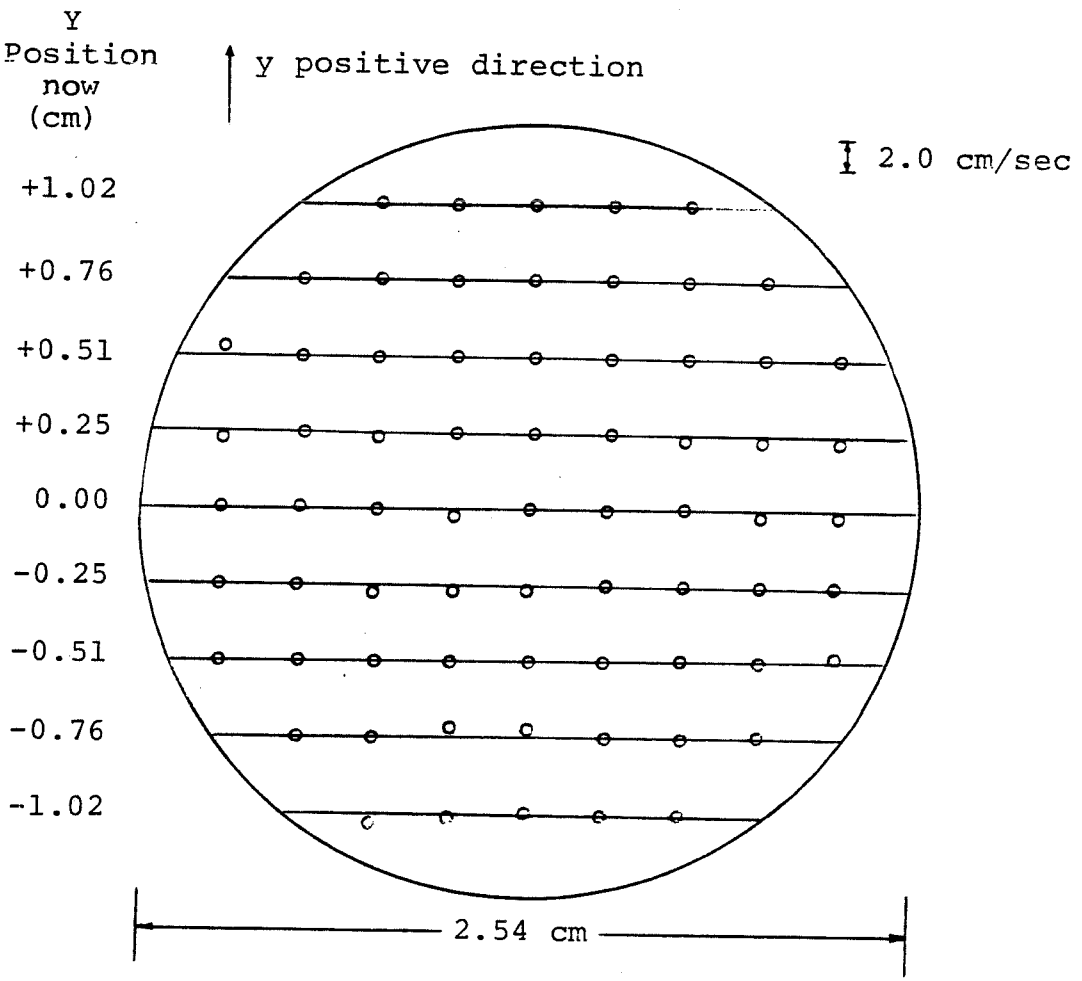

Figure 4.7

Y VELOCITY COMPONENT

R_e = 12,500

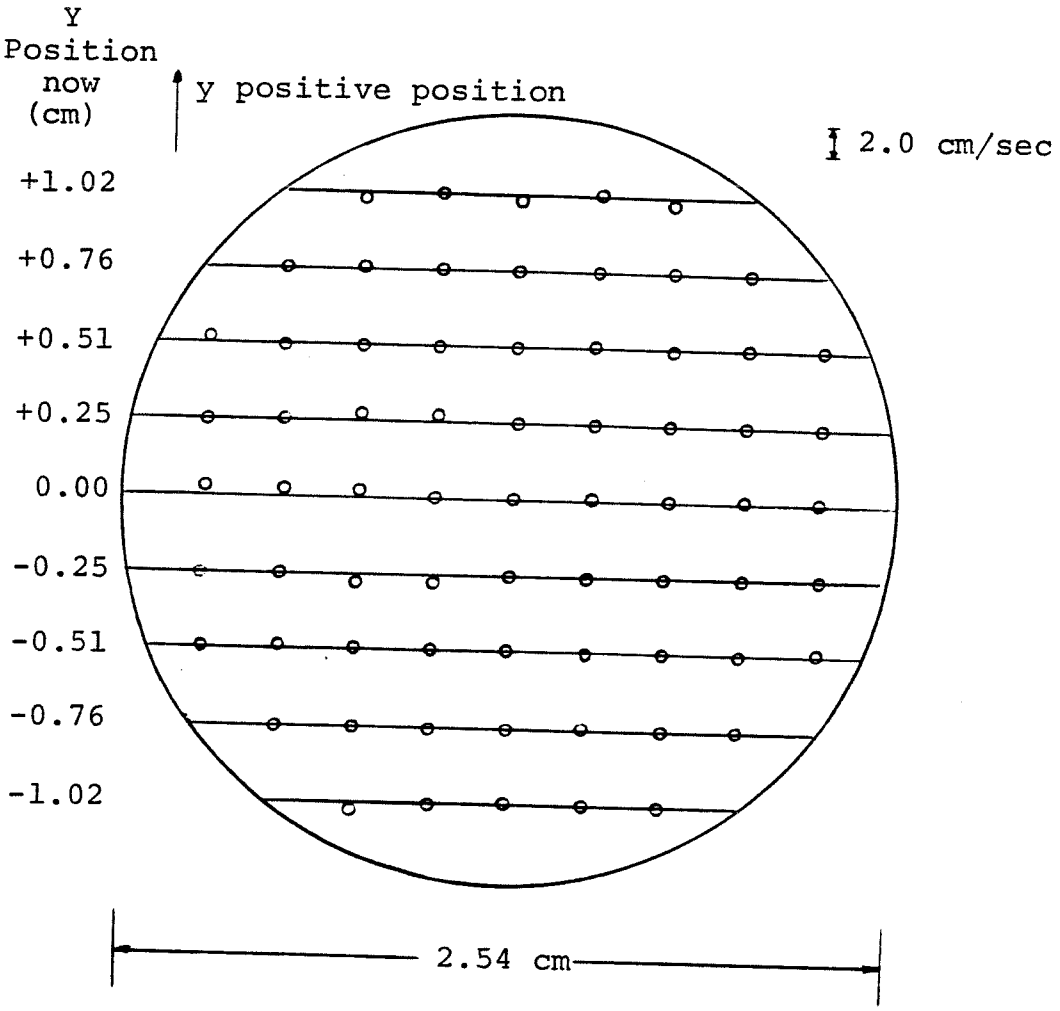

Figure 4.8

Y VELOCITY COMPONENT

R_e = 16,700

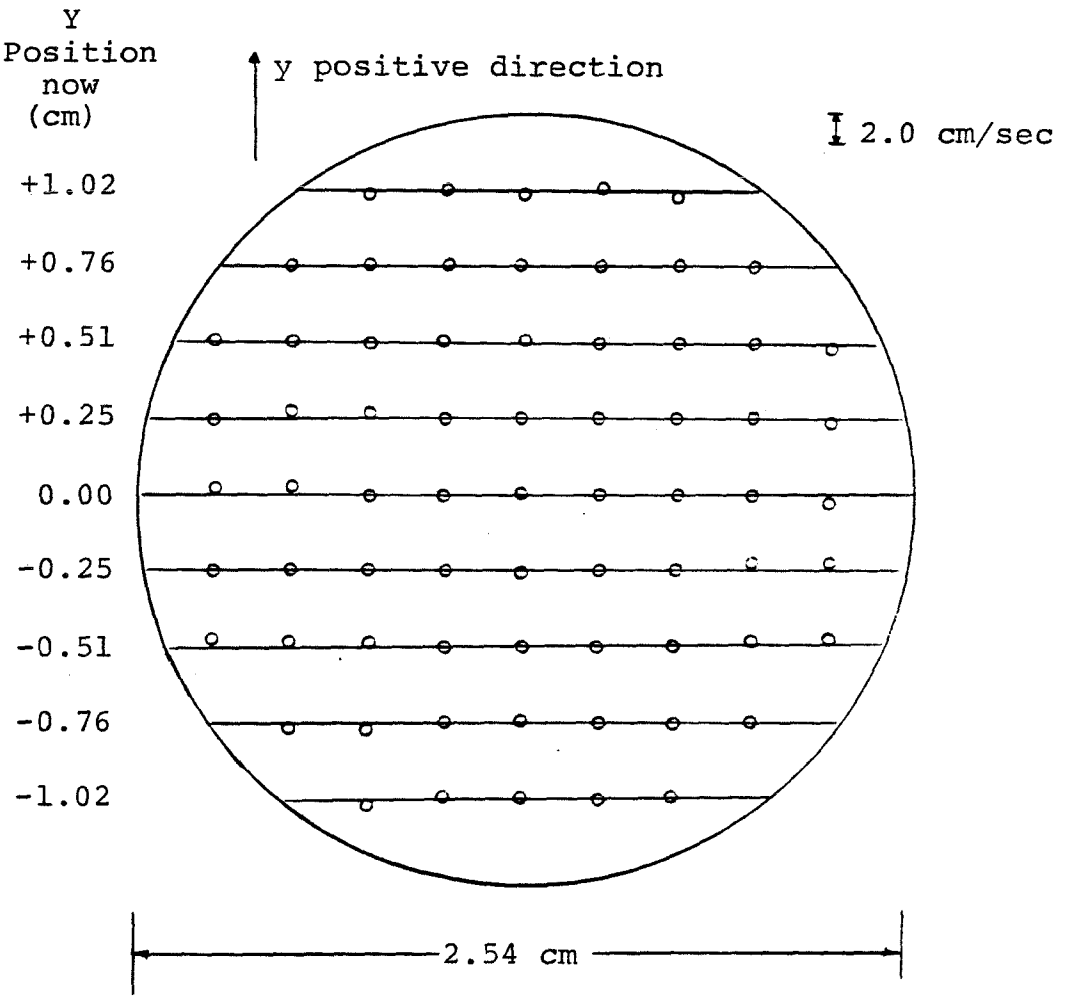

Figure 4.9

Y VELOCITY COMPONENT

R_e = 20,900

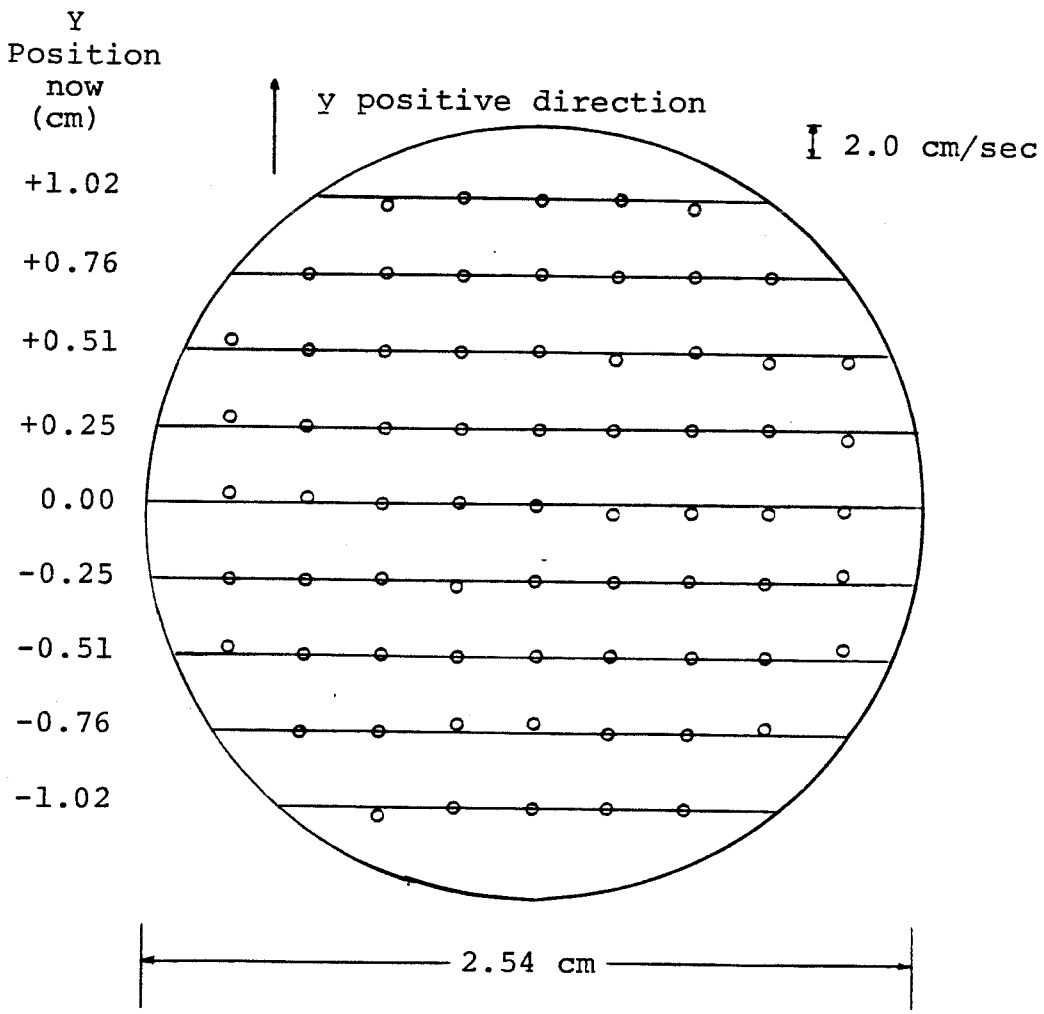

Figure 4.10

measurements the x coordinates were referenced to the inside wall on the horizontal centerline, Figure 4.6. The y coordinates were referenced to the horizontal centerline. In Tables 4.2 through 4.5 certain x coordinate positions are labeled "wall". These wall points were obtained by placing part of the measuring volume inside the wall of the flow channel, and part of the measuring volume in the flowing liquid. Under these conditions many stationary particles on the walls were measured giving zero velocity.

Measurements of the velocity components in the y (vertical) direction were also made at the same positions on the cross-section as the axial-velocity components. The y-velocity components were measured to determine if there was any secondary flow in the channel. Figures 4.7 through 4.10 show the measured y velocities. The data points plotted in these four figures are velocities relative to the closest line of constant vertical position. Data points located on these lines have no measurable velocity in the y direction. Data points above the line have a positive velocity. For all four flow-rates the maximum measured y velocity was ± 0.5 cm/sec. This value of velocity corresponded to a frequency tracker voltage of ± 0.005V around the center voltage. This voltage is the limit of sensitivity of the frequency tracker. Examination of Figures 4.7 through 4.10 shows no systematic trend in the positive or

negative velocities as was shown in Figure 3.2

It was found during the experiments that a voltage from a stationary wall signal could be changed by as much as ±0.001V depending on the alignment of the photomultiplier pinhole with the image of the measuring volume. It was also found on certain occasions that the laser beams entering the flow channel had to be adjusted slightly to get the beams to cross. The probable reason for these occasional adjustments was that small irregularities in the Plexiglas sould skew the beams.

Because the non-zero velocities in the y direction were at the limit of the frequency tracker and there was no visible trend of these velocities, it was thought that the mean velocitiy in the y direction was zero. The deviations in the velocity from zero were thought to be due to slight pinhole misalignment or to a small skewness in the laser beams causing only a partial crossing in the channel.

4.4 Pressure-Drop Measurements

Pressure-drop measurements were made in the same region as the velocity measurements. They were made so that the wall shear stress, $\tau_o = (\Delta pr_o)/(2L)$, and the friction velocity, $v^* = (\tau_o/\rho)^{\frac{1}{2}}$, could be calculated. Figure 4.11 shows the pressure-drop data for the four flow-rates used. Linear regression of the data points through the origin gives the solid lines shown in Figure 4.11. The slopes and

PRESSURE DROP DOWN THE FLOW CHANNEL

Initial Pressure Tap Located 76.2 cm
Downstream From the Flow Conditioner

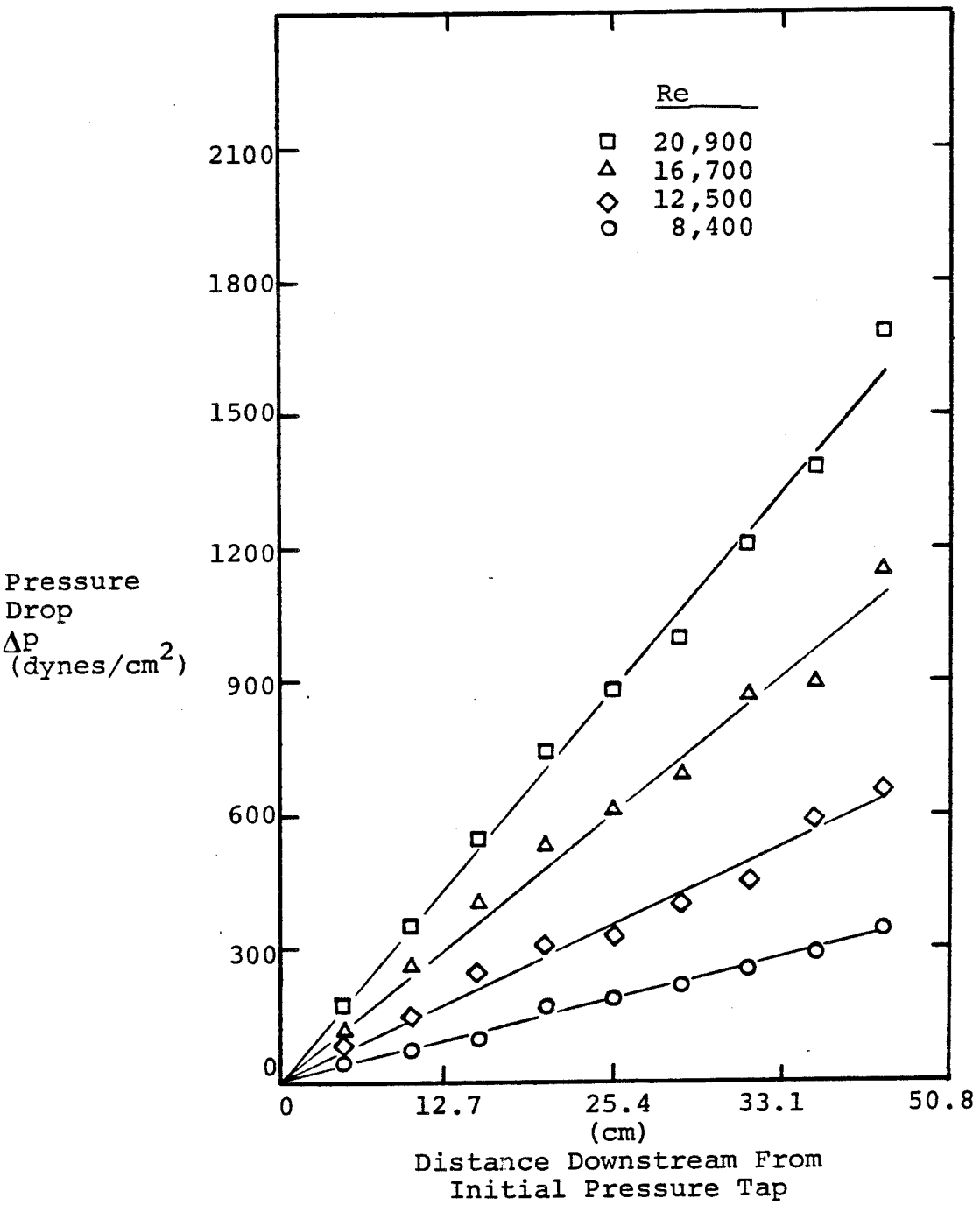

Figure 4.11

correlation coefficients are listed in Table 4.6.

Calculation of r_o and v* from the pressure-drop data compare to within 3% with the values of r_o and v* calculated using the Blasius friction factor correlation for turbulent flow in smooth pipes. This close agreement identifies the four flows used in the experiments as being fully developed turbulent flows.

4.5 Velocity Profiles

Figure 4.12 shows the profile of the axial velocities across the flow channel. The two error bars drawn in the figure indicate the uncertainty of the measured velocities in the region $0.8 \leq r/r_o \leq 1.0$. The uncertainty in measured velocity over the inner region, $0.0 \leq r/r_o \leq 0.08$, is on the order of 1cm/sec or smaller. The error bars were determined as the difference between the maximum and minimum velocities measured at grid points having the same radial positions in the channel. The data points that are plotted in Figure 4.12 are the average values of the axial velocities that were measured over the entire cross-section of the channel. The four velocity profiles were integrated using Simpson's rule, and the volumetric flow-rates were then calculated. Comparison of the volumetric flow-rates calculated from the velocity profiles with the volumetric flow-rates measured using the flowmeter in the system show the accuracy of the velocity measurements

CALCULATED SLOPES FOR THE PRESSURE DROP CURVES THAT WERE OBTAINED BY USE OF A LINEAR REGRESSION ANALYSIS

R_e $(DV_{avg}\rho)/\mu$	Slope (dynes/cm^2)/cm	Correlation Coefficient
8,400	7.3	0.99
12,500	14.1	0.98
16,700	24.1	0.99
20,900	35.0	0.99

Table 4.6

COMPARISON BETWEEN VALUES OF THE WALL SHEAR STRESS, τ_o, AND FRICTION VELOCITY, v^*, THAT WERE CALCULATED FROM THE DATA AND FROM THE BLASIUS EQUATION

	Data		Calculated	
R_e	τ_o	v^*	τ_o	v^*
$(DV_{avg}\rho)/\mu$	dynes/cm^2	cm/sec	dynes/cm^2	cm/sec
8,400	4.6	2.2	4.5	2.1
12,500	9.2	3.0	9.1	3.0
16,700	15.6	4.0	15.1	3.9
20,900	22.2	4.7	22.0	4.7

Table 4.7

AXIAL VELOCITY DISTRIBUTIONS 35 DIAMETERS DOWNSTREAM FROM THE FLOW CONDITIONER

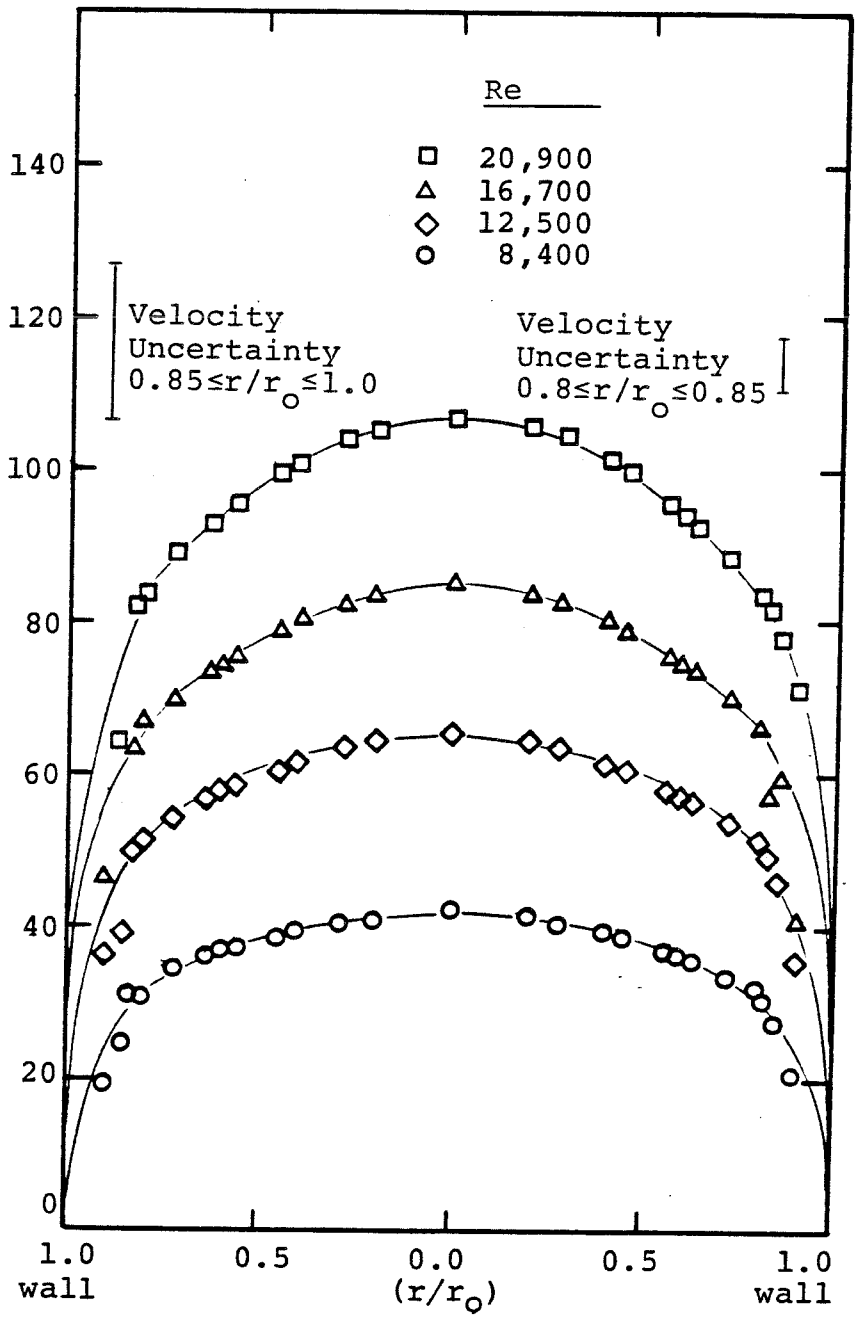

Figure 4.12

The agreement between the measured and calculated volumetric flow-rates in Table 4.8 is within 2%. This close agreement demonstrates that the velocity data are quite accurate.

4.6 Logarithmic Velocity Profile

The mean velocities in the axial direction for all four flows were put in non-dimensional form by using Equation 2.1 and 2.2 given in Chapter 2. A plot of u^+ versus $\ln y^+$ is presented in Figure 4.13. The data in the range from $y^+ = 50$ to $y^+ = 550$ for the four flow-rates can best be fitted by using

$$u^+ = 4.0 + 2.9 \ln y^+ . \qquad (4.1)$$

Also plotted in Figure 4.13 is the curve fit of Deissler (4-2),

$$u^+ = 3.8 + 2.8 \ln y^+ . \qquad (4.2)$$

Deissler's fit lies parallel and slightly below the data.

Figure 4.13 shows a deviation from Equation 4.1 beginning in the region from $y^+ = 40$ to $y^+ = 50$. The dashed line from $y^+ = 10$ to $y^+ = 50$ is meant to show the trend in the data and is not a fit to the data points in this region. There is a scarcity of data in the region from $y^+ = 10$ to 50 due to the fact that in the region from $y^+ = 10$ to 30 a portion of the measuring volume of the laser must be in the Plexiglas wall. Data points plotted in this re-

COMPARISON BETWEEN EXPERIMENTALLY MEASURED FLOW-RATES AND FLOW-RATES CALCULATED BY INTEGRATION OF THE MEAN-AXIAL-VELOCITY CURVES

Measured Flow-rate cm^3/sec	Calculated Flow-rate cm^3/sec
167	164
250	248
332	328
417	420

Table 4.8

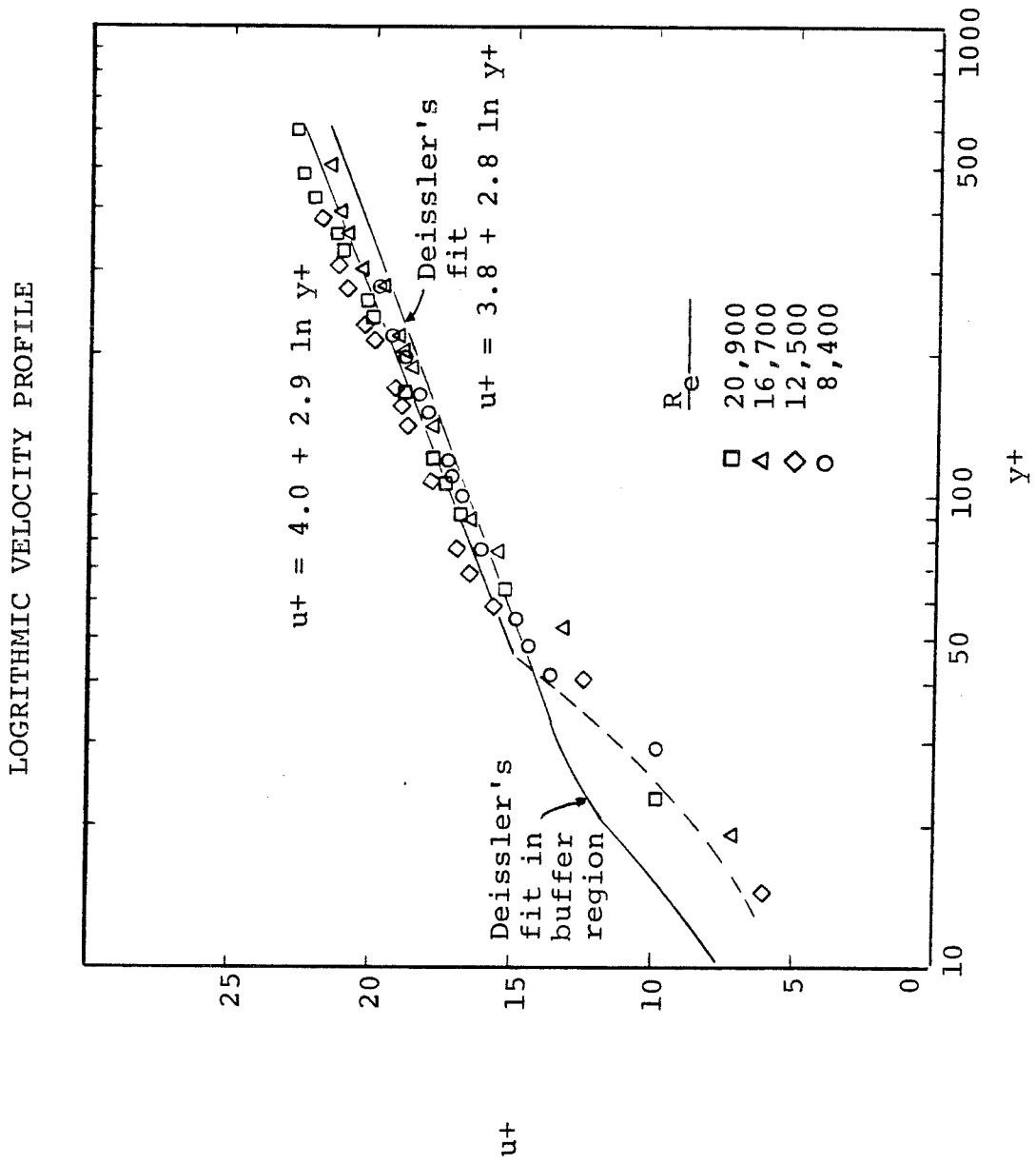
LOGRITHMIC VELOCITY PROFILE
u+ = 4.0 + 2.9 ln y+
Deissler's fit
u+ = 3.8 + 2.8 ln y+
Deissler's fit in buffer region
Re
20,900
16,700
12,500
8,400
u+
y+
0
5
10
15
20
25
10
50
100
500
1000

Figure 4.13

gion were velocity values obtained when the measuring volume was at the wall. The y^+ positions were obtained by assuming one half of the measuirng volume extended into the fluid. The data plotted in Figure 4.13 indicates that the buffer region between the viscous sublayer and the turbulent region extends to a distance of $y^+ = 50$. Deissler's fit for the buffer region, shown in Figure 4.13, matches his turbulent region profile at $y^+ = 26$. The extent of the buffer region is not a definite quantity. Many investigators have studied the transition from viscous flow, at the wall, to turbulent flow, away from the wall, and have determined different values of y^+ for the extent of the buffer region. Nedderman (4-8) determined that the buffer region extending to $y^+ = 30$, while Popovich and Hummel (4-9) found the buffer region extending to $y^+ \simeq 35$. Hettler, et al. (4-3) measured the buffer region extending to $y^+ \simeq 70$, and van Driest (4-14) found a value of $y^+ \simeq 60$ to be the extent of the buffer region.

4.7 Reynolds-Stress Calculation

Evaluation of $d\bar{U}_z/dr$ was obtained by first plotting the axial velocity data against the non-dimensional radial parameter $(r/r_o)^2$. By plotting the data in this manner the derivatives of the curves, $d\bar{U}_z/d[(r/r_o)^2]$, were non-zero at the centerline. Figure 4.14 shows the four profiles. Because the slopes of the curves were non-zero at the center-

AXIAL VELOCITIES 35 DIAMETERS DOWNSTREAM FROM THE FLOW CONDITIONER AS A FUNCTION OF THE SQUARE OF THE RELATIVE RADIAL POSITION

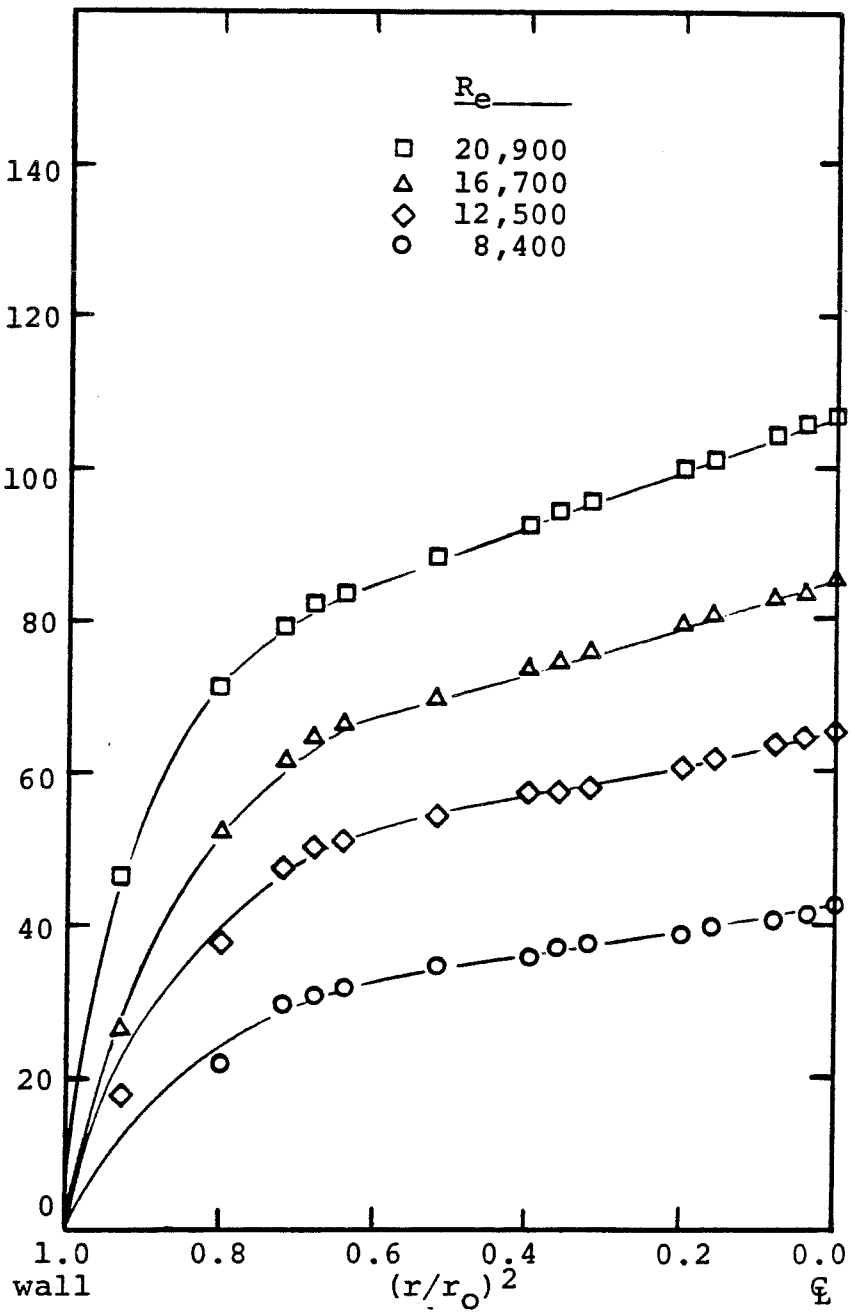

Figure 4.14

line, the derivatives of velocity with respect to $(r/r_o)^2$ were easier to evaluate across the channel than they would have been if the velocities were plotted relative to (r/r_o).

Values of $d\bar{U}_z/d[(r/r_o)^2]$ were obtained in two ways. First, the curves were fit to polynomials by use of a least squares routine. When a good curve fit had been obtained, the polynomial was differentiated to obtain $d\bar{U}_z/d[(r/r_o)^2]$. The second method of obtaining the derivatives was by using graphical differentiation methods on smooth curves through the data points.

Once the velocity data had been fitted to the polynomials, the velocity expression was integrated across the channel, and the volumetric flow-rates were calculated. These calculated flow-rates were then compared with the experimentally measured flow-rates as a check on the polynomial fits. All of the calculated flow-rates agreed with the measured flow-rates to within 3%. The derivatives of the velocity with respect to $(r/r_o)^2$ were converted to $d\bar{U}_z/dr$ by means of the following relation.

$$\frac{d\bar{U}_z}{dr} = \frac{2r}{r_o^2} \left[\frac{d\bar{U}_z}{d[(r/r_o)^2]}\right] \tag{4.3}$$

The graphical differentiation of the smooth curves drawn through the data points was undertaken as a further check on the polynomial fits. The values of $d\bar{U}_z/d[(r/r_o)^2]$ obtained by using graphical methods agreed to within 7% of

the derivatives generated by the polynomial. This agreement indicates that there is no problem with ripples in the fitting of the curves giving erroneous values of the velocity derivative.

The values of $d\bar{U}_z/dr$ used in the rest of this chapter will be those obtained from the polynomial fits.

The values of $\overline{v_r'v_z'}$ for the four flow-rates were obtained by use of the Equation 2.9. In Figure 4.15 the values of $\overline{v_r'\ v_z'}$, calculated at the relative radial positions where the velocities were measured, are non-dimensionalized with respect to the friction velocities and are plotted across one half of the channel. Two distrinct regions can be seen in Figure 4.15. In the inner region, $0 \leq r/r_o \leq 0.72$, the values of $\overline{v_r'\ v_z'}\ /v^{*2}$ collapse to a single value at any relative radial position. The values of $\overline{v_r'\ v_z'}/v^{*2}$ also proceed linearly to zero as the channel centerline is approached. A zero value of $\overline{v_r'\ v_z'}$ at the channel center does not mean that there are no velocity fluctuations on the centerline; instead it means that there is no correlation between the r and z velocity fluctuations at the channel center.

In the second region, $1.0 \geq r/r_o \geq 0.72$, the single valued behavior of $\overline{v_r'\ v_z'}/v^{*2}$ observed in the inner region is not seen. Two trends are seen in the curves in this second region. First, the maximum value of $\overline{v_r'\ v_z'}/v^{*2}$ increases as flow-rate increases. Second, the relative radial posi-

MEAN PRODUCT OF THE RADIAL
AND AXIAL VELOCITY FLUCTUATIONS

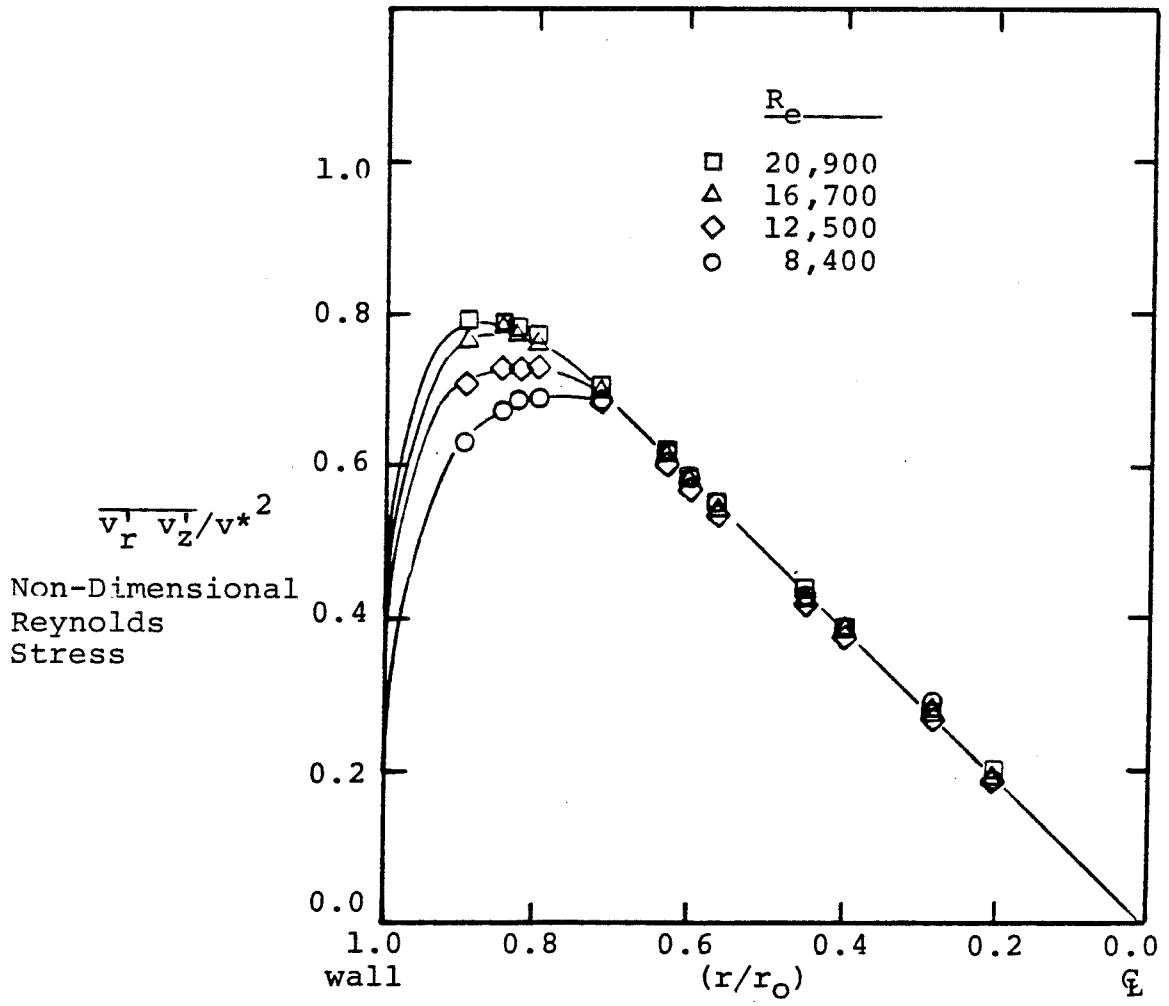

Figure 4.15

tion at which the maximum value is achieved increases as the flow-rate increases. Table 4.9 shows the range in which the maximum value of $\overline{v_r' v_z'}/v^{*2}$ occurs for each flow.

4.8 Eddy Viscosity

After calculating $\overline{v_r' v_z'}$ and $d\bar{U}_z/dr$, it was possible to calculate the kinematic eddy viscosity by using Equation 2.10. Figure 4.16 is a plot of these calculated eddy viscosities. The curves through the data in Figure 4.16 are smooth curves that pass through the plotted points and are not curve fits or calculated eddy-viscosity curves. The points, except for the three closest to the centerline, are plotted at the position in the channel that the velocities were measured. For each flow-rate the innermost three points were plotted to show the trend of the eddy viscosity as the center of the channel was approached. The kinematic eddy viscosity stays at a non-zero finite value at the centerline since both $\overline{v_r' v_z'}$ and $d\bar{U}_z/dr$ go to zero at the center of the channel. The centerline values of ν_e for the flows with Reynolds numbers of 8,400, 12,500, 16,700, and 20,900 respectively are: 0.08, 0.16, 0.28, and 0.33 cm^2/sec. In all four curves the maximum value of ν_e is found at $r/r_o \simeq 0.63$. The behavior of the eddy-viscosity curves shown in Figure 4.16 is similar to that found by Quarmby and Anad (4.10). In their work they used Reynolds numbers ranging from 18,500 to 155,000. Figure 4.17 shows the curve Quarmby

RELATIVE RADIAL POSITION FOR THE MAXIMUM VALUE OF THE NON-DIMENSIONALIZED REYNOLDS STRESS, $(\overline{v_r' v_z'}/v^{*2})_{max}$

R_e $(DV_{avg}\rho)/\mu$	$(\overline{v_r' v_z'}/v^{*2})_{max}$	(r/r_o)
8,400	0.69	0.72 - 0.83
12,500	0.73	0.80 - 0.85
16,700	0.78	0.85 - 0.89
20,900	0.79	0.89

Table 4.9

KINEMATIC EDDY VISCOSITIES ACROSS THE FLOW CHANNEL

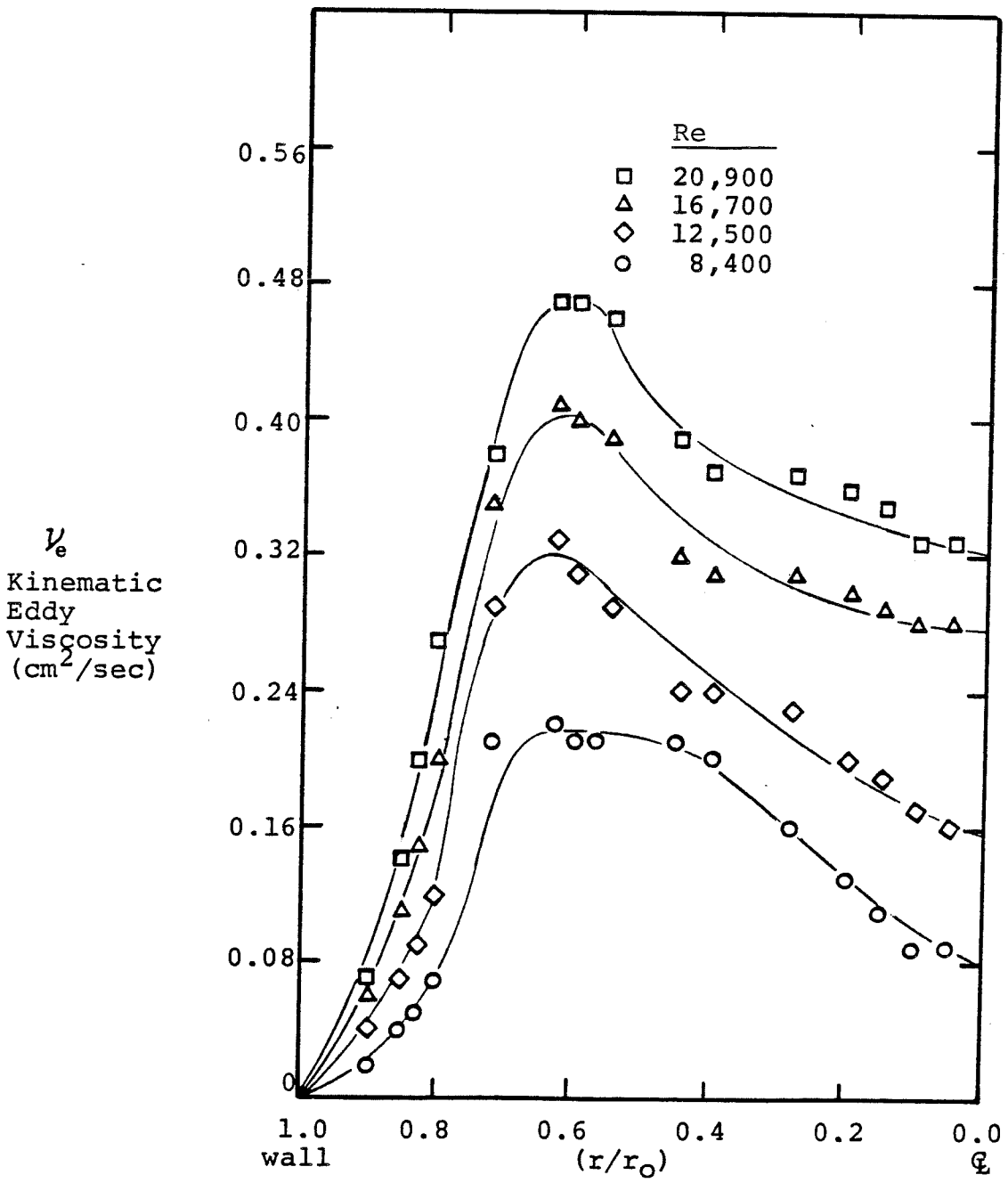

Figure 4.16

KINEMATIC EDDY VISCOSITIES
Comparison Between Present Work
and Experiments of Quarmby and Anad

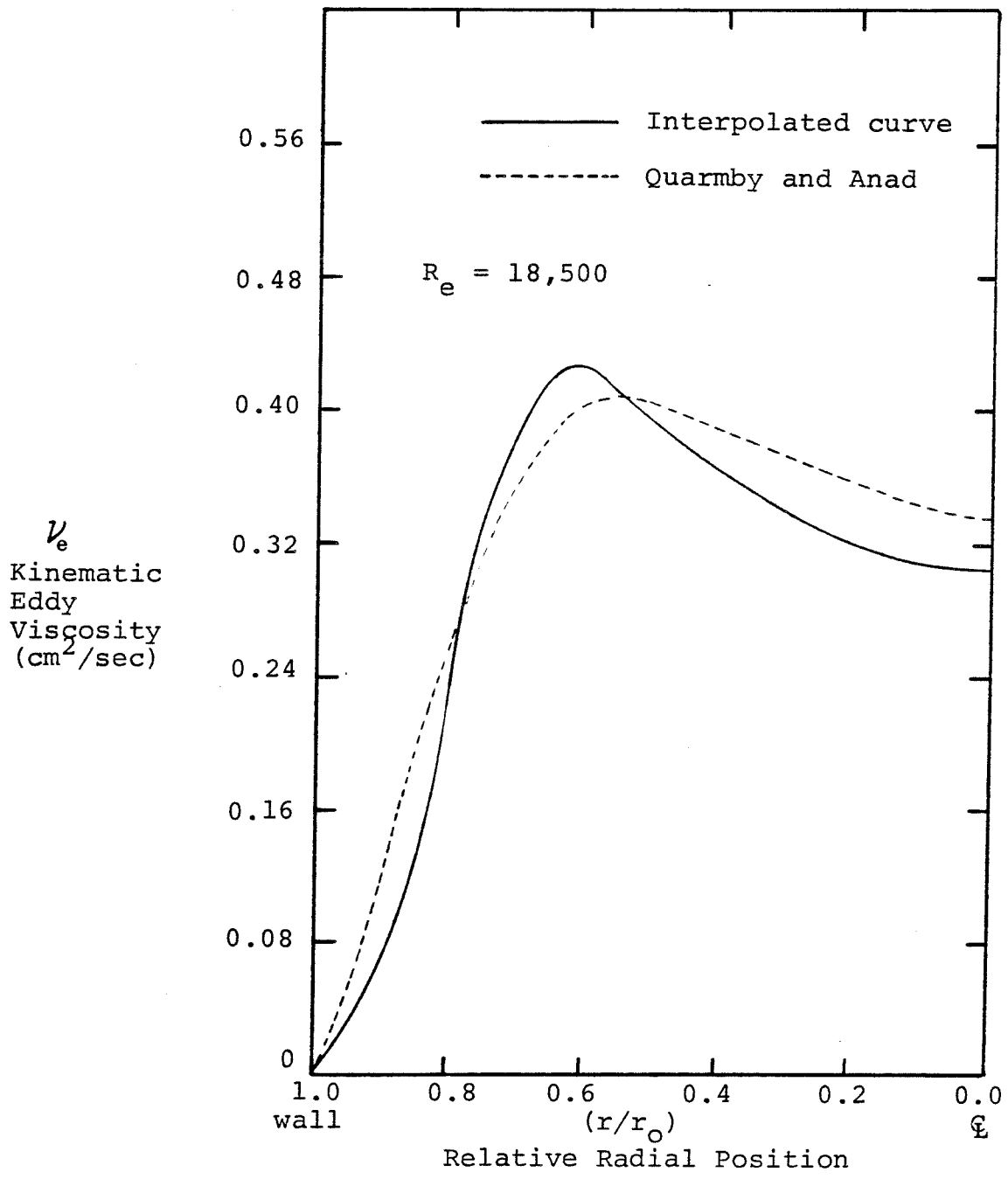

Figure 4.17

and Anad determined at R_e = 18,500 (dashed line) as well as a curve obtained by interpolating between the R_e = 16,700 and 20,900 curves from Figure 4.16 (solid line). Figure 4.17 shows the maximum value of ν_e obtained by Quarmby and Anad to be slightly less than that obtained by interpolation (0.41 vs. 0.43 cm^2/sec), and the relative radial position of the maximum value of ν_e is closer to the channel center for Quarmby and Anad's curve than for the interpolated curve (0.55 vs. 0.63 cm^2/sec). The other difference is the value of ν_e at the center of the channel (0.34 cm^2/sec for Quarmby and Anad vs. 0.31 cm^2/sec for interpolation) and the greater rate of increase from r/r_o = 1.0 for Quarmby and Anad as compared with the interpolated result.

4.9 RMS-Velocity Measurements

Measurements of the rms-velocity fluctuations were made at every point in the channel that the mean-velocity measurements were made. Figures 4.18 through 4.21 show the rms velocities measured at each flow-rate nondimensionalized with respect to the friction velocity. The experimental measurements were made using an rms voltmeter, and in all cases the indicator needle on the rms voltmeter fluctuated. The experimental data recorded was the high and low points between which the needle fluctuated. The points plotted in the four figures are the mean values of the needle fluctu-

DISTRIBUTION OF R, θ AND Z RMS VELOCITIES ACROSS THE CHANNEL

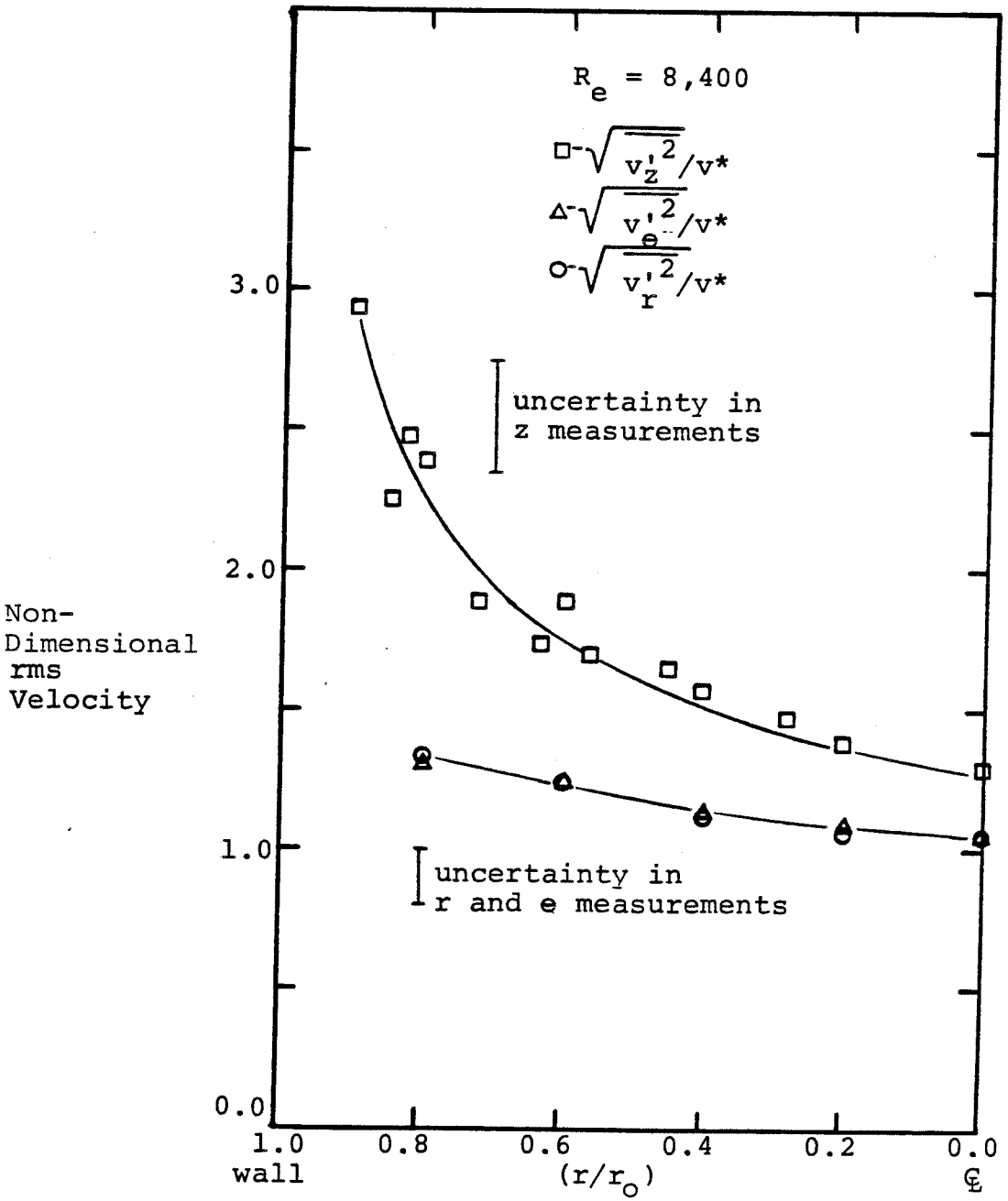

Figure 4.18

DISTRIBUTION OF R, Θ, AND Z RMS VELOCITIES ACROSS THE CHANNEL

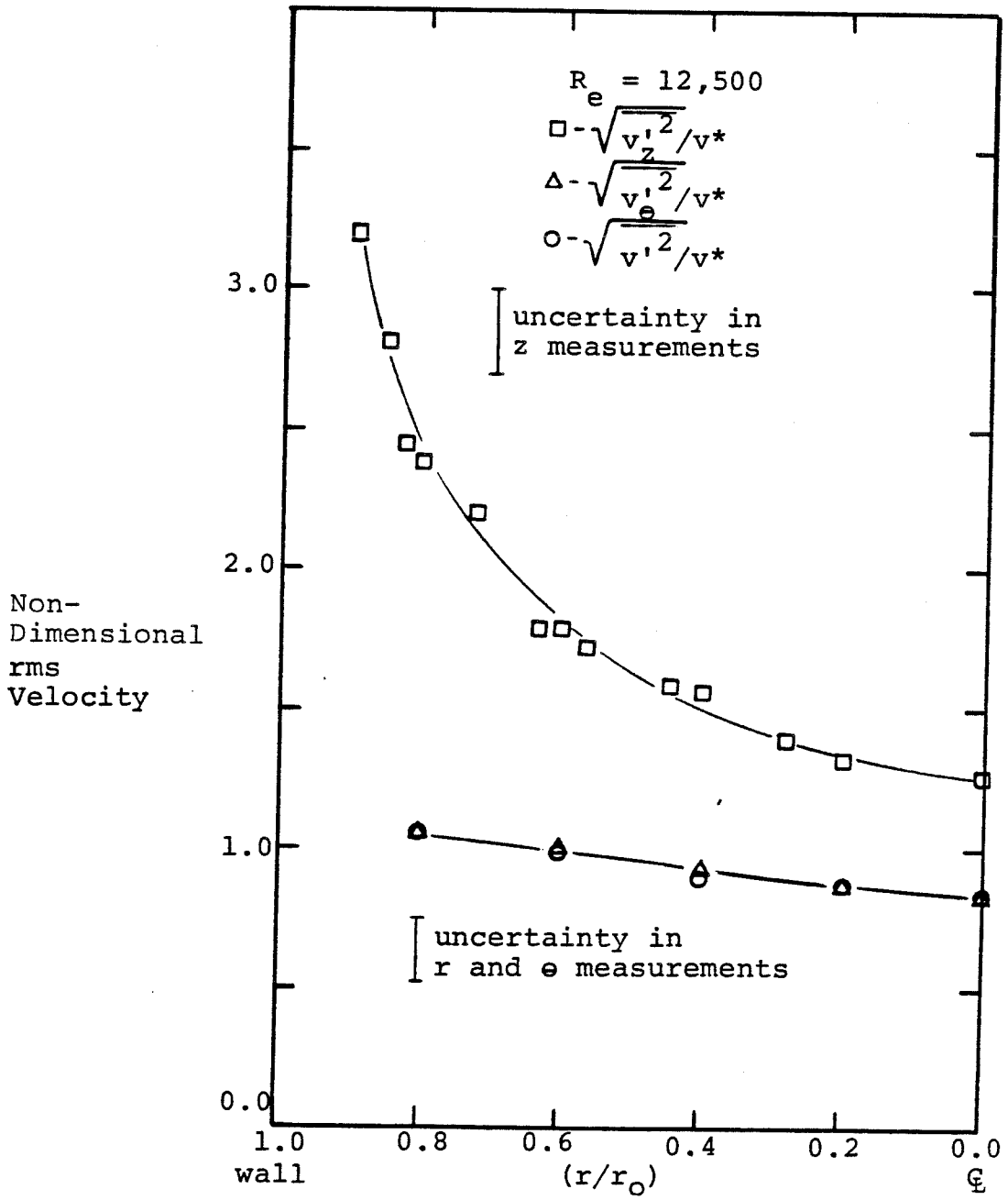

Figure 4.19

DISTRIBUTION OF R, θ AND Z RMS VELOCITIES ACROSS THE CHANNEL

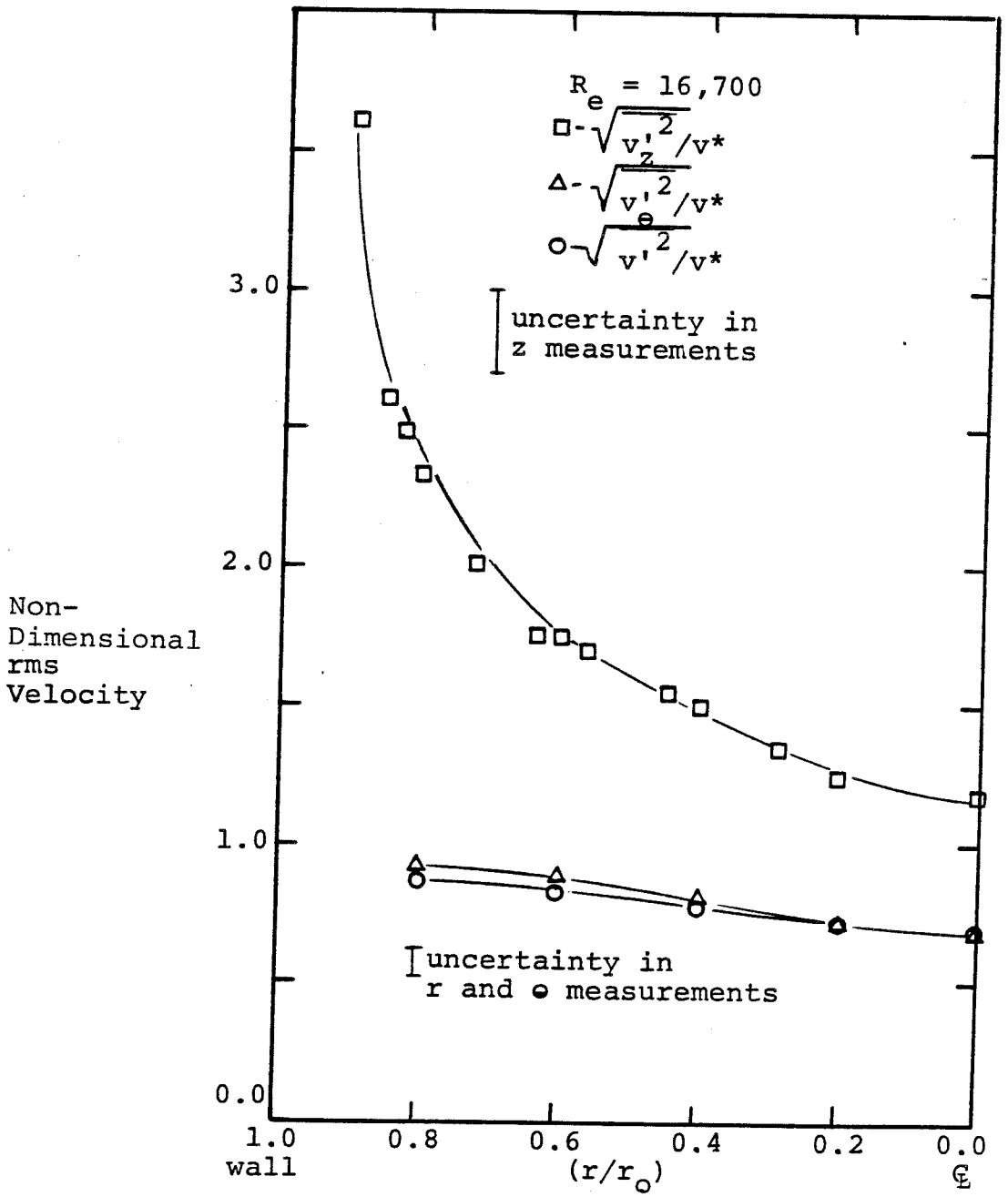

Figure 4.20

DISTRIBUTION OF R, θ, AND Z RMS VELOCITIES ACROSS THE CHANNEL

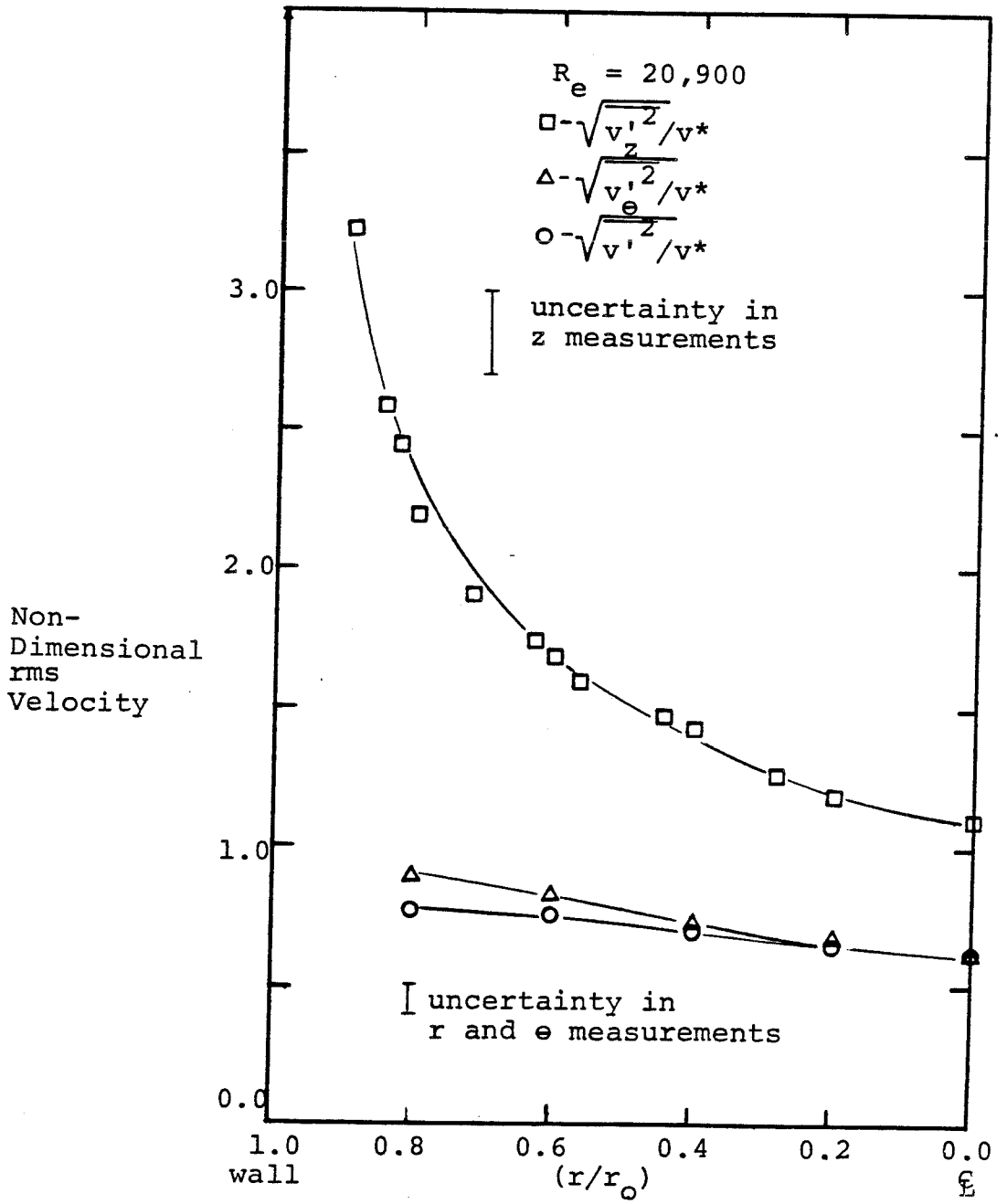

Figure 4.21

actions. The uncertainty bars shown in each figure are the mean values of all the needle fluctuations for measurements made in each coordinate direction. The absolute uncertainty in the rms measurements was the smallest for the flow at R_e = 8,400 and was the largest for R_e = 20,900. The bars plotted on Figures 4.18 through 4.21 were non-dimensionalized with respect to the friction velocity for each flow-rate.

The axial-rms velocity fluctuations, $(\overline{v_z'^2})^{\frac{1}{2}}$, were evaluated at all 69 interior points at which the mean-velocity data were measured. The radial and azimuthal-rms-velocity fluctuations, $(\overline{v_r'^2})^{\frac{1}{2}}$ and $(\overline{v_\theta'^2})^{\frac{1}{2}}$, were evaluated along the vertical and horizontal centerlines respectively. The reason for only using points on these two centerlines was that the laser optics rotated in a Cartesian reference frame so that the two coordinate directions that could be measured were the z and y directions. The y velocities corresponded directly to r and θ velocities only on the vertical and horizontal centerlines. All of the rms velocities for the y coordinate were measured, but those not on either centerline contained components from both the r and θ directions.

The shape of the $(\overline{v_z'^2})^{\frac{1}{2}}$ curves for all four flow-rates is the same. The minimum value is at the centerline, and the rms velocities increase as (r/r_o) increases. The maximum distance from the centerline at which no portion

of the measuring volume was in the Plexiglas was r/r_o = 0.89. In all four flow-rates the maximum value of $(\overline{v_z'^2})^{\frac{1}{2}}$ occurred at r/r_o = 0.89. This upward trend in $(\overline{v_z'^2})^{\frac{1}{2}}$ is the same as Laufer (4-5) found in his experiments. For his lowest flow-rate, R_e = 50,000, $(\overline{v_z'^2})^{\frac{1}{2}}$ increased steadily from the center of the channel until a maximum was reached at y^+ = 15. Between y^+ = 0 and 15 the wall damped the axial-rms-velocity fluctuations. For the flow-rates used here, R_e = 8,400, 12,500, 16,700, and 20,900, the non-dimensional distance from the wall, y^+, at r/r_o = 0.89 was 29, 41, 53, and 63 respectively. In order to make measurements closer to the wall it was necessary to place a portion of the measuring volume inside the Plexiglas wall and leave the rest of the measuring volume in the liquid. Experiments with the measuring volume partially in the wall were attempted at each horizontal crossing. During these measurements it was necessary to use a bandstop filter so that any signal scattered by a stationary particle on the wall was eliminated. Because no filter has an absolutely sharp cutoff at the desired frequency, some of the signal generated by slower-moving, scattering particles in the liquid would also be filtered out. With some of the actual signal filtered out, the rms velocity measured would be greater than the actual rms velocity. In addition to the problem of higher rms velocities arising from filtering,

the exact amount of the measuring volume in the liquid was not known, so it was assumed that one half of the measuring volume was in the wall and one half in the liquid. Using this assumption and averaging the rms velocities measured at the wall, the values listed in Table 4.10 were obtained. In Table 4.10 only the flow at R_e = 8,400 has a y^+ value less than 15. The values of $(\overline{v_r'^2})^{\frac{1}{2}}/v^*$ and $(\overline{v_\theta'^2})^{\frac{1}{2}}/v^*$ are also shown in Figures 4.18 through 4.21. It was not possible to determine the trend in $(\overline{v_r'^2})^{\frac{1}{2}}$ and $(\overline{v_\theta'^2})^{\frac{1}{2}}$ near the walls as it was to measure the trend for the rms velocity in the z direction. In order to measure $(\overline{v_r'^2})^{\frac{1}{2}}$ close to the wall it would have been necessary to place the measuring volume very close to the top and bottom of the flow channel. In these regions the curvature of the channel affected the laser beams considerably, and no signal could be detected. Measurement of $(\overline{v_\theta'^2})^{\frac{1}{2}}$ near the wall was not possible because the filtering necessary to eliminate the wall signal also filtered out these less intense fluctuations. Although the rms velocities in the r and θ directions could not be measured closer to the wall than r/r_o = 0.8, two separate trends can be seen in Figures 4.18 through 4.21. In Figures 4.18 and 4.19 the values of $(\overline{v_r'^2})^{\frac{1}{2}}/v^*$ and $(\overline{v_\theta'^2})^{\frac{1}{2}}/v^*$ are the same across the channel. In Figures 4.20 and 4.21, $(\overline{v_\theta'^2})^{\frac{1}{2}}/v^*$ increases at a greater rate than $(\overline{v_r'^2})^{\frac{1}{2}}/v^*$ as r/r_o increases. The depression of the radial-rms-veloc-

EXPERIMENTALLY MEASURED VALUES OF THE AXIAL-RMS-VELOCITIES, NON-DIMENSIONALIZED WITH RESPECT TO THE FRICTION VELOCITY, NEAR THE PIPE WALL

R_e	y^+	
$(DV_{avg}\rho)/\mu$	$(y/\nu)(\tau_o/\rho)^{1/2}$	$\sqrt{(v_z'^2)}/v^*$
8,400	10	2.8
12,500	15	3.5
16,700	19	4.6
20,900	23	4.3

Table 4.10

ities below the azimuthal-rms-velocities in the flows at R_e = 16,700 and 20,900 indicate that the tube wall was damping the radial fluctuations. For R_e = 8,400 and 12,500 the damping was not obvious in the region where the measurements were made. Laufer measured rms velocities in the r and θ directions, and found the r component depressed relative to the θ component across the entire channel. In his experiments, the r component reached a maximum value at r/r_o = 0.9 while the θ component reached a maximum value at $y^+ \simeq 50$.

Because of the needle fluctuations of the rms voltmeter it is not possible to say whether the axial-rms-velocity becomes equal to the rms velocities in the r and θ directions at the center of the channel for R_e = 8,400. For R_e = 12,500, 16,700, and 20,900, the uncertainty bars for the axial-rms-velocities and for the radial and azimuthal-rms-velocities not overlap at the channel center, showing the turbulence not to be isotropic. Because of the uncertainties in measurements it is not possible to determine any dependence of the rms velocities for the r, θ, and z directions on Reynolds number.

Comparison of the axial-rms-velocity at the center of the channel can be made with several investigators. Komasawa (4-4) measured $(\overline{v_z'^2})^{\frac{1}{2}}$ at the center of turbulent pipe flow by photographing 90-micron particles suspended in the

water. Martin and Johanson (4-7) measured $(\overline{v_z'^2})^{\frac{1}{2}}$ at the center of a pipe by means of a hot film probe; the flowing fluid was water. Sandborn (4-12) measured $(\overline{v_z'^2})^{\frac{1}{2}}$ for air flowing turbulently in a pipe. Figure 4.22 shows the three curves as well as the data from the present study. It is seen that the two non-invasive measurements, LDA and photographic, are greater in magnitude than the measurements made with either hot-film or hot-wire probes. The difference in the values of $(\overline{v_z'^2})^{\frac{1}{2}}/U_{\text{℄}}$ for the two types of measurements indicates that the presence of a probe in the flow tends to damp the velocity fluctuations.

4.10 Summary for Chapter 4

A summary for each section of Chapter 4 is written below.

4.2: Velocity measurements were made at 35 diameters downstream from the flow conditioner. At this position along the flow channel the velocity profiles had become fully developed. The condition of developed flow was checked by measuring the velocity profiles for the flows with R_e = 8,400 and 20,900 at 35, 65 and 105 diameters downstream from the flow conditioner. The velocity profiles for both flow-rates were the same at all three positions downstream from the flow conditioner.

4.3: Mean velocities in the z and y coordinate directions were made at the distance of 35 diameters

COMPARISON OF AXIAL-RMS-VELOCITIES NON-DIMENSIONALIZED WITH RESPECT TO THE MEAN CENTERLINE VELOCITY, $\bar{U}_{\mathcal{L}}$

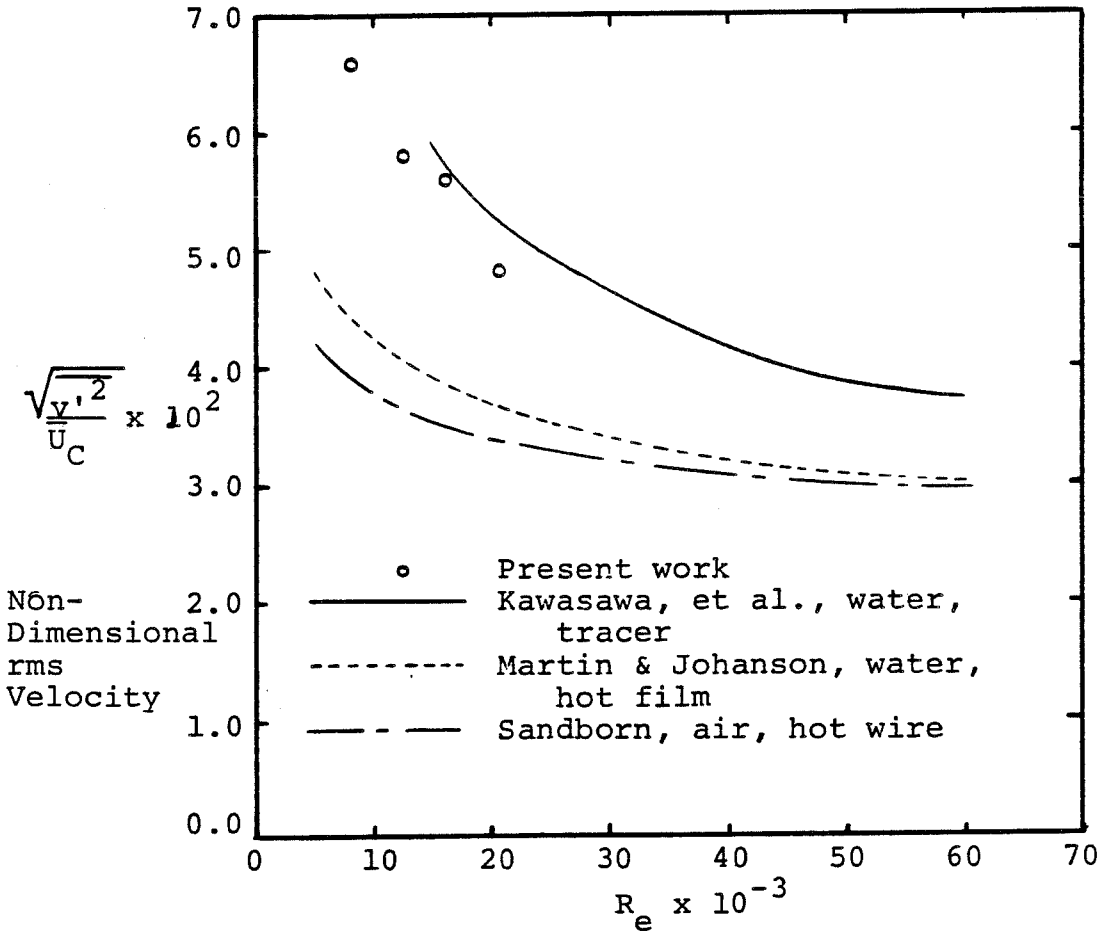

Figure 4.22

downstream from the flow conditioner. Contour plots of the axial velocities showed no irregularities in the circular contours of constant velocity. The mean velocity in the y direction was zero, which demonstrated the absence of secondary velocities.

4.4: Measurements of the pressure drop down the flow channel were made in order that τ_o and v* could be calculated. The values of τ_o and v* calculated by using the Blasius equation are also listed in Table 4.7. The excellent agreement between the values listed in Table 4.7 shows that the four flows used in the experiments are turbulent.

4.5: Determination of the accuracy of the velocity measurements made by the LDA was made by integrating the velocity profiles for the four flow-rates and calculating the volumetric flow for each. The calculated volumetric flow-rates agree very well with the measured values (Table 4.8). This agreement between calculated and measured flow-rates demonstrated the accuracy of the velocities measured by the LDA.

4.6: The mean-axial-velocity data were fitted using the general form of the logarithmic velocity profile. The data, in the range from $y^+ = 50$ to 550, were well fitted as

$$u^+ = 4.0 + 2.9 \ln y^+. \qquad (4.1)$$

In the range from $y^+ = 15$ to 50 the data fell below the curve represented by Equation 4.1. The data in this range showed the buffer region extending to $y^+ \simeq 50$.

4.7: The Reynolds stresses, $\overline{v_r' v_z'}$, were calculated by using $d\bar{U}_z/dr$ measured from the data and Equation 2.9. It was found for the four flows used in the experiment that the normalized Reynolds stress, $\overline{v_r' v_z'}/v^{*2}$, collapsed to a single line over the inner region of the flow channel, $0 \leq r/r_o \leq 0.72$. In the region from $r/r_o = 0.72$ to the wall, the maximum values of $\overline{v_r' v_z'}/v^{*2}$ increased as Reynolds numbers increased and the maximum values of $\overline{v_z' v_r'}/v_z^{*2}$ moved closer to the wall as Reynolds numbers increased (Table 4.9).

4.8: The kinematic eddy viscosities for the four flows were calculated by using Equation 2.10, experimentally determined values of $d\bar{U}_z/dr$, and the calculated values of $\overline{v_r' v_z'}$. The values of ν_e calculated for the four flow-rates all reached maximum values at a position in the channel of $r/r_o \simeq 0.63$. After reaching a maximum, ν_e then decreased to non-zero values at the channel center.

4.9: Measurements of the rms-velocities in the z and y directions were made over the entire cross-section of the channel at a position 35 diameters downstream from the flow conditioner. The y-coordinate measurements corresponded to r and e measurements on the vertical and horizontal centerlines, respectively. Figures 4.18 through 4.21 showed

the rms-velocities for the z components as always being larger than the rms-velocities of the r and θ components. The closest approach to equality occurred at the center of the channel where the rms-velocities for the r and θ directions were equal and the rms-velocities for the z direction was between 17 and 43% greater. At the highest two flow-rates (R_e = 16,700 and 20,900) the rms-velocities in the r direction did not increase to as large of a value at r/r_o = 0.8 as did the rms-velocities in the θ direction. The inhibition of the radial-rms-velocity arose from damping of the velocity fluctuations by the wall. Finally, Figure 4.22 showed that non-invasive methods of measuring rms-velocities produced larger values than those determined by invasive methods.

LITERATURE CITED

(4-1) Davies, J. T., "Turbulence Phenomena", New York, N.Y., Academic Press, Inc., 1972.

(4-2) Deissler, R. G., Natl. Advisory Comm. Aero., Tech. Note 2138 (1950).

(4-3) Hettler, J. P., Muntzer, P., Scrivener, O., Compt. Rend., 253, 4201 (1964).

(4-4) Komasawa, I., Kuboi, R., Otake, T., Chem. Eng. Sci., 29, 641 (1974).

(4-5) Laufer, J., Natl. Advisory Comm. Aero., Tech. Note 2123 (1950).

(4-6) Levich, V. G., "Physicochemical Hydrodynamics", Englewood Cliffs, N. J., Prentice-Hall, Inc., 1962.

(4-7) Martin, G. O., Johanson, L. N., AIChEJ, 9, 12 (1963).

(4-8) Nedderman, R. M., Chem. Eng. Sci., 16, 120 (1961).

(4-9) Popovich, A. T., Hummel, R. L., AIChEJ, 13, 854 (1967).

(4-10) Quarmby, A., Anad, R. K., JFM, 38 (1969).

(4-11) Rupe, J. H., JPL Tech. Rept., 32-207 (1962).

(4-12) Sandborn, V. A., Natl. Advisory Comm. Aero., Tech. Note 3266 (1955).

(4-13) Sleicher, C. A., Jr., Trans. ASME, 80, 693 (1958).

(4-14) van Driest, E. R., J. Aero. Sci., 23, 1007 (1956).

CHAPTER 5

PARTICLE VELOCITY AND DIFFUSION MEASUREMENTS

5.1 Particle Characterization

The PVC particles used in the experiments were obtained from Diamond Shamrock Corporation. They were non-spherical as is shown in Figure 5.1. The particles were screened to be nominally 100 microns, but the actual particle-size distribution was determined by taking pictures of the particles (using a photomicrograph) and then measuring the particle dimensions from the photographs. Due to the irregular shapes of the particles, the size of the particles was characterized in the following manner:

1) The longest axis of the particle was measured (ℓ_1)
2) The average width normal to the longest axis was measured (ℓ_2)
3) The characteristic particle size was calculated $\ell = (\ell_1 \ \ell_2)^{\frac{1}{2}}$

Particle sizes using this procedure were found for 245 particles. The mean and standard deviation for the particles were found to be 120 microns and 26 microns, respectively. A plot of the data and the calculated gaussian curve is shown in Figure 5.2.

The density and settling velocity of the particles were also measured. The particle density was found to be

PVC PARTICLES USED IN DIFFUSION STUDY

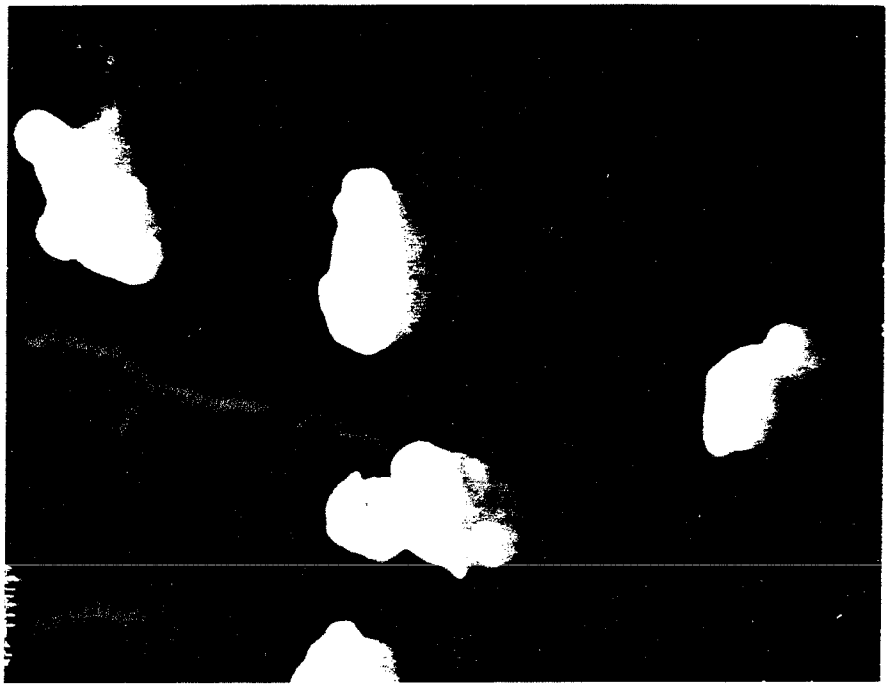

100 microns

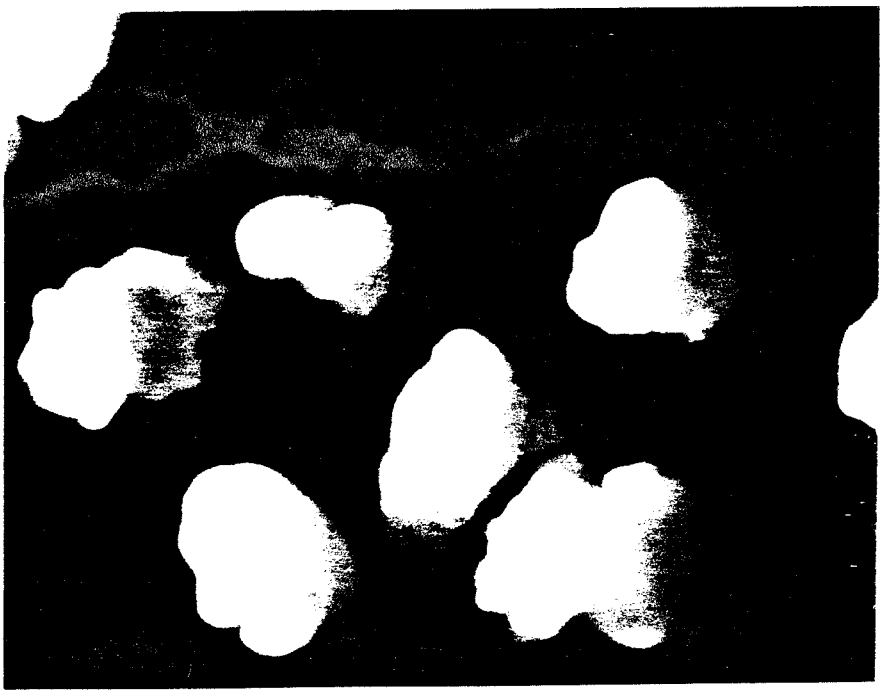

Figure 5.1

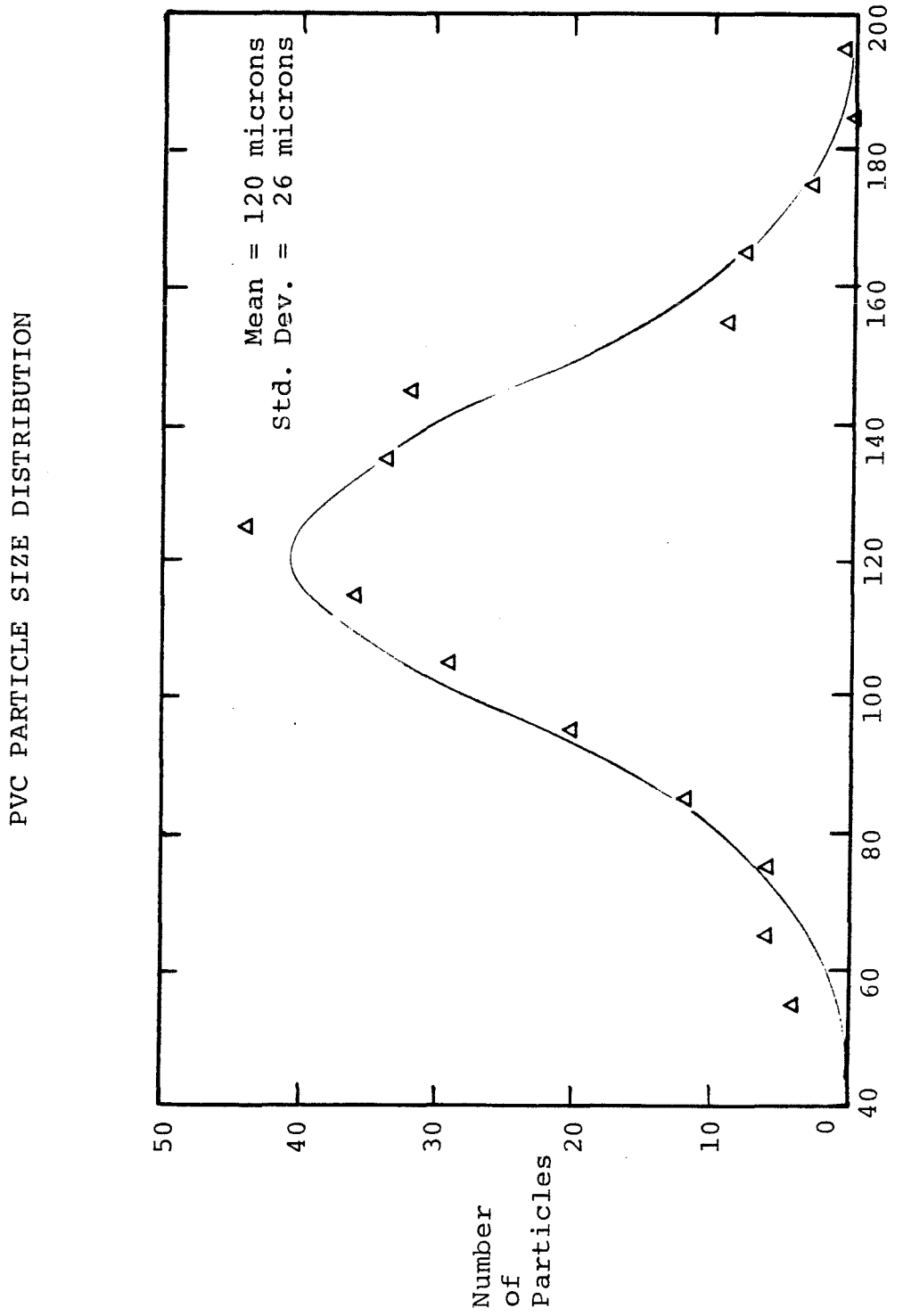
PVC PARTICLE SIZE DISTRIBUTION
Mean = 120 microns
Std. Dev. = 26 microns
Number of Particles
0
10
20
30
40
50
40
60
80
100
120
140
160
180
200
Particle Size (microns)

Figure 5.2

ρ_p = 1.15 gm/cm^3, and the mean particle settling velocity in water was determined as v_p = 0.38 cm/sec with a standard deviation of 0.14 cm/sec. The settling velocity of a 120 micron sphere in water can be calculated to be v_p = 0.47 cm/sec. This slower settling of the irregularly shaped particles can be attributed to increased drag arising from the irregular surface shape. Table 5.1 presents the results of the particle characterization.

5.2 Fluid Velocities Downstream From The Injection Tube

The fluid velocity in the axial direction and downstream from the injection tube was measured to determine what effect the injection tube had on the velocity profiles of the liquid. Velocity measurements were made across the horizontal diameter of the flow channel at distances of 0.2, 1, 3, 5, and 25 diameters downstream from the injection tube. No velocity measurements were taken at positions between 5 and 25 diameters because the flow channel could not be positioned to allow the laser beams to enter the tube in this region. Velocity profiles were measured using two limiting conditions:

1) No injection of fluid through the injection tube.
2) Injection of fluid at the velocity of the undisturbed centerpoint (no injection tube present).

CHARACTERISITCS OF THE PVC PARTICLES USED IN THE DISPERSE-PHASE MEASUREMENTS

Particle Composition	PVC
Particle Size	120 $\pm$ 26 microns
Particle Density	1.15 gm/cm^3
Particle Settling Velocity	0.38 $\pm$ 0.14 cm/sec

Table 5.1

At the closest distance to the injection tube, 0.2 diameters from injection, the velocity profiles that were measured are shown in Figures 5.3 and 5.4. When there was no injection into the flow channel (i.e., the fluid reservoir was not pressured), an extreme dip in the velocity profile was present, Figure 5.3. The dip in the velocity profiles arises from backflow into the injection tube from the flow channel. The flows into the injection tube were measured to be 0.17, 0.09, 0.08, and 0.04 cc/sec for the flows with Reynolds numbers of 20,900, 16,700, 12,500 and 8,400 respectively. Figures 5.4 shows the profiles measured when water was injected into the flow at the undisturbed centerpoint velocity. The injection velocities were within ± 4 cm/sec of the undisturbed velocities. Figure 5.4 shows the velocity profiles as being flatter than the undisturbed velocity profiles (Figure 4.11).

The velocity profiles shown in Figures 5.5 and 5.6 were measured 1 diameter downstream from the injection tube. The velocity profiles in these two figures are virtually the same. Both flows, with and without injection, exhibit a dip in the velocity profiles at the centerpoint of the channel.

Both of the deviations in the velocity profiles, namely the flattening of the profiles and the decrease in velocity at the centerpoint, can be attributed to the presence of the injection tube. The disturbance of the entire

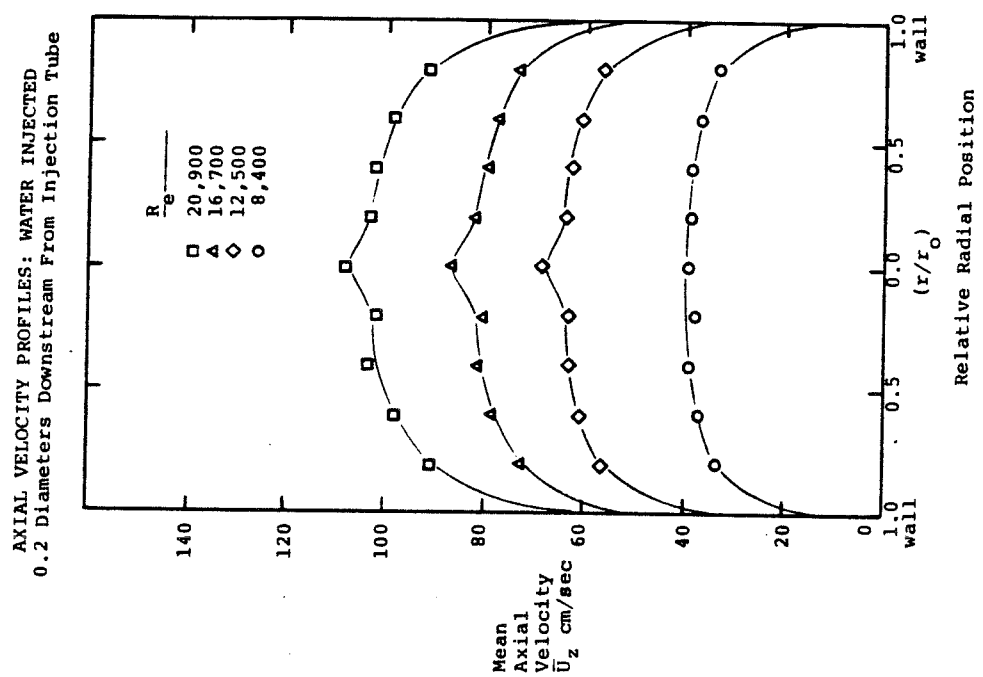

Figure 5.4

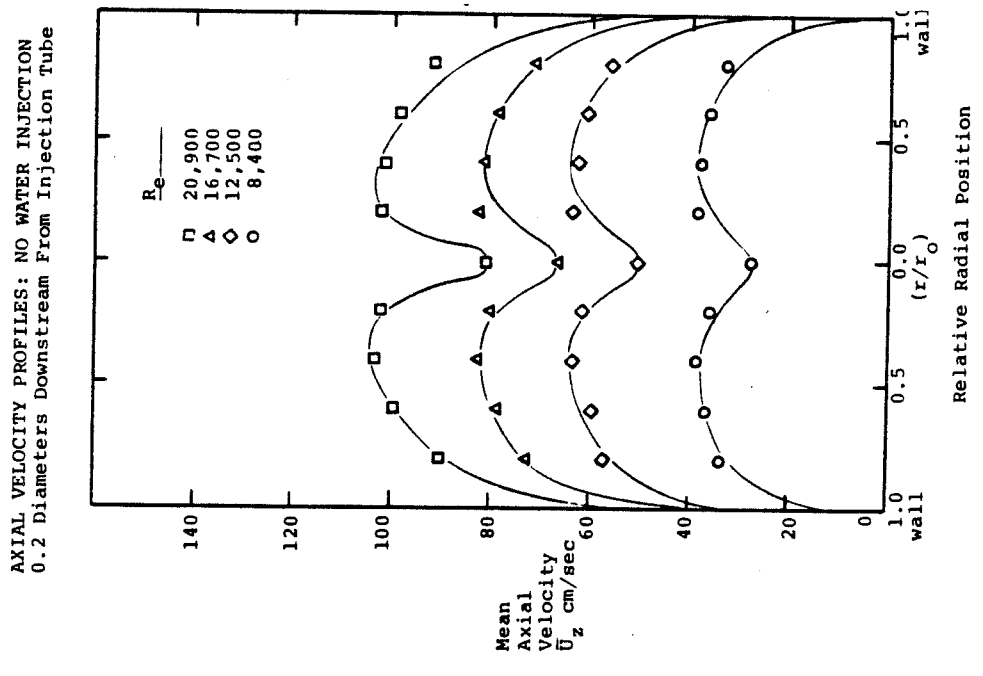

Figure 5.3

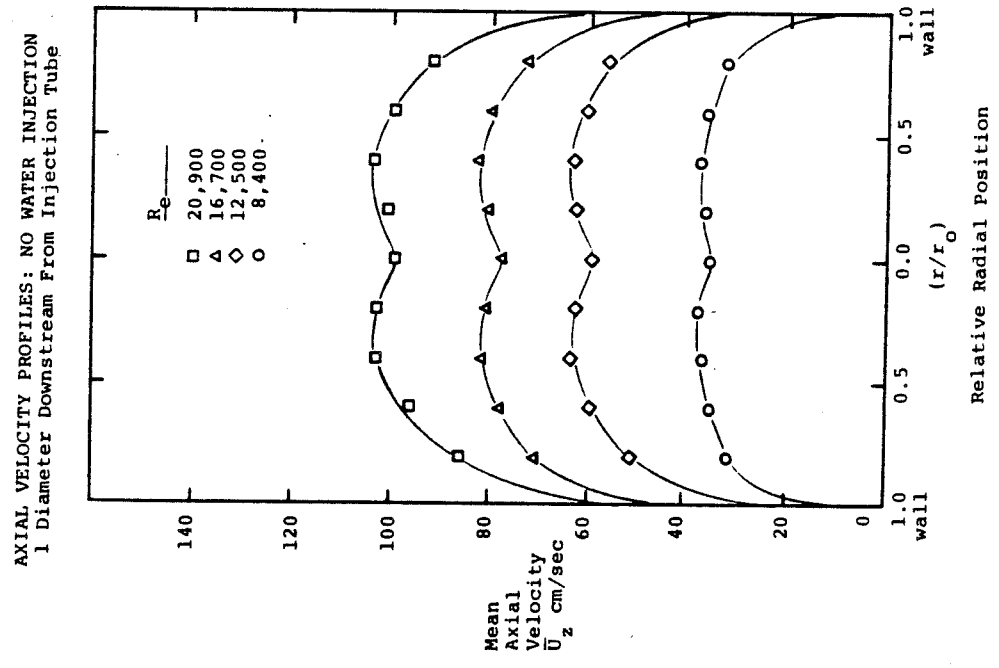

Figure 5.5

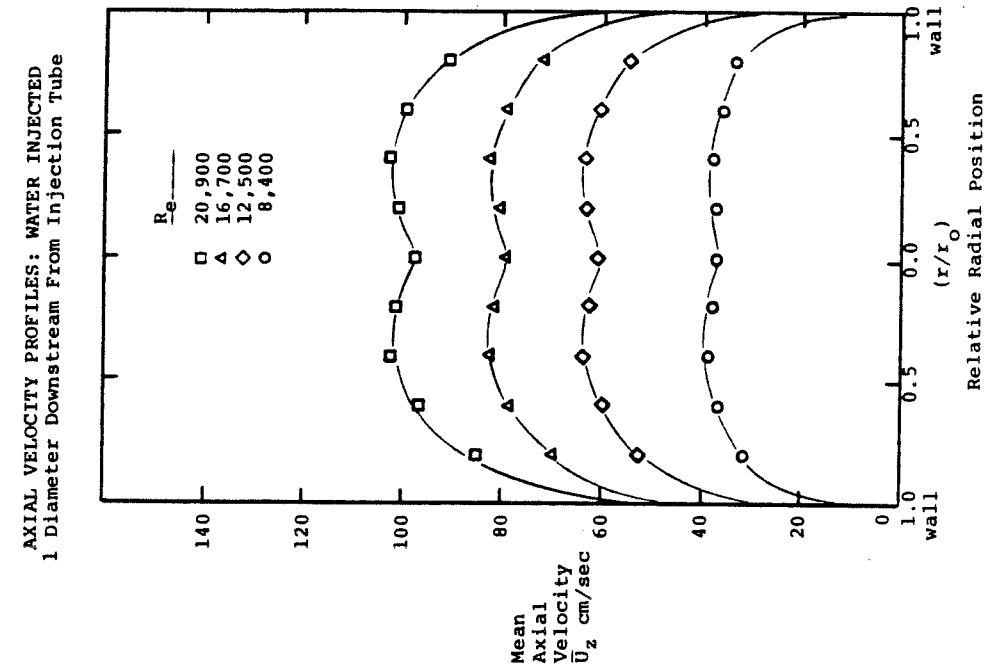

Figure 5.6

profile (i.e., the flattening) was believed to be caused by the portion of the injection tube that entered the flow channel and lay perpendicular to the direction of flow. The length of this portion of the injection tube was 1.27 cm (0.5 DIA). The decrease in centerpoint velocity shown in Figures 5.5 and 5.6 was believed to be caused by the 3.8 cm length of the injection tube running along the centerline of the channel.

Figures 5.7 and 5.8 show velocity profiles taken at a distance of 3 diameters downstream from the end of the injection tube, while Figures 5.9 and 5.10 are for 5 diameters downstream. These four figures do not show any depression of the velocity profiles at the centerline; however the profiles are still redeveloping as may be seen from the flat central portion of the profiles.

The velocities measured 25 diameters downstream from injection were the same as those shown in Figure 4.11.

5.3 Mean Particle Velocities

Figures 5.11 and 5.12 show both the continuous phase velocity profiles (solid lines) and the particle velocities (data points) at 5 and 25 diameters downstream from injection respectively. Comparison of the particle and water velocities was made by integrating the profiles over the region from $0.0 \leq (r/r_o) \leq 0.8$ and the evaluating the mean velocity over this region. The trapezoidal rule was used for the

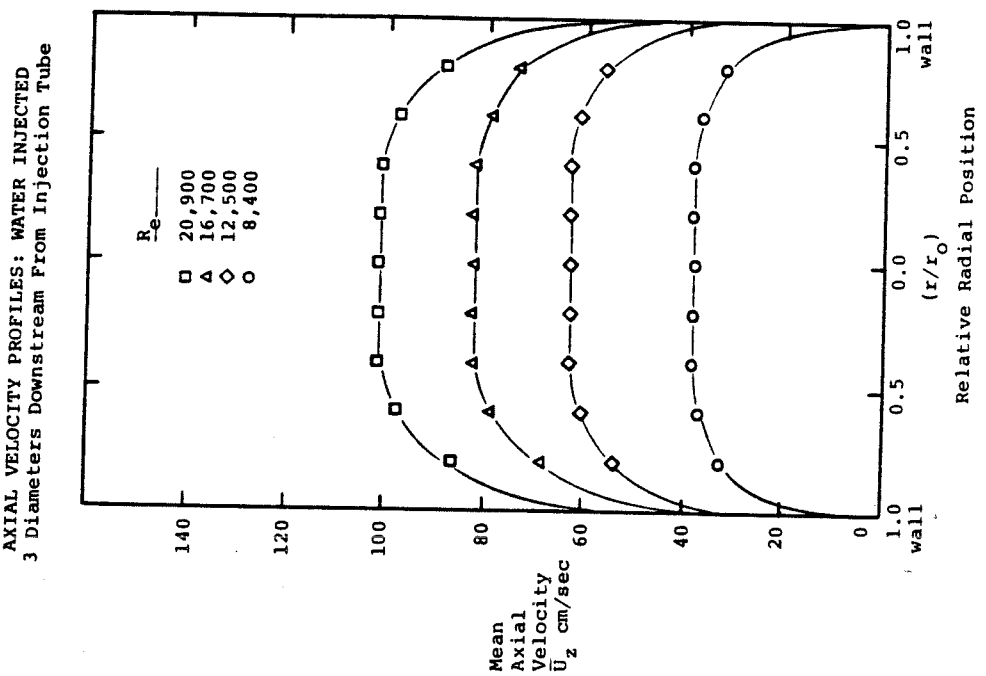

Figure 5.8

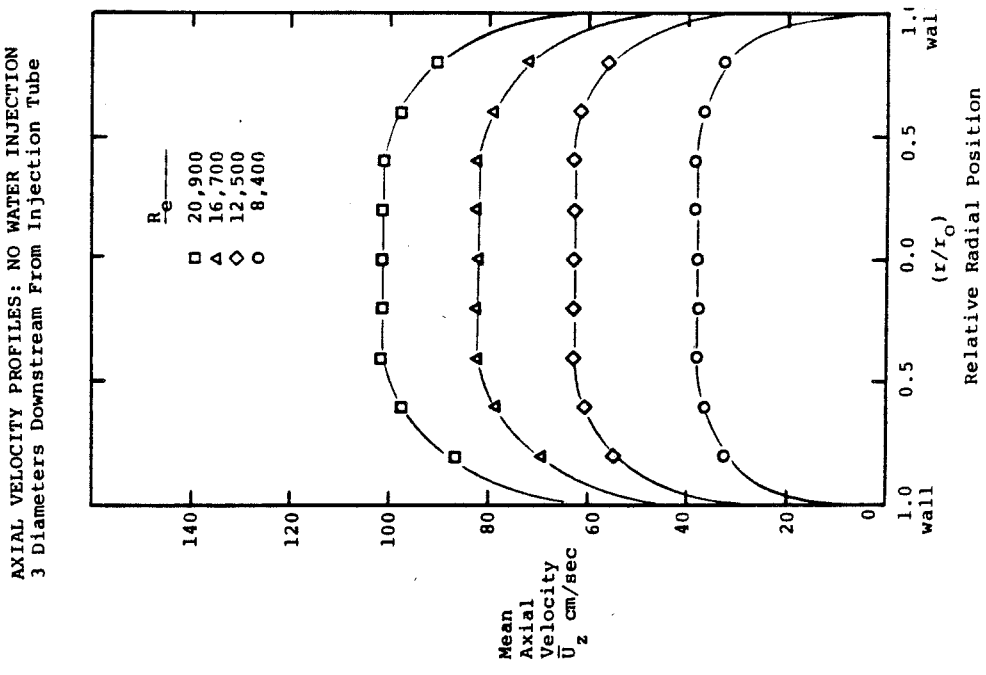

Figure 5.7

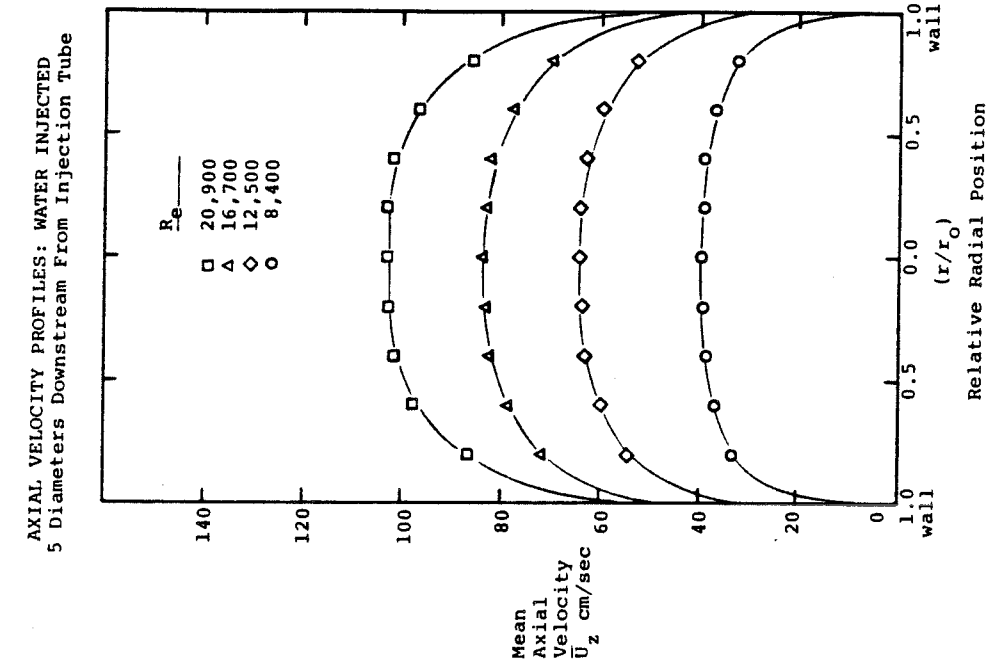

Figure 5.10

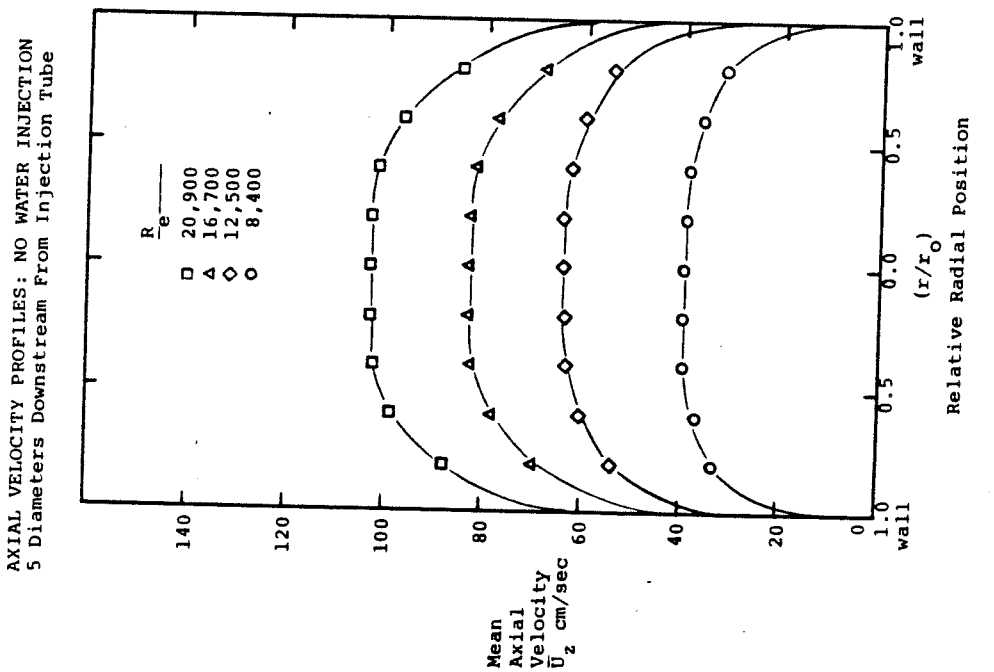

Figure 5.9

integration. Tables 5.2 and 5.3 show the resulting average velocities over the interior region.

Table 5.2 shows no definite trend for the mean velocities of the fluid and particles. At values of R_e = 8,400 and 16,700, the mean-particle-velocities are greater than the mean-fluid-velocities, while at R_e = 12,500 and 20,900 the mean-particle-velocities are less than the mean-fluid-velocities. In Figure 5.11 the data points for the particle velocities lie both above and below the fluid-velocity profiles for the flows with R_e = 16,700 and 20,900. The flow with R_e = 12,500 has the data points for the particles lying below the fluid-velocity profile, while the flow with R_e = 8,400 has the data points for the particles lying above the fluid-velocity profile. It appears that in this region immediately downstream from the injection tube, the particles travel with the fluid and exhibit little if any velocity lag.

Table 5.3 shows a definite relation between the particle and fluid velocities. At the lowest flow-rate, R_e = 8,400, the particle velocity is slightly larger than the fluid mean velocity. At the three higher flow-rates, the mean velocities of the particles are all smaller than those of the fluid. Figure 5.12 shows the particle velocities lying slightly above the liquid-velocity profile for the flow with R_e = 8,400. All three higher flow-rates show the

LIQUID AND PARTICLE VELOCITY CURVES 5 DIA FROM INJECTION

Solid lines: Liquid Velocities
Data points: Particle Velocities

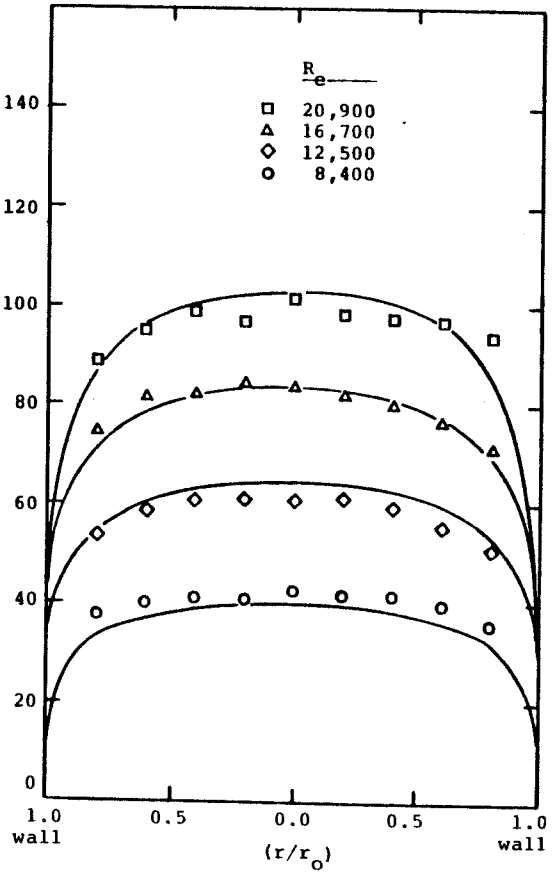

Mean Axial Velocity (cm/sec)

Relative Radial Position

Figure 5.11

LIQUID AND PARTICLE VELOCITY CURVES 25 DIA FROM INJECTION

Solid lines: Liquid Velocities
Data points: Particle Velocities

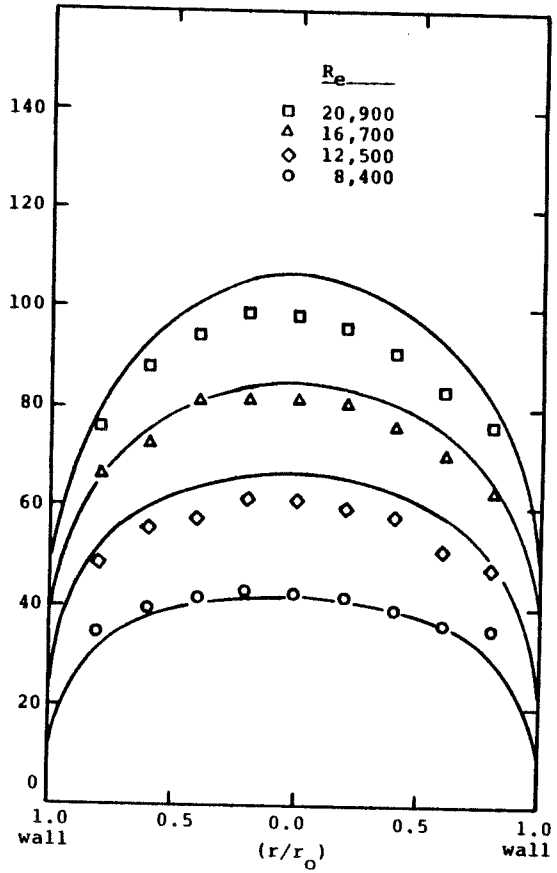

Mean Axial Velocity (cm/sec)

Relative Radial Position

Figure 5.12

AVERAGE VELOCITIES OVER THE REGION $0 \leq r/r_o \leq 0.8$ OF THE LIQUID-PHASE, $\bar{v}_l$, AND OF THE DISPERSE-PHASE, $\bar{v}_p$, MEASURED AT A DISTANCE OF 5 DIAMETERS DOWNSTREAM FROM THE INJECTION TUBE

R_e $(DV_{avg}\rho)/\mu$	$\bar{v}_l$ cm/sec	$\bar{v}_p$ cm/sec
8,400	36.5	39.7
12,500	59.8	57.0
16,700	77.7	78.3
20,900	95.9	95.4

Table 5.2

AVERAGE VELOCITIES OVER THE REGION $0.0 \leq r/r_o \leq 0.8$ OF THE LIQUID-PHASE, $\bar{v}_l$, AND OF THE DISPERSE-PHASE, $\bar{v}_p$, MEASURED AT A DISTANCE OF 25 DIAMETERS DOWNSTREAM FROM THE INJECTION TUBE

R_e $(DV_{avg}\rho)/\mu$	$\bar{v}_l$ cm/sec	$\bar{v}_p$ cm/sec
8,400	36.8	38.5
12,500	58.2	54.4
16,700	75.3	73.0
20,900	94.8	86.6

Table 5.3

particle velocities lying below the fluid-velocity curves. The greatest lag in particle velocity occurs at the highest rate of flow, R_e = 20,900, with the two intermediate flow-rates showing some velocity lag, and the lowest flow-rate, R_e = 8,400, has the particles moving with the liquid. The lag in the particle velocities compared with the fluid velocities at a distance of 25 diameters downstream from the injection tube is thought to be due to the velocity profiles of the particles not developing as fast as the velocity profiles of the fluid, once the influence of the injection tube had vanished. The additional time needed for the particle velocities to develop is attributed to the inability of the particles to follow all of the eddies present in the turbulent field, resulting in a longer time to reach the main fluid velocity.

Table 5.4 lists the particle Reynolds number, R_{ep}, the Kolmogorov-length scale, and the Stokes number of the particles, ψ, for the four flow-rates used. These three numbers will give an indication of whether the particles will follow all of the turbulent eddies, none of the eddies, or an intermediate number of eddies.

The particle Reynolds number and the Kolmogorov-length scale can be used to determine if the PVC particles are affected by all of the eddies present in the flow. If R_{ep} were on the order of unity or smaller or if the particle

DIMENSIONLESS GROUPS FOR PARTICLE CHARACTERIZATION

Reynolds Number Re	Particle Reynolds Number Re_p	Kolmogorov Length Scale (Microns)	Stokes Number ψ
8,400	40	50	0.01
12,500	60	40	0.02
16,700	80	30	0.02
20,900	100	30	0.03

Table 5.4

size were smaller than the Kolmogorov-length scale, the particles would follow all of the eddies present in the turbulent flow. The values of R_{ep} listed in Table 5.4 range from 40 to 100, and the Kolmogorov-length scale varies from ½ to ¼ of the particle size. These two results show that the particles do not follow all of the eddies present in the turbulence as was demonstrated by the additional time required for the velocity profiles of the particles to develop in comparison with the velocity profiles of the fluid phase.

The Stokes number is the ratio of particle-stopping distance to the characteristic length of the flow system. This ratio gives an indication as to whether the particles are affected by any of the turbulent eddies because the largest eddies present in the flow are on the order of the diameter of the flow channel which is the characteristic dimension of the flow channel used in this experiment. If ψ was order 1 or larger in the PVC particles would only be affected by the largest eddies in the flow. If ψ were much less than unity the PVC particles would respond to all eddies present in the flow. Table 5.4 shows ψ ranging from 0.01 to 0.03 for the four flow-rates used in the experiment. These values of Stokes number show that the PVC particles are affected by most of the eddies present in the system.

In summary, Table 5.4 shows that the PVC particles are moved by all but the small-scale eddies present in the turbulence.

5.4 RMS Particle Velocities

Measurements of the rms velocities of suspended particles in turbulent pipe flow have been made in the past by photographic techniques (5-7) or by calculation using Taylor's equation for turbulent diffusion (Equation 2.26) (5-2). Photographic methods for measuring rms velocities require magnification large enough for individual particles to be seen. The amount of magnification required limits the area of the turbulent flow viewed, so that the measurements of the rms velocities made by Kubol, et al. (5-7) were confined to the center of the channel and were of $(\overline{v_z'^2})^{\frac{1}{2}}$ only. Calabrese and Middleman (5-2) calculated $(\overline{v_r'^2})^{\frac{1}{4}}$ from turbulent diffusion data in the center of the pipe. These calculated values of $(\overline{v_r'^2})^{\frac{1}{2}}$ were average values across the central portion of the pipe where the diffusion data were taken. The measurements made in the present study were of the actual rms velocities in the r, θ, and z directions for the PVC particles as functions of the radial position in the flow channel.

Figures 5.13 through 5.24 are plots of the velocity fluctuations in the r, θ, and z directions, non-dimensionalized with respect to the friction velocity. Both the rms

NON-DIMENSIONAL AXIAL-RMS VELOCITIES ACROSS THE FLOW CHANNEL

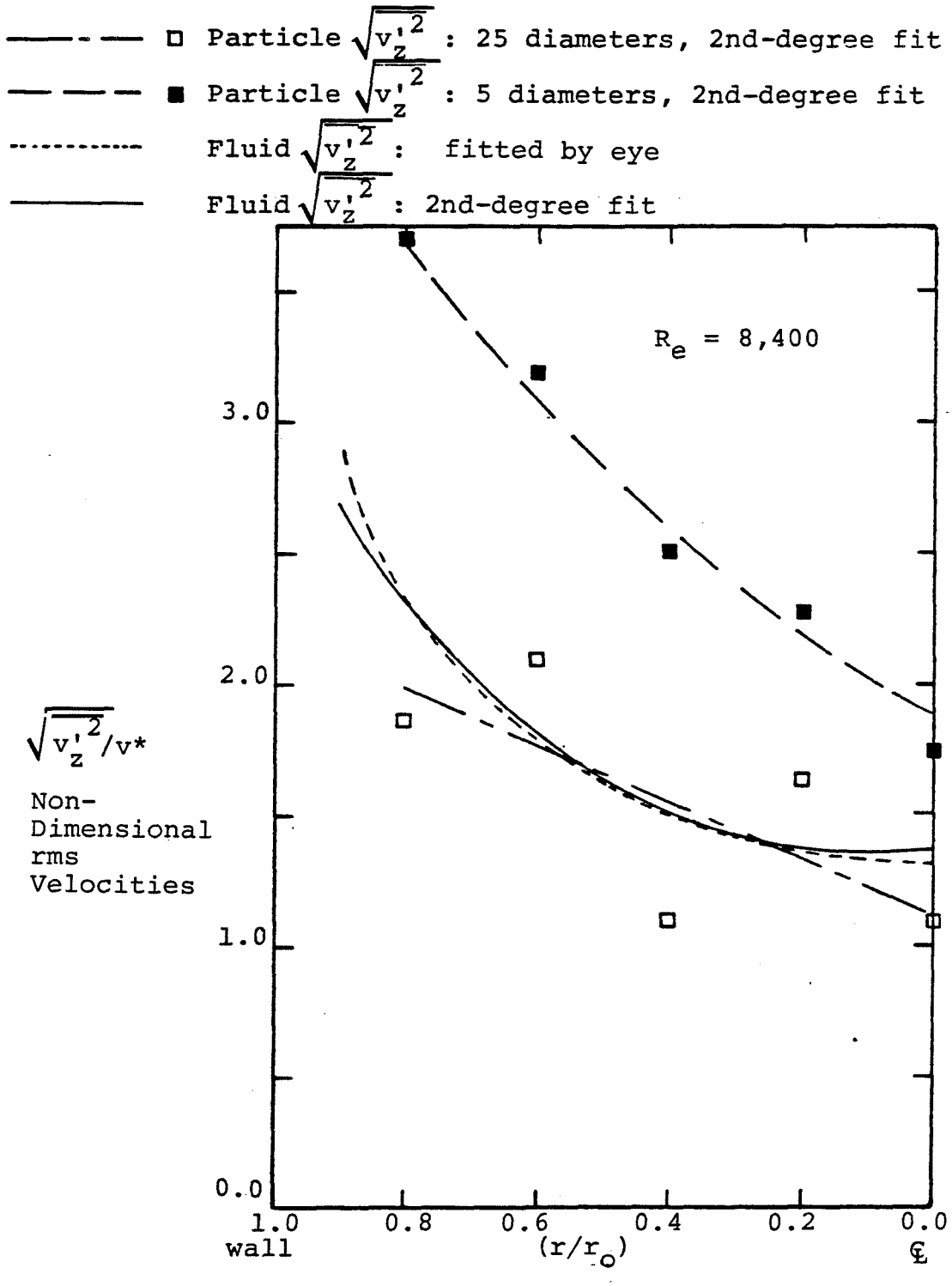

Figure 5.13

NON-DIMENSIONAL AXIAL-RMS-VELOCITIES ACROSS THE FLOW CHANNEL

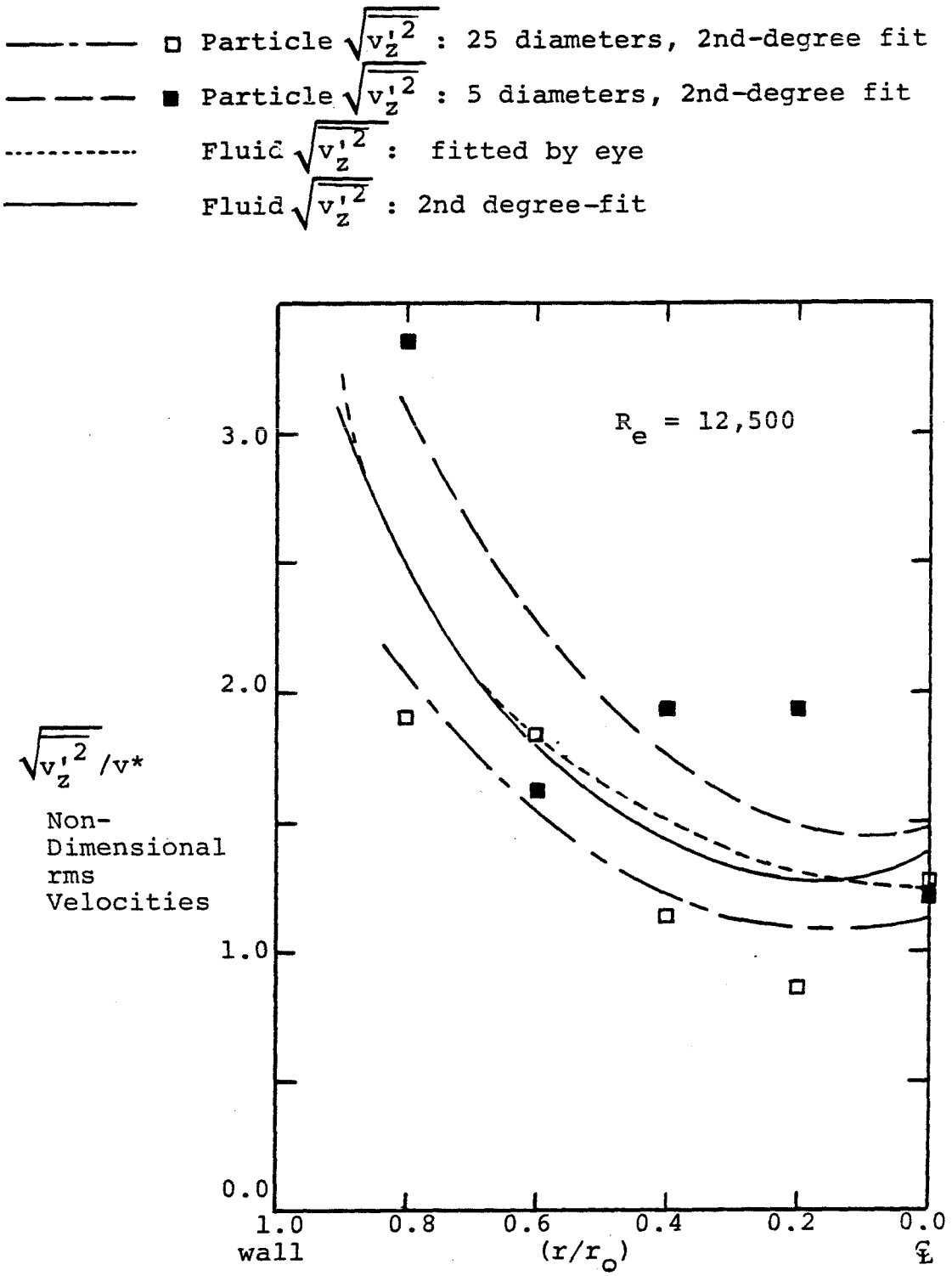

Figure 5.14

NON-DIMENSIONAL AXIAL-RMS-VELOCITIES ACROSS THE FLOW CHANNEL

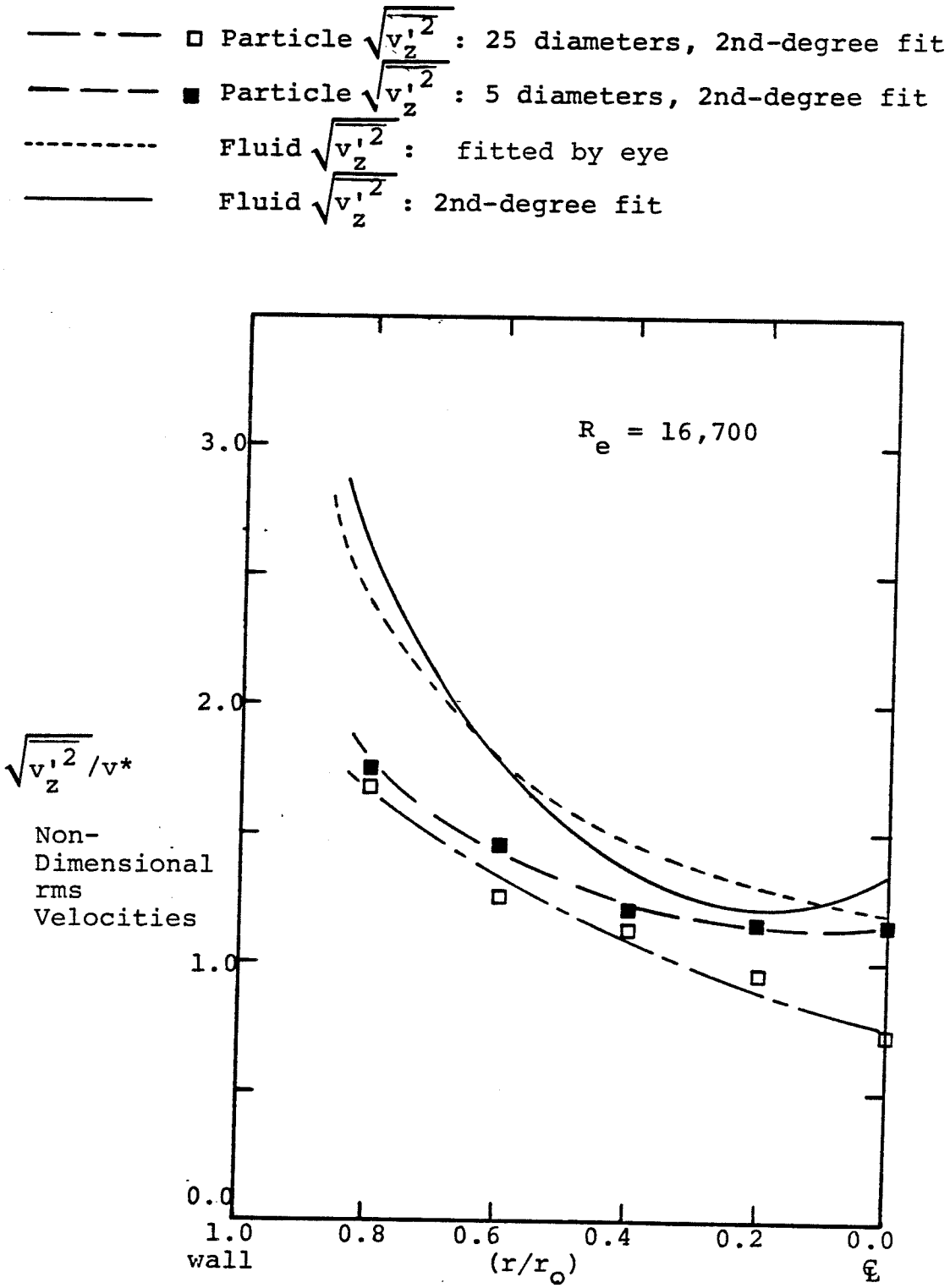

Figure 5.15

NON-DIMENSIONAL AXIAL-RMS-VELOCITIES ACROSS THE FLOW CHANNEL

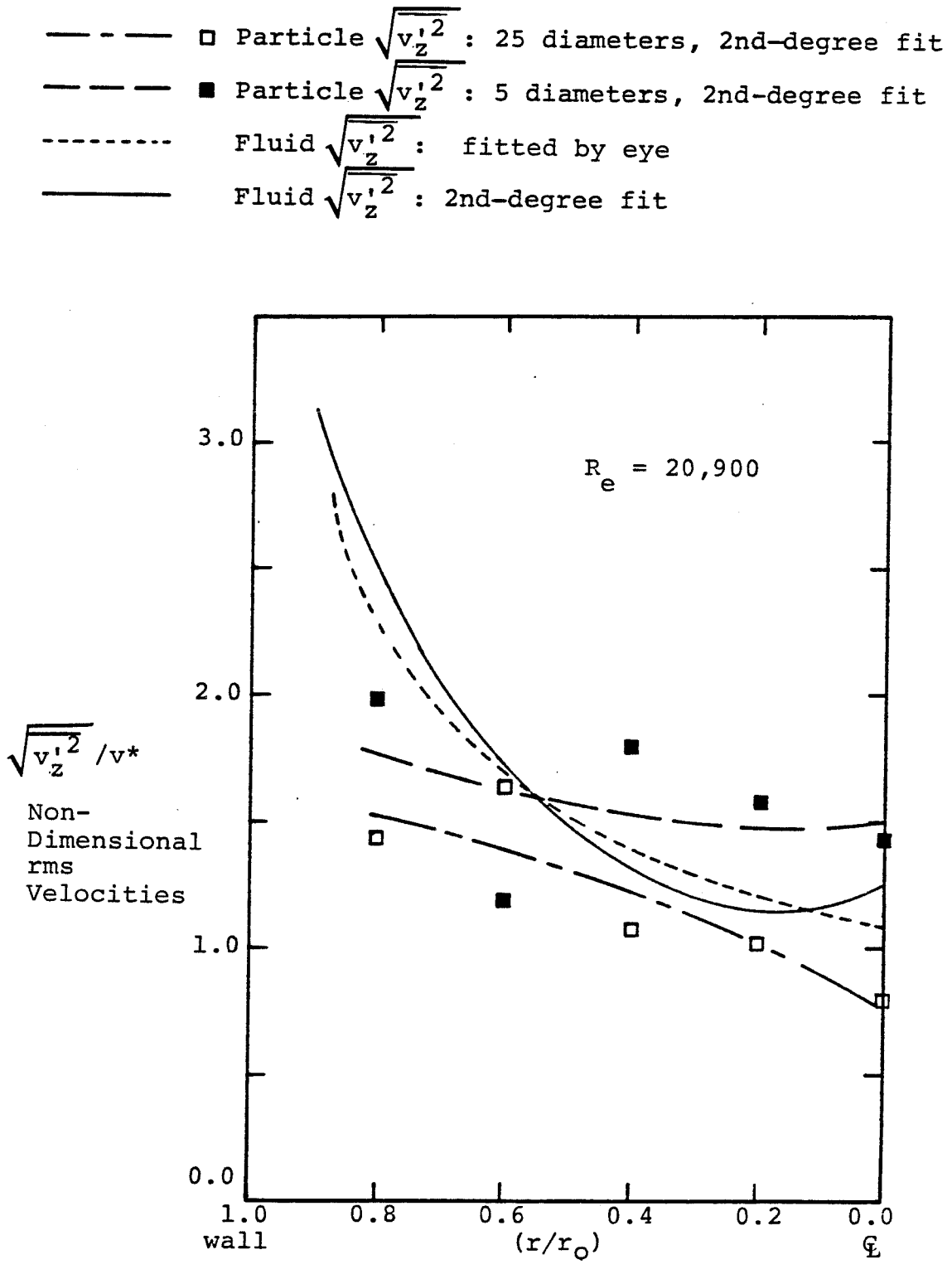

Figure 5.16

NON-DIMENSIONAL RADIAL-RMS-VELOCITIES ACROSS THE FLOW CHANNEL

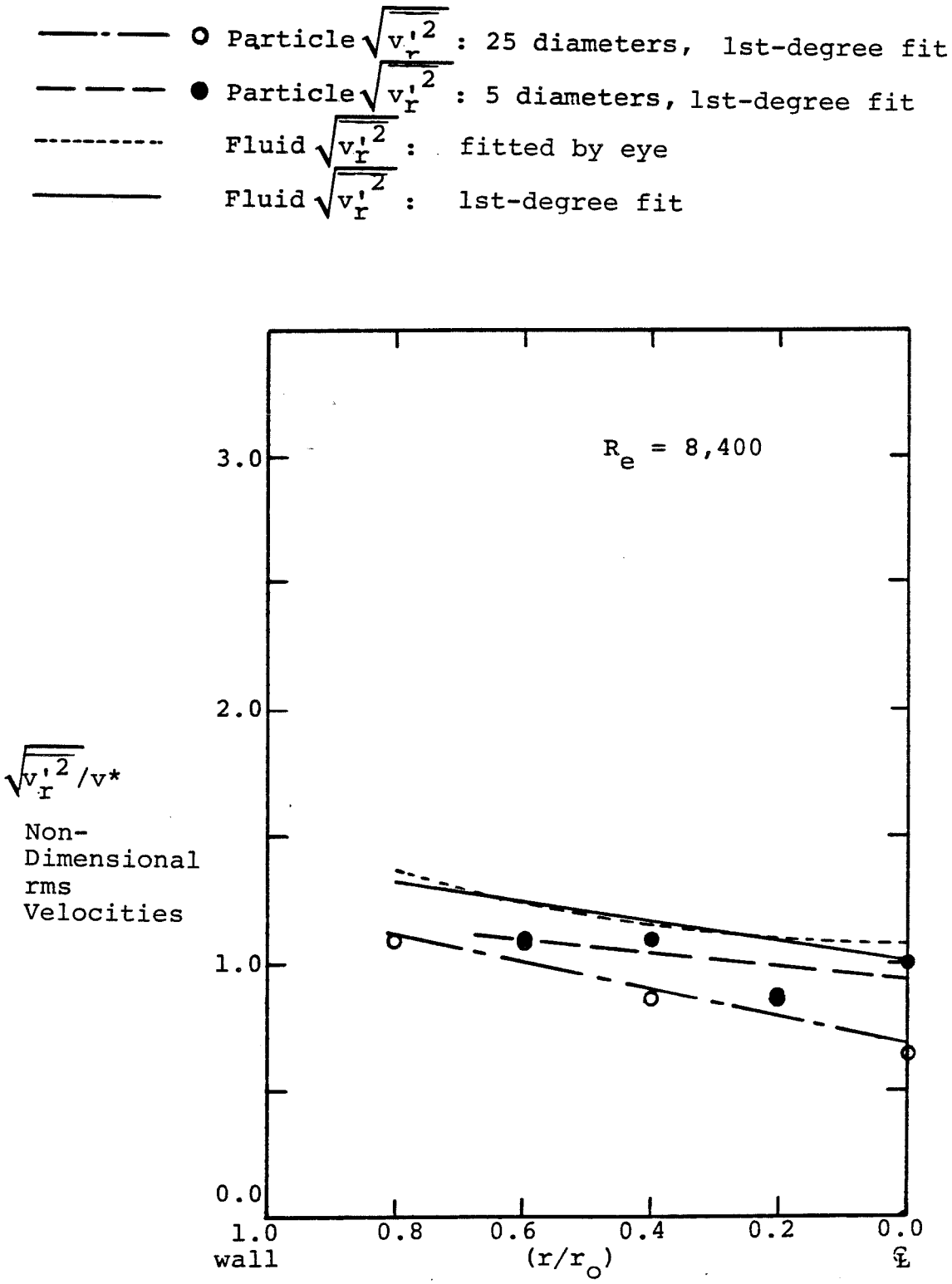

Figure 5.17

NON-DIMENSIONAL RADIAL-RMS-VELOCITIES ACROSS THE FLOW CHANNEL

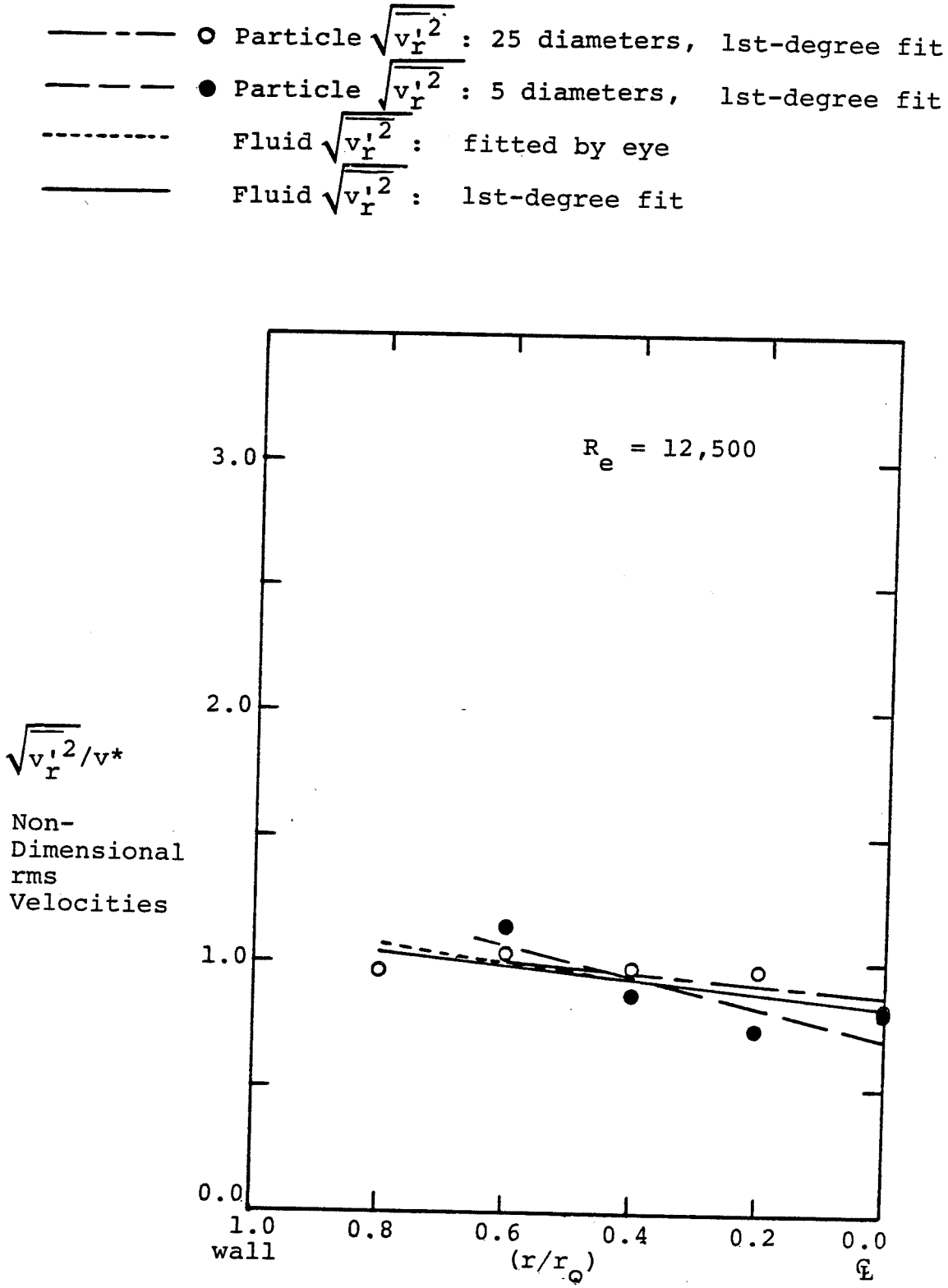

Figure 5.18

NON-DIMENSIONAL RADIAL-RMS-VELOCITIES ACROSS THE FLOW CHANNEL

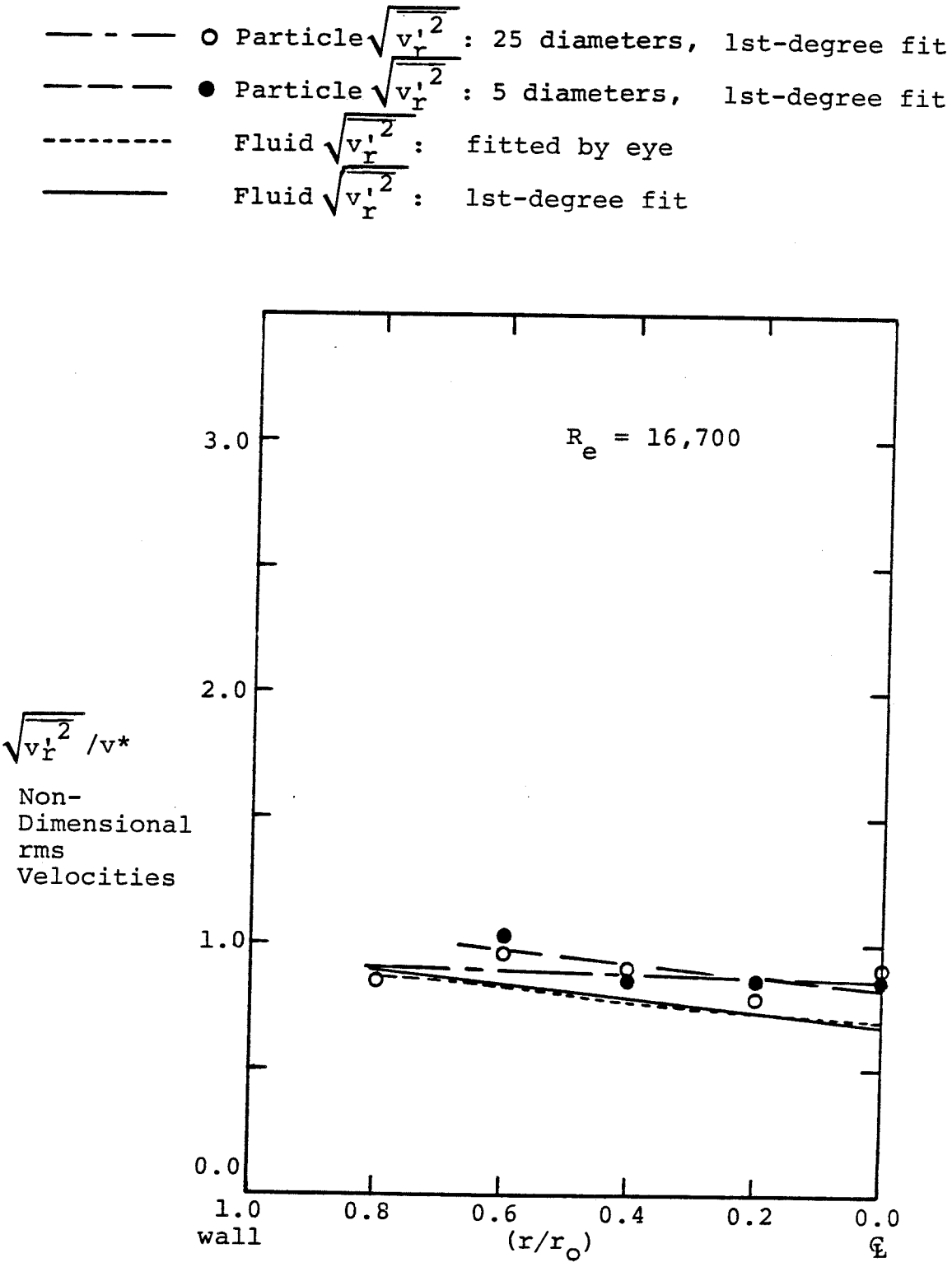

Figure 5.19

NON-DIMENSIONAL RADIAL-RMS-VELOCITIES ACROSS THE FLOW CHANNEL

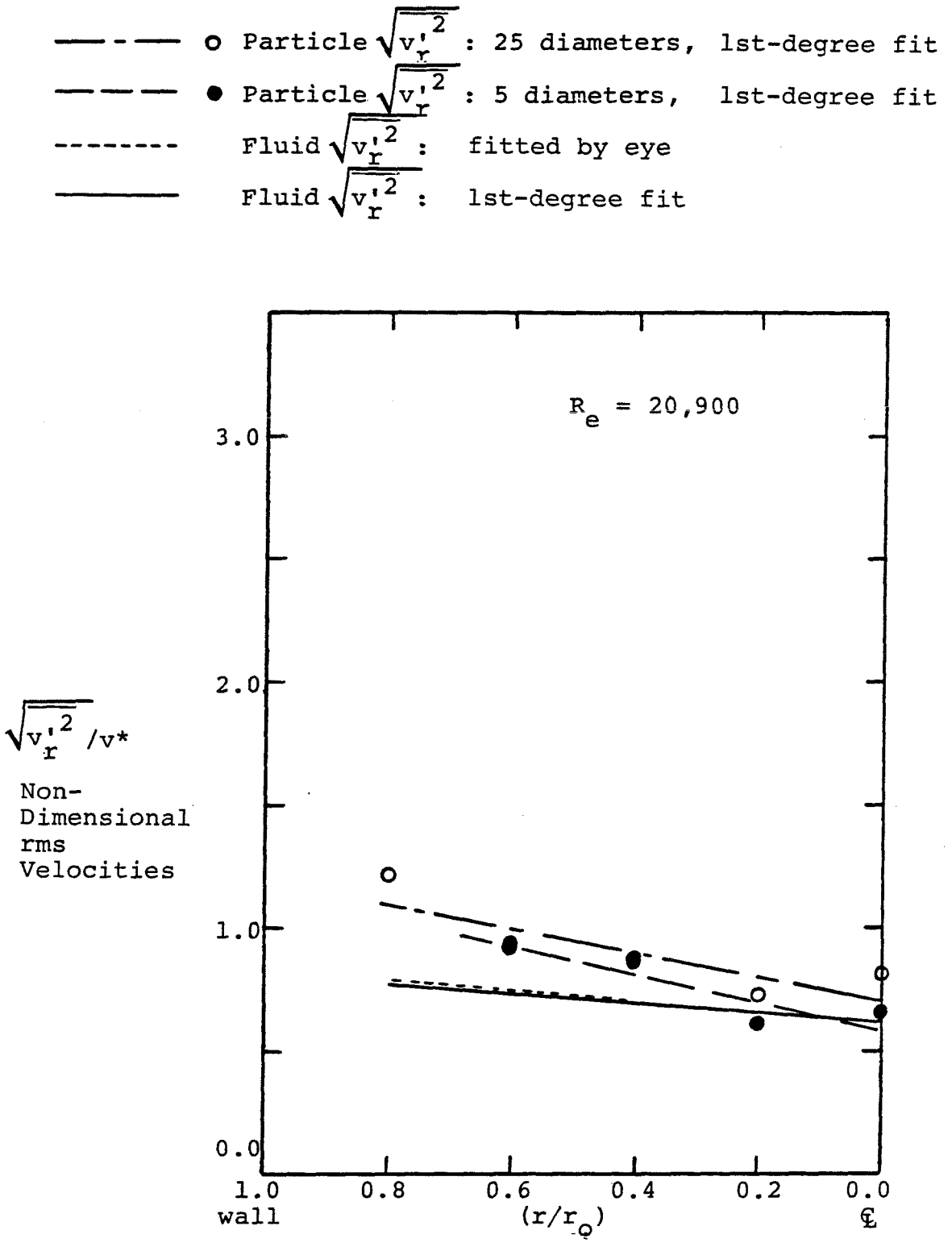

Figure 5.20

NON-DIMENSIONAL AZIMUTHAL-RMS-VELOCITIES ACROSS THE FLOW CHANNEL

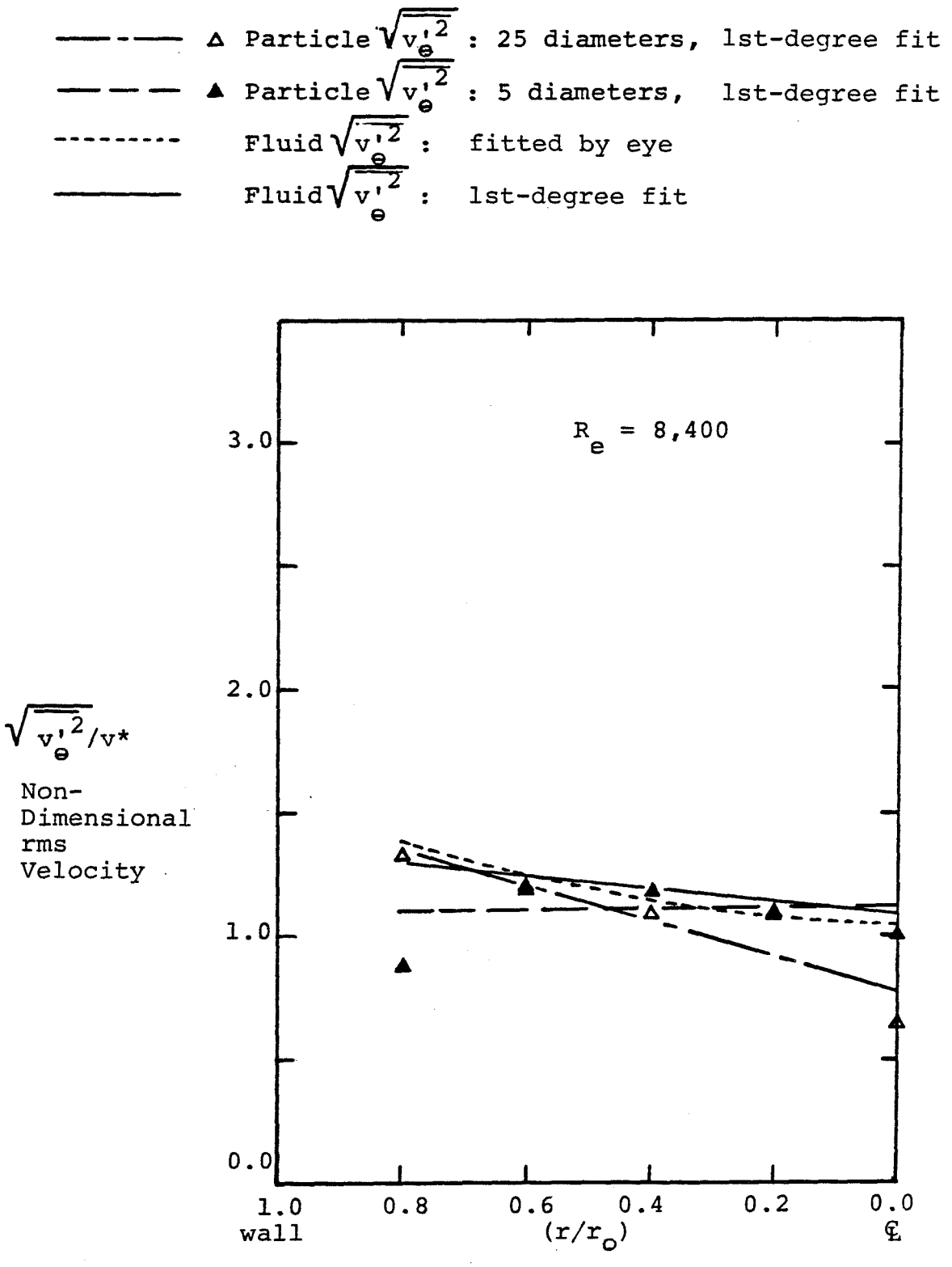

Figure 5.21

NON-DIMENSIONAL AZIMUTHAL-RMS-VELOCITIES ACROSS THE FLOW CHANNEL

— - — △ Particle $\sqrt{\overline{v_\theta'^2}}$: 25 diameters, 1st-degree fit

— — — ▲ Particle $\sqrt{\overline{v_\theta'^2}}$: 5 diameters, 1st-degree fit

- - - - - - - Fluid $\sqrt{\overline{v_\theta'^2}}$: fitted by eye

——— Fluid $\sqrt{\overline{v_\theta'^2}}$: 1st-degree fit

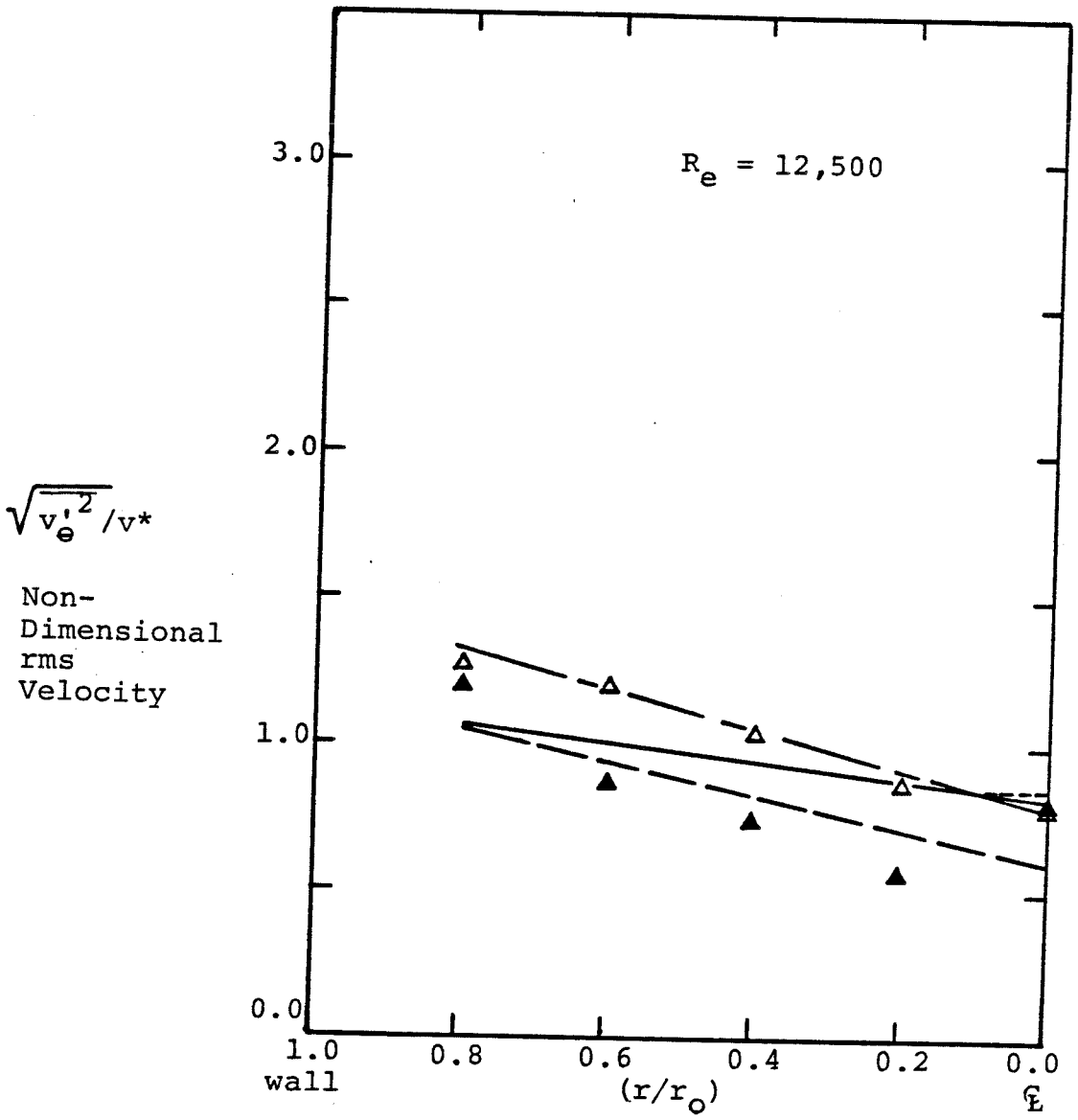

Figure 5.22

NON-DIMENSIONAL AZIMUTHAL-RMS-VELOCITIES ACROSS THE FLOW CHANNEL

— - — △ Particle $\sqrt{\overline{v_\theta'^2}}$: 25 diameters, 1st-degree fit

— — — ▲ Particle $\sqrt{\overline{v_\theta'^2}}$: 5 diameters, 1st-degree fit

-------- Fluid $\sqrt{\overline{v_\theta'^2}}$: fitted by eye

———— Fluid $\sqrt{\overline{v_\theta'^2}}$: 1st-degree fit

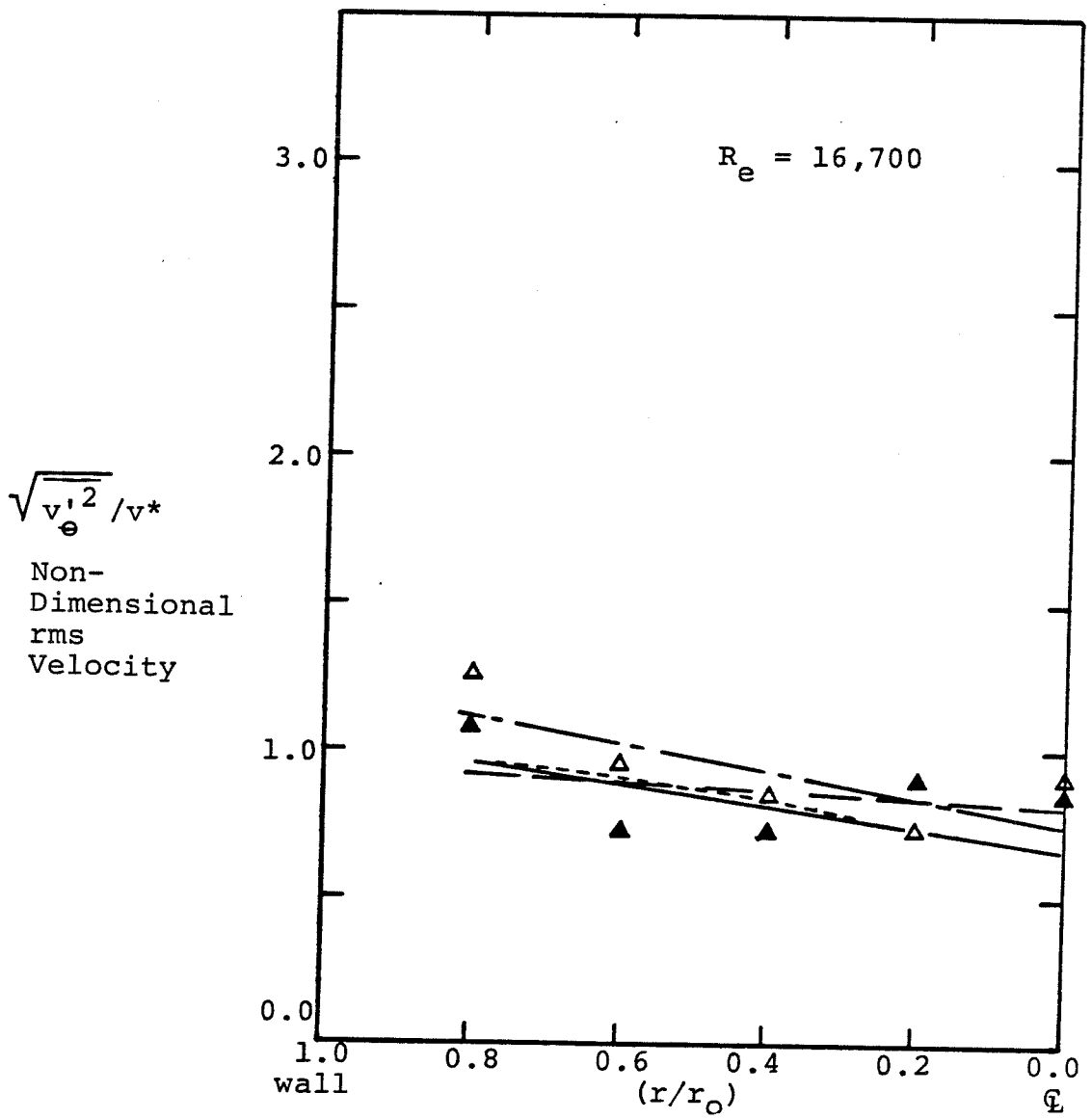

Figure 5.23

NON-DIMENSIONAL AZIMUTHAL-RMS-VELOCITIES ACROSS THE FLOW CHANNEL

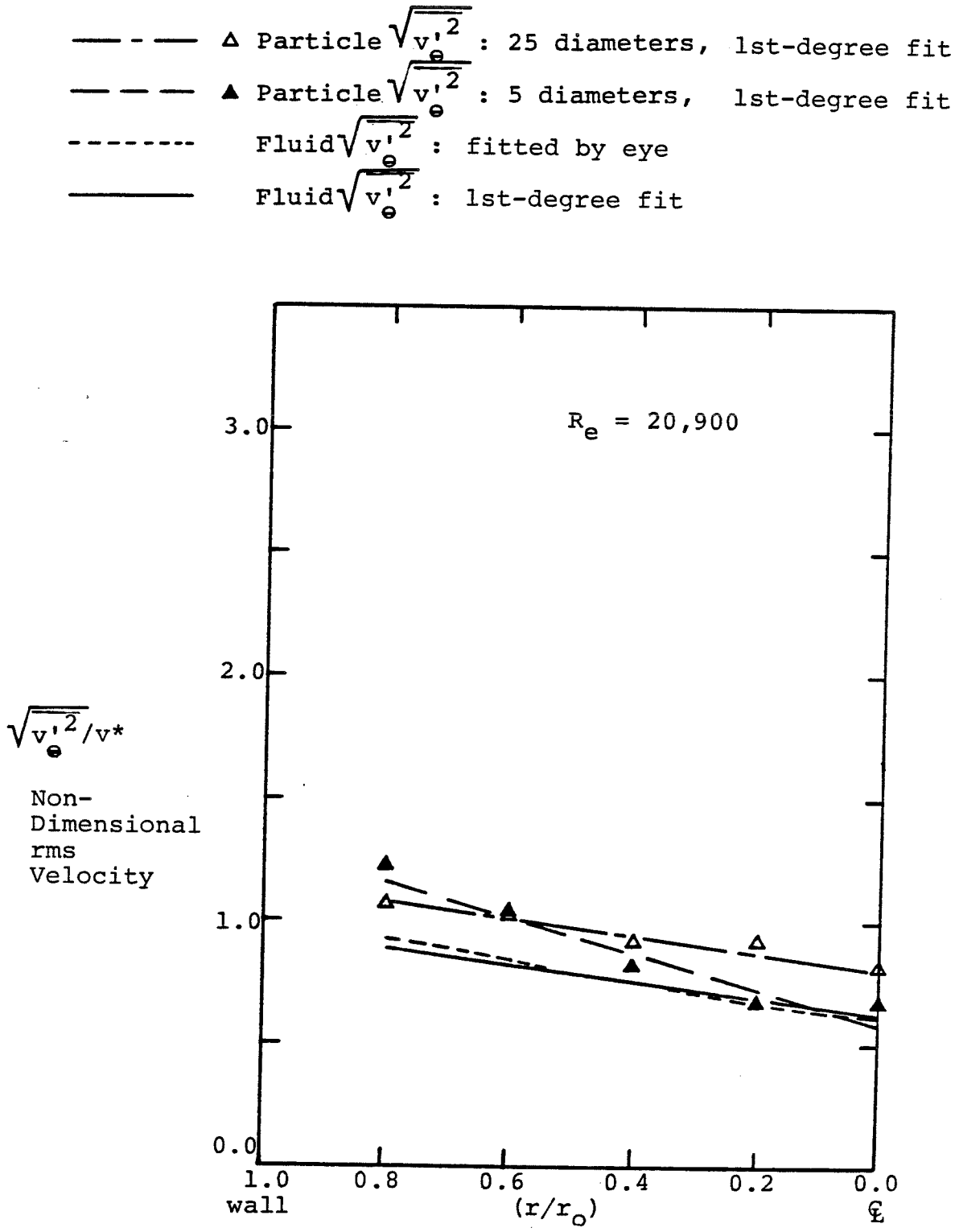

Figure 5.24

velocities of the particles (data points and curves) at 5 and 25 diameters downstream from injection, and the rms-velocity curves for the liquid-phase are plotted in the figures. A first-degree polynomial was chosen to fit the rms velocities for the particles in the r and θ directions. The first-degree polynomial was chosen to fit the data for these two coordinate directions because the rms velocities of the continuous-phase in the r and θ directions exhibited very little curvature (Figure 4.19 through 4.22). A second-degree polynomial was used to fit the rms velocities of the particles in the axial direction because the continuous-phase rms-velocity curves were paradobolic in shape. In Figures 5.13 through 5.24 there are two curves that were not fitted through the data points. The dashed line is the smooth curve that was drawn by eye through the continuous-phase rms-velocity data, while the solid line is the polynomial fit through the same data.

It was desired to measure the particle velocities without any interaction between the particles; so the injection concentration was kept low enough for there to be no more than 1 particle in 4 cc of water. Because of the dilute nature of the suspension, measurement of the rms velocities by means of an rms voltmeter was not possible. The particle rms velocities were therefore obtained by displaying individual doppler bursts on a storage oscilliscope

and counting the frequency manually. Each data point shown was calculated from 50 measurements at that position in the channel.

In Figures 5.13 through 5.16, the non-dimensionalized rms velocities in the axial direction have been plotted. In all four figures the rms velocities for the particles at 5 diameters downstream from injection are greater than those at 25 diameters downstream from injection. The rms fluctuations for the particles occurring at the 5 diameter distance from injection are also greater than the rms velocities of the water in all figures except for 5.13. If the rms velocities for the axial flow of the particles at 25 diameters downstream from injection are compared with the liquid curves for the four flow-rates, it is seen that the particle fluctuations are smaller than those of the liquid.

A decrease in magnitude of $(\overline{v_z'^2})^{\frac{1}{2}}/v^*$ for the particles at 25 diameters as compared with the liquid indicated that the particle was not completely following the fluid. This decrease in fluctuating velocities for the particles has been observed by other investigators. Kuboi, et al. (5-7) used photographic methods to measure the velocity fluctuations for axial flow of particles ranging in size from 0.045 to 0.18 cm. The region over which the fluctuating velocities of the particles was measured was the center of the pipe, and the water velocities varied from 100 to 420

cm/sec. They found decreases ranging from 1/3 to 3/4 in the magnitude of the mean-squared fluctuating velocity of the particles as compared to the liquid. If the experimentally measured mean-squared fluctuating velocities obtained in this study of the particles are compared with those of the liquid at the center of the flow channel, the decreases shown in Table 5.5 are obtained.

The larger values of the axial-rms-velocities for the particles at 5 diameters downstream from injection when compared with the axial-rms-velocities of both the continuous-phase and the particles at the distance of 25 diameters downstream from injection show that the disturbance of the flow caused by the injection tube increases the axial-rms-velocity of the liquid immediately downstream from the injection tube. Since measurements of the rms velocities of the water were not made in this region, the exact magnitude of the liquid fluctuations is not known. Table 5.5 shows, however, that the axial flucuations of the liquid would be at least as large as the particles and most probably greater.

Figures 5.17 through 5.20 show the radial velocity fluctuations of the particles and liquid. At 5 diameters downstream from injection the rms velocities for the particles were not measured at $r/r_o = 0.8$ because the time required to obtain 50 measurements would have been prohibi-

PERCENTAGE DECREASE OF THE AXIAL-RMS-VELOCITIES OF THE PARTICLES RELATIVE TO THOSE OF THE WATER AT THE CENTER OF THE FLOW CHANNEL

R_e $(DV_{avg}\rho)/\mu$	% Decrease
8,400	31
12,500	0
16,700	62
20,900	45

Table 5.5

tive. Figures 5.17 through 5.20 do not show any consistent relationships between the radial-rms-velocities for the particles at 5 and 25 diameters downstream from injection. At a Reynolds number of 8,400, the rms velocities 5 diameters from injection are greater than the rms velocities 25 diameters from injection, while at R_e = 20,900 the rms velocities 25 diameters from injection are larger than those 5 diameters downstream from injection. The values of the radial-rms-velocities for the particles are essentially the same at 5 and 25 diameters downstream from injection for the flows with Reynolds numbers of 12,500 and 16,700. In all four figures data for the rms velocities of the particls are nearly the same which means that the presence of the injection tube makes little if any difference in the rms velocities in the radial direction. Table 5.6 lists the mean values of the particle and liquid rms velocities. The mean values are calculated over the region between the centerline and r/r_o = 0.8. In Table 5.6 the mean value of the non-dimensionalized rms velocities in the radial direction for the water are seen to decrease as the Reynolds number increases. The mean value of the rms velocities in the radial direction for the particles decreases slightly as the Reynolds number increases 5 diameters from injection, while 25 diameters from in-

AVERAGE VALUES OVER THE REGION $0.0 \leq r/r_o \leq 0.8$ OF THE NON-DIMENSIONALIZED RMS VELOCITIES IN THE RADIAL DIRECTION FOR THE DISPERSE-PHASE, MEASURED AT 5 AND 25 DIAMETERS DOWNSTREAM FROM INJECTION, AND FOR THE CONTINUOUS-PHASE, MEASURED WITH NO INJECTION TUBE IN THE FLOW CHANNEL

R_e	$(\overline{v_r'^2})^{\frac{1}{2}}/v^*$	$(\overline{v_r'^2})^{\frac{1}{2}}/v^*$	$(\overline{v_r'^2})^{\frac{1}{2}}/v^*$
$(DV_{avg}\rho)/\mu$	Particles 5 Diameters From Injection	Particles 25 Diameters From Injection	Water
8,400	1.0	0.9	1.2
12,500	1.0	1.0	0.9
16,700	0.9	0.9	0.8
20,900	0.8	0.9	0.7

Table 5.6

jection the mean value remains constant as Reynolds number increases. Table 5.6 lists numerically the same trend that Figures 5.17 through 5.20 show. At R_e = 8,400 the curves for the liquid are above the curves for the particles, at R_e = 12,500 the liquid and particle curves are in the same region of the plots, and at R_e = 16,700 and 20,900 the liquid curves are below the particle curves.

Figures 5.21 through 5.24 show the non-dimensionalized rms velocities for the particles in the azimuthal direction. Data taken at 5 and 25 diameters downstream from injection are shown in the figures. The flows with R_e = 12,500, 16,700, and 20,900 all show the non-dimensionalized rms velocities of the particles to be greater at 25 diameters from injection than at 5 diameters from injection. At R_e = 8,400 the differences in the slopes of the curves through the data for the particles makes comparison difficult; however, the mean values of $(\overline{v_e'^2})^{\frac{1}{2}}/v^*$ for both distances from the injection tube are the same. Table 5.7 lists the mean values, over the region r/r_o = 0.0 to 0.8, for the rms velocities of the particles. The mean values of the non-dimensional rms velocities, in the azimuthal direction, for the water that are shown in Table 5.7 display the same decreases in magnitude, with increasing Reynolds number, that was shown for the rms velocities of the water in the radial direction, Table 5.6. The mean values of the rms velocities

AVERAGE VALUES OVER THE REGION $0.0 \leq r/r_o \leq 0.8$ OF THE NON-DIMENSIONALIZED RMS VELOCITIES IN THE AZIMUTHAL DIRECTION FOR THE DISPERSE-PHASE, MEASURED AT 5 AND 25 DIAMETERS DOWNSTREAM FROM INJECTION, AND FOR THE CONTINUOUS-PHASE, MEASURED WITH NO INJECTION TUBE IN THE FLOW CHANNEL

$(DV_{avg}\rho)/\mu$	$\overline{(v_\theta'^2)}^{1/2}/v^*$ Particles 5 Diameters From Injection	$\overline{(v_\theta'^2)}^{1/2}/v^*$ Particles 25 Diameters From Injection	$\overline{(v_\theta'^2)}^{1/2}/v^*$ Water
8,400	1.1	1.1	1.2
12,500	0.8	1.1	1.0
16,700	0.8	0.9	0.9
20,900	0.9	1.0	0.8

Table 5.7

for the particles, in the azimuthal direction, remain relatively constant as the Reynolds number increases, with the values at 25 diameters downstream from the injection tube being greater than the values 5 diameters downstream from injection.

In Figures 5.25 and 5.26 the linear fits for the non-dimensional rms velocities for the particles in the r and θ directions are plotted for distances of 5 and 25 diameters downstream from injection, respectively. The mean values for the non-dimensionalized rms velocities of the particles are listed in Table 5.8.

Both Figure 5.25 and Table 5.8 show no systematic relation between the radial and azimuthal fluctuations of the particle velocities 5 diameters downstream from injection. Figure 5.26 and Table 5.8 show the radial rms velocities of the particles to be smaller than the azimuthal rms velocities, for all Reynolds numbers at a position 25 diameters downstream from the injection tube. The lower value of $(\overline{v_r'^2})^{\frac{1}{2}}/v^*$ relative to $(\overline{v_\theta'^2})^{\frac{1}{2}}/v^*$ for the particles is the same relation that was seen in the water measurements at the two largest values of Reynolds number.

5.5 Particle Diffusion

Measurements on the diffusion of the PVC particles injected into the flow were made by using the LDA and by physically trapping the particles. The particle distribu-

RADIAL AND AZIMUTHAL-RMS-VELOCITY PROFILES 5 DIAMETERS FROM INJECTION

-------- Radial fluctuation profile

— — — Azimuthal fluctuation profile

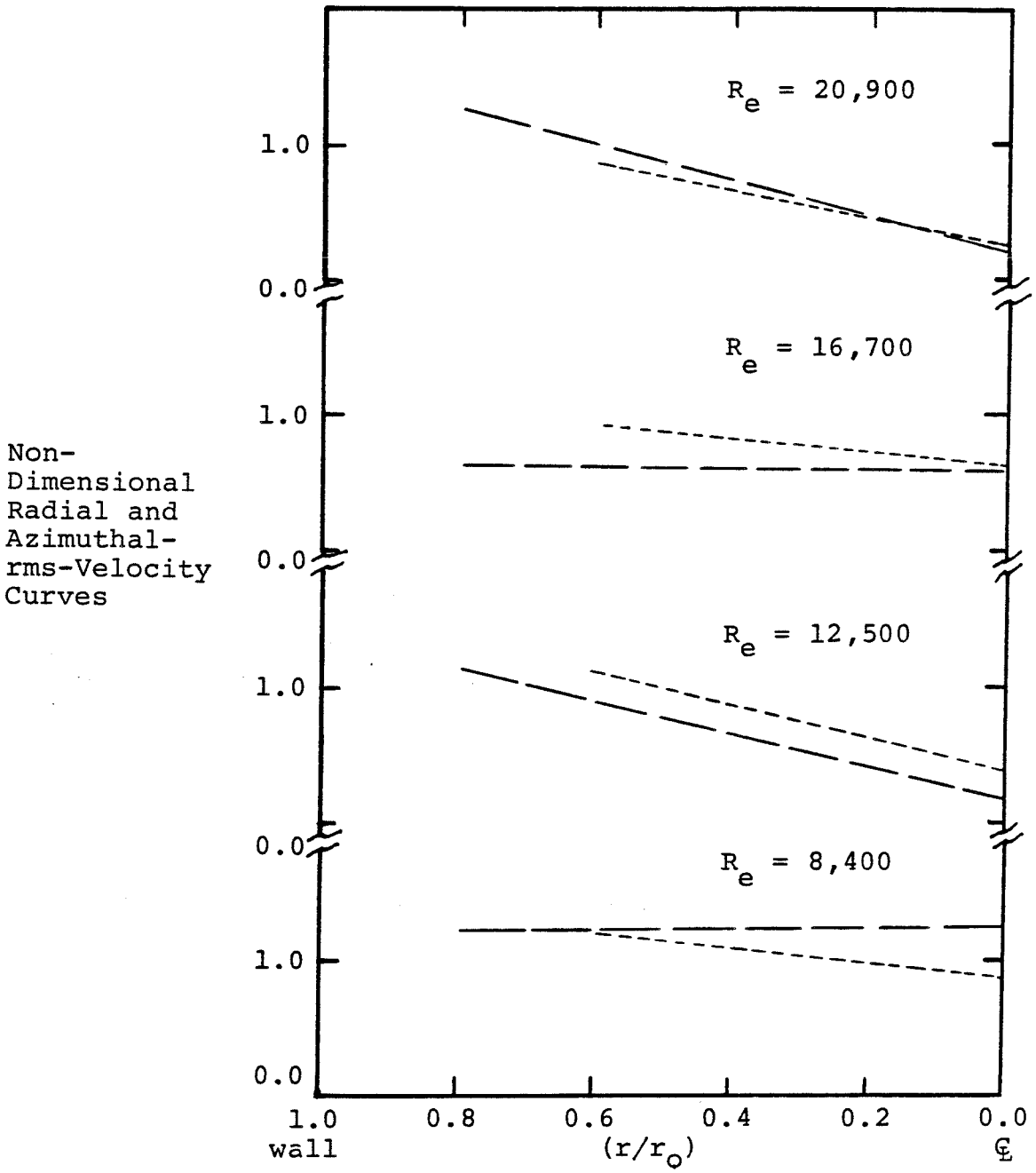

Figure 5.25

RADIAL AND AZIMUTHAL-RMS-VELOCITY PROFILES 25 DIAMETERS FROM INJECTION

--------- Radial fluctuation profile

— — — Azimuthal fluctuation profile

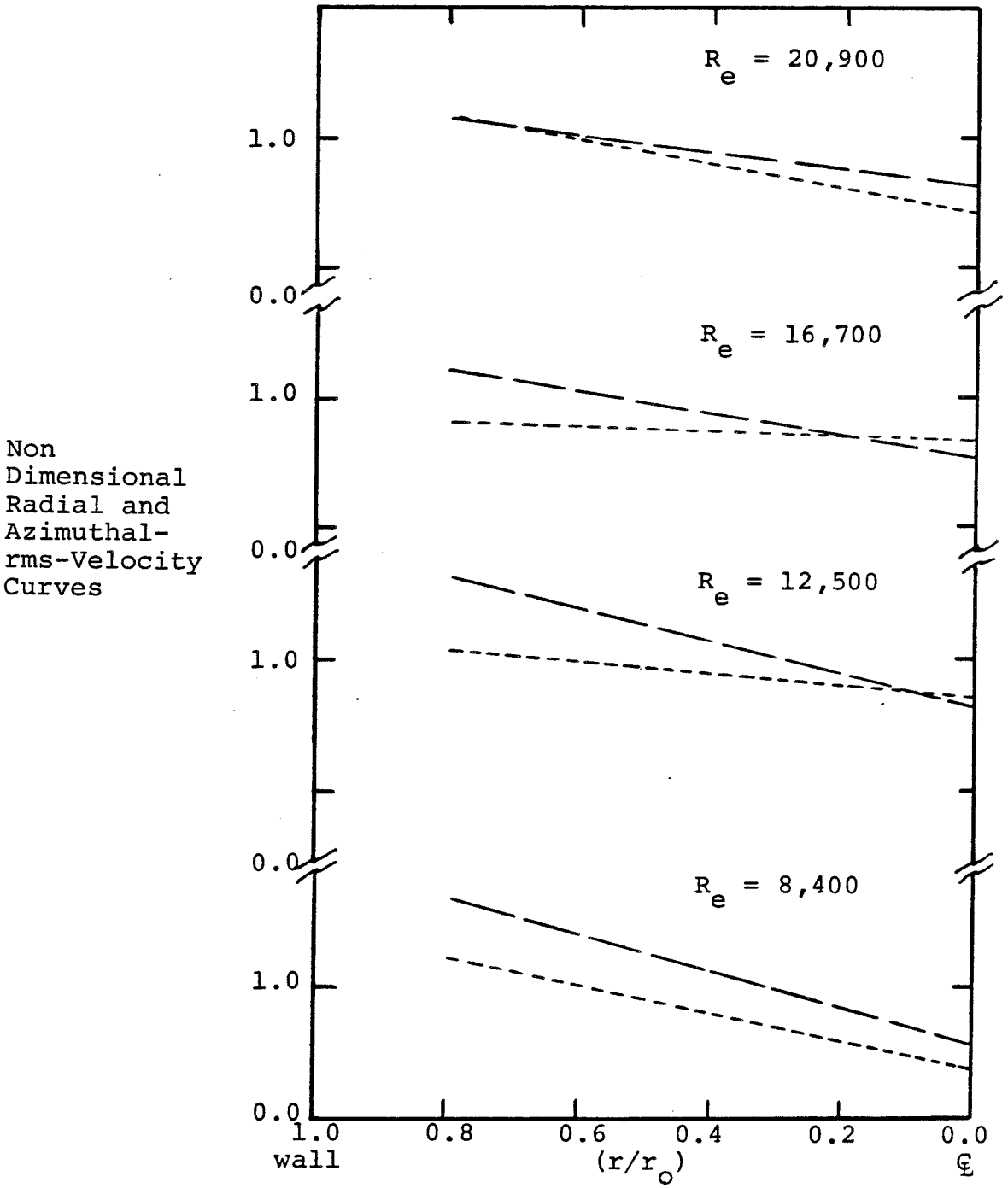

Figure 5.26

AVERAGED VALUES OF THE NON-DIMENSIONAL RMS VELOCITIES OF THE PARTICLES IN THE RADIAL AND AZIMUTHAL DIRECTIONS AT BOTH 5 AND 25 DIAMETERS FROM INJECTION

R_e	5 Diameters From Injection		25 Diameters From Injection	
$(DV_{avg}\rho)/\mu$	r	θ	r	θ
8,400	1.0	1.1	0.9	1.1
12,500	1.0	0.8	1.0	1.1
16,700	0.9	0.8	0.9	0.9
20,900	0.8	0.9	0.9	1.0

Table 5.8

tions across the channel were measured at distances ranging from 2 to 16 diameters downstream from injection, with the time for diffusion being defined as

$$t = (V_{avg})(z). \tag{5.1}$$

V_{avg} is the average velocity of the water and z is the distance from the injection tube at which the particle distribution was measured. The shape of the the curve describing the diffusion of a contaminant in the core region of turbulent pipe flow has been determined by experiments (5-2, 5-4) to be gaussian. Figure 2.1 shows the curve that is obtained by plotting the variance of the gaussian distribution describing the concentration of the contaminant in the core region of turbulent pipe flow versus the time of diffusion. By using a gaussian distribution to fit the data for the concentration of the PVC particles across the tube, the standard deviation σ, of the concentration profile was determined. Figures 5.27 through 5.30 show the increase of σ^2 as the diffusion time increases.

In all four figures the data was fitted by the use of two different curves. During the initial time of diffusion, shown by the dashed line, the particles diffuse in a manner that can be described by Equations 2.22 through 2.27. After the initial diffusion, the rate of increase

INCREASE OF THE VARIANCE OF THE GAUSSIAN CURVE DESCRIBING THE PVC-PARTICLE DISTRIBUTION ACROSS THE CHANNEL

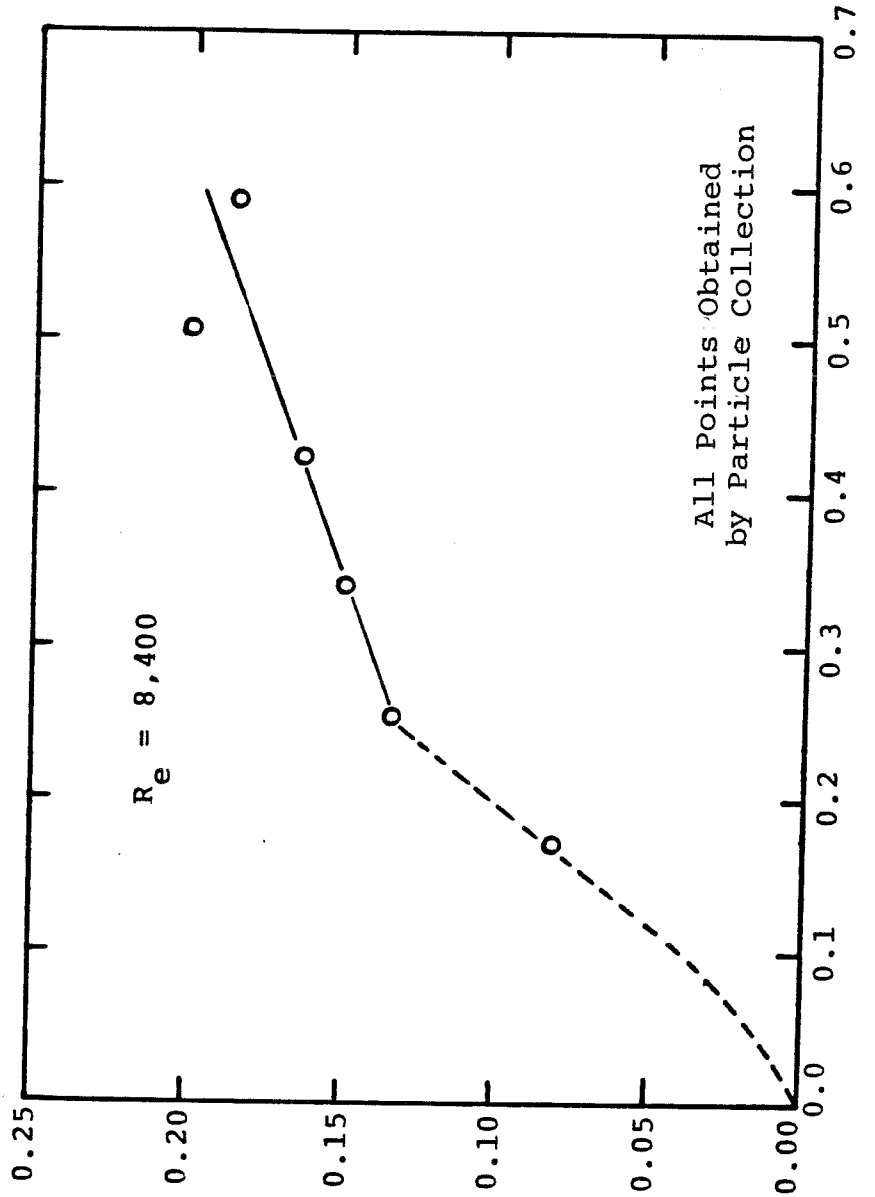

Figure 5.27

INCREASE OF THE VARIANCE OF THE GAUSSIAN CURVE DESCRIBING THE PVC-PARTICLE DISTRIBUTION ACROSS THE CHANNEL

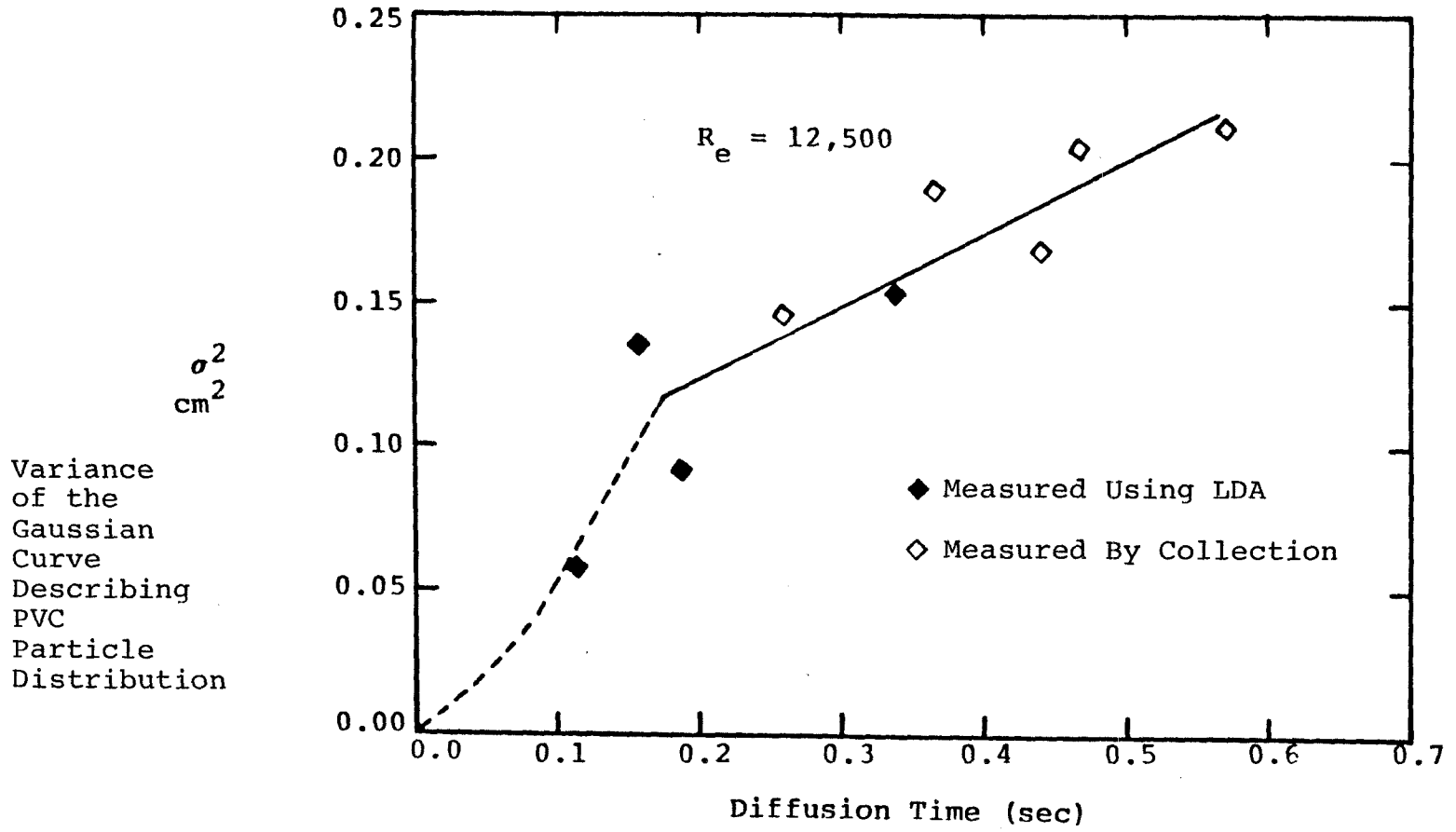

Figure 5.28

INCREASE OF THE VARIANCE OF THE GAUSSIAN CURVE DESCRIBING THE PVC-PARTICLE DISTRIBUTION ACROSS THE CHANNEL

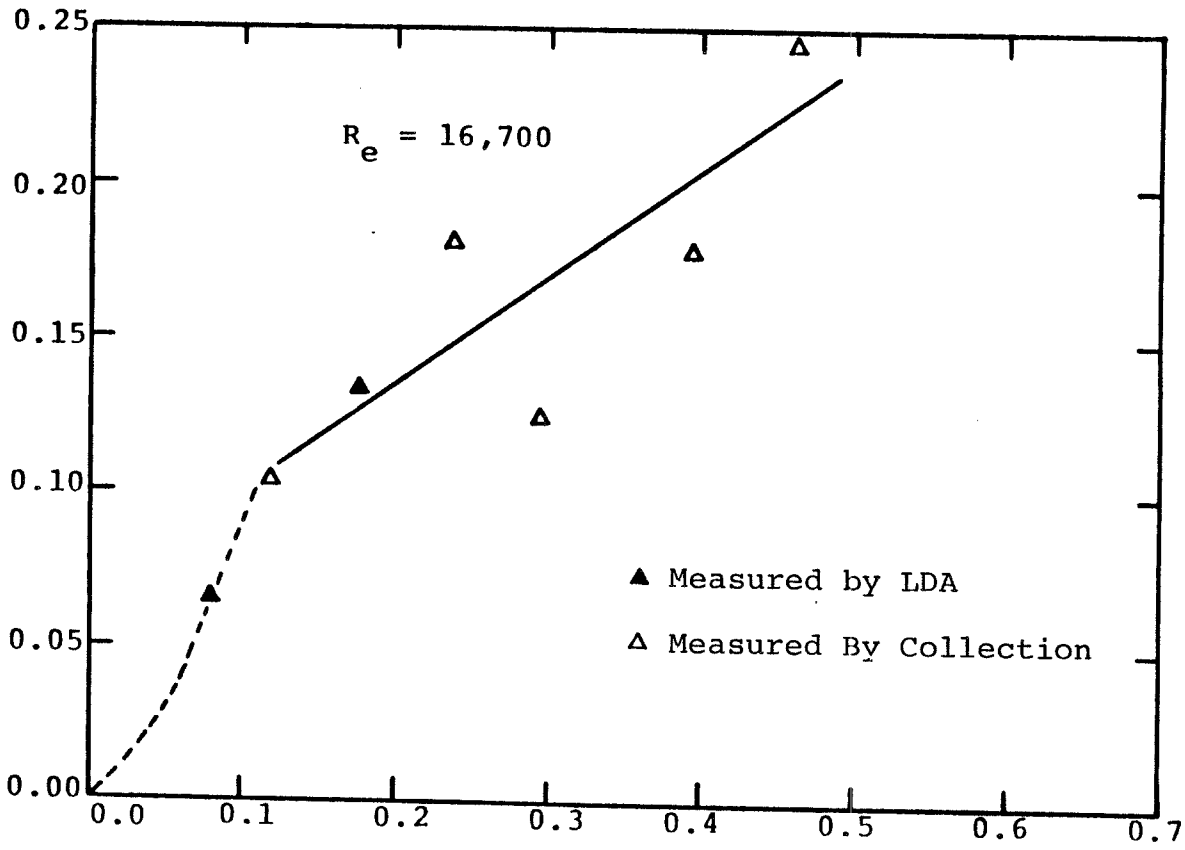

σ^2 cm^2

Variance of the Gaussian Curve Describing PVC Particle Distribution

Figure 5.29

INCREASE OF THE VARIANCE OF THE GAUSSIAN CURVE DESCRIBING THE PVC-PARTICLE DISTRIBUTION ACROSS THE CHANNEL

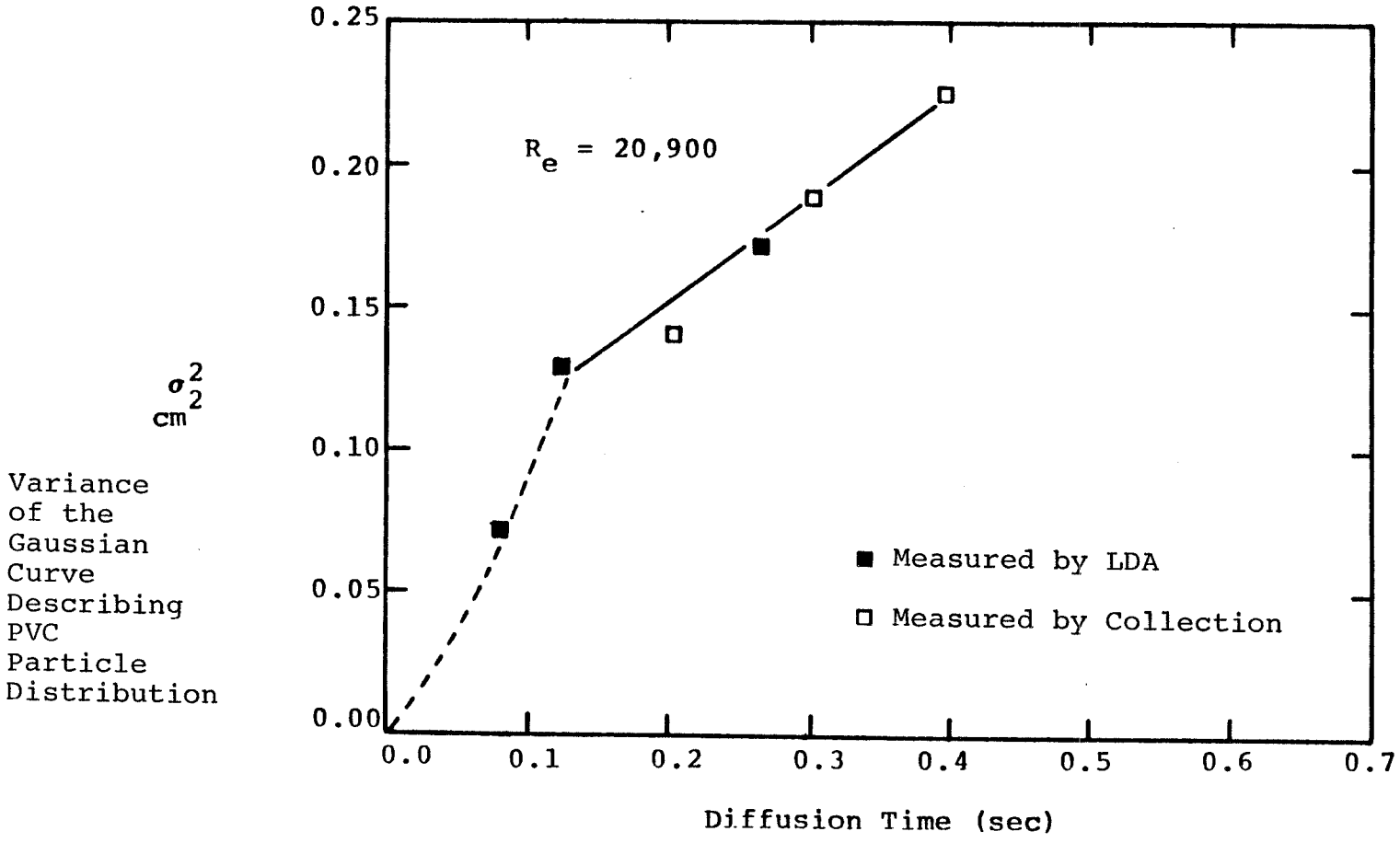

Figure 5.30

of the variance, σ^2, decreases from that shown by the dashed curve. In this second region, a straight line was fitted through the data and is shown as a solid line in all four figures.

During the initial diffusion times in Figures 5.27 through 5.30, the dashed lines through the origin and lower data points were found by using Equation 2.33. The correlation coefficient, $R_p(\omega)$, was assumed to decay exponentially in time,

$$R_p(\omega) = e^{-t/T_1}. \tag{5.2}$$

Although this form of the correlation coefficient does not exhibit the exact behavior of experimentally determined correlation coefficients, several investigators (5-2, 5-5) have shown Equation 5.2 to be good for fitting diffusion data. In using Equation 2.23 a value of $\overline{u_{1a}'^2}$ was needed. First it was assumed that the Lagrangian and Eulerian velocity fluctuations were equal. Finally, since the initial diffusion of the particles occurred in the central portion of the channel, the value of $\overline{u_{1a}'^2}$ was set equal to the average of the r, e, and z rms velocities of the particles measured 5 diameters downstream from injection,

$$\overline{u_{1a}'^2} = 1/3(\overline{v_z'^2} + \overline{v_e'^2} + \overline{v_r'^2}). \tag{5.3}$$

Once the curve had been fitted through the data by finding

the best value of T_1, the eddy diffusion coefficient, E_{ds}, was calculated from Equation 2.27.

Groenhof (5-4) measured the eddy diffusion coefficient, E_d, for an NaCl solution injected ito the core region of turbulent pipe-flow. He found that by non-dimensionalizing the eddy diffusion coefficient, the values of the dimensionless diffusion coefficient, a_d, were 0.04 for all Reynolds numbers used (R_e = 25,800 to 74,900). The non-dimensional diffusion coefficient, a_d, is defined as

$$a_d = E_d/(v^*D), \qquad (5.4)$$

where: v^* = friction velocity,

and D = pipe diameter

Groenhof also calculated the values of a_d from data of other investigators. He found a_d ranged from 0.03 to 0.04. The eddy diffusion coefficient of particles have been determined by several investigators for diffusion in the core region of pipe-flow. Table 5.9 shows the values of the non-dimensional eddy-diffusion coefficient, a_{ds}, for several different particles. Table 5.10 shows the values of E_{ds} and a_{ds} calculated from the initial region of diffusion shown by the dashed lines in Figures 5.27 through 5.30. The values of a_{ds} in Table 5.10 are constant at 0.06 over the range of Reynolds numbers used. This value of a_{ds} = 0.06 is greater than the value of a_d = 0.04 obtained by

NON-DIMENSIONAL EDDY-DIFFUSION COEFFICIENTS, a_{ds}, MEASURED BY OTHER INVESTIGATORS IN THE CORE REGION OF TURBULENT PIPE FLOW

Particles	Size (Microns)	gm/cc	a_{ds}	Ref.
Heptane Drops	642-809	0.695	0.021	(5-2)
CCL_4 Drops	529-946	1.595	0.015	(5-2)
Polythene Spheres	5.08×10^3	1.25	0.17	(5-1)
Plastic Spheres	2.54×10^3	1.035-1.126	0.19	(5-9)
Plastic Spheres	210-290	1.126	0.13	(5-6)

Table 5.9

Groenhof, but is only 1/2 to 1/3 as large as the values of a_{ds} for the solid spheres listed in Table 5.9. It appears that the 120-micron PVC particles behave more like the tracer than the larger spheres. The final column in Table 5.10 lists the turbulent Schmidt numbers, S_{C_T}, calculated for the initial period of particle diffusion. An averaged value of ν_e, calculated over the interior region of the pipe, was used in determing S_{C_T}. Comparison of the calculated Schmidt numbers with values obtained by the investigators listed in Table 5.9 was not possible because the eddy viscosity was not evaluated in those studies. For the four flow-rates studied in the present work, the value of S_{C_T}, determined for the initial period of diffusion, was essentially constant at $S_{C_T} = 0.45$.

Figures 5.27 through 5.30 show the diffusion of the particles becoming inhibited once the particles spread beyond the central region of the flow. The factors contributing to this decrease in the diffusion rate of the particles are the presence of a velocity gradient and a correlation between velocity fluctuations in the r and z directions. Corrsin (5-3) developed equations for prediction of the diffusion of a substance in a two-dimensional shear field of infinite extent. In these equations, Corrsin assumed that there was no correlation between in instantaneous velocities existing in the shear field. Lee and

EDDY-DIFFUSION COEFFICIENTS, E_{ds}, NON-DIMENSIONAL EDDY-DIFFUSION COEFFICIENTS, a_{ds}, AND TURBULENT SCHMIDT NUMBERS, S_{C_T}, MEASURED IN THE PRESENT STUDY DURING THE INITIAL TIME OF DIFFUSION

$(DV_{avg}\rho)/\mu$	E_{ds} cm^2/sec	a_{ds} ____	S_{C_T} ν_e/E_{ds}
8,400	0.31	0.06	0.45
12,500	0.48	0.06	0.42
16,700	0.66	0.06	0.47
20,900	0.72	0.06	0.47

Table 5.10

Dukler (5-8) extended the equations of Corrsin to include the case of complete correlation between the instantaneous velocities. Figure 5.31 shows two curves describing the diffusion of a contaminant in the two dimensional shear field. The labels on the curves refer to the degree of correlation existing between the instantaneous velocities. From the curves in Figure 5.31 it can be seen that the correlation between velocities acts to inhibit the diffusion of a contaminant, characterized by the increase of $(\overline{y_1^2})^{\frac{1}{2}}$.

In the present study of particle diffusion in pipe flow, the effect of the velocity gradient and correlation between the fluctuating velocities in the r and z directions is thought to inhibit the diffusion of the particles as is shown by the smaller slope of the solid line when compared with the dashed line in Figures 5.27 through 5.30. In Figures 5.27 and 5.28 the particles were diffusing toward the wall at all diffusion times measured. In Figures 5.29 and 5.30 the particles achieved a uniform concentraion across the tube before diffusion times of 0.5 sec could be reached.

The influence of the velocity correlations on the diffusion of the particles is first observed in the four figures when σ^2 reaches a value between 0.10 and 0.15. A value of the non-dimensional Reynolds stress was calculated

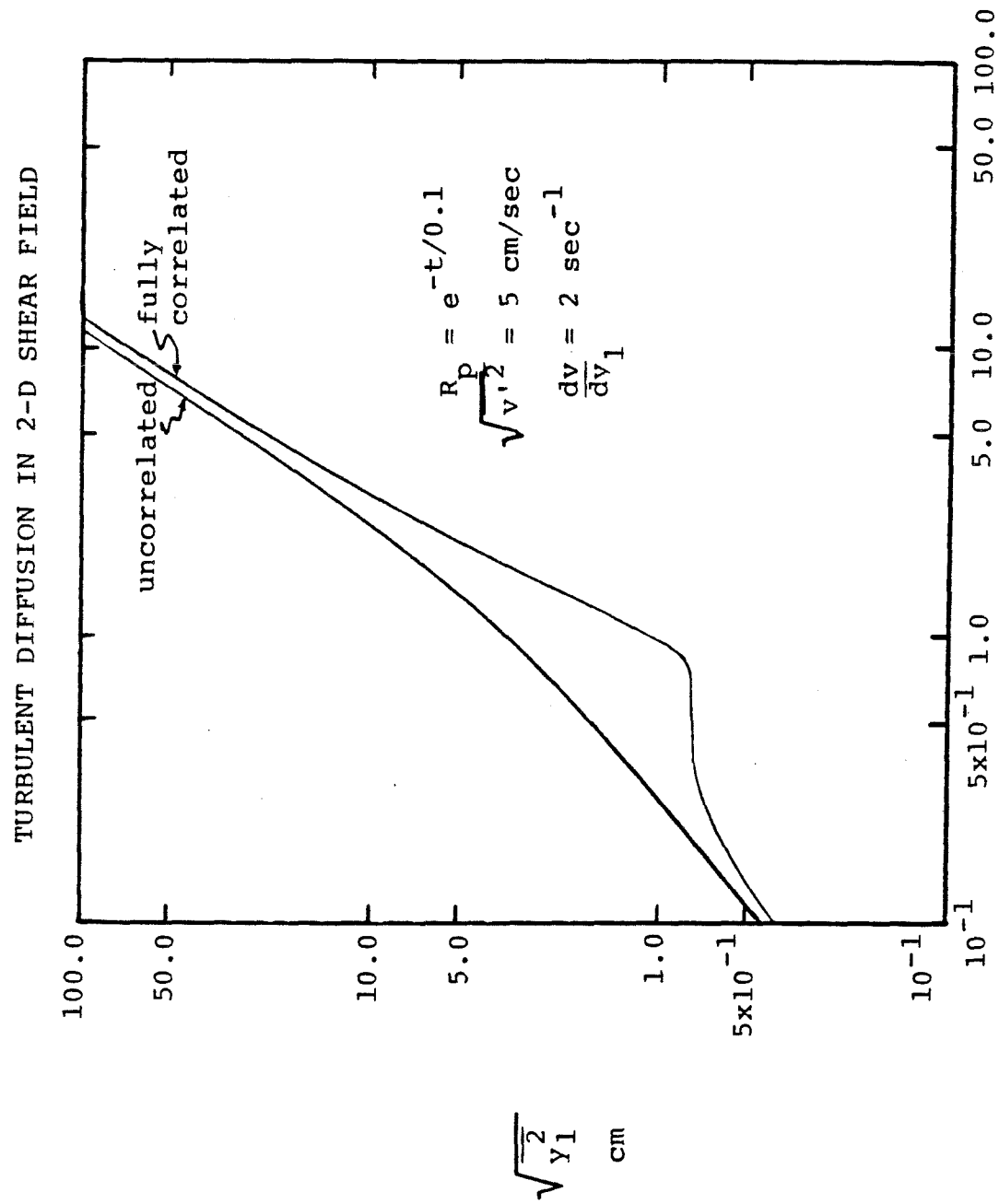
TURBULENT DIFFUSION IN 2-D SHEAR FIELD
uncorrelated
fully correlated
$R_p = e^{-t/0.1}$
$\sqrt{v'^2} = 5$ cm/sec
$\frac{dv}{dy_1} = 2$ sec^{-1}
$\sqrt{\overline{y_1^2}}$ cm
100.0
50.0
10.0
5.0
1.0
$5x10^{-1}$
10^{-1}
10^{-1}
$5x10^{-1}$
1.0
5.0
10.0
50.0
100.0
Time (sec)

Figure 5.31

at the position $r/r_o = \sigma$ where σ was the square root of the value of σ^2 where the change in the slopes in Figures 5.27 through 5.30 occurred. In addition to calculating $\overline{v_r' v_z'}/v^{*2}$, values of the eddy-diffusion coefficient, E_{ds}', and the non-dimensional eddy-diffusion coefficient, a_{ds}', were determined from the slopes of the linear fit through this area of the pipe where the correlation between fluctuating velocities had become important. Table 5.11 lists the values of $\overline{v_r' v_z'}/v^{*2}$, E_{ds}', and a_{ds}', that were calculated. From Table 5.11 it is seem that a_{ds}' is a constant over the range of Reynolds numbers used in the experiment. It is also seen in Table 5.11 that the value of the non-dimensional Reynolds stress, at $r/r_o = \sigma$, is approximately equal to 0.3. The turbulent Schmidt numbers, S_{C_T}', calculated from E_{ds}' and the averaged value of eddy viscosity across the entire pipe are listed in the final column of Table 5.11. The values of S_{C_T}' are larger than those listed in Table 5.10, which is due to the E_{ds}' being smaller than E_{ds}. The listed values of S_{C_T}' are relatively constant for the four flow-rates as was seen in Table 5.9.

From Figures 5.27 through 5.30 and Table 5.9 it appears that during the initial phase of diffusion, the particles behave as if the turbulence were isotropic and homogeneous. The non-dimensional diffusion coefficient in this phase was $a_{ds} = 0.06$. When the particles had diffused far enough for

VALUES OF THE EDDY-DIFFUSION COEFFICIENT, E'_{ds}, NON-DIMENSIONAL EDDY-DIFFUSION COEFFICIENT, a'_{ds}, AND TURBULENT SCHMIDT NUMBERS, S_{C_T}, IN THE REGION OF FLOW WHERE THE CORRELATION AMONG VELOCITY FLUCTUATIONS BECOMES IMPORTANT, AND VALUES OF THE NON-DIMENSIONAL REYNOLDS STRESS EVALUATED AT $r/r_o = \sigma$, WHERE σ^2 IS THAT AT WHICH THE DIFFUSION OF THE PARTICLES BECOMES INHIBITED

R_e $(DV_{avg}\rho)/\mu$	Non-Dimensional Reynolds Stress $\overline{v'_r v'_z}/v^{*2}$	E'_{ds} cm^2/sec	a'_{ds} ____	S_{C_T} ν_e/E_{ds}
8,400	0.31	0.127	0.02	1.39
12,500	0.29	0.165	0.02	1.54
16,700	0.28	0.219	0.02	1.54
20,900	0.30	0.245	0.02	1.56

Table 5.11

the correlation between the velocity fluctuations in the r and z directions to be felt, the rate of increase of σ^2 drops by 1/3 with the non-dimensional diffusion coefficient for this region, a'_{ds}, being equal to 0.02.

5.6 Summary for Chapter 5

A summary for each section of Chapter 5 is given below.

5.1: Characterization of the particles was obtained by using their mean-length scale, $\ell = (\ell_1 \ \ell_2,)^{\frac{1}{2}}$, their density and their mean-settling velocity. A gaussian curve with mean of 120 microns and standard deviation of 26 microns was fit through the size distribution of the particles. The particle density was measured as 1.15 gm/cm^3 and their mean-settling velocity was 0.38 cm/sec.

5.2: Disturbance of the flow was caused by the presence of the injection tube in the flow channel, as could be seen in Figures 5.3 through 5.10. The velocity across the horizontal centerline were flattened, and at 1 diameter downstream from the end of the injection tube there was an indentation at the velocity of the undisturbed centerpoint. This indentation was thought to be caused by the disturbance of the flow arising from that portion of the injection tube lying along the channel centerline. All of the profiles had redeveloped by 25 diameters downstream from the injection tube.

5.3: Measurements of the mean velocities of the particles in the axial direction were made at 5 and 25 diameters downstream from the injection tube. These velocity profiles were measured across the horizontal centerline of the flow channel. From the mean velocities calculated over the region $0.0 \leq r/r_o \leq 0.8$ for both the particles and the water, it appeared that at 5 diameters downstream from injection the particles and fluid moved at the same velocities while at 25 diameters from injection the particle-velocity profile for the three highest flow-rates had not become fully developed as had the fluid-velocity profiles. The values of R_{ep} calculated for the four flow-rates ranged from 40 to 100, and the Kolmogorov-length scale of the turbulence ranged from 50 to 30 microns. The fact that the particle-velocity profiles did not develop as fast as the fluid-velocity profiles, and that the particles were larger than the microscale of turbulence indicate that the particles did not follow all the eddies present in the turbulent flow.

5.4: Measurements of $(\overline{v_z'^2})^{\frac{1}{2}}$, $(\overline{v_r'^2})^{\frac{1}{2}}$, and $(\overline{v_\theta'^2})^{\frac{1}{2}}$ were made at the positions of 5 and 25 diameters downstream from the injection tube. The values of $(\overline{v_z'^2})^{\frac{1}{2}}$ measured showed the rms velocities for the particles at 5 diameters downstream from injection to be larger than the rms velocities for the liquid phase. The rms velocities of the liquid-phase were, however, greater than the rms velocities of the

particles at 25 diameters from injection The comparison of the particle data at 25 diameters from injection with the water data also demonstrates that the particles don't follow all of the eddies in the turbulence. If the same trend were to occur at 5 diameters from injection, then the corresponding rms velocities of the water would be larger than the measured particle velocities.

Values of $(\overline{v_r'^2})^{\frac{1}{2}}$ and $(\overline{v_\theta'^2})^{\frac{1}{2}}$ for the particles were also measured at 5 and 25 diameters from injection. Unlike the axial-rms-velocity measurements, the values of the rms velocities for the particles in the r and θ directions did not show a constant trend with the values taken 5 diameters from injection being greater than those at 25 diameters from injection. It was also noted that the non-dimensionalized rms velocities in the r and θ directions remained fairly constant for the four flow-rates used. Over the same range of flow-rates, the rms velocities for the water in the r and θ directions decreased noticeably as the Reynolds number increased. Finally it was observed that the measurements of $(\overline{v_\theta'^2})^{\frac{1}{2}}$ and $(\overline{v_r'^2})^{\frac{1}{2}}$ at 25 diameters from injection showed the rms value in the θ direction to be greater than that in the r direction for all four flow-rates. The relationship, $(\overline{v_\theta'^2})^{\frac{1}{2}} \quad (\overline{v_r'^2})^{\frac{1}{2}}$, is the same that was observed in the data for the two highest flow-rates for water.

5.5: The radial diffusion of the particles injected into the center of the channel was found to be divided into two regions. The initial diffusion could be described using Taylor's expressions. In the first region, the values of the eddy-diffusion coefficients for the particles were determined to be 0.31, 0.48, 0.66, and 0.72 cm^2/sec for Reynolds numbers of 8,400, 12,500, 16,700, and 20,900, respectively. When the eddy-diffusion coefficient were non-dimensionalized with respect to the pipe diameter and the friction velocity, a constant value of $a_{ds} = 0.06$ ($a_{ds} = E_{ds}/v*D$) was calculated for all four flow-rates. The value of $a_{ds} = 0.06$ can be compared with values of non-dimensional eddy-diffusion coefficients obtained by other investigators for the diffusion of tracer material and particles in the core region of turbulent pipe flow. Groenhof (5-4) found values of a_{ds} ranging from 0.13 to 0.19 for particles ranging in size from 250 microns to 0.5 cm (5-1, 5-6, 5-9). The value of $a_{ds} = 0.06$ for the 120-micron PVC particles used in the present work indicates the particles initially diffuse at an intermediate rate between that of tracer material and larger heavier particles.

Once the particles had moved into the region where the correlation between velocity fluctuations starts to influence their motion, the diffusion of the particles de-

creases sharply. In this region of inhibited diffusion the values of $d(\sigma^2)/dt$ dropped by 2/3 for all four flow-rates. The values for the eddy-diffusion coefficients for the particles in this area of inhibited diffusion were 0.13, 0.17, 0.22, and 0.25 cm^2/sec for Reynolds numbers of 8,400, 12,500, 16,700 and 20,900, respectively. These four values of the eddy-diffusion coefficient were non-dimensionalized and gave $a'_{ds} = 0.02$. Comparison of this non-dimensional eddy-diffusion coefficient with other investigators is not possible because other studies of diffusion in this region have not been made.

LITERATURE CITED

(5-1) Barnard, B. J. S., Binnie, A. M., JFM, 15, 35 (1963).

(5-2) Calabrese, R. V., Middleman, S., AIChEJ, 25, 1025 (1979).

(5-3) Corrsin, S., Proc. Iowa Thermo. Symp., 5 (1953).

(5-4) Groenhof, H. C., Chem. Eng. Sci., 25, 1005 (1970).

(5-5) Hanratty, T. J., Latinen, G., Wilhelm, R. H., AIChEJ, 2, 372 (1956).

(5-6) Karabelas, A. J., AIChEJ, 23, 426 (1977).

(5-7) Kuboi, R., Komasawa, I., Otake, T., Chem. Eng. Sci., 29, 651 (1974).

(5-8) Lee, N., Dukler, A. F., AIChEJ, 22, 449 (1976).

(5-9) Sharp, B. B., O'Neill, I. C., JFM, 45, 575 (1971).

(5-10) Taylor, G. I., Proc. London Math Soc., 20A, 196 (1921).

CHAPTER 6

SUMMARY AND RECOMMENDATIONS

6.1 Summary

The purpose of the present study was to investigate the motion and diffusion of non-neutrally buoyant 120-micron PVC particles as they were carried along in turbulent pipe-flow. There were four flow-rates used in the experiments: 167, 250, 232, and 417 cm^3/sec with corresponding Reynolds numbers of 8,400, 12,500, 16,700 and 20,900. The liquid was de-ionized water, and the flow channel was Plexiglas tubing with a diameter of 2.54 cm. The experimental measurements that were made included rms velocities in the r, θ and z directions for the particles as a function of radial position in the channel and the eddy-diffusion coefficients for the particles in the region of turbulent pipe-flow where the velocity gradients and Reynolds stresses were of consequence. Previous studies of particle diffusion in pipe-flow were for larger particles and measured diffusion coefficients for the particles only in the region of the pipe where the velocity gradients and Reynolds stresses were small. The evaluation of the rms velocities of the particles in previous studies was obtained by either measuring the axial component of particle velocity at the pipe's center or by calculating mean values of the rms velocities of the particles

over the central region of the pipe.

Before the data on particle motion and diffusion were obtained, the mean and rms velocities of the continuous-phase in the r, θ, and z directions were measured using the LDA. These velocities were measured at a position in the channel where the flow had become fully developed. The purpose of measuring the mean and rms velocities of the fluid was to characterize the flow and to provide a means of comparison for the data taken on the velocities and diffusion of the 120-micron particles.

The mean axial velocities of the water were fitted to a logarithmic velocity profile, and in the range from $y^+ = 50$ to 550 the best fit of a line was found to be described as

$$u^+ = 4.0 + 2.9 \ln y^+. \qquad (4.1)$$

In the region from $y^+ = 15$ to 50 the data points fell below the curve predicted by Equation 4.1 (Figure 4.13). These data were interpreted as showing the buffer region extending out to $y^+ = 50$. Values of the extent of the buffer region determined by other investigators are listed in Section 4.6. These values for the extent of the buffer region range from $y^+ = 26$ to $y^+ = 70$. Differences in the measurements of the extent of the buffer region could be due to possible disturbances of the flow by invasive measurements

and to effects of the pipe-wall curvature on the flow in the near vicinity of the wall.

Values of the Reynolds stress, $\overline{v_r' v_z'}$, were calculated by using Equation 2.9, and it was found that the non-dimensionalized Reynolds stresses, $\overline{v_r' v_z'}/v^{*2}$, for all four flow-rates fell on a single line over the region $0.72 \geq r/r_o \geq 0.0$. By using the values of $\overline{v_r' v_z'}$ that were calculated, and the values of the velocity gradients determined from the experimental measurements, the kinematic eddy viscosities were calculated for the four flow-rates. The curves describing the variation of ν_e across the channel all behaved similarly. They increase from zero at r/r_o = 1.0 (the channel wall) to maximum values of 0.22, 0.33, 0.43, and 0.46 cm^2/sec for the flow with Reynolds numbers of 8,400, 12,500, 16,700, and 20,900, respectively. Maximum values of the eddy viscosities for the four flow-rates occurred at $r/r_o = 0.63$. The magnitude of ν_e then decreased until the center of the channel was reached. The values of the eddy viscosities for the four flows at $r/r_o = 0.0$ were 0.08, 0.16, 0.28, and 0.33 cm^2/sec, respectively.

Measurements of rms velocities in the r, e, and z directions were made on the flowing water. It was found that the r and e components collapsed to the same values at the channel center. The z components was always larger than the r and e components, with the closest approach occur-

ring at the center of the tube. At the two highest flowrates R_e = 16,700 and 20,900, the r component did not increase to as large a value as to θ component as the wall was approached. The smaller values of the radial component as compared with the azimuthal component show that the wall is damping the fluctuations of the radial velocity. A comparison of the axial-rms velocities at the center of the channel was made with values obtained by other investigators. Figure 4.22 shows this comparison. Values of $\overline{(v_z'^2)}^{\frac{1}{2}}/\bar{U}_{\mathfrak{L}}$ is the centerline velocity in the axial direction, that were measured non-invasively are greater than those measured using invasive methods such as hot-wire or hot-film probes. This difference probably arises from the presence of the probe in the flow which can disturb the measurements that the probe is to make.

Once the fluid phase has been characterized, the velocities and diffusion coefficients of the particles were measured. The injection tube was found to disturb the velocity profiles of the fluid and particles in the first 5 diameters downstream from particle injection. The fluid velocity profiles had redeveloped by 25 diameters downstream from the injection tube, but the particle velocity profiles had not finished developing by this point in the flow. This lag in the development of the particle velocity profile, and the calculated values of the Kolmagorov length scales,

ranging from 50 to 30 microns, showed that the PVC particles did not follow all of the eddies present in the flow field.

The rms velocities of the PVC particles in the r, θ, and z directions were also measured. The values of $(\overline{v_z'^2})^{\frac{1}{2}}$ at 25 diameters downstream from the injection tube (the flow had re-developed by this point) were found to be smaller than the values of the rms velocities of the fluid in the z direction. Values of $(\overline{v_z'^2})^{\frac{1}{2}}$ at 5 diameters downstream from the end of the injection tube, however, were found to be larger than the fluid values. This increase in $(\overline{v_\theta'^2})^{\frac{1}{2}}$ for the particles at the 5 diameter position was attributed to an increase in the level of turbulence of the liquid brought about by the presence of the injection tube in the flow channel. The values of $(\overline{v_r'^2})^{\frac{1}{2}}$ and $(\overline{v_\theta'^2})^{\frac{1}{2}}$ for the particles as obtained at 5 and 25 diameters from the injection tube did not exhibit the relationship with the value at 5 diameters downstream from injection being greater than the value at 25 diameters from injection that was seen wtih the rms fluctuations in the z direction. It was seen instead that $(\overline{v_r'^2})^{\frac{1}{2}}/v^*$ remained fairly constant for the four flow-rates used. It was also determined that at 25 diameters downstream from injection, the values of $(\overline{v_r'^2})^{\frac{1}{2}}$ were less than those of $(\overline{v_\theta'^2})^{\frac{1}{2}}$ for all four flow-rates. This relationship is the same between r

and θ components that was seen for the rms values for the water at the two highest flow-rates.

The diffusion of the PVC particles from a point source located at the channel's center was found to be represented by two different diffusion coefficients. The initial spread of the PVC particles was fitted by the use of Equations 2.22 through 2.27. The eddy-diffusion coefficients for the particles in the first region were 0.31, 0.48, 0.66, and 0.72 cm^2/sec for the flows with Reynolds numbers of 8,400, 12,500, 16,700 and 20,900, respectively. These eddy-diffusion coefficients were non-dimensionalized with respect to the pipe diameter and the friction velocity, and the non-dimensional diffusion coefficient, $a_{ds} = E_{ds}/v^*D$, was found to be 0.06 for all four flow-rates. Values of a_d for tracer materials have been found to range from 0.03 to 0.04, while a_{ds} for larger particles (250 to 500 microns) was found to range from 0.13 to 0.19. It is therefore seen that in the initial region of diffusion the PVC particles behave in a manner in between the tracer material and the large particles. Once the value of the standard deviation, σ, describing the gaussian fit to the concentration profile, had reached the position in the channel where $\overline{v_r' v_z'}/v^{*2} \simeq 0.3$ the rate of diffusion of the particles was sharpely decreased. The eddy-diffusion coefficients evaluated in this region were 0.13, 0.17, 0.22, and 0.25 cm^2/sec for the four flows. When

these eddy diffusion coefficients were non-dimensionalized it was found that a'_{ds} was equal to 0.02 for all four flow-rates. There are no other data for comparison of the results obtained for the particle diffusion in the region of pipe flow where the velocity gradient and the correlation among the fluctuating velocities are important.

6.2 Recommendations

The studies carried out in this work were performed with the use of an LDA system. The measurements taken were of both mean and rms velocities of the liquid and particles and the changes in the concentration profiles of the particles as they flowed downstream from their injection point. There are several possible studies that could be carried out as extensions to the work presented in this thesis. Further experiments are suggested as follows:

1). The effect of particle density and size on the diffusion of particles in the turbulent flows studied in this work could be investigated. The rate of change of the variances, σ^2, describing the gaussian fit to the profile for the concentration distribution of the particles could be correlated with ρ_p and ℓ. From this data the relative radial position at which the inhibition in particle diffusion occurs could be studied as a function of particle inertia.

2). Simultaneous measurements of mean and rms velocities for the continuous and disperse-phases could be made by

fluorescently tagging the particles. Stevenson, et al. (6-2) measured velocities as great as 10 m/sec by detecting the fluorescent signal from tagged particles. An experiment of this type could differentiate between the Doppler signal generated by small scattering elements in the fluid and the signal generated by the particles.

3). The mean and rms velocities of both the continuous and disperse phases of a dilute suspension could be studied around the mechanical portions of artificial heart valves by using the LDA in the backscatter mode. In addition to the velocities of the particles, the concentration distribution of the particles could be measured. Measurements of this type would allow determination of the stresses acting on a particle as it moves through the heart valve.

4). The experiment described in 3) could be performed using concentrated ghost cell suspensions with fluorescently-tagged tracers among the particles. The measurement of velocities of ghost cells by use of fluorescent tracers has been shown to work at low flow-rates (6-1). Data obtained for the concentrated suspensions flowing through the heart valve could then be compared with the dilute-suspension data from 3).

5). The use of the PDP 11/34 computer for collecting and analyzing the velocity data from the LDA allows the calculation of Eulerian correlation coefficients for

both the liquid and the particles. The storage capability of the computer allows evaluation of particle data even when the particle concentrations are dilute. This storage capacity could be applied to any of the previous recommendations in this section.

LITERATURE CITED

(6-1) Chung, Ying Chee, PhD Thesis, California Institute of Technology, 1980.

(6-2) Stevenson, W. H., Santos, R., Mettler, S. C., App. Phys. Lett., 27 (7), 395 (1975).

APPENDIX A

The figures presented in Appendix A are plots of the particle distributions measured across the flow channel. The gaussian curves fitted through the data are those having the means and standard deviations calculated from the data.

PVC DISTRIBUTION ACROSS THE FLOW CHANNEL

DATA OBTAINED BY : PARTICLE COLLECTION

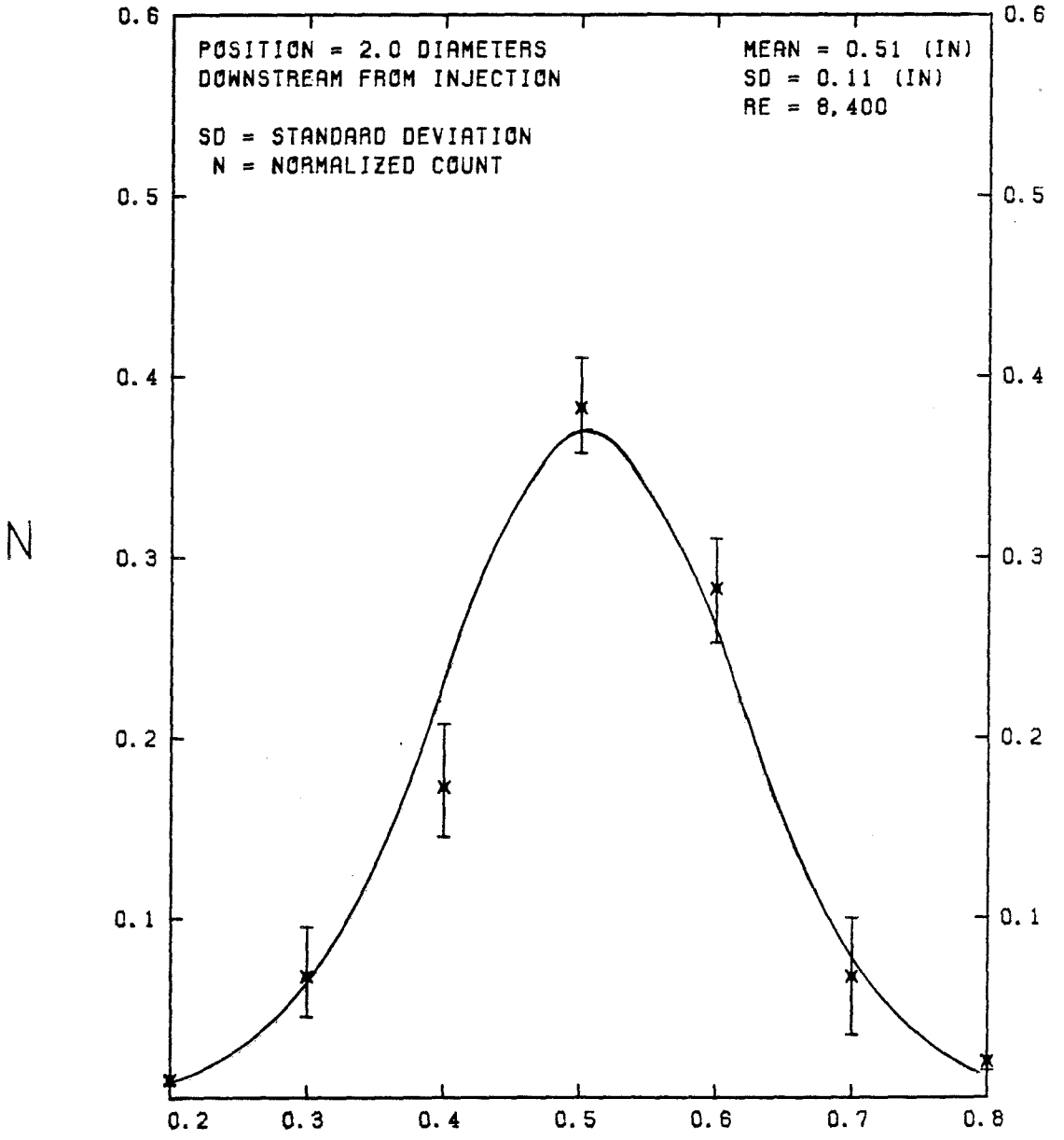

FIGURE A. 1

PVC DISTRIBUTION ACROSS THE FLOW CHANNEL

DATA OBTAINED BY : PARTICLE COLLECTION

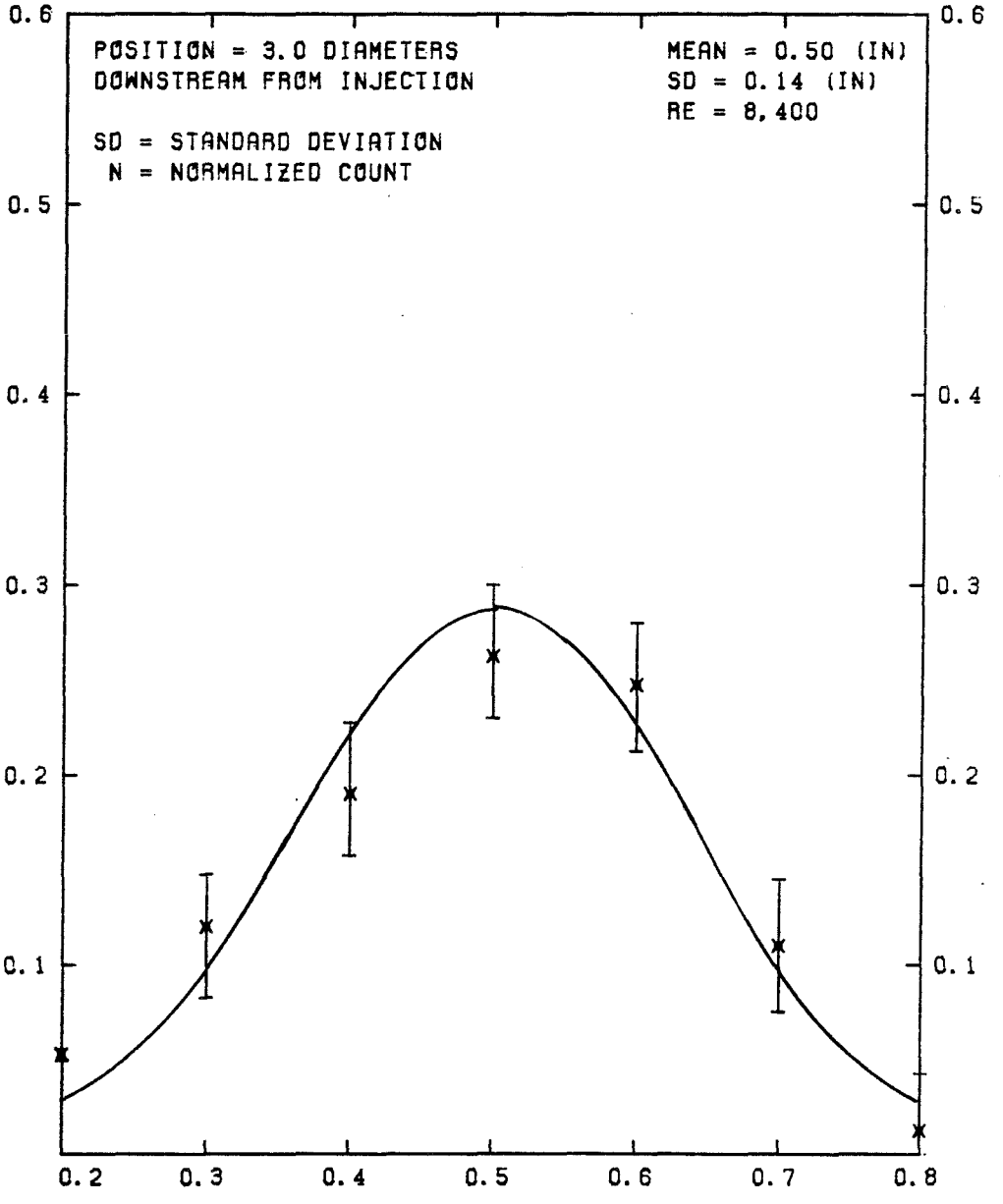

FIGURE A.2

PVC DISTRIBUTION ACROSS THE FLOW CHANNEL

DATA OBTAINED BY : PARTICLE COLLECTION

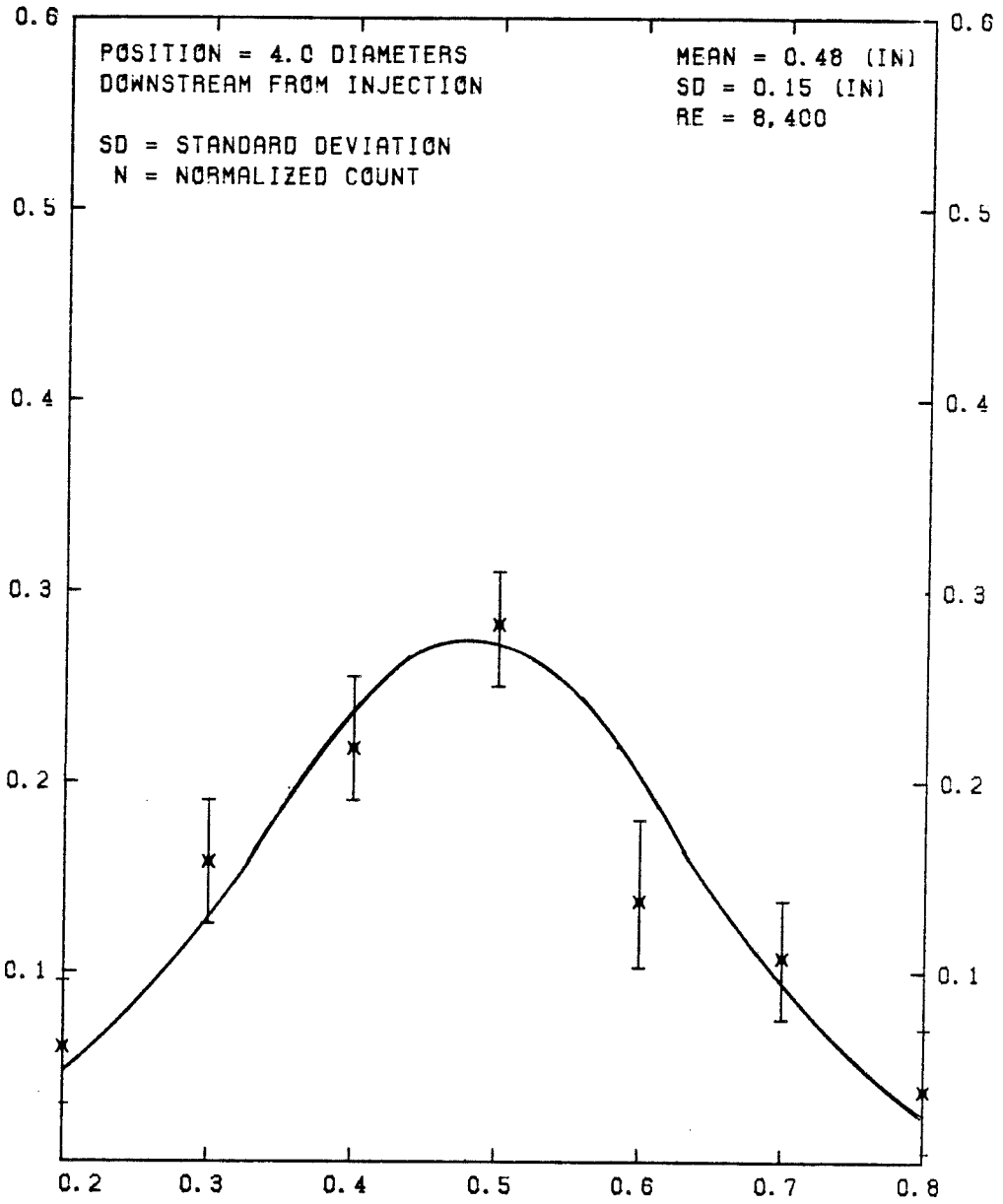

FIGURE A.3

PVC DISTRIBUTION ACROSS THE FLOW CHANNEL

DATA OBTAINED BY : PARTICLE COLLECTION

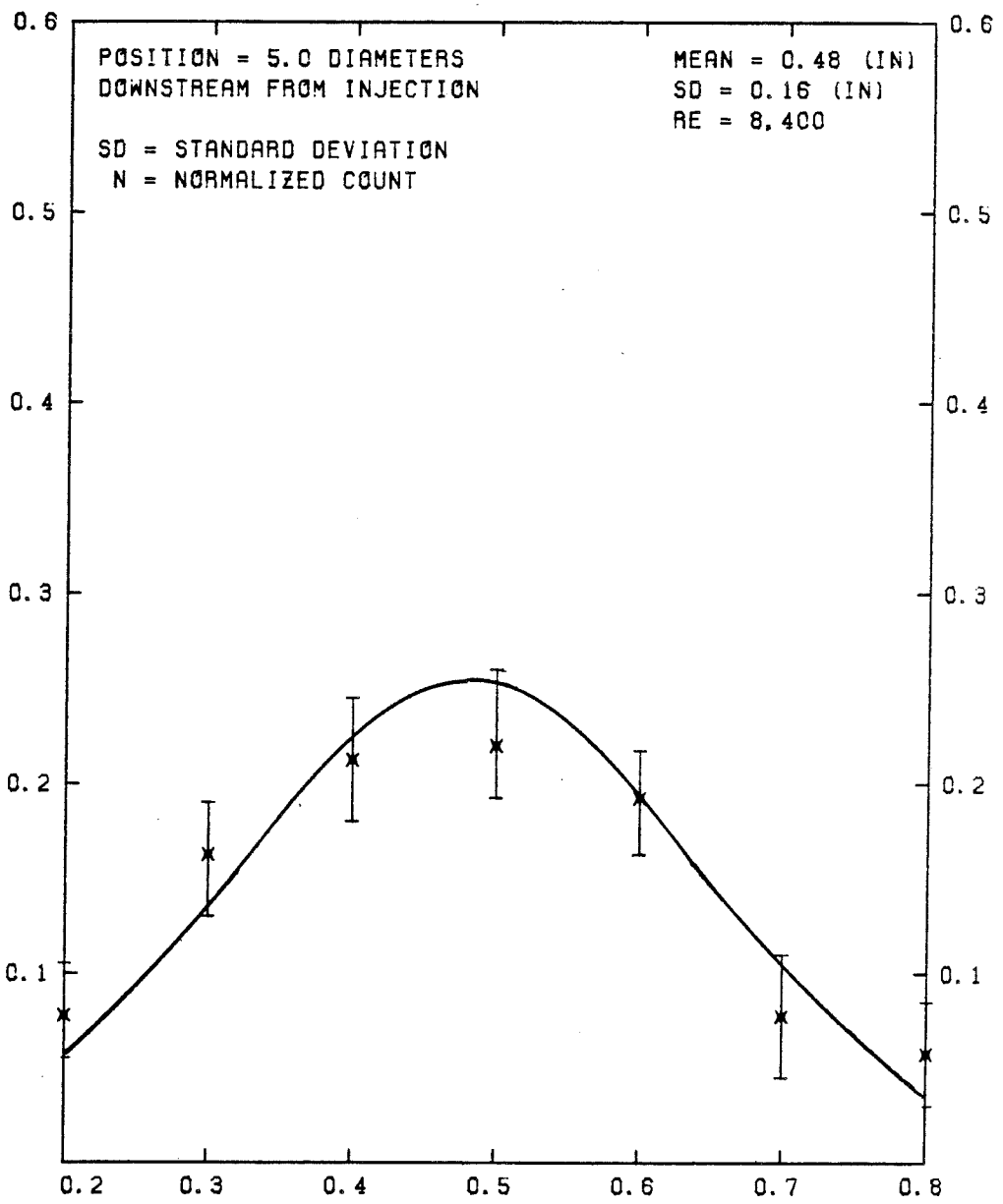

FIGURE A. 4

PVC DISTRIBUTION ACROSS THE FLOW CHANNEL

DATA OBTAINED BY : PARTICLE COLLECTION

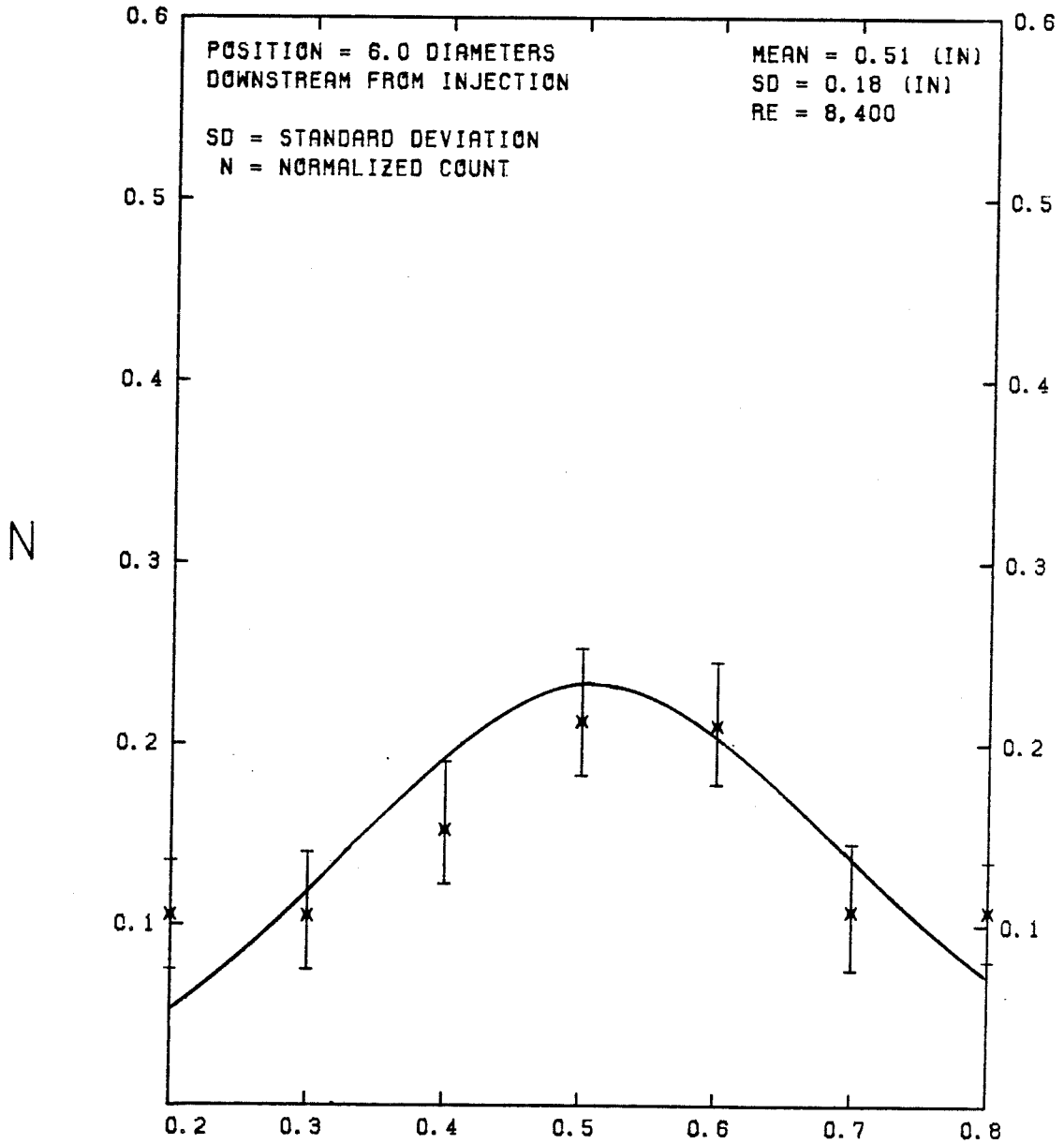

FIGURE A.5

PVC DISTRIBUTION ACROSS THE FLOW CHANNEL

DATA OBTAINED BY : PARTICLE COLLECTION

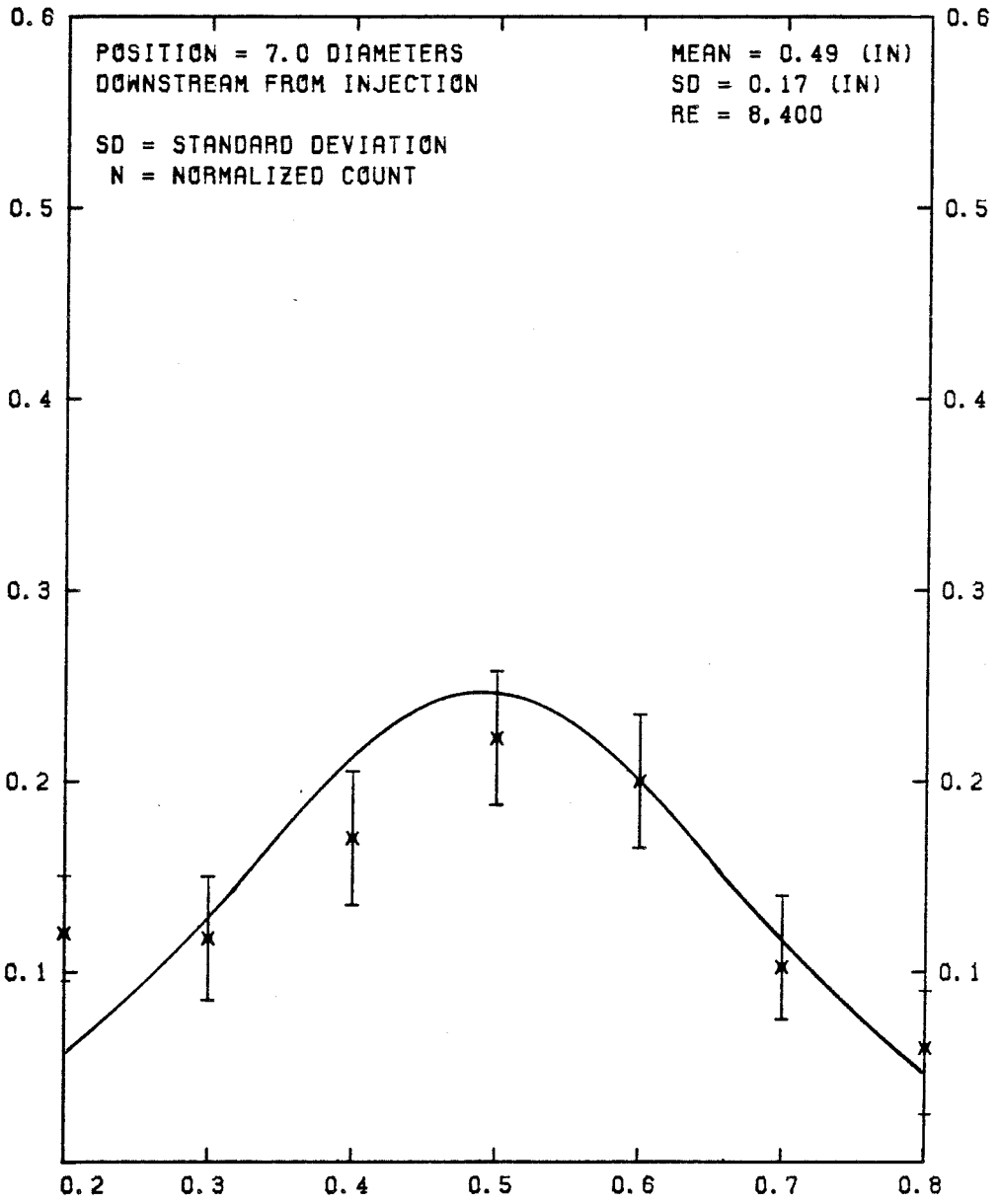

FIGURE A.6

PVC DISTRIBUTION ACROSS THE FLOW CHANNEL

DATA OBTAINED BY : LDA COUNTING

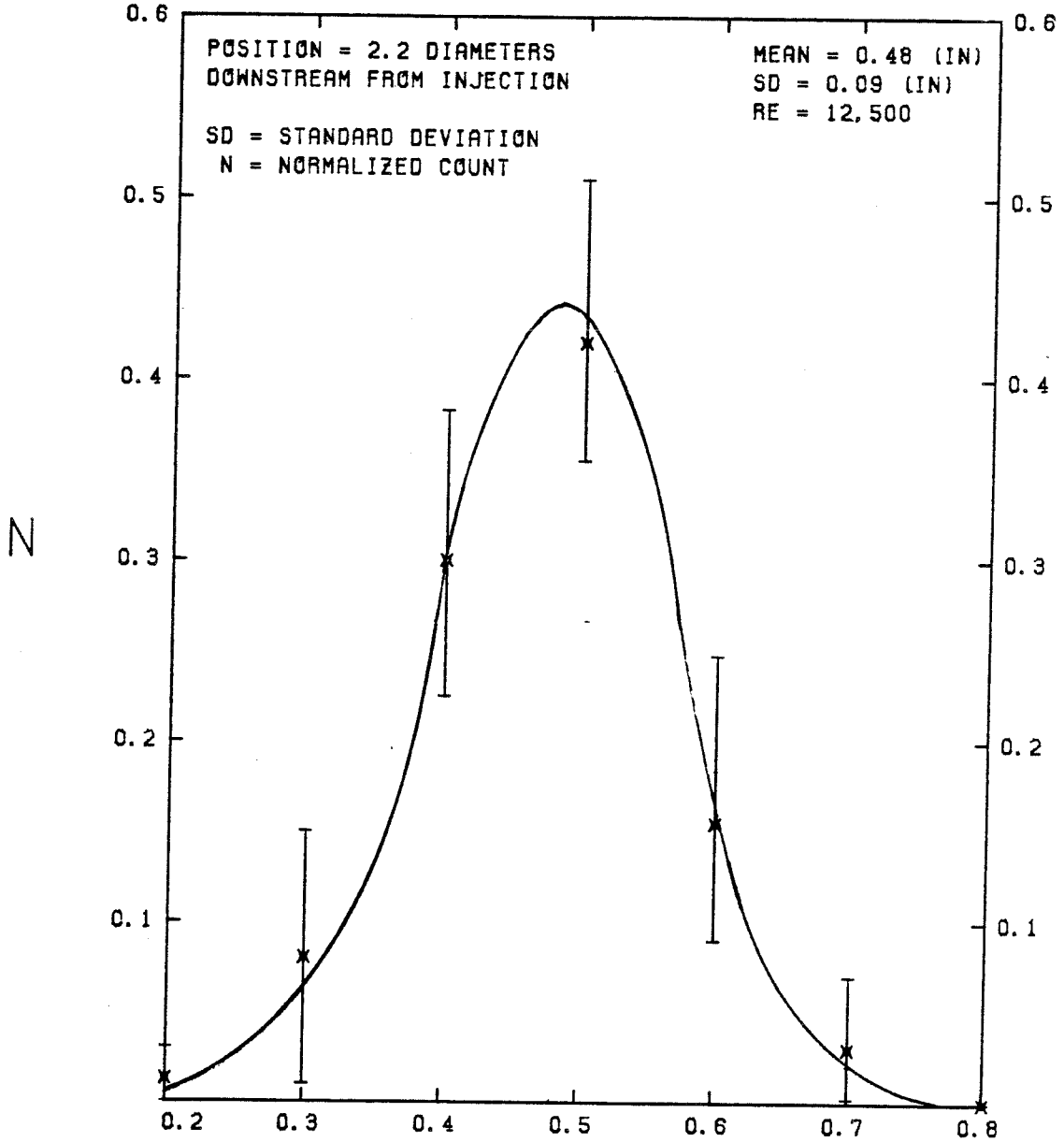

FIGURE A.7

PVC DISTRIBUTION ACROSS THE FLOW CHANNEL

DATA OBTAINED BY : LDA COUNTING

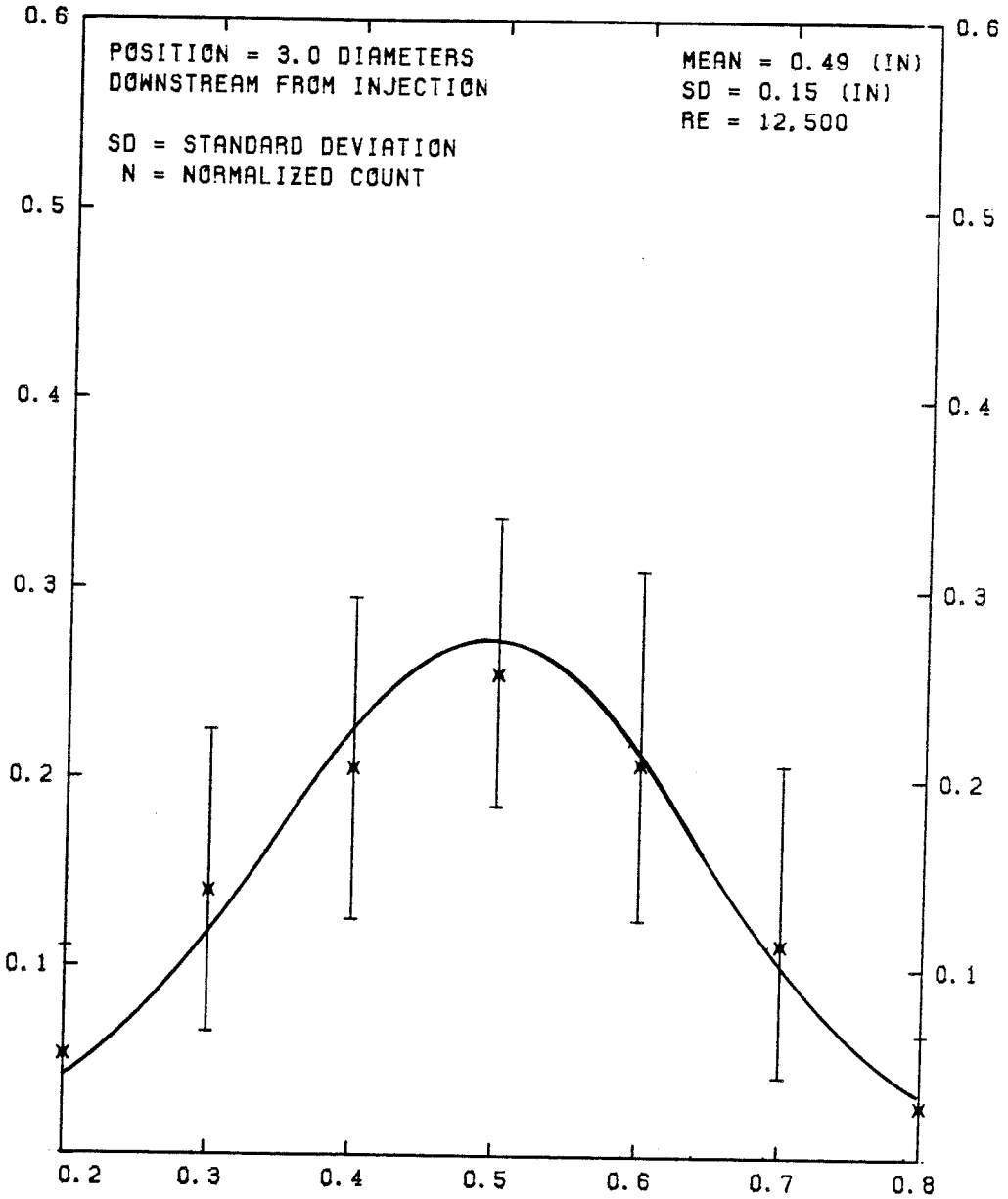

FIGURE A.8

PVC DISTRIBUTION ACROSS THE FLOW CHANNEL

DATA OBTAINED BY : LDA COUNTING

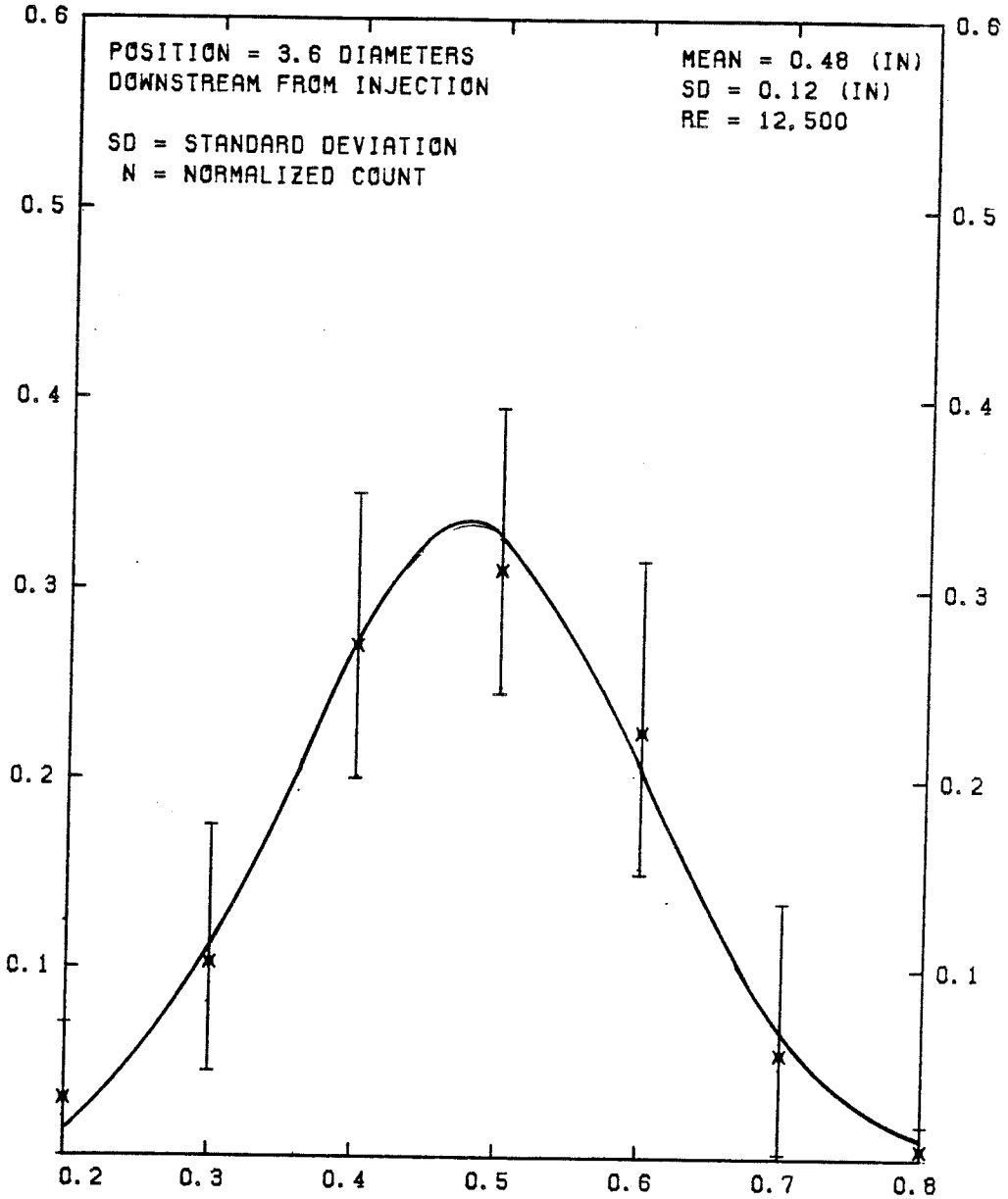

FIGURE A.9

PVC DISTRIBUTION ACROSS THE FLOW CHANNEL

DATA OBTAINED BY : PARTICLE COLLECTION

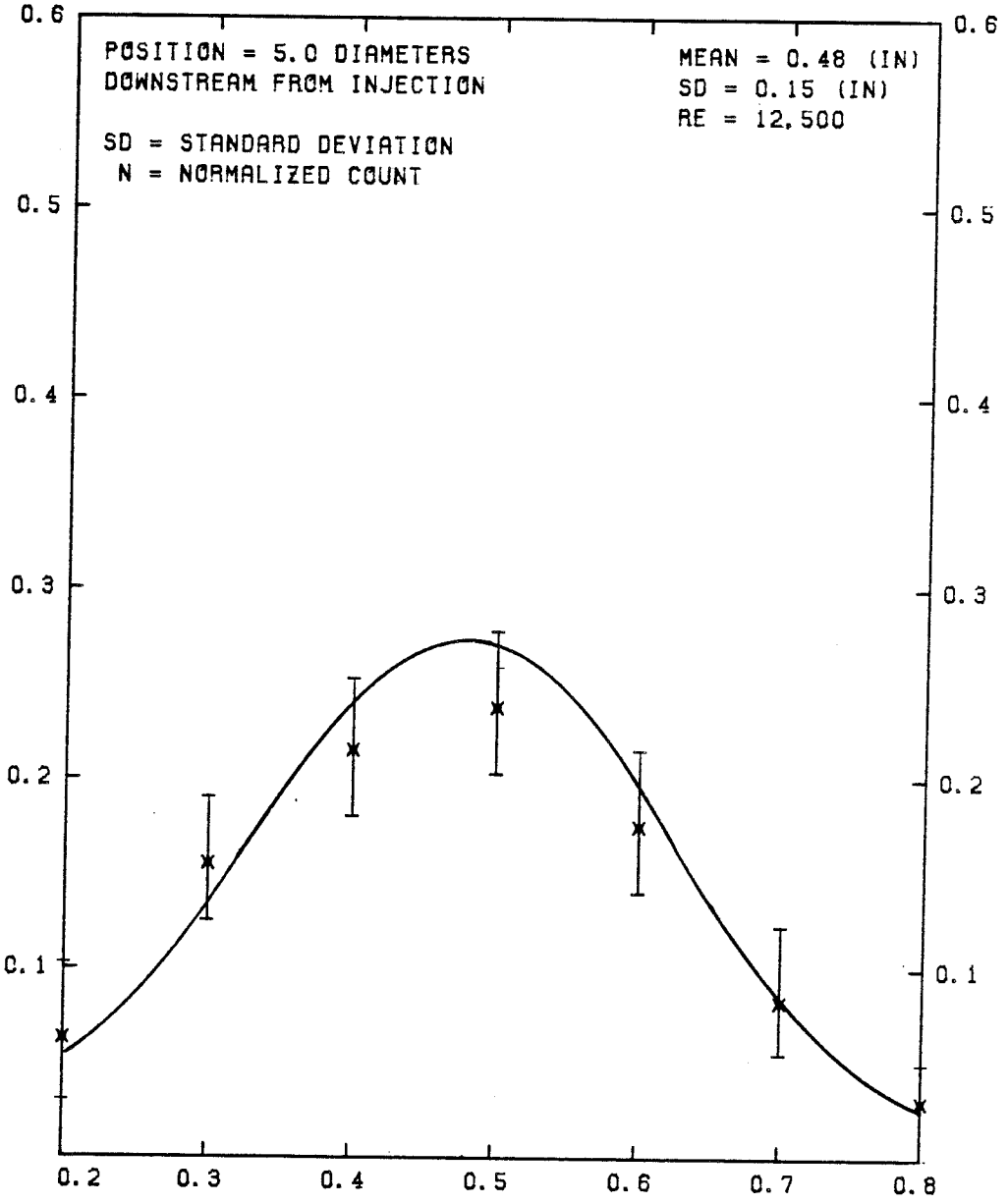

FIGURE A. 10

PVC DISTRIBUTION ACROSS THE FLOW CHANNEL

DATA OBTAINED BY : LDA COUNTING

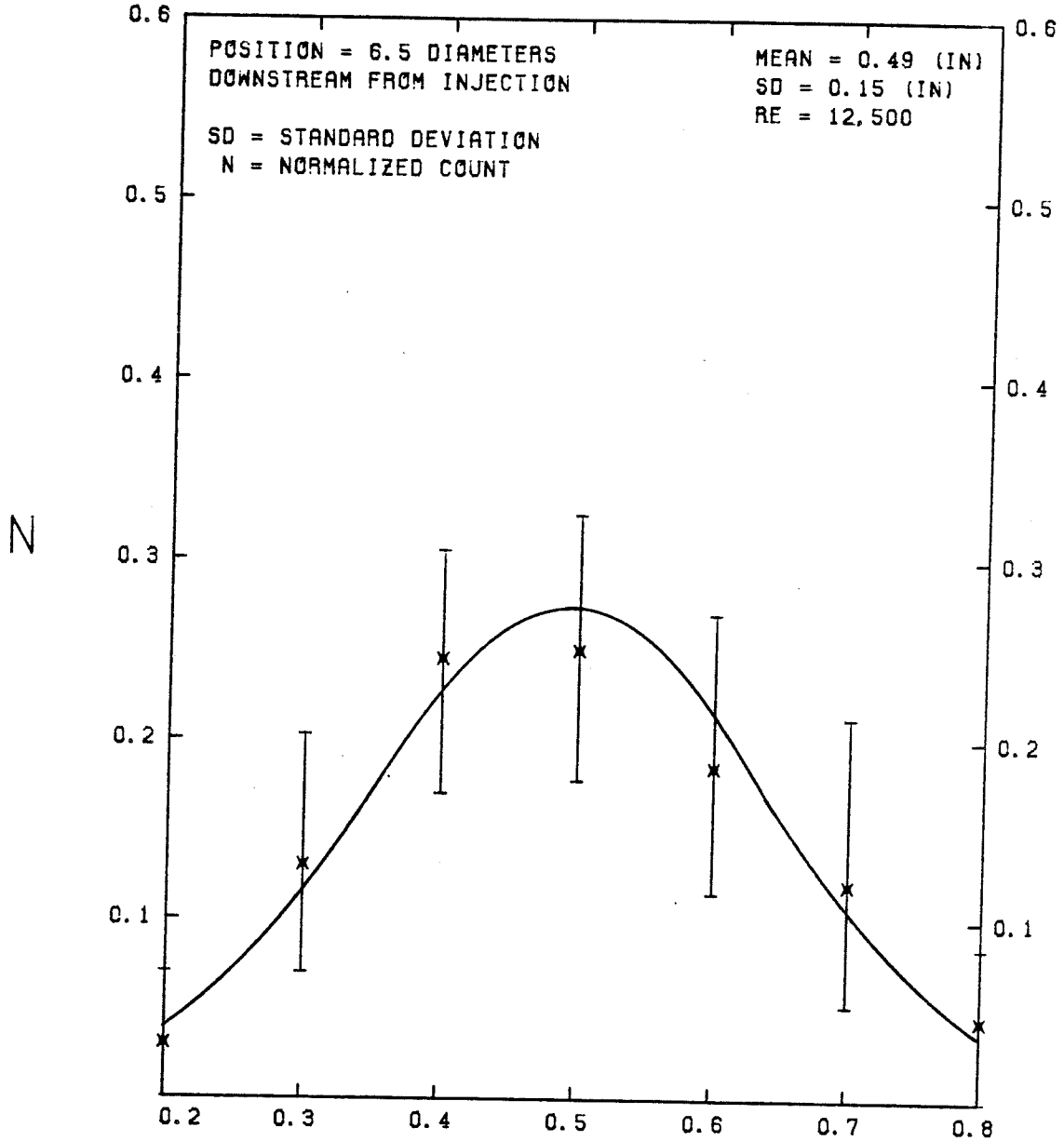

FIGURE A. 11

PVC DISTRIBUTION ACROSS THE FLOW CHANNEL

DATA OBTAINED BY : PARTICLE COLLECTION

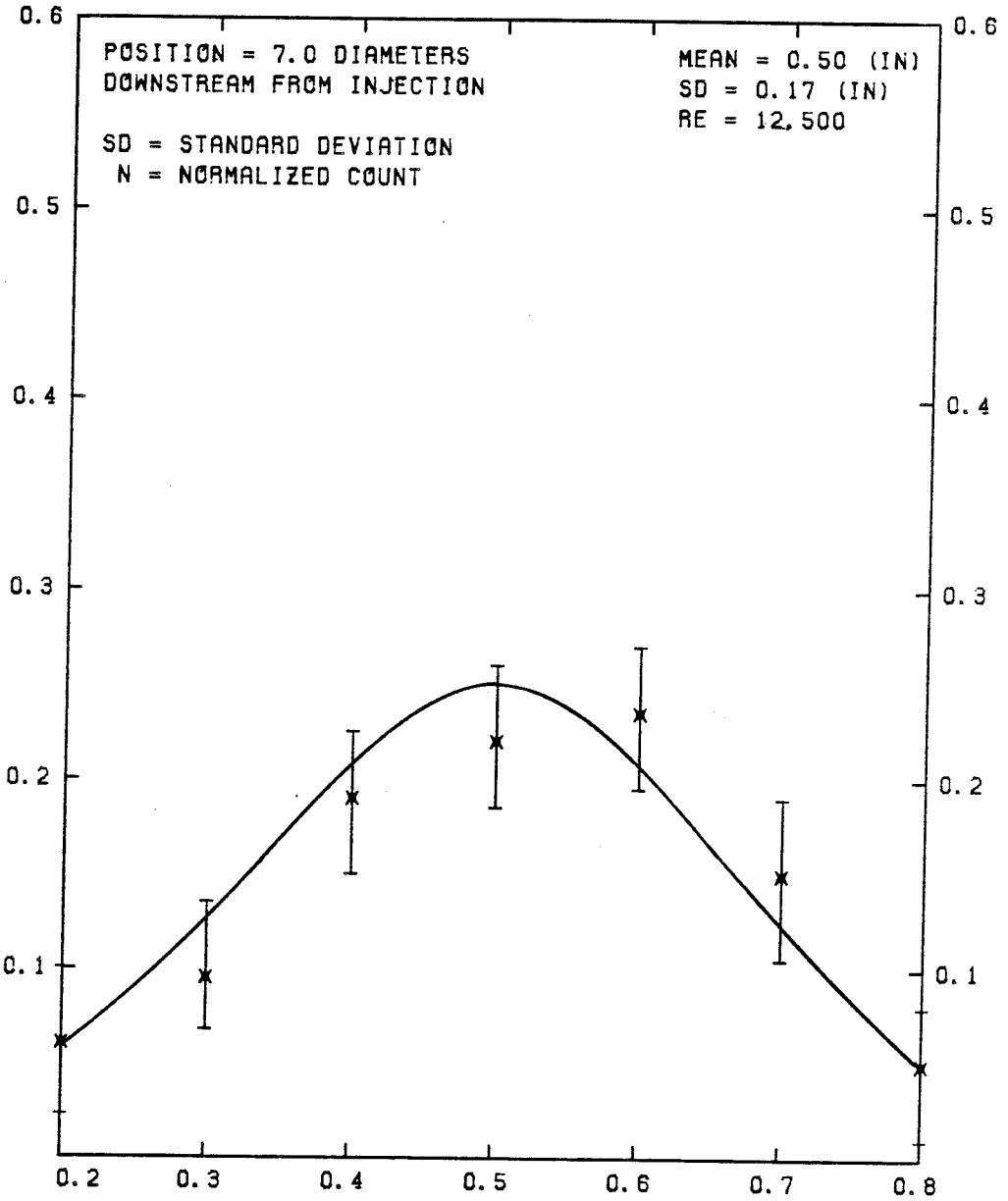

FIGURE A.12

PVC DISTRIBUTION ACROSS THE FLOW CHANNEL

DATA OBTAINED BY : PARTICLE COLLECTION

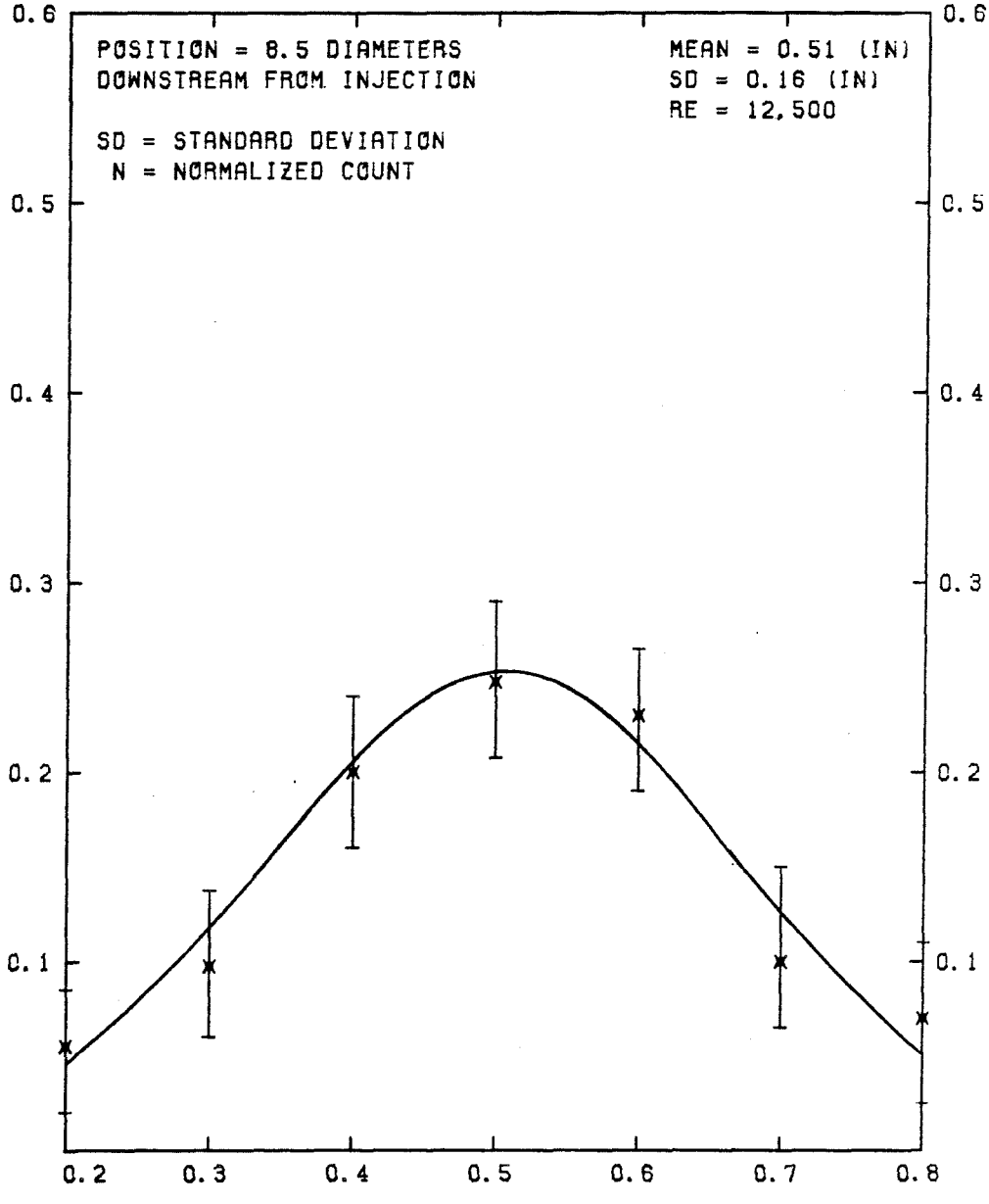

FIGURE A.13

PVC DISTRIBUTION ACROSS THE FLOW CHANNEL

DATA OBTAINED BY : PARTICLE COLLECTION

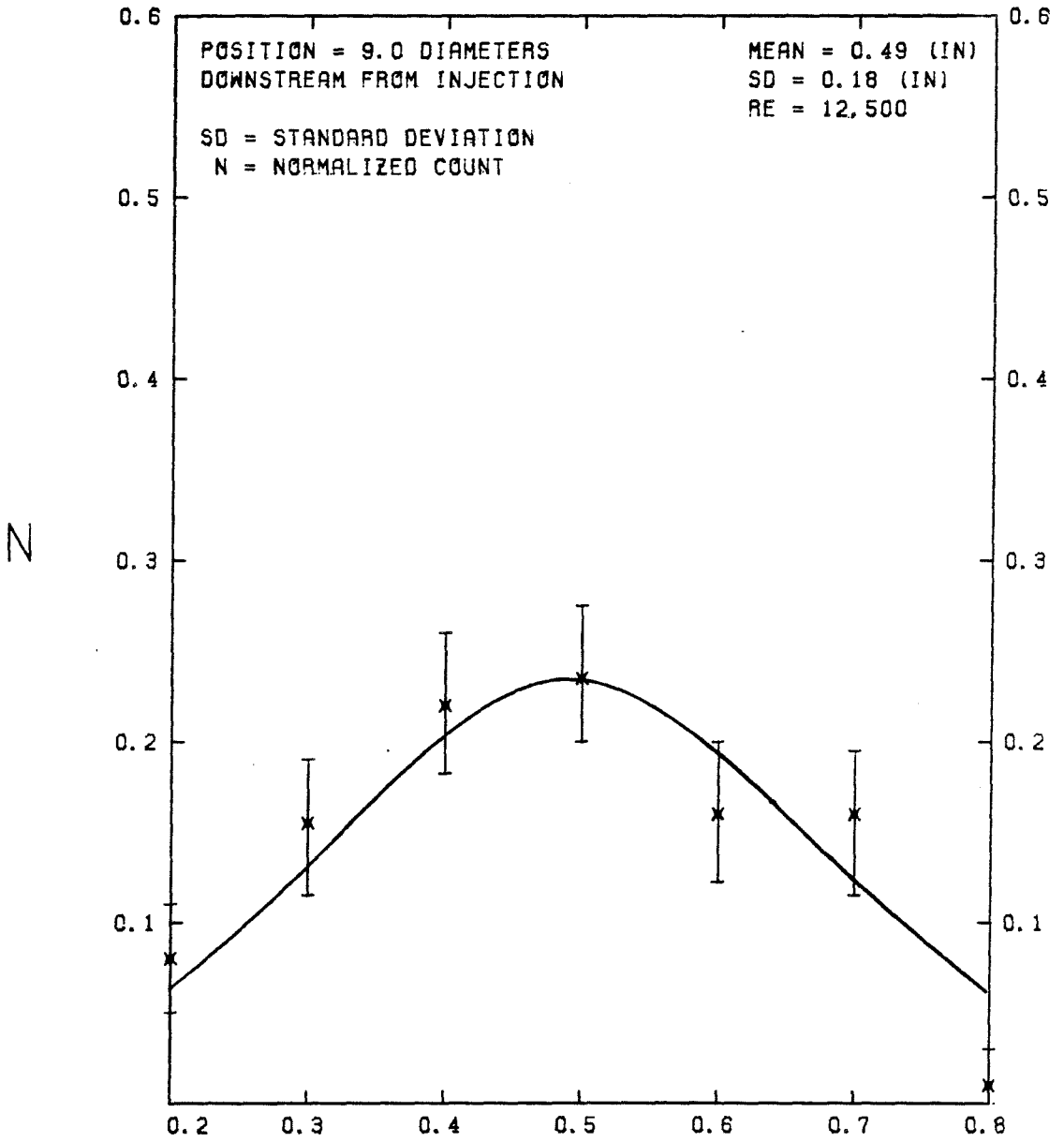

FIGURE A.14

PVC DISTRIBUTION ACROSS THE FLOW CHANNEL

DATA OBTAINED BY : PARTICLE COLLECTION

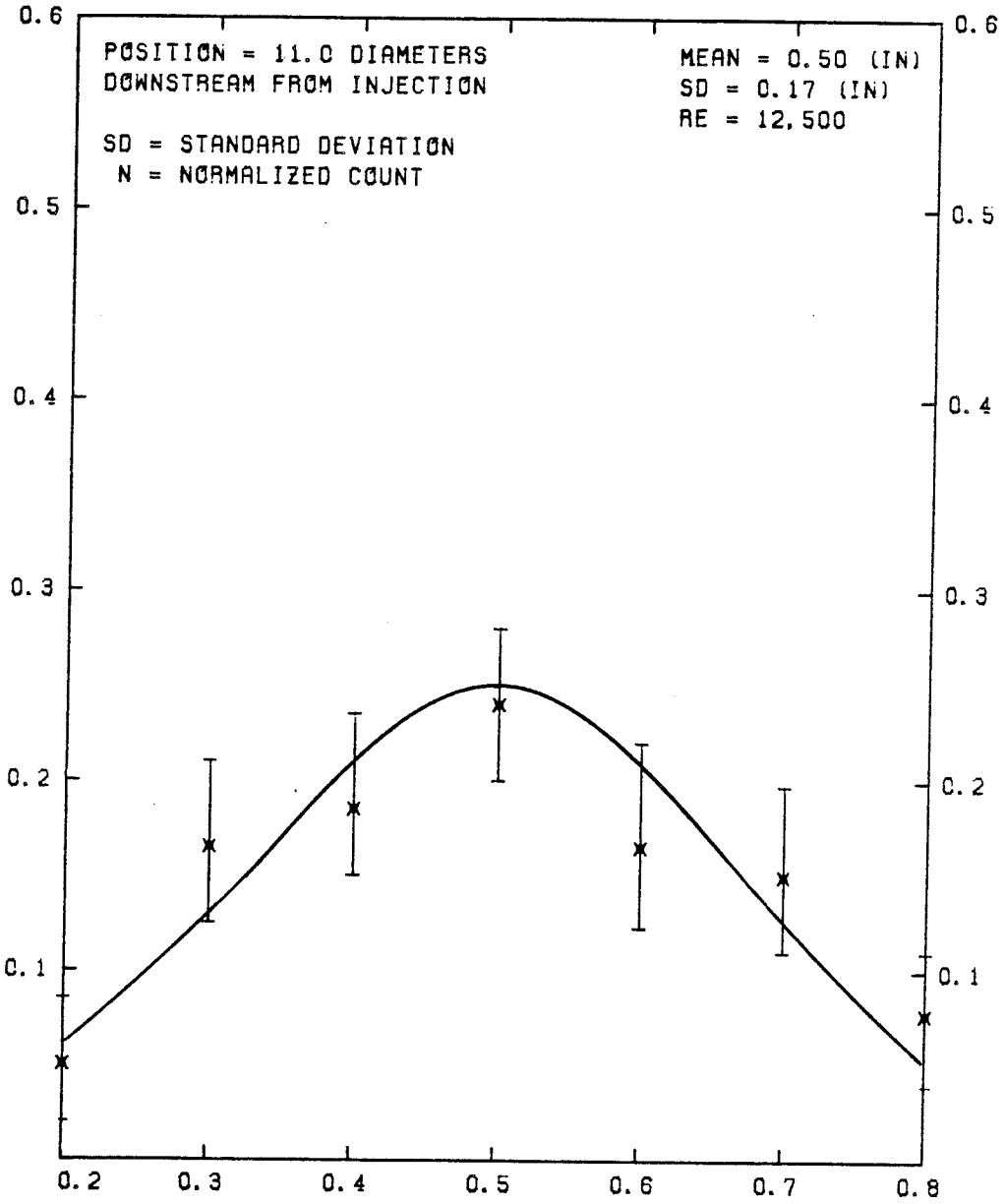

FIGURE A.15

PVC DISTRIBUTION ACROSS THE FLOW CHANNEL

DATA OBTAINED BY : LDA COUNTING

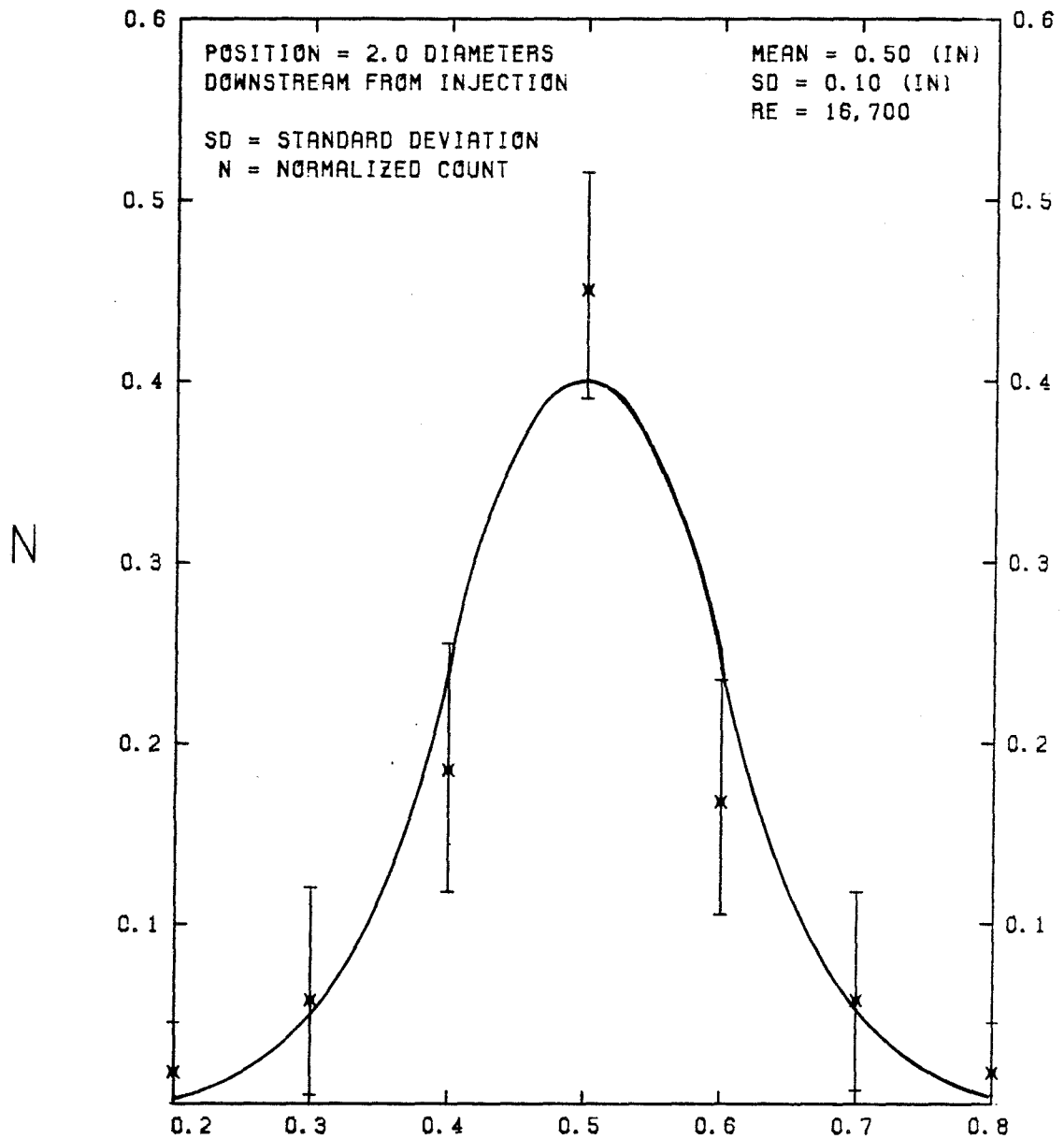

FIGURE A.16

PVC DISTRIBUTION ACROSS THE FLOW CHANNEL

DATA OBTAINED BY : PARTICLE COLLECTION

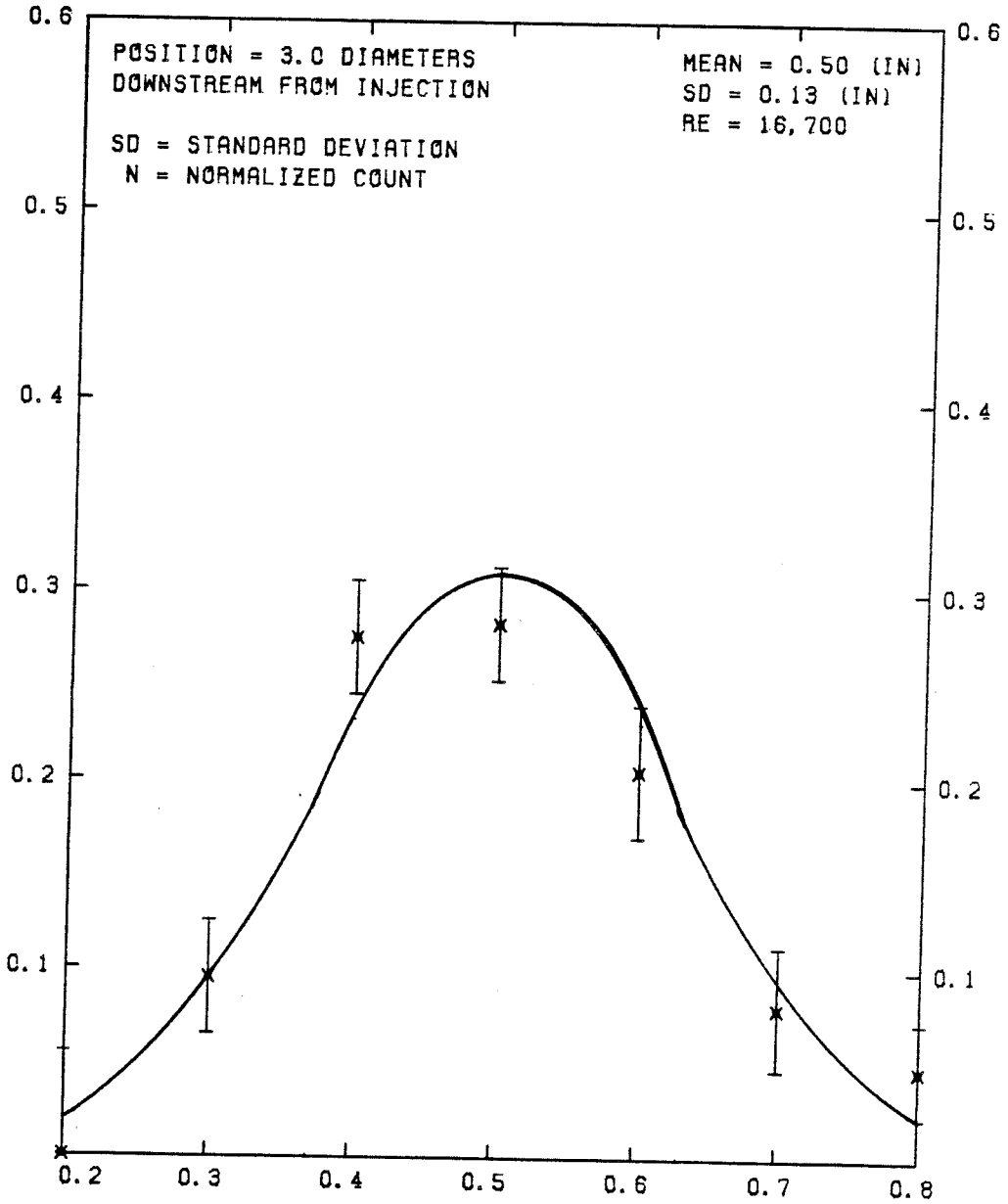

FIGURE A.17

PVC DISTRIBUTION ACROSS THE FLOW CHANNEL

DATA OBTAINED BY : LDA COUNTING

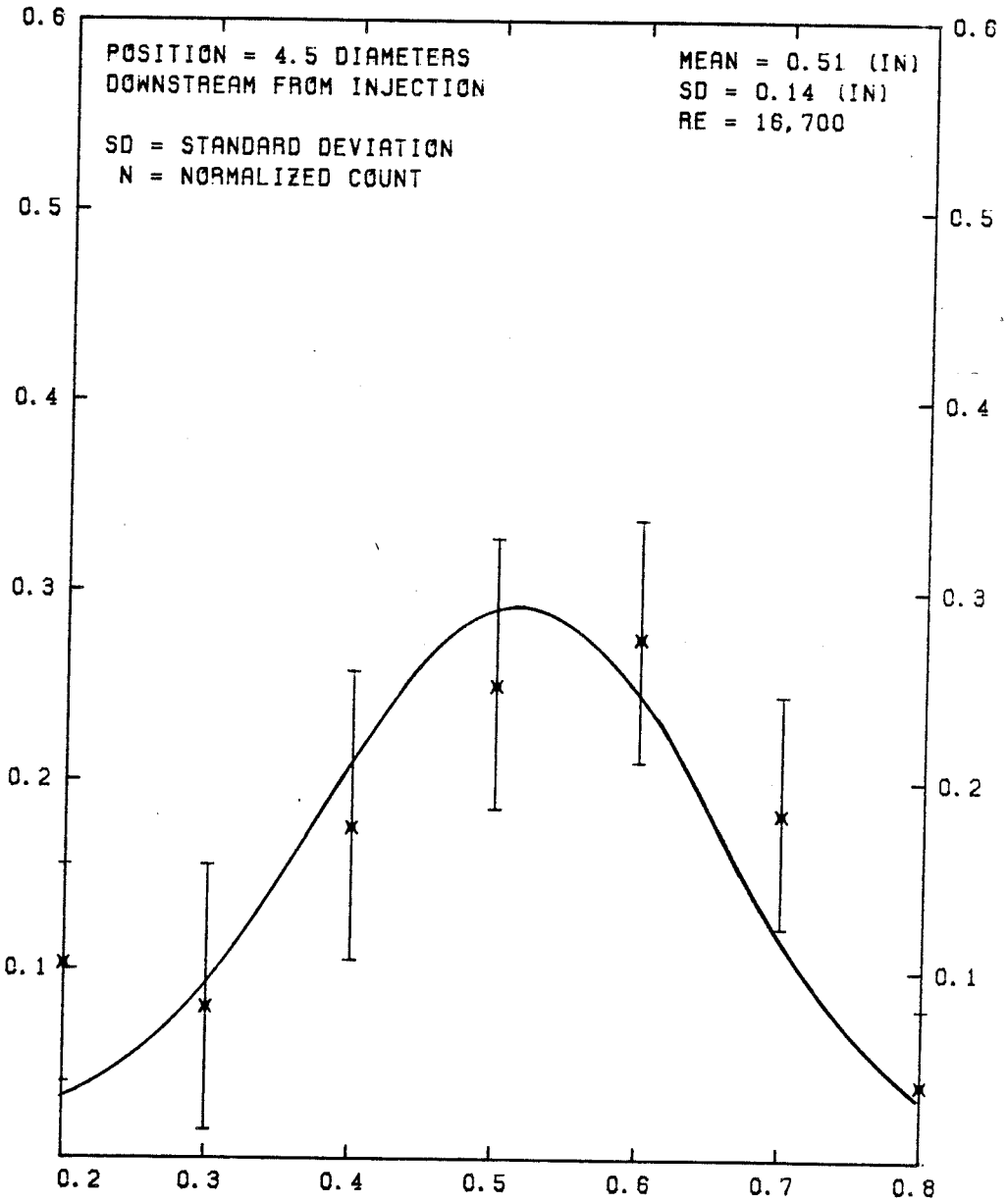

FIGURE A.18

PVC DISTRIBUTION ACROSS THE FLOW CHANNEL

DATA OBTAINED BY : PARTICLE COLLECTION

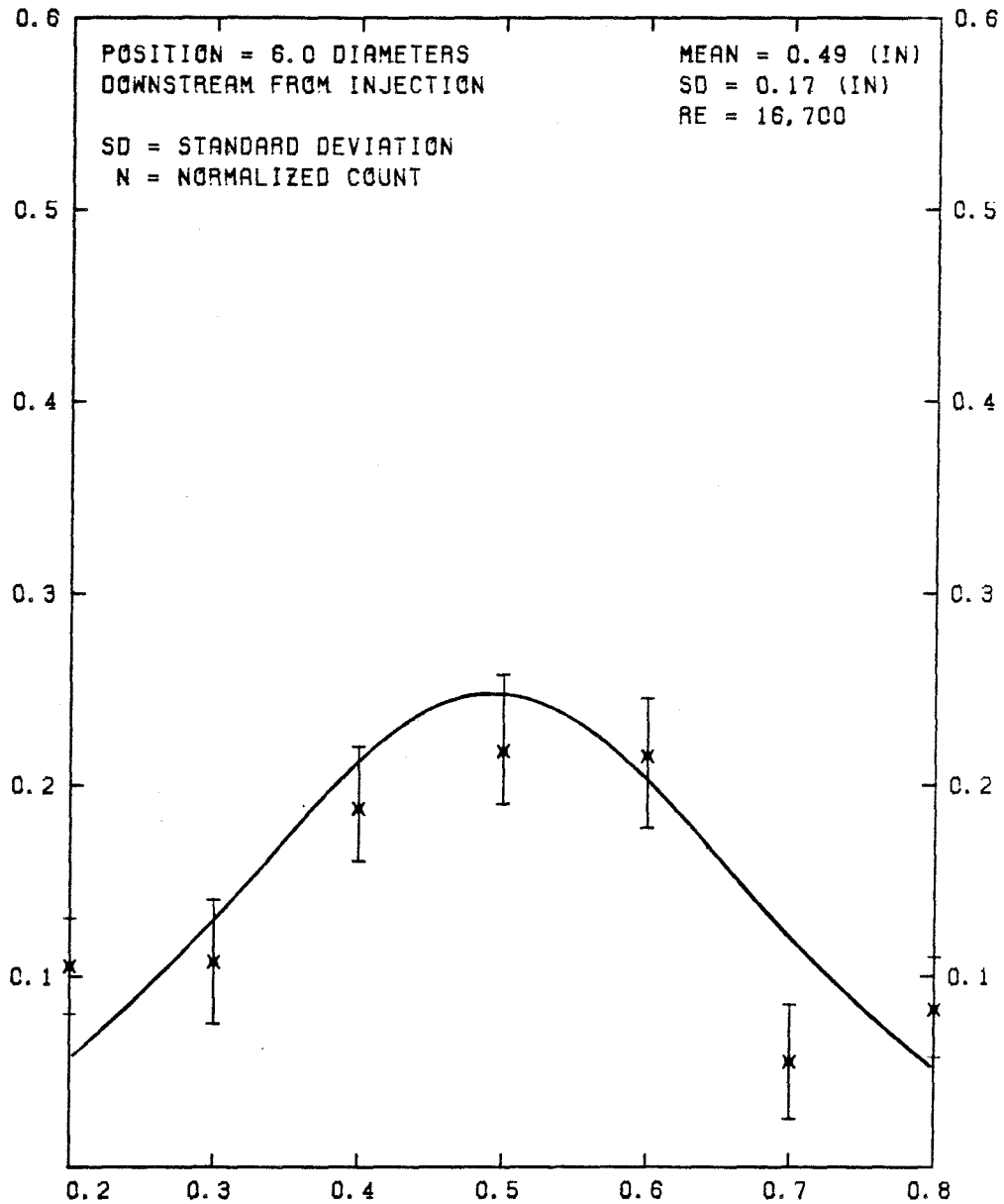

FIGURE A.19

PVC DISTRIBUTION ACROSS THE FLOW CHANNEL

DATA OBTAINED BY : PARTICLE COLLECTION

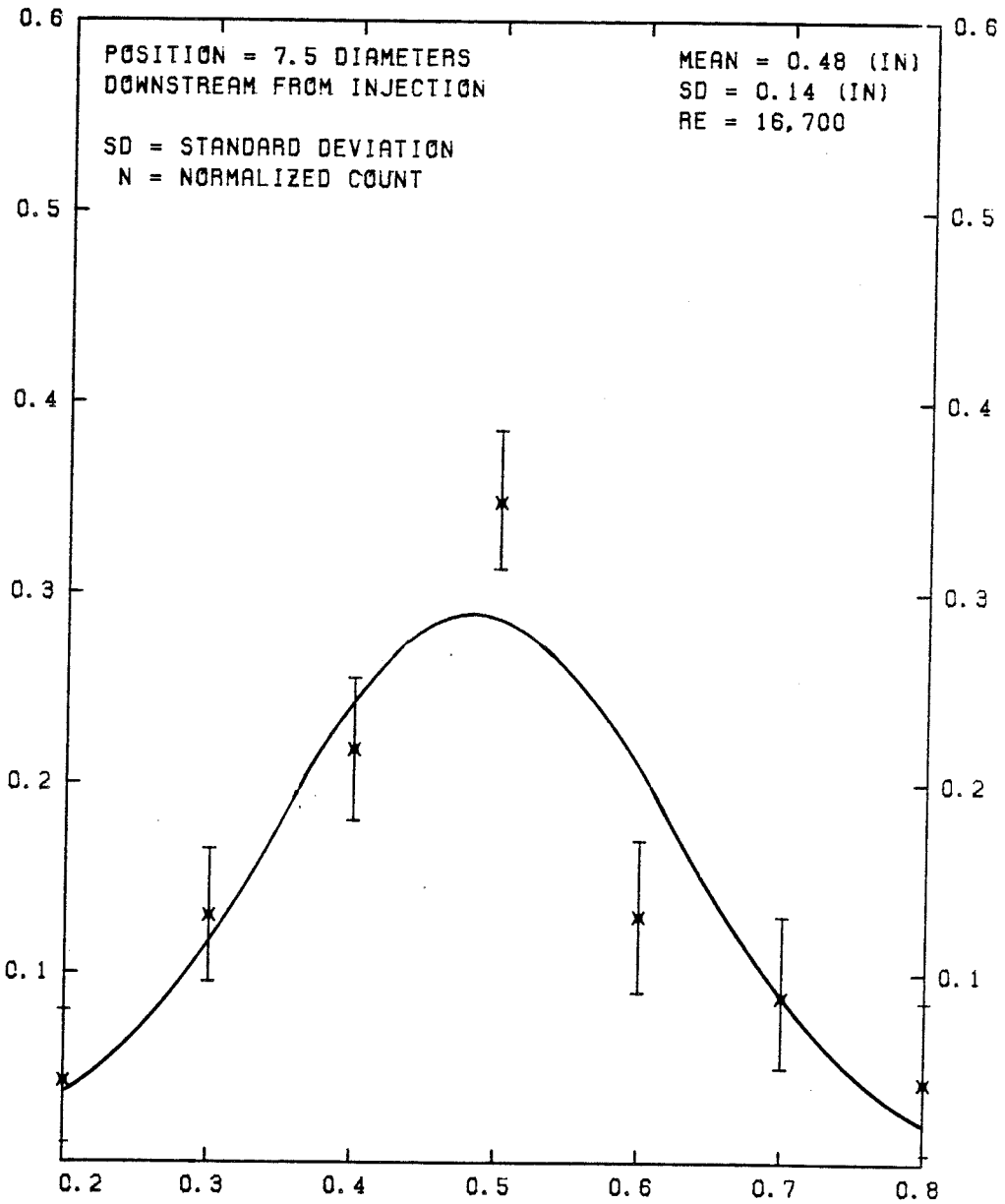

FIGURE A.20

PVC DISTRIBUTION ACROSS THE FLOW CHANNEL

DATA OBTAINED BY : PARTICLE COLLECTION

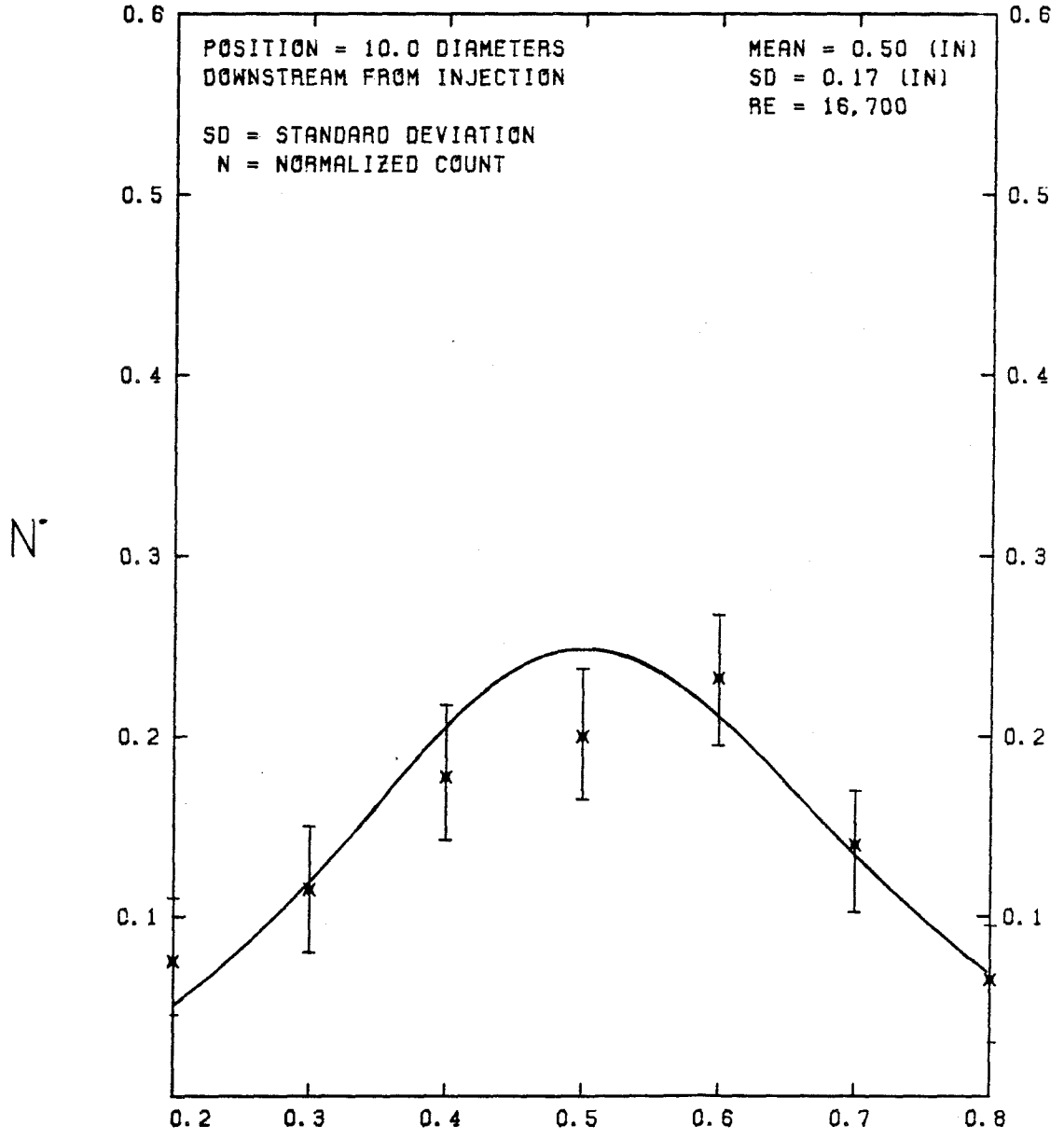

FIGURE A.21

PVC DISTRIBUTION ACROSS THE FLOW CHANNEL

DATA OBTAINED BY : PARTICLE COLLECTION

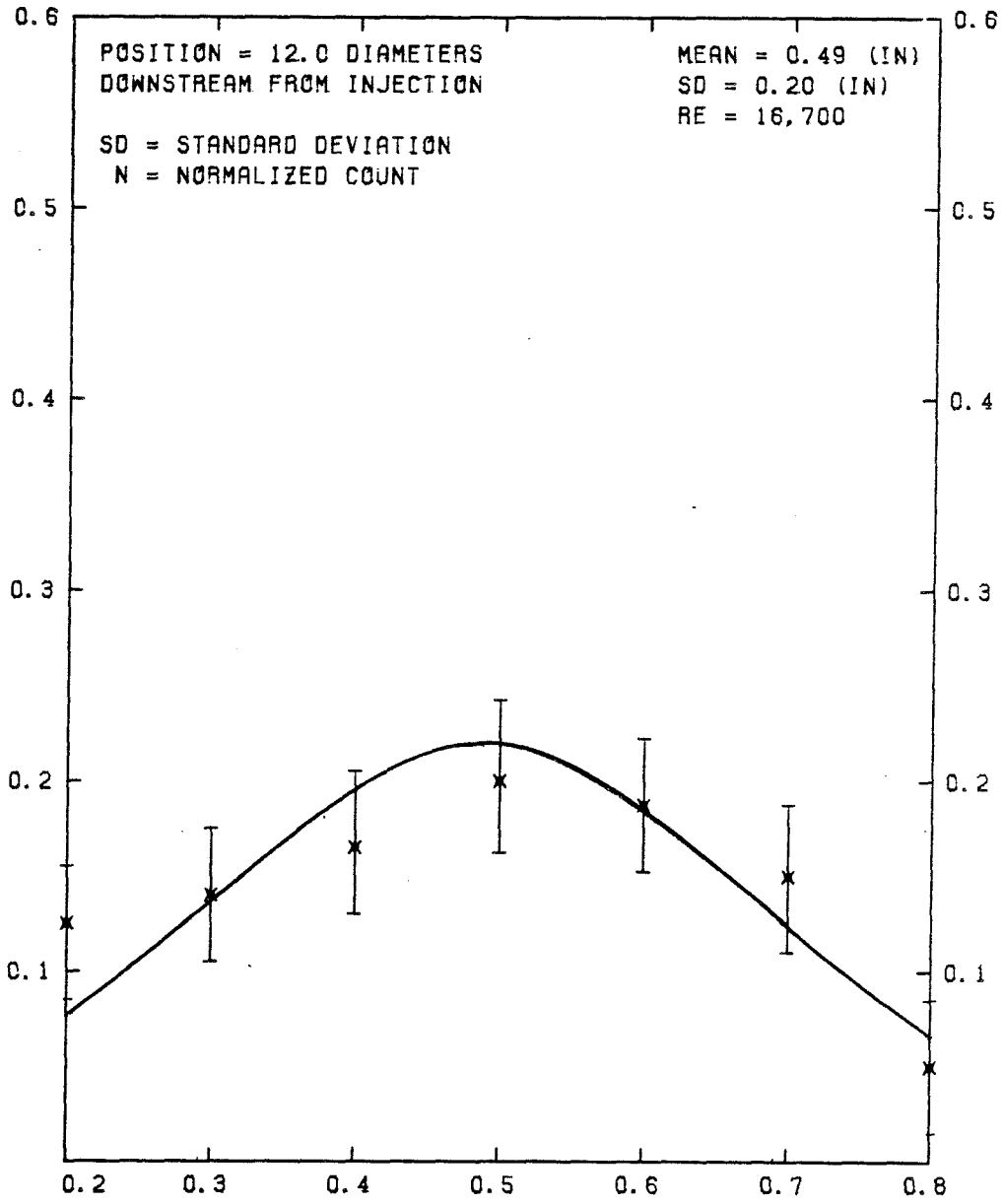

FIGURE A.22

PVC DISTRIBUTION ACROSS THE FLOW CHANNEL

DATA OBTAINED BY : LDA COUNTING

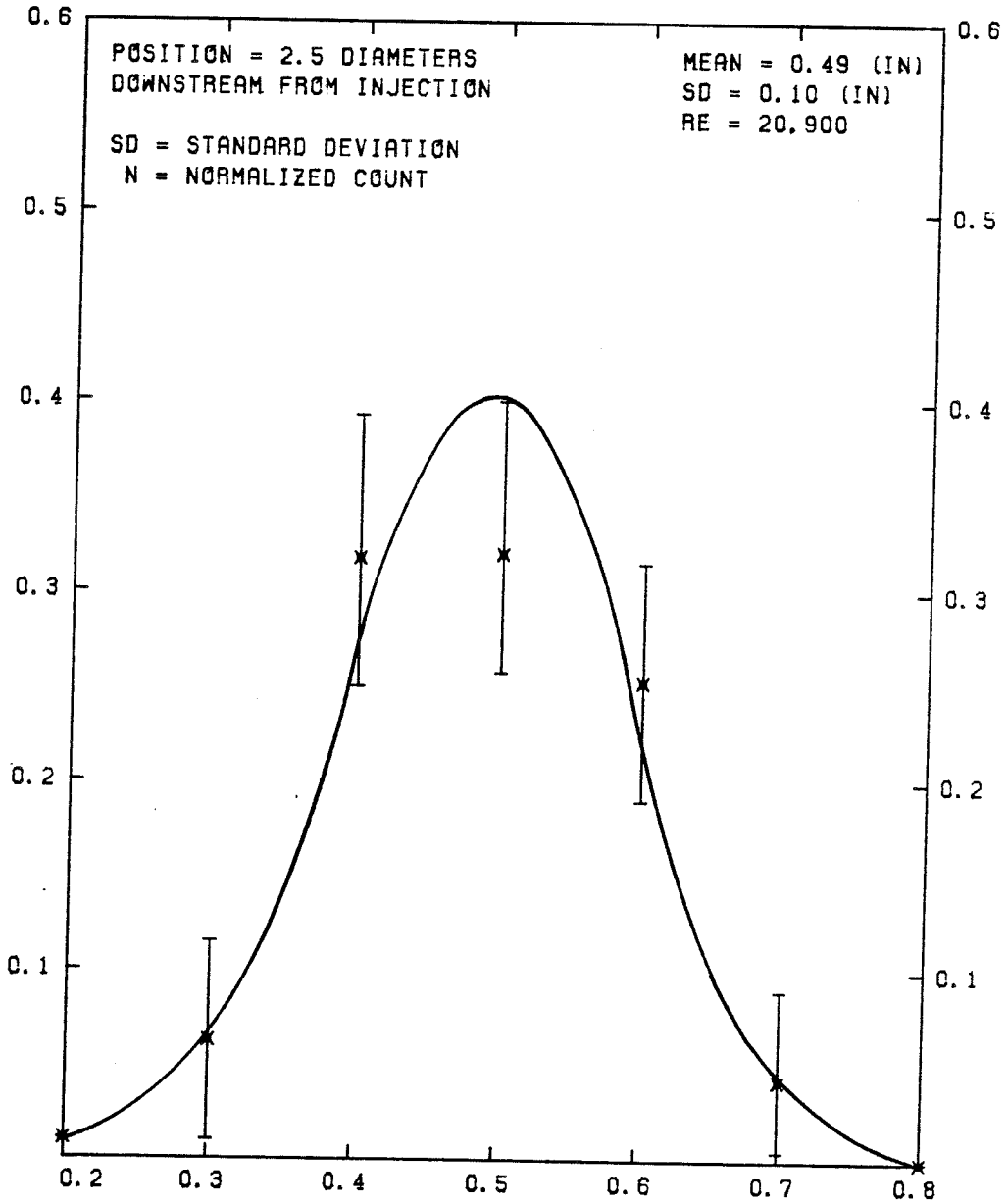

FIGURE A.23

PVC DISTRIBUTION ACROSS THE FLOW CHANNEL

DATA OBTAINED BY : LDA COUNTING

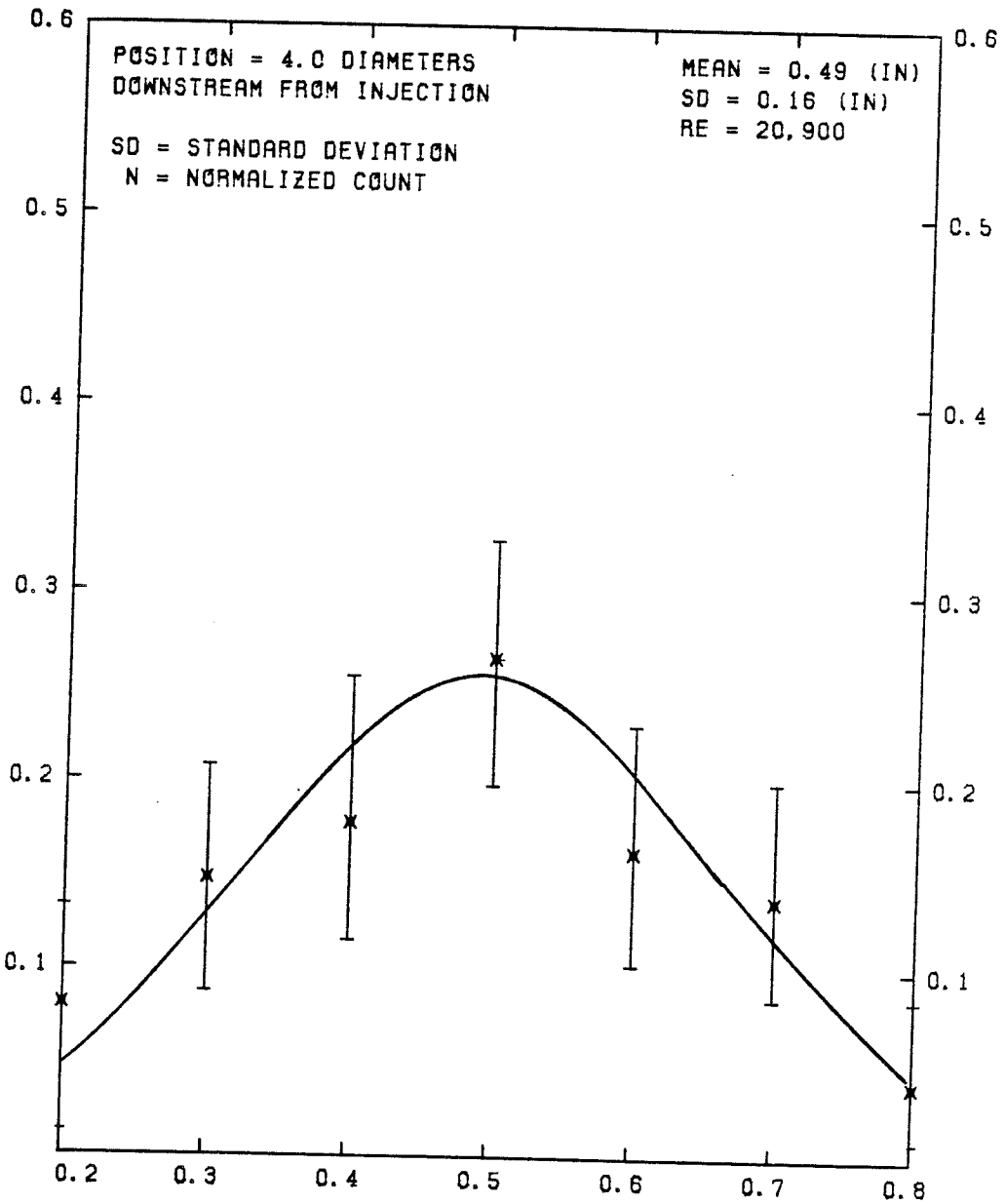

FIGURE A.24

PVC DISTRIBUTION ACROSS THE FLOW CHANNEL

DATA OBTAINED BY : PARTICLE COLLECTION

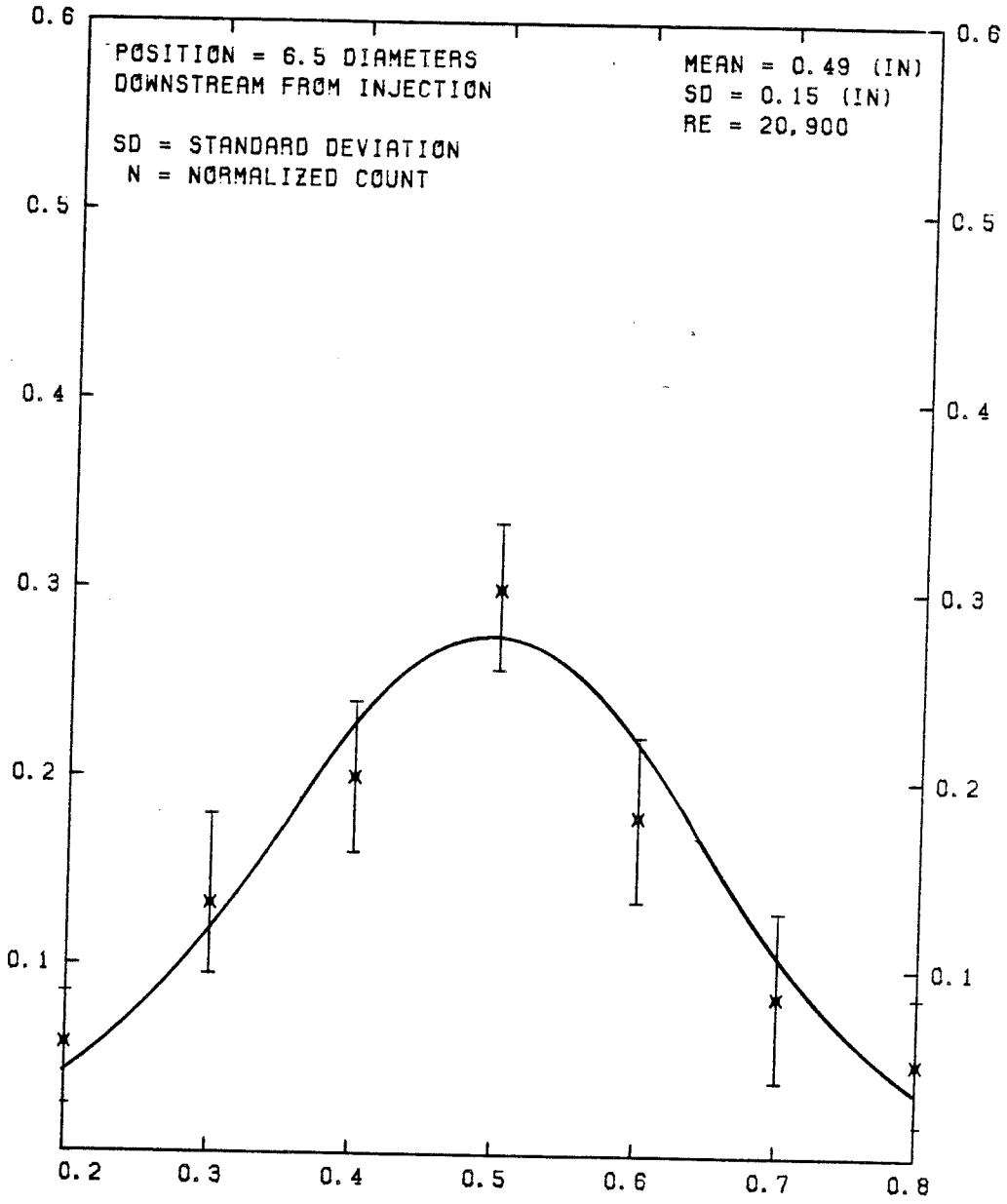

FIGURE A.25

PVC DISTRIBUTION ACROSS THE FLOW CHANNEL

DATA OBTAINED BY : LDA COUNTING

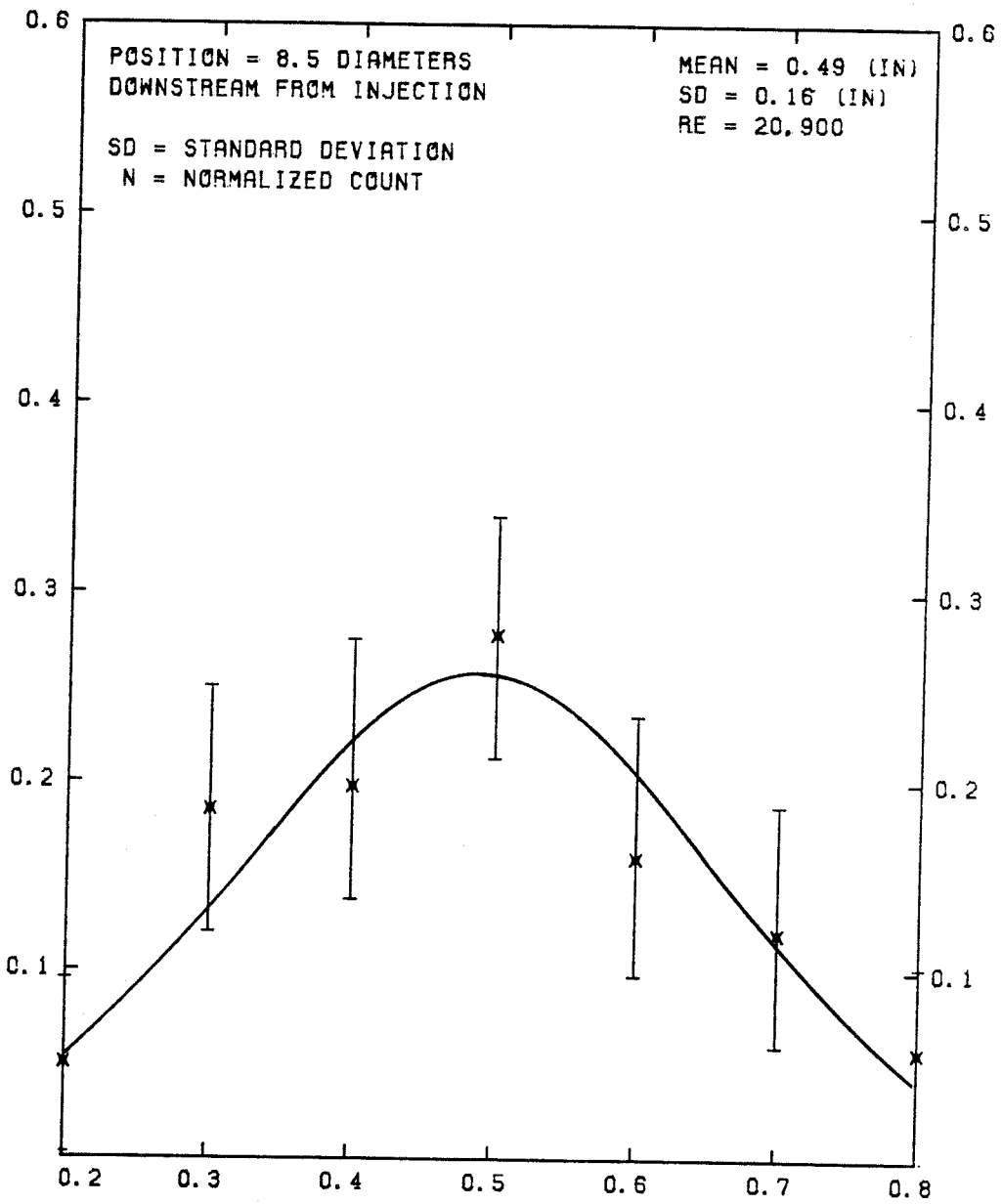

FIGURE A.26

PVC DISTRIBUTION ACROSS THE FLOW CHANNEL

DATA OBTAINED BY : PARTICLE COLLECTION

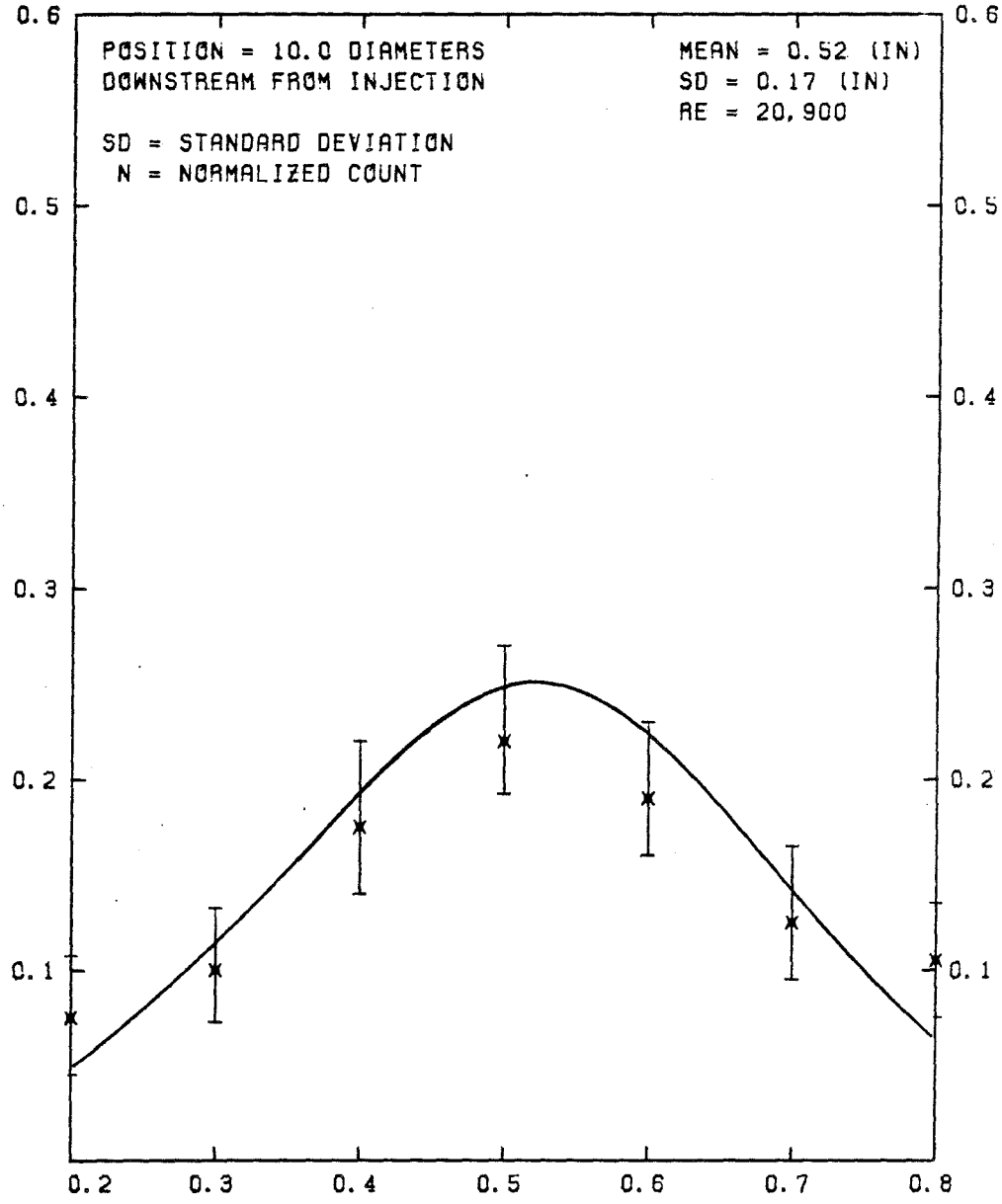

FIGURE A.27

PVC DISTRIBUTION ACROSS THE FLOW CHANNEL

DATA OBTAINED BY : PARTICLE COLLECTION

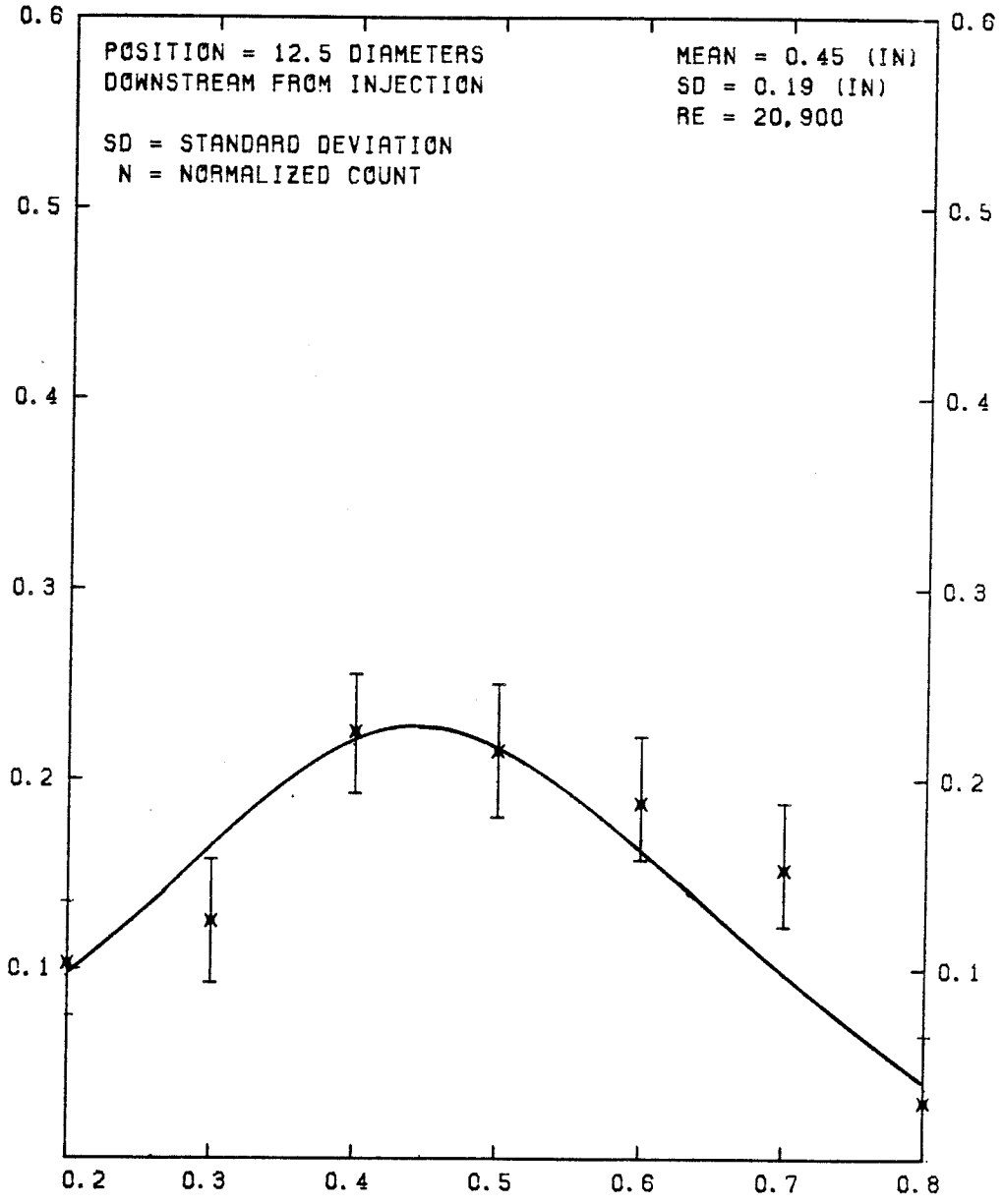

FIGURE A.28